# Application of Quartz Crystal Microbalance to Measure the Rheology of Complex Colloidal Suspensions

Johannes Andries Botha

Submitted in accordance with the requirements for the degree of
Doctor of Philosophy

The University of Leeds
School of Chemical and Process Engineering

November, 2018

The candidate confirms that the work submitted is his/her own, except where work which has formed part of jointly-authored publications has been included. The contribution of the candidate and the other authors to this work has been explicitly indicated in Chapter 4. The candidate confirms that appropriate credit has been given within the thesis where reference has been made to the work of others.

## Acknowledgements

I would firstly like to thank David Harbottle for his support in helping me improve myself at a professional and academic level. Your input in key areas including presentation skills, oral and written communication and networking has both aided me professionally and helped me to improve the overall project to be of a better standard. The skills and talents I have learned thanks to your input is something that extends well beyond this project, and I am very thankful for it.

I would also like to thank Timothy Hunter. Your warm and approachable nature is part of the reason why I asked you for a summer placement back in 2012. Because of your passion, I have since grown to love the colloids/rheology subject area which made me choose this project in the first place. Your input helped me remain calm and focused throughout the project, and your academic knowledge has also been of great support every step of the way. I am very thankful to have been under both your and David's academic supervision throughout this project.

I am indebted to Diethelm Johannsmann for his academic input and technical discussions. I am very thankful you invited me to work with you and your team at the Clausthal University of Technology, Germany. Your excitement and suggestions have led to significant improvements to the overall project and has also enabled me to look at information from a different perspective. I loved my stay there and your effort to ensure that I always feel included and comfortable is greatly appreciated as well.

Many thanks also to the members of professor Johannsmann's team for their support and friendship during my stay. Arne, your technical insight and enthusiasm for new ideas and concepts has been fantastic and added to making our coffee breaks so much more interesting. Your German wordplays also helped me form a basic grasp to the language and was very entertaining even though I only managed to understand about

10% of it! Frederick, many thanks for your help and support with my experiments, especially during the latter half of my stay. Your absolute willingness to help whenever possible was greatly appreciated. I am also thankful for Astrid and Judith for their technical support in operating QCM devices. You were always there to help, and you always had a smile on your faces. Heike, your friendliness and warm, supportive nature is greatly appreciated. I always enjoyed our discussions about random daily events. I also love how we still stayed in contact even after I left where we try to compare to see who has the most snow. You always won. Rebecca, thank you for your friendship and always inviting me to every event. I loved our evenings over at the Kellerclub. I never knew one place could have so many board games, and learning how you guys play Doppelkopf has been very entertaining; especially when watching how the hidden alliances and betrayals unfold in a single card game. Philipp, I had a great time sharing the office with you and Bruce. Every day, like clockwork, you'd stop by and remind me that it's time for a coffee break. You are always calm and composed, which helps everyone unwind during these breaks. Alena, I always enjoyed having coffee breaks and going for lunch with you and the others. I will never forget going to my first proper German Christmas market with you and Rebecca. I hope everything is going well with your project (I remember you had just started it at the time of my visit).

I am also very thankful for the technicians and staff within the university's department who have trained me in several analytical techniques and helped me sort out any issues with administration. Abigail Ward, Ben Douglas, Stuart Micklethwaithe, Chris Hodges and Susanne Patel, the contributions you made to the department is what significantly adds to its overall value. I am certain that there are many other staff members who show the same level of performance that I have not been in direct

contact with who have also contributed to helping me sort out any equipment training or issues with bureaucracy; you have my profound thanks.

My father, Renier Hanekom, is half the reason why I could even pursue a PhD in the first place. You have been a great support throughout my academic career. Your ability to make the difficult decisions in life which provided me with an endless amount of opportunities is something I will always be thankful for. The other half of the reason is because of my mother Adrie Hanekom. Your strong drive, positivity and understanding helped me keep my head above the water and your practical solutions to any problem I had made the whole process a lot simpler. Thanks to the input from you both, I was given the chance to make the best out of this opportunity.

My brother Pieter Botha has always been there for me when I needed to relax after a difficult week. Your relaxed attitude and our fun gaming experiences have always helped me unwind. Your loyalty and integrity are the things I look up to. Megan Botha, you have been a fantastic sister since before the start of the project. You have always provided me with a warm welcome and always made me feel included. To know that I have you both to support me is invaluable.

Weixuan Ding, our travels were needed buddy. We have been through some tough, but necessary times together. You have shown me how to learn and benefit from many different situations in life. You have helped me become a better scientist and be more analytical. Our late-night discussions with a nice cup of koffie in the office have resulted in some fantastic theoretical additions to the project. It was fantastic to have someone to share my project and ideas with. This doesn't end here though, we still have a lot of little projects to work on, sights to see, and nasties to discover. Your otherwise unique and rare enthusiasm always necessitates other normal communal engagements.

I also thank my friends Alex and Enya for their friendship and support, and for being available to go on nice walks or play a few games during the evening. I thank Charly for being there in the latter stages of my project where your emotional support, our fun walks and adventures helped keep me on track and sane during the hectic write-up period. You have always been there to lend an ear and see things from an outside perspective.

I would also like to thank my office friends and colleagues for helping provide a pleasant environment on a daily basis. Rob, it was a pleasure staring at your face for an entire year. May our future chillies cause much pain in the stomachs of any unsuspecting victims who dare eat them. Thoko, our XRD runs were always a treat, the burgers at Rustica will never be forgotten, including all of that sweet, sweet goss. May the quartet with you, Rob and Wei stand strong. Ben and Tom, thanks for all the fun and interesting office chats. I also loved our ESO games. Also, thanks Nathaniel, Alex, EJ, John, Josh and James for their charismatic support. I also thank Yrina for the support and listening when I needed to get things off my chest.

I would also like to acknowledge the Engineering and Physical Sciences Research Council (EPSRC) and the National Nuclear Laboratory (NNL) for providing financial support. I also thank my industrial supervisors Graham Mackay, Robin Cowley and Simon Woodbury for their support and technical input.

We have within ourselves the ability to understand absolutely anything, as long as the information is explained clearly enough. All we need to do is learn how to ask the right questions to help us reach that knowledge in a format that makes it possible for us to interpret. The key is to realise within ourselves when there is a lack of knowledge that we possess and to then go and ask the relevant questions. – *adapted from a speech given by James Burke.*

## Abstract

The United Kingdom nuclear industry is currently experiencing challenges relating to the safe transfer and processing of legacy waste sludge due to its complex physical and chemical properties. The radioactive nature of the sludge makes conventional methods used to characterise its rheology costly. The use of a quartz crystal microbalance (QCM) to measure the rheological properties of concentrated suspensions is considered. The device is small, portable, and can provide rheological data *in-situ*, allowing for significant cost reductions to be made. The QCM consists of a gold-coated piezoelectric quartz crystal oscillating in the MHz-range when an alternating current is supplied to it. When the QCM is immersed into a medium, a shift in the sensor oscillation frequency ($\Delta F$) is observed, where the magnitude of the shift is proportional to the bulk properties of the medium and the nature of its contact to the resonator surface. In most cases an increased dampening due to a loss in vibrational energy is also observed, i.e. a shift in circuit resistance across the sensor ($\Delta R$), or a broadening in the electrical conductance vs. frequency curve ($\Delta\Gamma$). When the QCM sensor is submerged into concentrated sludge at fixed pH, $\Delta\Gamma$ or $\Delta R$ is proportional to the shear yield stress of the sludge measured using conventional vane viscometry. A stronger suspension network therefore increases both the QCM sensor dampening as well as the suspension bulk yield stress. For sludge composing of large surface area $TiO_2$ (anatase) particles that are sensitive to pH changes, the QCM $\Delta F$ and $\Delta\Gamma$ or $\Delta R$ response correlated well with changes in the theoretical particle-sensor interaction strength using the Derjaguin, Landau, Verwey and Overbeek (DLVO) theory. No significant resonance shifts were observed at suspension pH values where the particle-sensor interaction is expected to be repulsive. The change in QCM response with particle-sensor interaction allows for the charge characteristics of suspension particles to be inferred. The QCM response when in concentrated suspensions can be explained via the 'point contact load' model based on these findings. Concentration tests using zinc oxide particles was performed at different resonance frequency overtones (5 - 55 MHz initial frequency). An overtone dependency that cannot be explained by the point contact model alone was observed. The QCM data was compared to viscoelastic models where the raw data fitted well with model predictions. The high frequency storage modulus of the sludge correlated well with conventional rheometry data. The QCM response when it is submerged into a concentrated sludge can therefore be described through a combination of the point contact load model and the viscoelastic model, where the relative contribution from each depends on the physical and chemical composition of the suspension particles and the nature of the experiment involved.

# Table of Contents

# List of Figures

# 1. Introduction

During the 1950s and 1960s, the expanding nuclear programme of the United Kingdom and delays in Magnox fuel reprocessing resulted in the build-up of spent Magnox fuel being stored in open-air ponds (Fig. 1.1) [1, 2]. The reactivity of the magnesium-based cladding and its fuel coupled with extended storage times in water resulted in enhanced levels of corrosion, forming sludge of complex chemistry and physical properties [1]. The First-Generation Magnox Storage Pond in Sellafield, Cumbria (Fig. 1.1) contains approximately 1200-1500 $m^3$ of radioactive sludge that is mostly composed of $Mg(OH)_2$, spent radioactive wastes, organic material and dust [1-3]. The pond is also located at the centre of the Sellafield site which add to the complexity of designing suitable sludge transport and storage facilities due to the limited amount of available land which greatly adds to the overall cost of the process. It is therefore important for any new facilities to be designed to the correct specification where accurate sludge rheological data would have to be obtained to achieve this objective.

**Figure 1.1: Appearance of the Sellafield First Generation Magnox Storage Pond. Adapted from Hastings et al. [2].**

Previous attempts made to measure the rheology of the sludge primarily include conventional sampling followed by lab measurement techniques [4]. These methods however introduce a significant amount of history effects in the sample structure which result in measured rheological properties that are different from the undisturbed sludge. To reduce the influence of history effects on sample rheology, a new method termed 'freeze sampling' was introduced where a metallic sampler probe is submerged into the suspension, and a volume of sludge around the probe is rapidly frozen in an attempt to preserve its rheological properties [5]. Only a small volume of the suspension is frozen however, and most conventional methods used to measure sludge rheology (viscometer or a rheometer) require larger volumes of sludge. Thawing the sample will in most cases not be instantaneous which may also introduce its own form of history effects on the sample. Sampling protocols may also result in extensive turnaround periods between collection and the production of results. The

sampling of toxic radioisotopes also poses an increased risk to personnel who are directly involved in the sampling process.

Due to these setbacks, there is a strong drive to measure the rheological properties of radioactive suspensions *in-situ* without the need for operator sampling. Direct vane viscometry has been used in an attempt to eliminate the inaccuracies produced by material sampling, where work with BHR Group resulted in the construction of a rotational vane penetrometer that is placed above the sludge pond and is submerged directly into it, allowing for measurements to be made *in-situ* (Fig. 1.2) [4]. The large size of the equipment however makes positioning of the vane difficult to measure the yield stress of the sludge at a desired location. The length of the vane rod and the relatively small size of the vane spindle would also result in a reduction in the accuracy of the readings. Repositioning of the equipment to a new location would also be challenging since the equipment may become contaminated and there is likely to be limited room available near the ponds that would allow for ease of access.


**Figure 1.2: (A) physical appearance of the rotational vane penetrometer prototype developed by BHR Group. (B) an enlarged image showing the appearance of the vane used to measure the rheology of the suspension is included. Adapted from Alderman et al. [4].**

There is therefore a need to obtain meaningful rheological information from these suspensions *in-situ* using equipment that can accommodate small spaces and simple re-mobilisation in new environments to allow for measurements to be made in a variety of different locations that are not limited to the First-Generation Magnox Storage Pond alone.

The quartz crystal microbalance (QCM) was chosen as a potential candidate due to its ability to serve as a portable sampling probe that is simple to use and consists of very few mechanical parts near the material being sampled. The QCM is essentially an ultrasensitive mass balance that consists of a dip probe which contains a thin AT-cut quartz sheet with two electrodes plated onto it. When an alternating current is passed through the two electrodes, the crystal oscillates at a characteristic frequency that can lie between 5 MHz and 20 MHz, where more commercial QCM devices usually operate in the 5 MHz to 10 MHz range [6, 7].

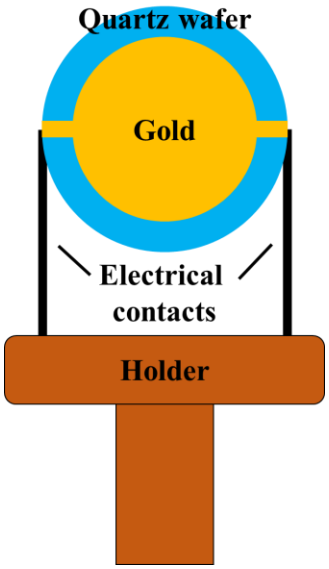


**Figure 1.3: Schematic showing a typical QCM setup. Two electrical contacts are connected to the back end of a gold coated piezoelectric AT-cut quartz crystal wafer. A holder can be used to contain the two electrical wires. The overall thickness of the setup therefore does not have to be significantly more than the diameter of the crystal waver itself (typically 25.4 mm). Adapted from O'sullivan et al. [6].**

When the crystal sensor is exposed to a new medium of different physical properties, it experiences a shift in its resonance that is proportional to the properties of the new medium. Traditionally the QCM has been used as a quartz-based device for measuring small 'micro' masses per unit area as its name suggests [8], however the device has a sensitivity that extends well into the ng/cm$^2$ range [9]. The QCM has since had its use extended to include measurements in liquid environments where the shift in crystal resonance was found to be proportional to the product of the viscosity and density for a non-adsorbing Newtonian fluid [10] [11-14]. Measurements in liquid environments also enabled its ability to measure the amount of mass transfer in electrochemical processes [15-18] and to probe the viscoelastic properties of more complex materials since a bulk fluid can be considered a viscoelastic medium numerically [9, 19, 20]. More recently however, point contact measurements have been performed where the interaction behaviour of discrete particles in solution are investigated [19, 21-24]. The physical properties of these linked particles could therefore also be determined, enabling for the QCM to be used as a basic characterisation tool for suspensions containing discrete particles that have no significant interaction with one-another [23, 25].

## 1.1. Aims and Objectives

The overall aim of the project is to extend the applicability of the QCM to include concentrated (networked) suspensions where shifts in the resonance properties of the sensor can be correlated to changes in the suspension bulk rheological behaviour. By understanding the QCM behaviour when its resonator surface is exposed to less complex colloidal suspensions, the information can be used to describe the underlying processes involved when the QCM resonator surface is exposed to networked suspensions of complex particle geometries instead. This information can be related

to colloidal theory, allowing for comparisons to be made with other conventional methods of measuring suspension rheology, enabling for the applicability of the QCM to measure concentrated suspension rheology to be realised.

## 1.2. References


1. Jackson, S.F., S.D. Monk, and Z. Riaz, *An investigation towards real time dose rate monitoring, and fuel rod detection in a First Generation Magnox Storage Pond (FGMSP).* Applied Radiation and Isotopes, 2014. **94**: p. 254-259.
2. Hastings, J., et al., *New approaches for sludge management in the nuclear industry.* Powder Technology, 2007. **174**(1-2): p. 18-24.
3. Gregson, C.R., et al., *Combined electron microscopy and vibrational spectroscopy study of corroded Magnox sludge from a legacy spent nuclear fuel storage pond.* Journal of Nuclear Materials, 2011. **412**(1): p. 145-156.
4. Alderman, N.J., Heywood, N. I., *The Importance of Rheological Assessment in the Mobilisation, Mixing and Transport of Nuclear Waste Sludges - 11195*, in *Waste Management 2011*. 2011: Phoenix, Arizona.
5. Kennedy, V.C., *Freezing-type sediment sampler*. 1967, Google Patents.
6. O'Sullivan, C.K. and G.G. Guilbault, *Commercial quartz crystal microbalances - theory and applications.* Biosensors & Bioelectronics, 1999. **14**(8-9): p. 663-670.
7. Marx, K.A., *Quartz crystal microbalance: A useful tool for studying thin polymer films and complex biomolecular systems at the solution-surface interface.* Biomacromolecules, 2003. **4**(5): p. 1099-1120.
8. Sauerbrey, G., *Verwendung Von Schwingquarzen Zur Wagung Dunner Schichten Und Zur Mikrowagung.* Zeitschrift Fur Physik, 1959. **155**(2): p. 206-222.
9. Johannsmann, D., *The Quartz Crystal Microbalance in Soft Matter Research*. 2014: Springer, Cham.
10. Kanazawa, K.K. and J.G. Gordon, *The Oscillation Frequency of a Quartz Resonator in Contact with a Liquid.* Analytica Chimica Acta, 1985. **175**(Sep): p. 99-105.
11. Mason, W., et al., *Mechanical properties of long chain molecule liquids at ultrasonic frequencies.* Physical Review, 1948. **73**(9): p. 1074.
12. McSkimin, H., *Measurement of dynamic shear viscosity and stiffness of viscous liquids by means of traveling torsional waves.* The Journal of the Acoustical Society of America, 1952. **24**(4): p. 355-365.
13. Mason, W., et al., *Measurement of shear elasticity and viscosity of liquids at ultrasonic frequencies.* Physical Review, 1949. **75**(6): p. 936.
14. McSkimin, H., *Measurement of the Shear Impedance of Viscous Liquids by Means of Traveling Torsional Waves.* The Journal of the Acoustical Society of America, 1952. **24**(1): p. 117-117.
15. Alder, J.F. and J.J. McCallum, *Piezoelectric crystals for mass and chemical measurements. A review.* Analyst, 1983. **108**(1291): p. 1169-1189.
16. Bruckenstein, S. and M. Shay, *Experimental aspects of use of the quartz crystal microbalance in solution.* Electrochimica Acta, 1985. **30**(10): p. 1295-1300.

17. Nomura, T. and M. Okuhara, *Frequency shifts of piezoelectric quartz crystals immersed in organic liquids.* Analytica Chimica Acta, 1982. **142**: p. 281-284.
18. Nomura, T. and O. Hattori, *Determination of micromolar concentrations of cyanide in solution with a piezoelectric detector.* Analytica chimica acta, 1980. **115**: p. 323-326.
19. Johannsmann, D., *Viscoelastic, mechanical, and dielectric measurements on complex samples with the quartz crystal microbalance.* Physical Chemistry Chemical Physics, 2008. **10**(31): p. 4516-4534.
20. Voinova, M.V., et al., *Viscoelastic acoustic response of layered polymer films at fluid-solid interfaces: Continuum mechanics approach.* Physica Scripta, 1999. **59**(5): p. 391-396.
21. Pomorska, A., et al., *Positive Frequency Shifts Observed Upon Adsorbing Micron-Sized Solid Objects to a Quartz Crystal Microbalance from the Liquid Phase.* Analytical Chemistry, 2010. **82**(6): p. 2237-2242.
22. Pomorska, A., et al., *QCM study of the adsorption of polyelectrolyte covered mesoporous TiO2 nanocontainers on SAM modified Au surfaces.* Journal of colloid and interface science, 2011. **362**(1): p. 180-187.
23. Tellechea, E., et al., *Model-Independent Analysis of QCM Data on Colloidal Particle Adsorption.* Langmuir, 2009. **25**(9): p. 5177-5184.
24. D'amour, J., et al., *Capillary aging of the contacts between glass spheres and a quartz resonator surface.* Physical Review Letters, 2006. **96**(5): p. 058301.
25. Johannsmann, D., I. Reviakine, and R.P. Richter, *Dissipation in films of adsorbed nanospheres studied by Quartz Crystal Microbalance (QCM).* Analytical Chemistry, 2009. **81**(19): p. 8167-8176.

# 2. Literature Review

The aim of this section is to provide the reader with sufficient background information relating to QCM and colloidal theory. The basic QCM principles relating to mass addition, bulk fluid effects, viscoelasticity and particle adsorption will be discussed. Background colloidal information relating to the Derjaguin, Landau, Verwey and Overbeek (DLVO) theory and how it affects bulk rheological measurements such as shear yield stress will also be discussed. The following chapters will include work that combine QCM and colloidal theory to explain the underlaying mechanisms that may result in QCM resonance shifts.

## 2.1. Mass loading and dampening processes on a QCM resonator

When the QCM sensor crystal resonates, its deformation pattern is essentially a standing plane wave with antinodes located at its surface (Fig. 2.1a) [1, 2]. When a thin, rigid film is deposited onto the surface of the crystal, the mass acts as an extension to the thickness of the crystal (Fig. 2.1b), increasing the wavelength and decreasing the frequency of the standing shear wave [3]. Since the acoustic properties of the film might differ from the resonator, a more detailed analysis was made by Günter Sauerbrey [3] showing that the reduction in the frequency is proportional to the mass per unit area of the deposited film, regardless of the film's physical properties (Equation 2.1). The film must be completely rigid for this relationship to hold however [3], meaning that any changes in motional resistance or other dampening processes are zero by definition [2, 3]. The film does not have to be uniform for its area-averaged mass per unit area to be measured accurately [2, 4, 5], however entrainment of a bulk medium such as water may be a concern for heterogeneous films since it may add to the detected QCM mass and therefore introduce frequency shifts that do not accurately reflect the mass per unit area of the deposited film [1, 2].

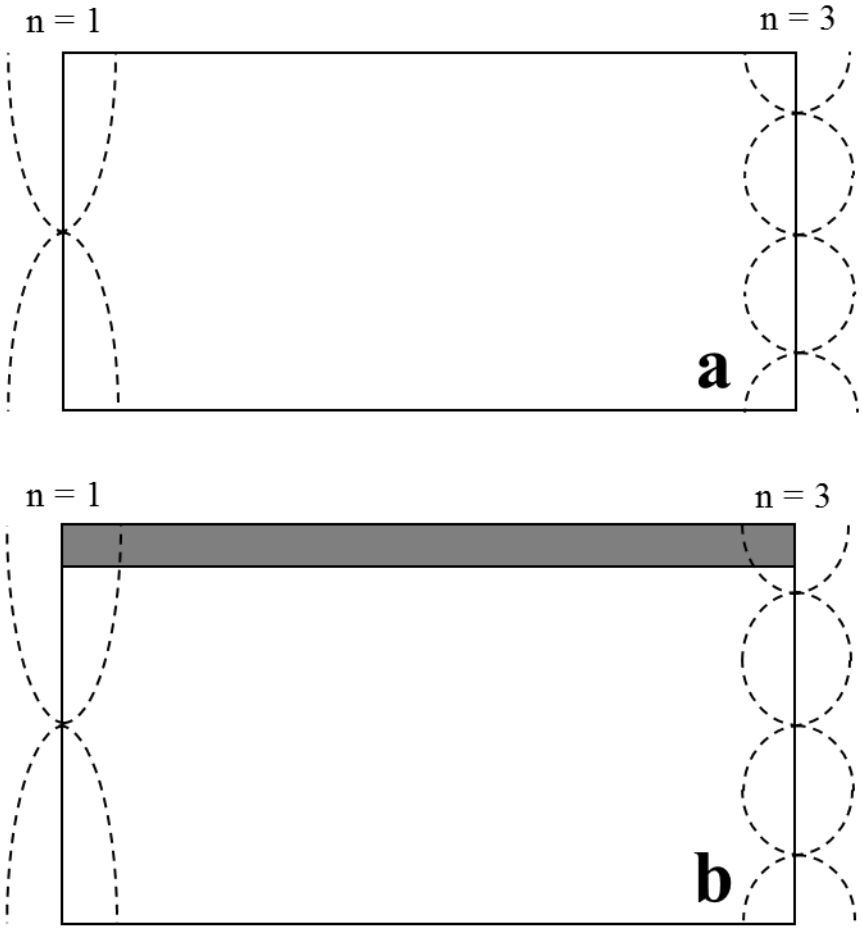


**Figure 2.1: Standing wave pattern in the QCM resonator for an (a) unloaded and a (b) loaded sensor. An added rigid film will increase its wavelength and therefore reduce its frequency. Resonances at the fundamental (n = 1) and 3rd overtone (n = 3) is shown. Adapted from Johannsmann [1, 2] and Reviakine et al. [6].**

$$\Delta f = -2\Delta m n f_0^2 / \left(A\sqrt{\mu_q \rho_q}\right) \qquad \textbf{Equation 2.1}$$

Where $\Delta f$ = change in frequency of oscillation (Hz), $\Delta m$ = area-averaged change in mass of the system (g), $n$ = overtone number (related to the initial frequency of operation), $f_0$ = fundamental mode oscillation frequency (Hz), $A$ = contact unit area ($cm^2$), $\mu_q$ = shear modulus of quartz (g $cm.s^{-2}$) and $\rho_q$ = density of quartz (g $cm^{-3}$).

Vogt et al. [7] performed polymer adsorption tests onto the QCM resonator surface. They found that during the adsorption of poly(4-ammonium styrenesulfonic acid), a shift in resonance frequency is observed [7]. After the films became sufficiently thick,

either via initial adsorption or via the accumulation of water, significant dampening of the oscillator resonance was observed [7]. Vogt et al. used the Sauerbrey relationship (Equation 2.1) to experimentally determine the deviation in the calculated Sauerbrey $\Delta m$ to other theoretical predictions [7] (Fig. 2.2). They found that a significant deviation of the QCM data to the Sauerbrey relationship is observed for thicker films (Fig. 2.2) which also corresponds to an increase in the relative dampening across the oscillating resonator [7]. These findings help confirm that the Sauerbrey relationship is only valid for rigid films that produce an insignificant amount of oscillation dampening.

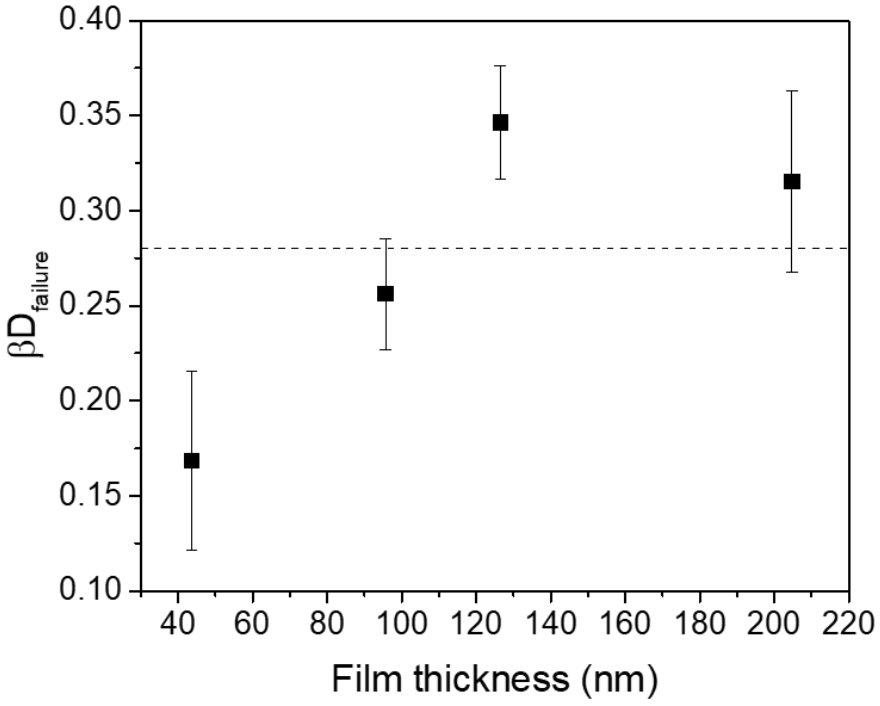


**Figure 2.2: Deviations of the QCM experimental response from the Sauerbrey relationship for adsorbed poly(4-ammonium styrenesulfonic acid) films of varying thicknesses. A $\beta D_{failure}$ value of > 0.28 (horizontal dashed line) implies that the Sauerbrey relationship becomes less valid to describe the behaviour of the polymer film. Adapted from Vogt et al. [7].**

Non-rigid films such as point contact loads from particle adsorption or materials behaving viscoelastically create dampening processes in addition to a shift in resonance frequency [1, 2, 6, 8, 9]. Different methods are used to measure these dampening processes, with the primary three being dissipation factor ($D$), half-band-half-width ($\Gamma$) and motional resistance ($R_1$) [1, 2, 6, 8, 9]. When the crystal is excited using an AC-voltage, and the frequency matches the resonance frequency of the thickness-shear mode for the crystal ($f_r$), the crystal displacement becomes large and follows a sine wave (Fig. 2.1) [1, 2, 10]. The displacement however decreases as the frequency moves away from $f_r$. By performing a frequency sweep and measuring the conductance at the different frequencies, a curve is obtained with the peak of maximum conductance being at $f_r$ (Fig. 2.3). The half-band-half-width of the conductance-frequency curve is defined as $\Gamma$ (Fig. 2.3). When the sensor experiences a dissipative load, the peak position shifts (frequency shift, $\Delta F$) and broadens (half-band-half-width shift, $\Delta\Gamma$) (Fig. 2.3), enabling for both changes in frequecy and dampening processes to be quantified [1, 2]. The QCM with impedance monitoring (iQCM) employs this simple method for determining the resonance parameters of a resonator [1, 2].

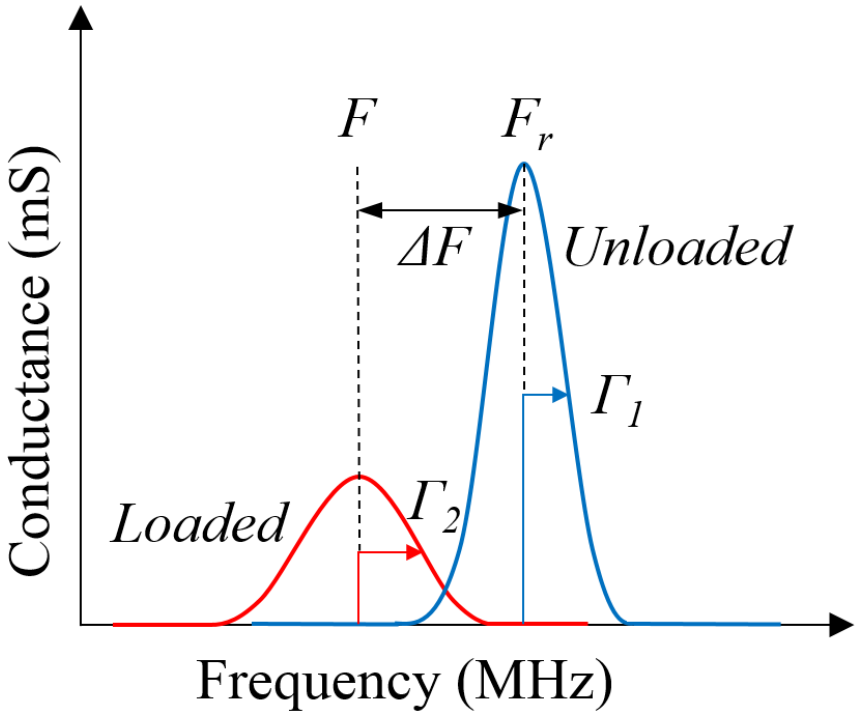


**Figure 2.3: Impedance analysis of a conductance-frequency curve. Adapted from Johannsmann, D. [1, 2].**

To measure the dissipation factor $D$ in an experiment, once the crystal frequency is at its expected resonance frequency, the excitation is turned off, allowing the crystal resonance to decay freely (Fig. 2.4) [2, 11, 12]. During this process, the current into the electrodes is recorded, resulting in a cosine wave of decaying amplitude with time (Fig. 2.4) [1, 2, 11, 12]. The time taken for the wave to decay by a factor of e is termed the 'decay time' and is equal to $1/2\pi\Gamma$, and $D$ is equal to $2\Gamma/f_r$, making $D$ and $\Gamma$ equivalent to one-another. The QCM with dissipation monitoring (QCM-D, trademark owned by Q-sense) uses $D$ as a parameter to measure dampening processes.

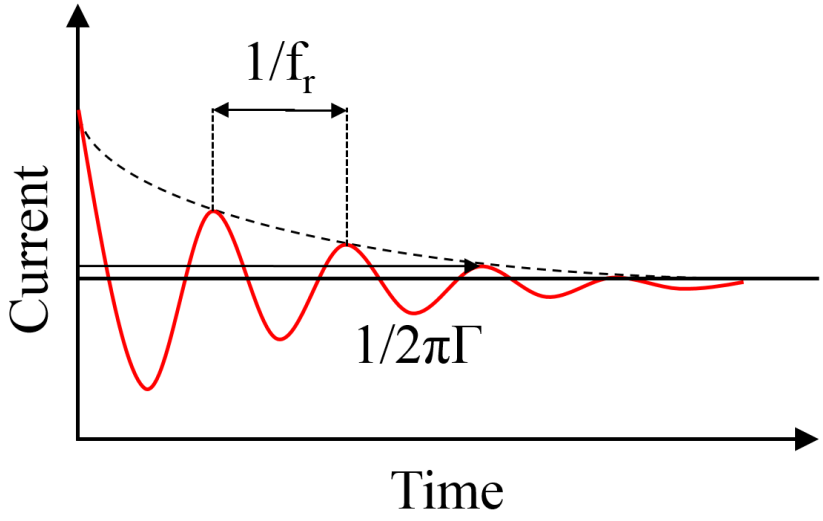


**Figure 2.4: decaying cosine observed during 'ring-down' when the crystal excitation is turned off. Adapted from Johannsmann [1, 2] and Reviakine et al. [6].**

Quantifying the motional resistance ($R_1$) in terms of $D$ or $\Gamma$ is not as trivial since $R_1$ is not derived through the so-called impedance analysis as previously discussed (Figs. 2.3 and 2.4). Traditional QCM devices that measure $R_1$ as a parameter for dampening processes use the 4-element circuit model termed the 'Butterworth-van Dyke' (BvD) equivalent circuit (Fig. 2.5) [13, 14].

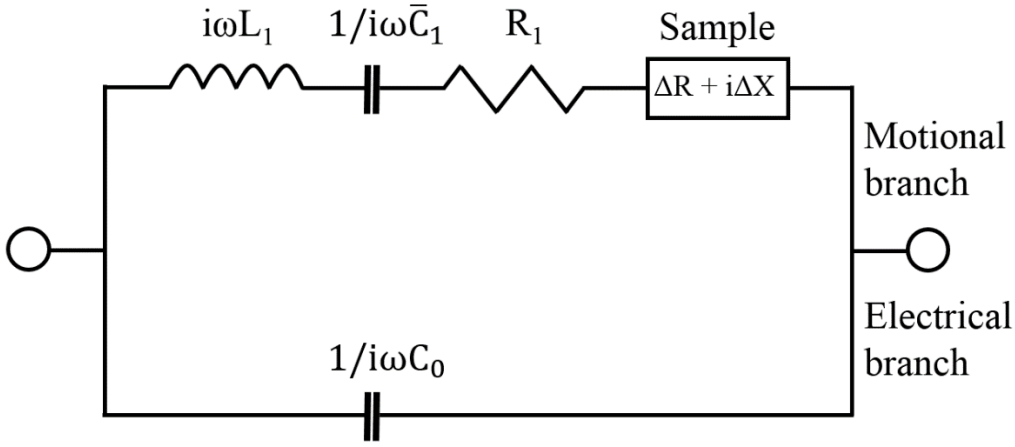


**Figure 2.5: Butterworth-van Dyke equivalent circuit with the loaded sample represented as an electrical element [1, 13, 14].**

Where ω = angular frequency (=$2\pi f$), $L_1$ = motional inductance, $C_1$ = motional capacitance of the 4-element circuit, $R_1$= motional resistance (Ohm), ΔR = air-to-sample motional resistance shift (Ohm), ΔX = reactance and $C_0$ = parallel capacitance.

ΔX can be converted to $\Delta f$ (air-to-sample frequency shift) via the following relationship (Equation 2.2) [2, 15], making its interpretation simpler:

$$\Delta R + \mathrm{i}\Delta X = -\mathrm{i}\frac{\pi}{16}\frac{Z_q^3}{Ae_{26}^2\rho_q^2 f_0^3}(\Delta f + \mathrm{i}\Delta\Gamma) \qquad \textbf{Equation 2.2}$$

Where $A$ = Effective area on the resonator plate ($cm^2$), $e_{26}$ = piezoelectric stress coefficient ($C\ m^{-2}$), $\rho_q$ = density of crystalline quartz ($2.65\ g/cm^3$), $Z_q$ = acoustic wave impedance of AT-cut quartz ($8.8 \times 10^6$ kg $m^{-2}$ $s^{-1}$) and $f_0$ = resonance frequency at the fundamental (Hz).

In most experiments, two of the four parameters are exploited: $\omega_r' = (L_1C_1)^{1/2}$ and $\omega_r'' = \frac{R_1}{(2L_1)}$, ($\tilde{\omega}_r = \omega_r' + \mathrm{i}\omega_r''$ where $\tilde{\omega}_r = 2\pi\tilde{f}_r = 2\pi(f_r + \mathrm{i}\Delta\Gamma)$), which enables for a frequency determination that has a better precision than the impedance itself [1, 2, 15]. Even though $R_1$ is derived by measuring changes in an equivalent circuit, and Γ and $D$ can be derived via impedance monitoring, $R_1$ can be directly converted to Γ via Equation 2.3 [15].

$$R_1 = \frac{\pi}{16Ae_{26}^2}\frac{Z_q^3}{\rho_q^2 f_0^3}\Gamma \qquad \textbf{Equation 2.3}$$

A disadvantage with using $R_1$ to measure dampening processes is that $A$ is a parameter that should be known which may be difficult for complicated non-uniform contact loads. $A$ reduces significantly with increasing overtone order $n$ ($n$= 1, 3, 5 is equivalent to 5, 15, 25 MHz initial resonance frequency for a 5 MHz sensor) [1, 16], making comparison at different overtones more complicated. QCM devices that use $R_1$, such

as the QCM200 from Stanford Research Systems or the RQCM from Maxtek Inc., are therefore incapable of taking measurements at various frequency overtones.

## 2.2. Bulk fluid effects and viscoelasticity

A QCM resonator will experience a shift in its resonance frequency and dampening process ($D$, $\Gamma$ or $R_1$) in a way that is proportional to the viscosity-density product of a non-adsorbing Newtonian fluid in contact with the crystal [2, 4, 8, 9, 17]. The Gordon-Kanazawa-Mason result (Equation 2.4) demonstrates this relationship.

$$\Delta f = -f_0^{2/3}\left(\frac{\rho_L \mu_L}{\pi \rho_q \mu_q}\right)^{1/2} \qquad \textbf{Equation 2.4}$$

Where $\rho_L$ (g cm$^{-3}$) and $\mu_L$ (Pa s) are the absolute density and viscosity of the fluid, respectively.

Interestingly, for Newtonian liquids that follow the relationship in Equation 2.4, $-\Delta f = \Delta \Gamma$ (e.g. for water $\Delta f$ is expected to be around -700 Hz and $\Delta \Gamma$ is expected to be around 700 Hz as well) [1, 2]. The values also scale with overtone order $n^{1/2}$ [1, 2], allowing for a simple assessment on if a given fluid may behave Newtonian at MHz frequencies.

Martin and co-workers [9] also determined the expected motional resistance shift for a non-adsorbing Newtonian fluid (Equation 2.5).

$$\Delta R = \left(\frac{\omega L_1}{n\pi}\right)\left(\frac{2\omega \mu_L \rho_L}{\rho_q \mu_q}\right)^{1/2} \qquad \textbf{Equation 2.5}$$

Rodahl et al. [18] investigated the QCM response in liquid environments and compared their resulting experimental resonance shifts to the Gordon-Kanazawa-Mason result (Fig. 2.6). They found that for glucose-in-water mixtures, the QCM frequency and dissipation shifts (ΔF and ΔD, respectively) show a linear relationship with $(\rho_L \mu_L)^{1/2}$, confirming the validity of the relationship (Fig. 2.6) [18]. The

experimental values of ΔF and ΔD are also larger than the calculated theoretical values, where the difference increases with increasing $(\rho_L \mu_L)^{1/2}$ (Fig. 2.6) [18]. An unpolished crystal was used for their experiments, causing a significant portion of the bulk fluid to be entrained within the rough edges of the resonator surface [18]. The entrained fluid will oscillate along with the resonator and behave as adsorbed viscoelastic materials, creating an increased ΔF and ΔD response compared to theoretical predictions that would not take this factor into account (i.e. the fluid has to be non-adsorbing) [18].

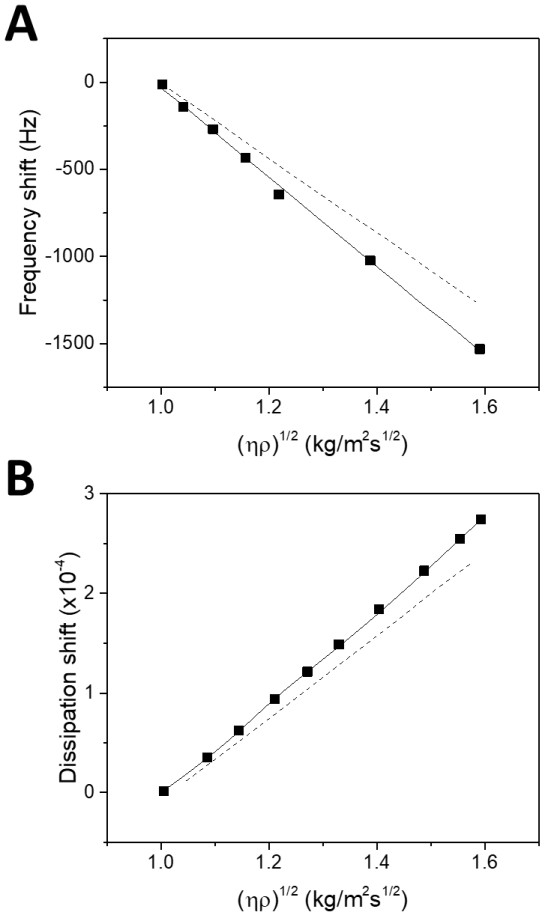


**Figure 2.6: Shifts in air-to-solution resonance frequency (A) and dissipation (B) when the sensor is immersed into glucose-in-water solution of increasing glucose concentration (therefore also increasing $(\rho_L \mu_L)^{1/2}$). A fit (black solid line) of the experimental values (black squares) showed an increased gradient compared to theoretical predictions (dashed line) due to the entrainment of fluid within the rough crystal surface. Adapted from Rodahl et al. [18].**

A bulk liquid can be thought of as a viscoelastic medium where the fluid will relax its structure at a rate relative to the frequency of the experiment [1, 2, 6]. On the one extreme case, you have the Newtonian liquid where the rate of relaxation is significantly faster than the frequency of the experiment [1, 2, 6], resulting in a very small storage modulus (G') and a loss modulus (G'') that is proportional to ω (G'' = $\omega\mu_L$) [1, 2, 6]. Water for example will adapt its structure to external stresses within a few nanoseconds [19]. The opposite extreme case is the elastic solid that has an infinitely slow rate of relaxation, resulting in G' that is much larger than G'' where G' is also independent on the frequency of the experiment [1, 2, 6]. A viscoelastic medium will have viscoelastic properties that lie somewhere in-between these extreme cases, and by analysing the QCM ΔF and ΔΓ or Δ*D* response at different overtones, one can infer the viscoelastic properties of the medium [1, 2, 20].

The Voigt-based model [20] or the acoustic multilayer formalism (AMF) model [1] have been proposed to describe how changes in G' and G'' of overlaying films may affect the QCM response. The two models are numerically equivalent [1, 2], however the Voigt model uses *D* to quantify dampening processes. Because both *F* and Γ share the same units (Hz), Γ was chosen as the preferred parameter to model the viscoelasticity of over-layers, making the AMF model the preferred choice.

Equations 2.6 – 2.9 show the relationship between the material viscoelastic properties (G' and G'') and the QCM response [1, 2, 20, 21].

For a viscoelastic film inside a liquid environment:

$$\frac{\Delta f^*}{f_F} = \frac{-Z_\mathrm{f}}{\pi Z_q}\frac{\tan(k_\mathrm{f}d_\mathrm{f}) - \mathrm{i}Z_\mathrm{liq}}{Z_\mathrm{f} + \mathrm{i}Z_\mathrm{liq}\tan(k_\mathrm{f}d_\mathrm{f})} \qquad \textbf{Equation 2.6}$$

Where $\Delta f^*$ is the complex resonance frequency shift ($\Delta f^* = \Delta f + i\Delta\Gamma$), $f_F$ is the fundamental mode frequency (Hz), $Z_\mathrm{f}$ is the acoustic impedance of the film, a material

property that governs the reflectivity at acoustic interfaces $\left(Z_{\mathrm{f}} = (\rho_{\mathrm{f}} G_{\mathrm{f}})^{1/2} = \rho_{\mathrm{f}} c_{\mathrm{f}}\right)$, $\rho_{\mathrm{f}}$ is the film density (g cm$^{-3}$), $G_{\mathrm{f}}$ is the film shear modulus (Pa), $c_{\mathrm{f}}$ is the speed of sound in the film (m s$^{-1}$), $Z_{\mathrm{liq}}$ is the acoustic impedance of the liquid (kg m$^{-2}$ s$^{-1}$), $k_{\mathrm{f}}$ is the wave vector of the film (rad m$^{-1}$) and $d_{\mathrm{f}}$ is the film thickness (typically quoted in nm).

For a semi-infinite viscoelastic medium:

$$\frac{\Delta f^*}{f_F} = \frac{1}{\pi Z_q}\frac{-1+\mathrm{i}}{\sqrt{2}}\sqrt{\rho\omega(\eta' - \mathrm{i}\eta'')} = \frac{\mathrm{i}}{\pi Z_q}\sqrt{\rho(G' + \mathrm{i}G'')} \qquad \textbf{Equation 2.7}$$

Where $\eta$ is the viscosity ( $\eta = \eta' - \mathrm{i}\eta''$).

$$\eta' = \frac{G''}{\omega} = -\frac{\pi Z_q^2}{\rho_L f_0}\frac{\Delta f \Delta\Gamma}{f_F^2} \qquad \textbf{Equation 2.8}$$

$$\eta'' = \frac{G'}{\omega} = \frac{1}{2}\frac{\pi Z_q^2}{\rho_L f_0}\frac{(\Delta\Gamma^2 - \Delta f^2)}{f_F^2} \qquad \textbf{Equation 2.9}$$

To fit QCM data to the viscoelastic model, one would need to employ ΔF and ΔΓ at each overtone [1, 2]. There are however also two unknown viscoelastic parameters at each overtone (G' and G'', Equation 2.7) as well as an unknown film thickness (Equation 2.6, which is used to obtain $Z_{\mathrm{f}}$ by calculating the load on the sensor over several different layers) meaning that the number of free parameters is larger than the number of known parameters. By assuming a smooth, homogenous viscoelastic spectrum, the frequency dependence on the viscoelastic properties of a material will show broad curves extending over several magnitudes on the ω-scale (Fig. 2.7) [1, 2]. The QCM however only covers a very narrow frequency range of slightly over a magnitude (5 MHz – 55 MHz) meaning that the broad curves can be approximated through power laws [1]. Equations 2.10 and 2.11 show the power law relationship between G' and G'' to the QCM response, respectively [1, 2].

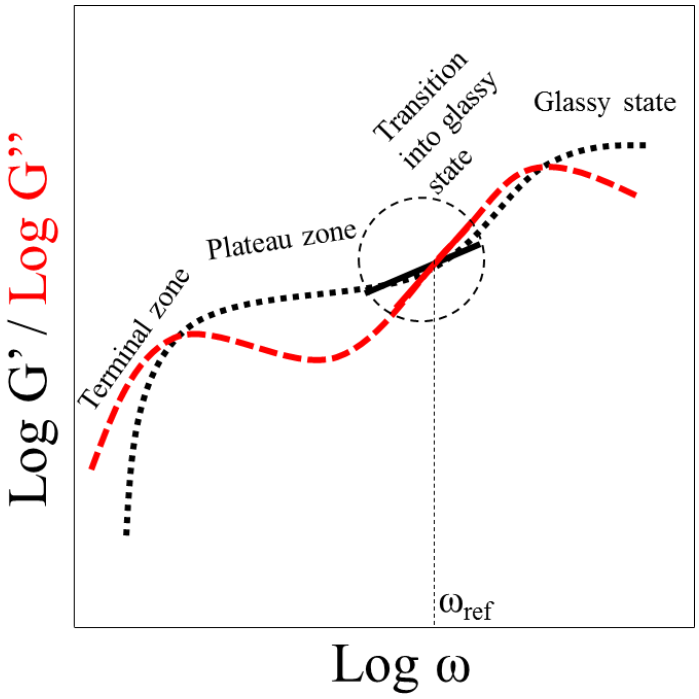


**Figure 2.7: Variation in G' and G'' with frequency. Changes in the viscoelastic properties of a given material may span over several magnitudes of ω; for QCM experiments operating at a narrow ω range, G' and G'' can be approximated by using power laws. Adapted from Pakula et al. [22].**

$$G'_{(\omega)} \approx G'_{\omega_{ref}} \left(\frac{\omega}{\omega_{ref}}\right)^{\beta'} \quad 0 < \beta' < 2 \qquad \textbf{Equation 2.10}$$

$$G''_{(\omega)} \approx G''_{\omega_{ref}} \left(\frac{\omega}{\omega_{ref}}\right)^{\beta''} \quad -1 < \beta'' < 1 \qquad \textbf{Equation 2.11}$$

Where the index *ref* denotes a reference frequency. For a QCM operating in the 5 – 55 MHz range, 25 MHz would suffice for a reference as this frequency is located at approximately the centre of the frequency range, however any reference frequency within the range can be used [1, 2]. $\beta'$ and $\beta''$ are power law exponents (the slope in a log-log plot).

Using this method to estimate the viscoelastic properties for the overlaying material will reduce the number of free parameters to 5 ($G'_{ref}$, $G''_{ref}$, β', β'' and the film thickness), making fitting possible when three or more overtones are used [1, 2].

Johannsman, D. adsorbed thick (>100 nm) polymer gel onto a QCM resonator surface and compared the resulting ΔF and ΔΓ response to the AMF viscoelastic model (Fig. 2.8) [1]. Good fits were obtained both with a layer thickness, $d_f$, of 140 nm (full lines, Fig. 2.8) and 180 nm (dashed lines, Fig. 2.8), implying that there may be a large degree of error when using the model simply to obtain the true geometric thickness of the viscoelastic layer [1]. For the 140 nm layer thickness, $G' = 2.2\ \text{MPa} \times \left(\frac{f}{f_{ref}}\right)^{1.5}$ and $\frac{G''}{G'} = 1.2 \times \left(\frac{f}{f_{ref}}\right)^{1.5}$. The 180 nm thickness showed $G' = 1.6\ \text{MPa} \times \left(\frac{f}{f_{ref}}\right)^{1.7}$ and $\frac{G''}{G'} = 0.36 \times \left(\frac{f}{f_{ref}}\right)^{1.63}$. Both fits had a sample density of 1 g cm$^{-3}$ and a reference frequency of 35 MHz was used (Fig. 2.8) [1]. The large variation in possible thicknesses (~25% variation in this case) will reflect variations in the obtained viscoelastic properties of the material [1]. In our case however, the sensor will be submerged into a sludge suspension whose viscoelastic thickness would extend to infinity. In this case it would therefore be more beneficial to select a thickness value that results in the closest obtainable fit to the raw data. The thickness in this case could be related to how deep the resonator penetrates into the suspension, however this is not certain. By performing a fit in this way, G' and G'' values will be obtained that best represents the sample (closest fit) with the knowledge that deviations may exist due to the use of an imaginary thickness and non-viscoelastic based interactions that include particle adsorption.

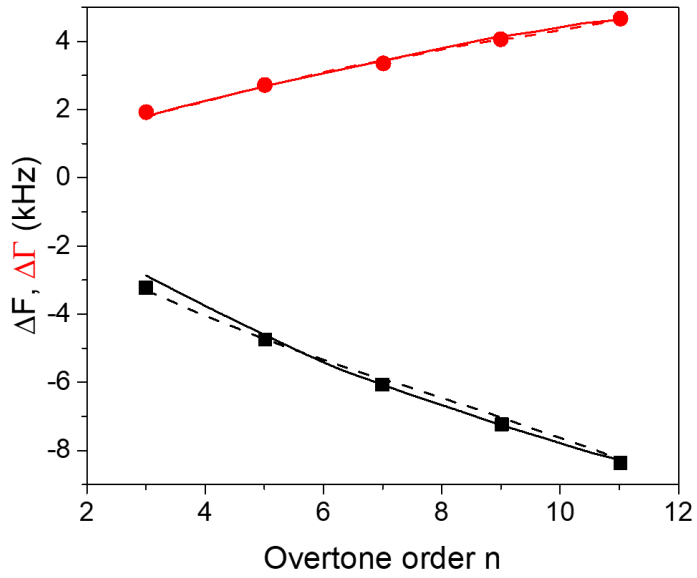


**Figure 2.8: Experimental QCM frequency shift (black squares) and half-band-half-width shift (red circles) data and fits using the acoustic multilayer formalism model. A fit at both a 140 nm (solid line) and 180 nm (dashed line) layer thicknesses were performed. Sample density = 1 g cm$^{-3}$ and a reference frequency of 35 MHz (n = 7) was used. Adapted from Johannsmann, D [1].**

## 2.3. Point contacts on the QCM resonator

The modelling of bulk fluids and viscoelastic materials assumes that the medium has no in-plane structure. For particle adsorption however, this assumption will not suffice since the particles themselves may act as external objects leaving a contact on the sensor with space or bulk fluid in-between [1, 5, 6]. If the particle contact has a diameter smaller than both the wavelength of sound and the size of the overall particle, a so-called 'point contact' is formed. If the particles are small (i.e. colloidal particles or bacteria), the linked particles may themselves resonate whilst also being affected by the resonating sensor [5, 23, 24], giving rise to coupled resonances. Equation 2.12 numerically describes the coupled resonance model for a QCM resonator [5, 23, 24].

$$\frac{\Delta f+\mathrm{i}\Delta\Gamma}{f_F}=\frac{N_S m_S \omega}{\pi Z_q}\frac{(\omega_S^2+\mathrm{i}\omega\gamma)}{(\omega^2-\omega_S^2-\mathrm{i}\omega\gamma)}=\frac{-N_S m_S \omega}{\pi Z_q}\frac{1}{1-\frac{\omega^2}{\omega_S^2+\mathrm{i}\omega\gamma}}\approx\frac{-N_S m_S \omega}{\pi Z_q}\frac{1}{1-\frac{\omega^2}{\omega_S^2}} \qquad \textbf{Equation 2.12}$$

Where $\omega_S$ = angular frequency of the sphere (particle) (rad $s^{-1}$), $N_S$ = number density of the spheres ($cm^{-2}$), $m_S$ = mass of a sphere (ng) and $\gamma$ quantifies the dissipative components of the sphere-plate interaction.

By changing the angular frequency of the sphere ($\omega_S$) relative to the angular frequency of the sensor ($\omega$), the QCM response will experience significant changes in its resonance [5, 24]. By performing a Taylor expansion on Equation 2.12 for large and small $\omega$ relative to the sphere, one finds (Equation 2.13 and 2.14):

For $\omega \ll \omega_s$:

$$\frac{\Delta f+\mathrm{i}\Delta\Gamma}{f_F}\approx\frac{-N_S m_S \omega}{\pi Z_q}\frac{1}{1-\frac{\omega^2}{\omega_S^2}}\approx\frac{-N_S m_S \omega}{\pi Z_q}=\frac{-2f N_S m_S}{Z_q} \qquad \textbf{Equation 2.13}$$

The result in Equation 2.13 is the Sauerbrey equation (Equation 2.1) with $N_S m_S=\frac{m}{A}$ and $Z_q=\sqrt{\mu_q\rho_q}$. For the Sauerbrey case, the complex frequency shift ($\Delta f+\mathrm{i}\Delta\Gamma$) is purely real where no shift in Γ is observed [5, 24].

For $\omega \gg \omega_S$:

$$\frac{\Delta f+\mathrm{i}\Delta\Gamma}{f_F}\approx\frac{-N_S m_S \omega}{\pi Z_q}\frac{1}{1-\frac{\omega^2}{\omega_S^2}}\approx\frac{N_S m_S \omega_S^2}{\pi Z_q \omega}=\frac{1}{\pi Z_q}\frac{N_S \kappa_S}{\omega} \qquad \textbf{Equation 2.14}$$

Where $\kappa_S$ = the stiffness of the sphere-plate contact (N $m^{-1}$). The final step in Equation 2.14 made use of the fact $\omega_S=\sqrt{\frac{\kappa_S}{m_S}}$ (derived from Hooke's law).

Equations 2.13 and 2.14 are the result of the two extreme cases observed for a point contact load experiencing coupled resonance. In the Sauerbrey-like case (Equation 2.13), an increase in the number of spheres would result in a more negative ΔF ($N_S m_S \propto -\Delta f$). This is termed *inertial loading*. For the Dybwad case however

(Equation 2.14), an increase in the number of spheres would have the opposite effect and enhance the sensor frequency ($N_S\kappa_S \propto +\Delta f$) [5, 23, 24]. This behaviour is termed *elastic loading*. This positive frequency shift is also strongly dependent on the stiffness of the contact between the particle and sensor ($\kappa_S$) [5, 23, 24]. The same may also be true for a non-ideal Sauerbrey case where a stronger contact may result in a greater amount of particle mass ($m_S$) being detected as a result in a potential increase in energy transfer between the two systems.

It should be noted that Equation 2.13 and 2.14 only applies to spheres in the dry state [5, 24]. In liquids, additional factors should be considered such as possible motion of the particles that lie within the evanescent acoustic wave, additional stress being transported by the liquid due to high frequencies, gradients in hydrostatic pressure due to particle movement and the derived mass may include co-moving liquid near the crystal surface that will move along with it [5]. Pomorska et al. performed point-contact experiments in the liquid environment and found that these relationships still hold (Fig. 2.9) [5]. An increase in the sphere size (resulting in a reduced $\omega_S$ as larger objects vibrate more slowly) or an increase in the QCM resonator overtone order (i.e. an increase in $\omega$, Fig. 2.9) will result in the loading regime to shift from inertial to elastic loading ($\omega_S \gg \omega \rightarrow \omega \gg \omega_S$), resulting in a change in the ΔF response from -ΔF to +ΔF (Fig. 2.9) [5]. At the transition point, Pomorska et al. observed that ΔΓ is at its maximum (Fig. 2.9) [5]. This may be because when $\omega \approx \omega_S$, one object no longer appears stationary relative to the other. A sphere linked to the resonator will cause an increased amount of energy loss when both the sphere and resonator is moving at the same frequency due to an enhanced destructive interference, resulting in an increased dampening effect and hence a larger ΔΓ.

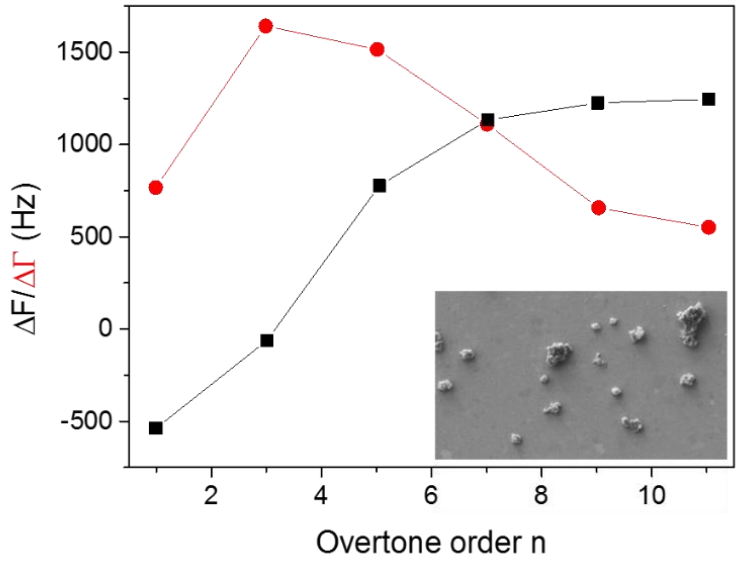


**Figure 2.9: QCM frequency shift (black squares) and half-band-half-width (red circles) observed after the complete adsorption (t = > 90 min) of negatively charged PSS-terminated NC particles (shown in figure inset; horizontal width = 25 µm) onto a positively charged QCM resonator modified with a self-assembled monolayer of amine-terminated thiol in water. Adapted from Pomorska et al. [5].**

Interestingly, the magnitude of ΔF increased (-ΔF or +ΔF depending on whether the sphere exhibits inertial or elastic loading behaviour) for both loading regimes when the strength of the sphere-plate interaction ($\kappa_S$ for elastic loading and possibly $m_S$ for inertial loading due to a greater amount of the sphere's mass being detected) increased as well [5]. This observed correlation may be of great importance since the strength of the sensor-sphere interaction is strongly dependent on the chemical and physical properties of the sphere itself [25-27]. The Derjaguin, Landau, Verwey and Overbeek (DLVO) theory has been shown to describe the nature of interactions between particles in an aqueous dispersion [25-27] which may be applicable to describe the underlaying factors that will affect the particle-resonator contact strength [28].

## 2.4. Derjaguin, Landau, Verwey and Overbeek (DLVO) theory

The DLVO theory is essentially a balance between the attractive and repulsive potentials between two colloidal particles under a given set of conditions. It is therefore capable of predicting the likelihood of the particles attracting to form a link between one-another as well as the relative strength of such an interaction [25-27]. An introduction to the underlaying theory will firstly be discussed.

When a colloidal metal oxide particle (high surface area to volume ratio and a small gravitational force) is immersed into an aqueous environment, the unresolved chemical bonds at the surface of the particle will cause electrostatic charges to be present at its surface (Fig. 2.10) [29-32]. When this surface is submerged into water, the charged ions and polar water molecules will be attracted to the opposite charges on the metal oxide surface (Fig. 2.10) [29-32]. An immobile layer of ions (termed the Stern layer) will form near the metal oxide surface (Fig. 2.10) [25, 29-32]. For a metal oxide that has an overall negative surface charge relative to the charge of the bulk solution, the ions forming the Stern layer will overcompensate for this charge difference, making the particle positively charged overall [25, 32]. The zeta potential of a particle is the potential difference between the outer Helmholtz plane (Fig. 2.10) and the bulk solution beyond the diffuse layer (Fig. 2.10) [33] and can be used to quantify the charging behaviour of particles in aqueous media.

As the distance from the particle surface increases, the magnitude of the charge difference reduces and weaker links are formed between the charged species. Forces from Brownian motion (random movement of molecules in the medium) become more significant beyond the outer Helmholtz plane due to the weaker links, causing the charged molecules to be mobile [25, 32, 33]. This diffuse layer continues until the difference in potential compared to the bulk solution is zero. [25-27, 32]. Due to the

increased drive to neutralise the charge difference, the region between the inner Helmholtz plane and the diffuse layer will contain a greater number of ionic species relative to the bulk solution [25-27]. This layer of increased concentration is termed the 'electrical double layer' [25-27]. When two particles come within a proximity to one-another, their electrical double layers may overlap, resulting in an osmotic pressure to form, driving the two particles away from one-another [25-27].

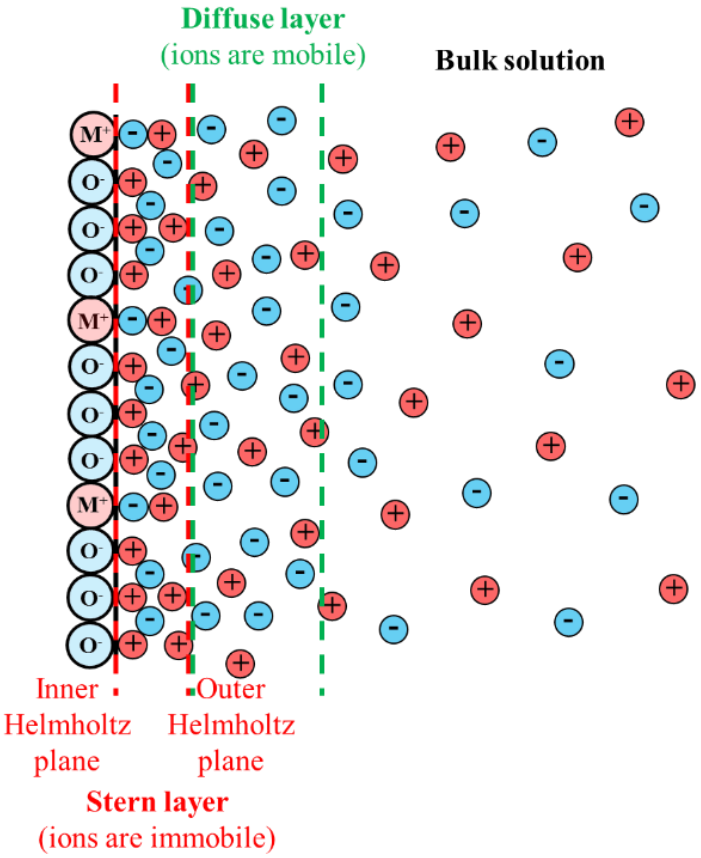


**Figure 2.10: Hydration of a metal oxide in water – charged surface species will attract polar water molecules as well as charged ions. Ions near the metal surface form stronger bonds due to a smaller separation distance, making them immobile.**

The electrical double layer can be characterised for a simple sphere via Equation 2.15 [25-27, 34, 35]:

$$F_{EDL} = \frac{2\pi a\, \varepsilon_0 \kappa \zeta^2 e^{-\kappa H}}{1+e^{-\kappa H}} \qquad \textbf{Equation 2.15}$$

Where $F_{EDL}$ = force on the sphere due to electrical double layer effects (nN), $a$ = sphere radius (μm), $\varepsilon_0$ = the permittivity of free space (J $V^{-2}$), $\kappa$ = inverse of the Debye length (the length of the electrical double layer from the particle surface to the point where the local concentration = bulk) ($nm^{-1}$); $\kappa^{-1} = \left(\frac{2z^2 n_0 e^2}{\varepsilon_0 \varepsilon k T}\right)^{-\frac{1}{2}}$, $z$ = ionic valence for any present symmetrical $z:z$ electrolyte species, $n_0$ = number concentration of ions in the bulk solution, $e$ = electronic charge ($1.602176634\times10^{-19}$ C), $\varepsilon$ = dielectric constant of the bulk solution (F/m), $k$ = Boltzmann constant ($JK^{-1}$), $T$ = absolute temperature (K), $\zeta$ = electrical zeta potential (V) and $H$ = separation distance (nm).

There are two main parameters that affect the strength of the electrical double layer: ionic concentration and the particle zeta potential [25, 34, 35]. Electrolytes such as NaCl for example create highly charged ions ($Na^+$ and $Cl^-$) in aqueous media that, when attracted to a particle surface, they can compensate for a greater amount of the charge difference that is present, meaning that fewer charged species are required to neutralise the particle charge relative to the bulk solution [25, 35]. The overall length of the electrical double layer (Debye length) will therefore reduce with an increase in ion concentration or valency (i.e. $Na^+Cl^-$ vs. $Mg^{2+}[SO_4^{2-}]$).

The chemical composition and crystal structure of the colloidal particle will affect the overall charge of the unresolved bonds at its surface relative to the bulk solution (Fig. 2.10) [25, 34, 35]. This will in turn change the zeta potential of the particle ($\zeta$), changing the difference in the number of molecules located within the electrical double layer relative to the bulk solution (the Debye length however remains

unchanged in this case, only the 'intensity' of the electrical double layer is changed). A weaker (reducing $\zeta$) or shorter (increasing $z$ or $n_0$) double layer means that the particles can come within a closer proximity before a significant amount of Osmotic force takes place that drives the particles away from one-another.

The main attractive force that drive particles to be closer to one-another is the London van der Waals force of attraction [25-27, 35]. The atoms that comprise the colloidal particles will generate instantaneous dipoles due to a fluctuation in the centre of mass of the electron spin around the atoms [25]. This produces an electromagnetic field that interacts with neighbouring atoms in the particle, causing them to correlate their orientations (position of the negative electron cloud centre of mass and the positive nuclei) to help reduce their interaction energy with one-another [25, 36]. The instantaneous dipoles will also affect the atoms in neighbouring particles, inducing further instantaneous dipoles within the neighbouring particle [25, 36]. The correlated dipoles that are produced within each particle will cause an attractive force to be formed between them that increases as the inter-dipole separation decreases [25, 36]. These interactions lead to a macroscopic overall attraction that follows the relationship shown in Equation 2.16 if the two particles are identical and spherical [25, 36].

$$F_{VDW} = -\frac{a A_H}{12H^2} \qquad \textbf{Equation 2.16}$$

Where $F_{VDW}$ = the London van der Waals force of attraction, $a$ = sphere radius, $H$ = separation distance and $A_H$ = Hamaker constant.

The Hamaker constant in Equation 2.16 is a materials specific property [37] whose quantification is not trivial [38]. One of the more well-known methods used to calculate $A_H$ for a material is via the Lifshitz method [39] that looks at the particle's bulk dielectric constants and refractive indices of its dispersed and continuous phases

[39]. Other authors have estimated the Hamaker constant of materials by employing contact angle experiments [40], by comparing the yield stress of concentrated suspensions to its $\zeta^2$ and using DLVO theory to back-calculate the Hamaker constant [40], using surface force apparatus techniques [41, 42], via atomic force microscopy [42-44] and via various simplifications to the Lifshitz method [41, 42, 45]. Normally the $A_{131}$ value would be quoted in the literature which is the Hamaker constant value for a material $M$ (1) being attracted to the same material $M$ with a bulk fluid in-between (3) (Fig. 2.11) [25, 35].

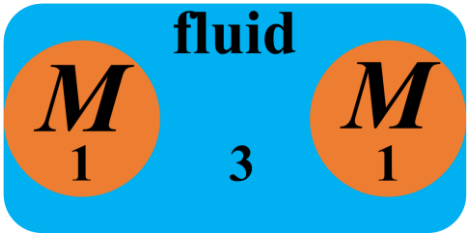


**Figure 2.11: Illustration of the systems that affect the overall value of the Hamaker constant used in calculating the London van der Waals force of attraction between two similar particles [25, 35].**

A sum of the repulsive Osmotic force from the electrical double layer interaction (Equation 2.15) and the London van der Waals force of attraction (Equation 2.16) are the two components that make up the DLVO theory [26, 27]. Based on a balance between these two forces, one can predict if two particles are likely to be attractive or repulsive at a given separation distance between them (Fig. 2.12) [26, 27, 46].

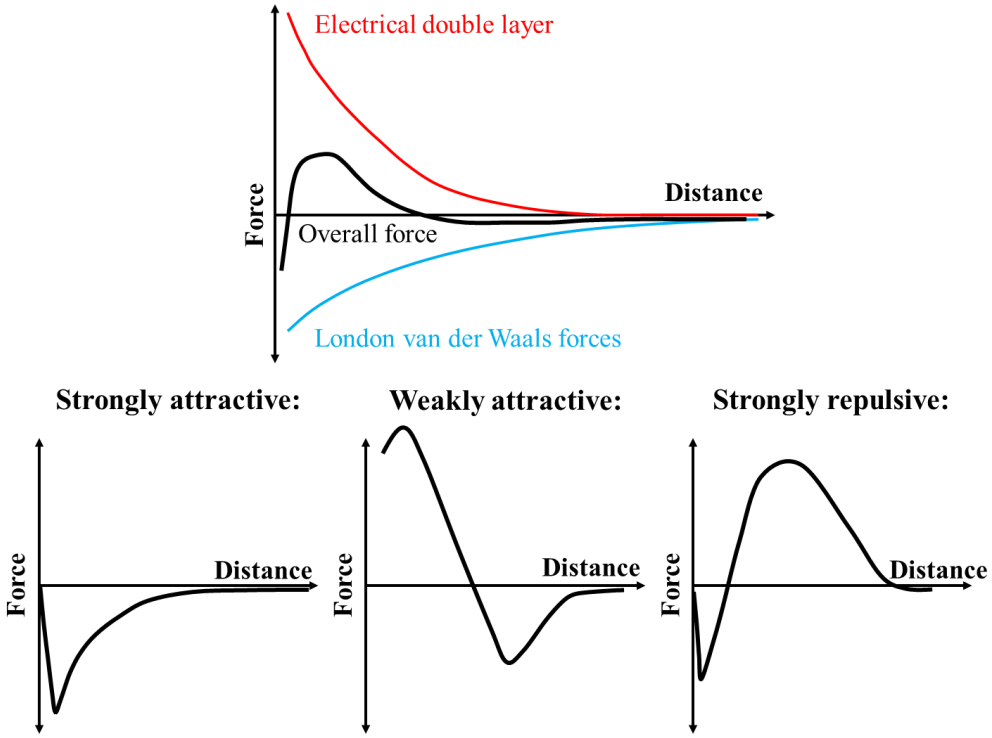


**Figure 2.12: DLVO force diagrams illustrating the likelihood of particles interacting with one-another as a function of separation distance (Adapted from Johnson et al. [25]). Negative forces correspond to attraction.**

The DLVO theory however does not take the following additional forces into consideration [25]:

- *Hydration forces* – When the electrolyte concentration of a particle suspension is increased, the particles are expected to undergo an increased rate of coagulation [25, 47]. Coagulation occurs when two neighbouring particles acquire enough energy from Brownian motion to overcome the repulsive potential barrier to link together [47]. Some colloids such as silica showed to not follow this behaviour where coagulation does not occur even at high electrolyte concentrations when the electrical double layer's Debye length is expected to be very small [47, 48]. The repulsive force is believed to be due to the organisation of water in the near vicinity of a charged colloid surface [25, 47, 49] where the repulsion is enhanced for particles that possess stronger hydrogen bonding capability or for solutions at high electrolyte concentrations

[47]. An energy barrier would need to be overcome to break the organised water structure around the polar sites of the colloidal particle to allow for the two surfaces to coagulate [25, 47]. In addition to the structured water, the forced dehydration of surface-bound cations as the two colloidal particles move closer together may also serve as a repulsive force, where the strength of this repulsion generally depends on the cation hydration number [50 – 52].

- *Hydrophobic forces* – When a non-polar substance is introduced into solution, water molecules near the substance will have to re-orientate themselves to better optimise their hydrogen bonding capacities, creating a structured water cage around the particle surface [25]. The re-orientation of water to form a more well-defined structure is entropically unfavourable [25]. There is therefore a drive to reduce the volume of structured water present by driving neighbouring hydrophobic particles to coagulate [25].
- *Steric and electrosteric forces* – When particles are coated in surfaces that are non-rigid and are deformable, a steric repulsion is often observed where the overlapping of these layers may cause an increase in Osmotic pressure as well as an elastic force due to compression of the layer [25]. When the layer carries charge with it, an additional double layer may be formed that will in turn create additional Osmotic pressure, preventing coagulation of the colloidal particles [25].
- *Bridging and depletion forces due to polymer interactions* – A bridging force occurs when a long chain polymer or polyelectrolyte adsorbs onto more than one particle, pulling them closer together and inducing flocculation (the sedimentation of larger and heavier polymer-particle matrix called a *floc*) [25]. Polymer-based depletion forces occur when two colloids in a suspension concentrated with non-adsorbing polymer approach one-another and the

polymer is forcibly excluded [25]. This action leaves a region of relatively pure solution, causing an Osmotic pressure to form that will drive the particles closer together [25].

## 2.5. Shear yield stress of concentrated suspensions

For rigid particles with no organic or polymer-based additives in solutions containing low to moderate concentrations of electrolyte, the effect of non-DLVO based interactions should be minimised. Changes in the bulk rheological properties of concentrated suspensions that adhere to these conditions could therefore more reliably be explained using the DLVO theory. One of the main bulk rheological parameters considered by many authors for concentrated suspensions is its *shear yield stress* [53-55]. The traditional definition for the yield stress of a material is defined as 'the minimum shear stress that must be applied to the material to produce a shearing flow' [56], and is considered by Liddell and Boger as being the stress value when the sludge undergoes a transition from its elastic solid-like behaviour to a viscous liquid-like behaviour [53]. When the concentration of a suspension increases, it will eventually reach a solids content that is above its so-called *gel point* where the particles in the suspension volume are concentrated enough to form a continuous three-dimensional network structure as the particles interact with one-another [54, 57, 58]. The yield stress in this case can therefore be regarded as the overall stress required to break these network bonds between the particles to induce flow [54].

Zukoski and co-workers defined two yield stresses for a given material; the static yield stress and the dynamic yield stress [53, 59] (Fig. 2.13). It was shown that at stresses below the static yield stress, the material elastically deforms to a fixed finite amount upon the application of a stress, however when this stress is removed, the material undergoes complete strain recovery (elastic deformation). Between the static and

dynamic yield stress, which is in the viscoelastic region, the strain on the material increased in a non-steady rate as a function of time after the application of stress, where the strain recovery upon removal of the shear stress is incomplete (plastic deformation) [53, 59]. In the viscous region above the dynamic yield stress (the sludge behaves like a viscous fluid since particle-particle network bonds have been broken down), a steady-state strain rate can be achieved once again, however there is very little to no strain recovery upon removal of the stress [53, 59]. The dynamic yield stress is therefore regarded as being the definitive yield stress of the material [53, 60] since steady state flow and structural breakdown is normally observed at strains beyond the dynamic yield stress [53].

Boger, Nguyen and Keentok first adopted the vane method to measure the shear yield stress of sludge suspensions [54, 56, 61]. It has since become a well-known method for sludge yield stress measurement where its results were found to be reproducible throughout several different studies [25, 53, 61, 62]. The vane has been used in a rate controlled mode rather than a stress controlled mode by several authors since the values showed a good agreement with those obtained though extrapolation and stress relaxation techniques [53, 54, 63, 64]. For the rate controlled mode, a slow and constant rotational velocity is applied to the vane after it had been immersed into the suspension and the torque that is required to maintain the set velocity is recorded and converted into a stress (Fig. 2.13) [53].

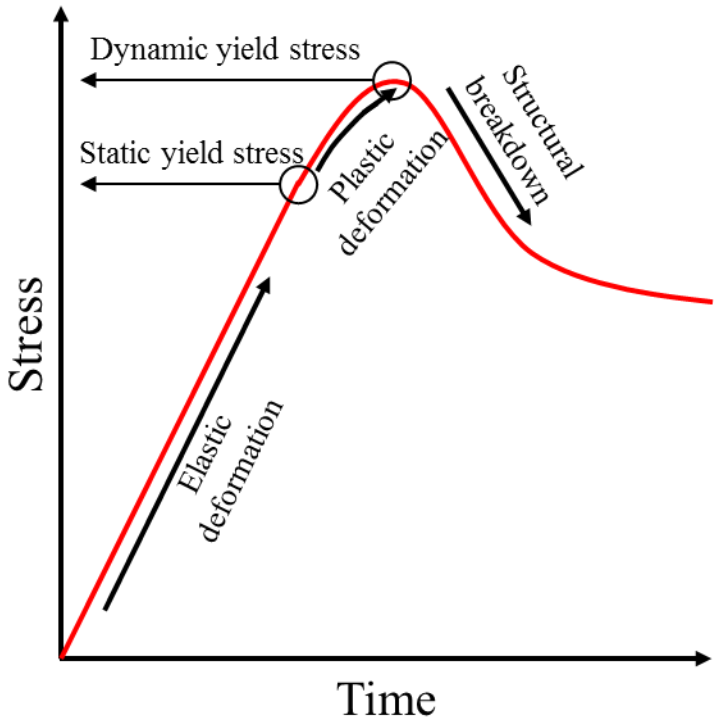


**Figure 2.13: Typical shear stress response of a suspension during a rotational vane viscometry test in a rate controlled mode (adapted from Liddell and Boger [53]). The static yield stress is the stress at which the material no longer deforms elastically. The dynamic yield stress is the maximum stress obtained; the material behaves like a viscous fluid beyond this point.**

By treating the vane as a cylinder of known diameter, the maximum measured torque on the rotating vane ($T_{max}$) can be converted into a dynamic yield stress ($\tau_y$) via Equation 2.17 [53, 61, 65] 25.

$$\tau_y = \frac{6T_{max}}{(\pi D^2)(L+D)} \qquad \textbf{Equation 2.17}$$

Where $D$ = vane blade diameter and $L$ = length of submerged portion of the vane.

The relationship has been derived by making two main assumptions. Firstly the shearing only takes place in the cylindrical volume produced by the vane, where the diameter of the cylinder is the diameter of the vane. This assumption can be slightly incorrect; the diameter of the sheared cone can be up to 5% larger than that of the vane [53, 56, 66]. Earlier studies however have shown that this increase in area for soils is

normally very small, making this error insignificant [67]. And secondly the stress over the surface of the cylinder undergoes a uniform distribution. The stress in fact peaks at the edges of the vane, however it has been shown that the error this assumption causes is relatively insignificant as well [54, 61-63, 68].

The vane have several advantages over using a standard cylinder which include a large sample contact area, low slip and it does not displace a large amount of sludge when the vane is submerged into the sludge sample [53, 54]. Dzuy and Boger [54] have shown that there is also a negligible difference in the yield stress values obtained when the vane is rotated at different speeds between 0.1 to 8 rpm.

## 2.6. Relationship between the shear yield stress and the attractive and repulsive forces acting between colloids in aqueous solution

Yang et al. [69] have shown that the bulk rheological behaviour of titanium dioxide suspensions (i.e. its bulk yield stress) strongly depend on the charging of the particles themselves (Fig. 2.14A and B). The isoelectric point of their $TiO_2$ particles were found to be at pH ~ 5.7 (Fig. 2.14A) which coincided with a maximum in its yield stress (Fig. 2.14B).

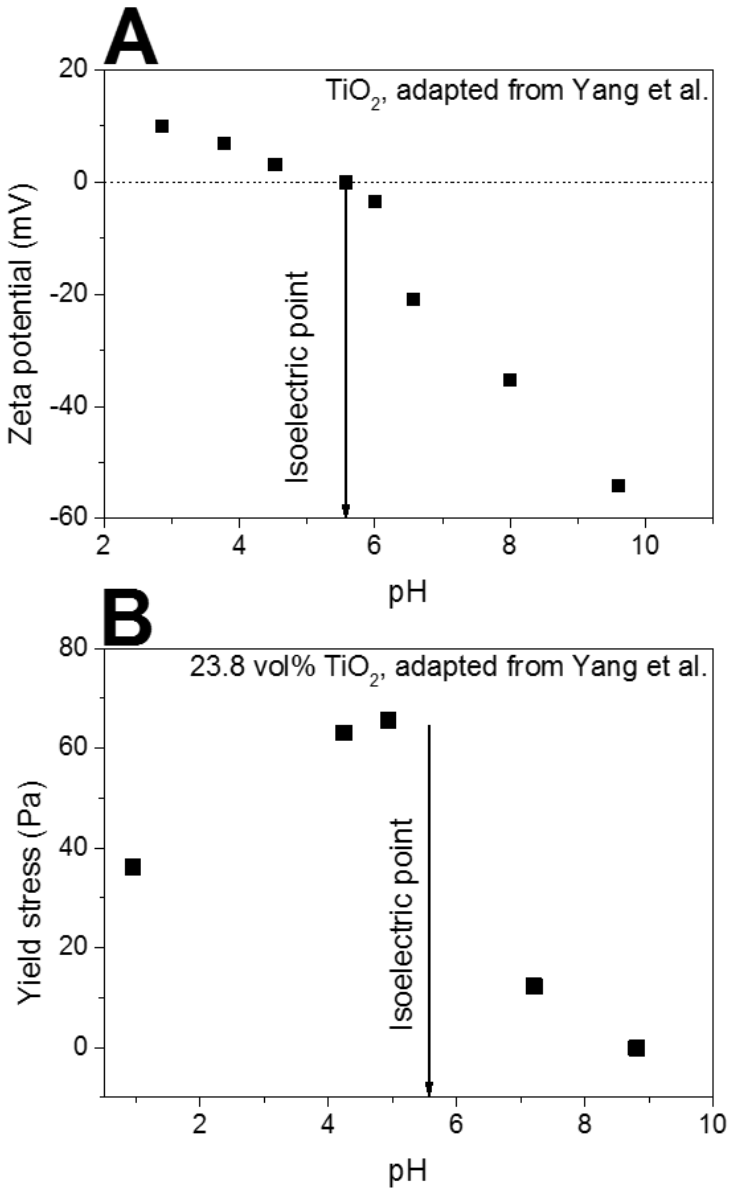


**Figure 2.14: Comparison between the charging behaviour of $TiO_2$ particles (A) and its changes in bulk yield stress when part of a concentrated suspension (B). Adapted from Yang et al. [69].**

These findings also coincide with the results obtained for Mikulášek et al. [70], Leong et al. [71-73], Scales et al. [55], Johnson et al. [25, 74, 75] and Franks et al. [76] where maximum yield stresses or bulk shear thickening behaviour were observed near the isoelectric points for $TiO_2$, silica, α-alumina and zirconia suspensions. The authors made use of the DLVO theory to describe the underlaying processes involved in changing suspension bulk rheology. When the particles are near their isoelectric points, the charge of the particle surface is close to that of the bulk fluid, meaning that

the intensity of the electrical double layer is greatly reduced ($\zeta^2$ in Equation 2.15 is significantly smaller) [35]. The particles can therefore come into closer proximity when they are being attracted via the London van der Waals forces of attraction [35]. The closer proximity of the particles will greatly enhance the strength of the London van der Waals forces of attraction ($H^2$ in Equation 2.16 becomes smaller), meaning that the overall particle-particle links will become stronger and therefore stiffer, increasing the amount of energy (or torque) required to break these bonds to induce flow.

The experimental methodologies from Yang et al. [69], Mikulášek et al. [70] and Leong et al. [71-73] show a key difference to that used by Scales et al. [55], Johnson et al [25, 74, 75] and Franks et al. [76] in that the first three authors did not use a background electrolyte when performing pH tests for their suspensions. Equation 2.15 shows that for pH experiments at fixed solids concentrations, two main factors may contribute to changes in the structure of the electrical double layer; zeta potential, $\zeta$, which affects the 'intensity' of the electrical double layer, and the concentration of ions in the bulk solution, $n_0$, which affects the electrical double layer's Debye length ($\kappa^{-1}$). When additional acid or base is added to the suspension, both $\zeta$ and $n_0$ will change due to an increased concentration of ions that will also affect the bulk solution pH. The resulting bulk rheological changes will therefore be due to changes in both $n_0$ and $\zeta$. To make a clear comparison between the QCM response and bulk rheological changes, the contributing factors affecting both the QCM resonator and the sludge bulk yield stress would need to be investigated separately. To partially achieve this goal, methodologies from Scales et al. [55], Johnson et al. [25, 74, 75] and Franks et al. [76] should instead be followed where a background electrolyte of at least 10 mMol/L is used. This would allow for insignificant changes in electrolyte concentrations when the pH of a suspension is altered between pH values of ~ 3 – 11

(1 mMol/L $H^+$ at pH 3 and 1 mMol/L $OH^-$ at pH 11, representing a maximum increase of 10% in the electrolyte concentration). pH alterations should also be made to separate batches of material; if the pH of a single sample has been raised using a base, reducing its pH for a subsequent test using an acid will result in additional electrolyte ions being present compared to the same sample that only had its pH reduced.

Significantly altering the background electrolyte concentration of a suspension may also change the surface properties of the materials involved [77, 78]. For example, when NaCl is used as an electrolyte, the gold surface is known to become chlorinated [77], reducing the surface isoelectric point to lower pH values and therefore also altering the surface charge of the material [77, 79]. This effect changes how strongly particles may be attracted to the surface. This will therefore potentially create an additional unwanted effect that contribute to changes in the QCM resonator response when investigating effects of electrolyte concentration.

Introducing additional particles into the bulk suspension will cause extra links to form between each particle, resulting in a stiffening of the overall three-dimensional network and therefore increasing the shear yield stress of the suspension [25, 55, 71-73]. Figure 2.15 is an adaptation of the data obtained from Scales et al. [55] (A) and Leong et al. [71-73] (B) showing changes in the bulk suspension yield stress with changes in the suspension solids volume fraction. An exponential relationship is observed which is predicted by Kapur et al. [80] and Scales et al. [55].

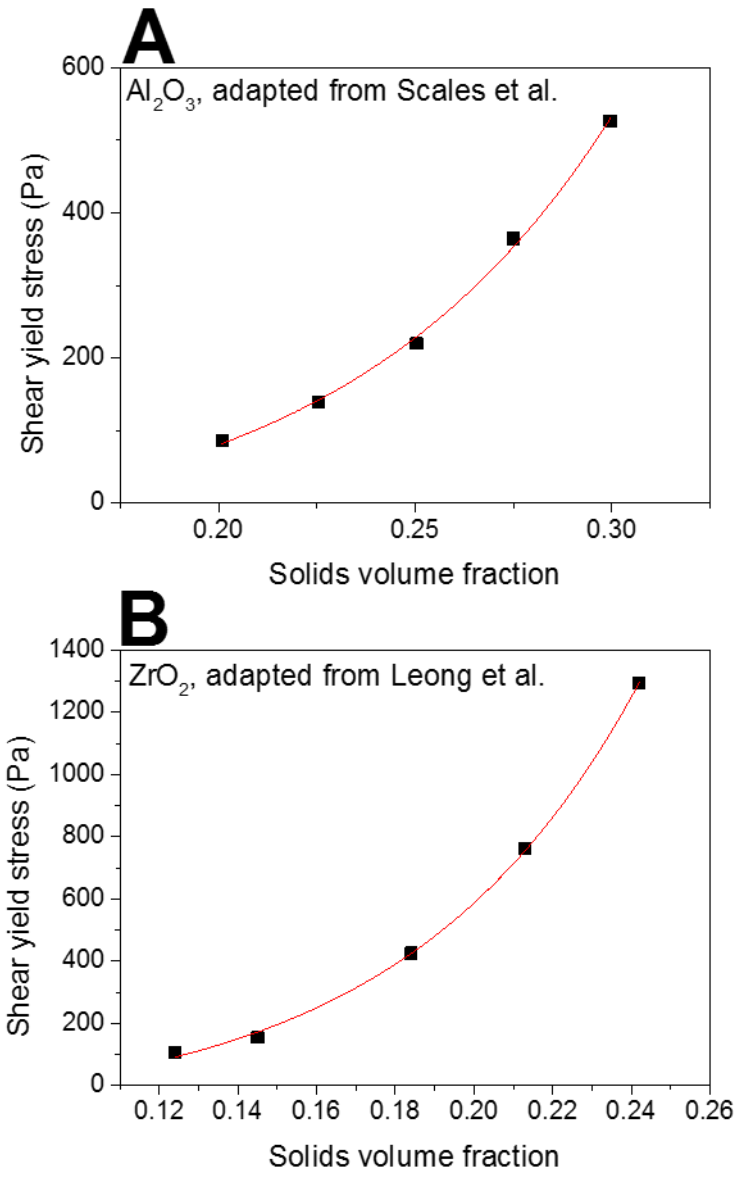


**Figure 2.15: Maximum shear yield stress values for $Al_2O_3$ (A) and $ZrO_2$ (B) at their isoelectric points at different solids volume fractions. Adapted from Scales et al. [55] and Leong et al. [71-73].**

Due to this exponential relationship, small changes in the suspension volume fraction could create significantly large changes in bulk suspension yield stress. It is therefore essential to ensure that drying or additional dilution of the suspension network is kept to a minimum. Sample beakers will be sealed as much as possible to help reduce evaporation. When pH adjustments are made, the acid/base should be at high concentrations to minimise dilution effects. Mineral oil has also shown to be effective at preventing water evaporation when a sufficiently thick layer is present in-between

the water-air interface [81]. In addition to sealing the sample holders, mineral oil should also be used to prevent evaporation for long-term studies.

The work discussed here have shown that changes in the solids volume fraction and suspension pH change the bulk suspension yield stress due to comparatively different underlaying mechanisms; suspensions that therefore show an increase in yield stress due to both pH and concentration effects may show a different QCM resonator response. By referring to the DLVO and QCM theory, the differences in response may be explained, leading to a better understanding on how the QCM performs when used as a device to measure changes in suspension rheology.

## 2.7. Review on previous work relating to QCM particle adsorption

To the best of the author's knowledge, there have been no other studies involving the use of the QCM to measure the rheological properties of concentrated (networked) sludge. There have however been studies investigating the contact behaviour of particles in dilute aqueous suspensions onto a QCM resonator surface. By forming an understanding on the underlaying mechanisms involved when particles in aqueous media adsorb to the QCM resonator surface, the QCM signal could be better understood after it had been submerged into concentrated suspensions instead.

Previously the work from Pomorska et al. [5] has been discussed where particles in contact with a QCM resonator can be considered as a coupled resonance system (the resonating QCM is in contact with a particle that is also resonating at its natural frequency of vibration). This model creates two extreme cases where if the particles resonate at a much greater frequency than the sensor, inertial loading occurs and the system behaves similarly to that described by Sauerbrey [3, 5] where you get a negative frequency shift (Equation 2.13). In the opposite case elastic loading occurs

and you have the Dybwad case [4, 5, 23] where a positive frequency shift is observed (Equation 2.14). A review of QCM literature revealed that the amount of work discussing positive frequency shifts are fairly limited compared to the more well-known negative shift behaviour. Marxer et al. [82] described the positive frequency shifts they obtained after cells adsorbed and spread across the QCM resonator surface as an increase in the stiffness of the cell matrix from a viscoelastic point of view, and that this change would affect the sensitivity of the QCM (Fig. 2.16). Obtaining frequency shifts that are positive after the introduction of a viscous medium is to the author's knowledge not possible (refer to Equations 2.4, 2.7, 2.8 and 2.9 for the mathematical representation). The sensitivity of the QCM is also known to extend well into the ng/cm$^2$ range [1, 3], meaning that a frequency shift of +40 Hz (Fig. 2.16) could likely not be attributed to a decrease in sensitivity. In this case the stiffening of the cell matrix could be a result of stronger links between the individual cells, resulting in the QCM detecting these cells as larger particles due to them interacting with each other more strongly. The larger particles would have a reduced natural frequency of vibration, resulting in elastic loading behaviour.

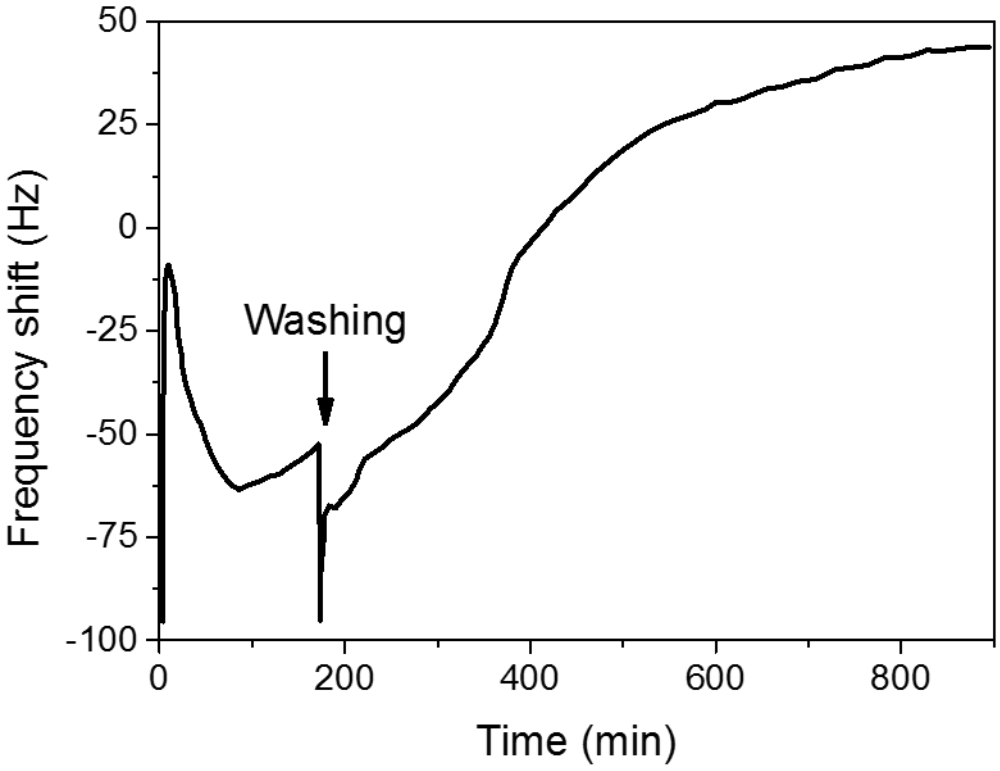


**Figure 2.16: QCM background solution to loaded solution frequency shift during the adsorption of A549 70E4 cells onto the resonator surface. The cell network stiffens and adsorb more firmly over time, possibly resulting in a transition from inertial to elastic loading behaviour. Adapted from Marxer et al. [82].**

Lapidot et al. [83] performed crystallisation experiments on the QCM resonator surface (Figure 2.17A and B) and derived a model that can be used to analyse surface crystallisation using a QCM-D. In their experimental results they also experienced positive frequency shifts at higher overtones (Figure 2.17A). They concluded that smaller crystals have a natural resonance frequency that is much higher than the resonator, resulting in an 'inertial driven behaviour' that is akin to the Sauerbrey behaviour [83]. When the crystals grow into a more macroscopic structure, a frequency inversion occurs when the crystal's elasticity becomes the dominating impedance [83]. The results and reasoning from Lapidot et al. [83] coincide well with the findings from Pomorska et al. [5] and Johannsmann et al. [84] and their description of the underlaying mechanics involved.

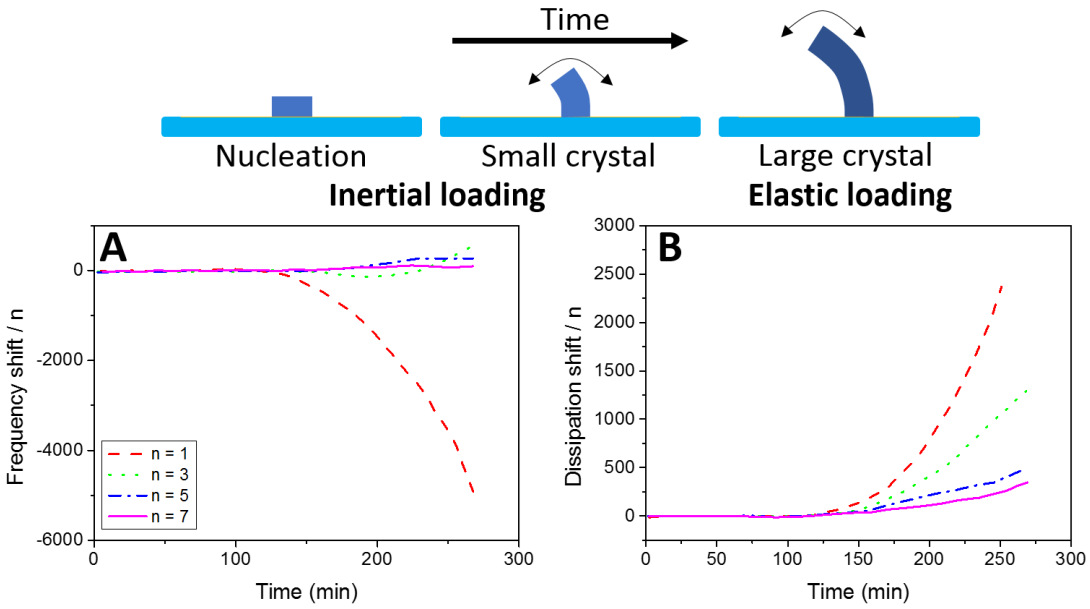


**Figure 2.17: QCM-D response during the crystallisation of calcium sulphate onto the resonator surface from a solution with a supersaturation index of 3.22. Adapted from Lapidot et al. [83].**

Several recent publications involving QCM particle adsorption focuses on DLVO theory to explain the underlaying mechanisms involved. Chen et al. [85] investigated the aggregation and deposition behaviour of fullerene nanoparticles in the presence of monovalent and divalent electrolyte species at different pH values. Larger overall frequency shifts are observed when the suspension background electrolyte concentration is increased (Fig. 2.18) due to a compression of the electrical double layer resulting in additional particle adsorption [85]. The QCM response also showed a greater negative frequency shift in divalent electrolyte solutions at pH values where they are expected to be more strongly attracted to the resonator surface (Fig. 2.18), confirming that the electrical double layer strongly affects the amount of deposition and hence the QCM response [85].

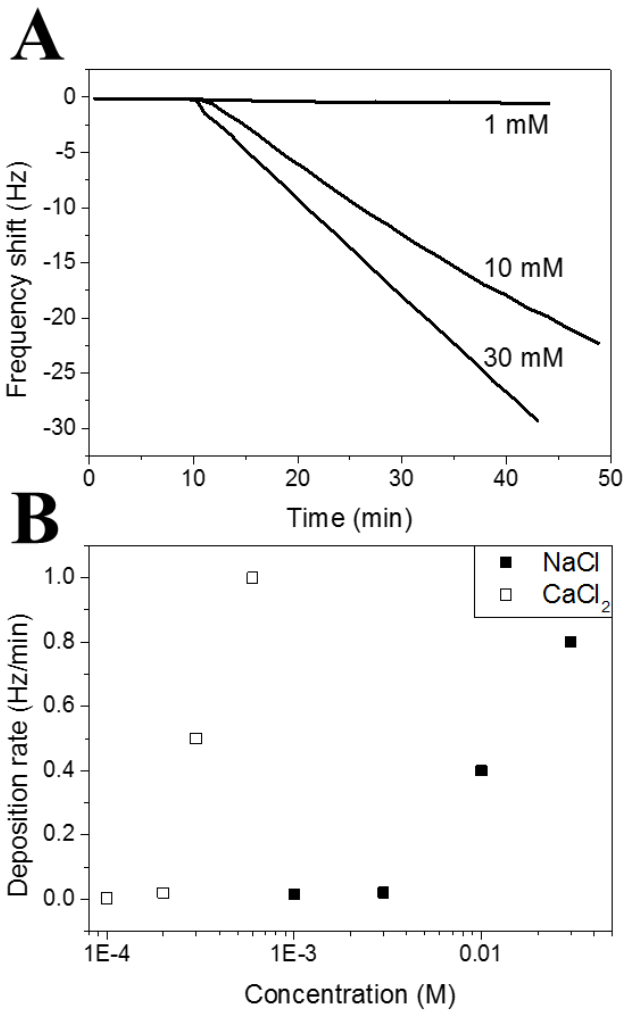


**Figure 2.18: (A) QCM frequency response during the deposition of fullerene nanoparticles onto an oppositely charged QCM resonator surface at different NaCl electrolyte concentrations. (B) the gradient of each line was taken for both NaCl + $CaCl_2$ and plotted as a function of the initial electrolyte concentration. Adapted from Chen et al. [85].**

Fatisson et al. [86] reported similar results in their investigation where they monitored the rate of deposition of $TiO_2$ nanoparticles onto a silica-coated QCM resonator surface at varying pH and electrolyte concentration. They found that the slope of the QCM frequency shift and dissipation factor over time proved to be a useful indicator to measure particle deposition rates where the rate of change in the QCM response correlated to expected deposition rates based on DLVO theory [86]. Gotoh et al. [87] also found similar results to Fatisson et al. [86] where the QCM response was shown to correlate well to deposition rates for different sensor coatings.

Pham et al. [88] evaporated suspensions of particles of known sizes on the QCM surface. They found that the QCM response is sensitive to the size distribution of particles and that smaller sized particles would adsorb more rigidly, resulting in a more Sauerbrey-like response [88]. As the particle size increases, the frequency shift initially becomes more negative as one would expect, however the magnitude of the frequency shift would begin to reduce again for larger particles (Fig. 2.19). The motional resistance increases with increasing particle size, meaning that the response deviates further from an ideal Sauerbrey case, suggesting that the entirety of the particle's added mass is not detected at larger sizes as a significant portion of the vibrational energy from the QCM resonator is dissipated (Fig. 2.19) [88].

These findings indicate that there is an inefficient transfer of vibrational energy between the QCM and linked particles that may be dependent on the strength of the particle-sensor link, and the physical properties of the particle (i.e. its size).

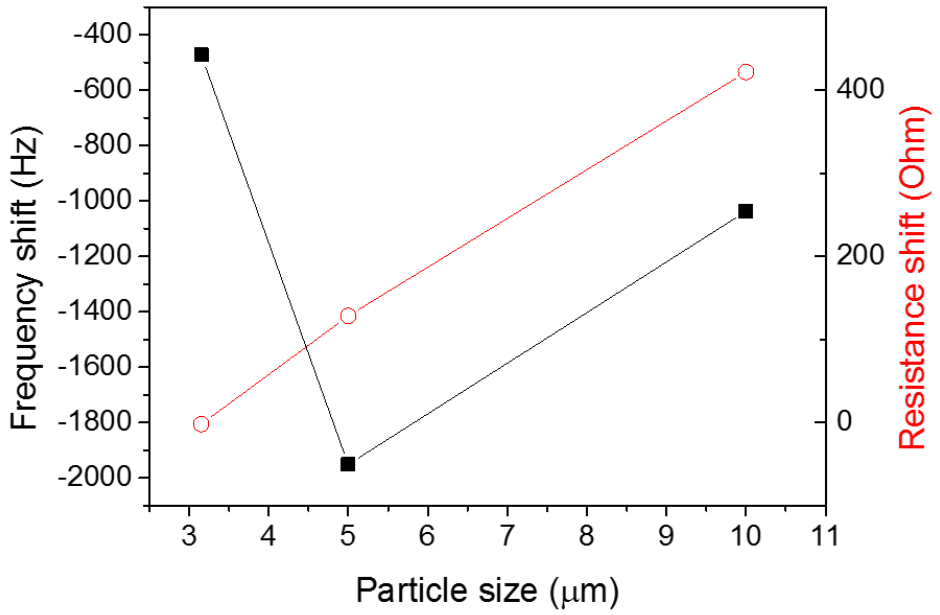


**Figure 2.19: QCM frequency (black squares) and resistance (red open circles) shift as a function of adsorbed particle size after the complete evaporation of 0.5 µL of an aqueous suspension containing 1 wt% monodisperse latex particles on the resonator surface. Adapted from Pham et al. [88].**

Zhuang et al. [89] performed similar evaporation tests on the QCM surface using alumina suspensions. They found that as they performed evaporation tests on 1 µm particles of different solids concentrations, a plateau in the frequency shift is observed at concentrations above ~3 wt% [89]. The QCM may therefore only detect a given layer of particles, depending on its penetration depth. The 1 µm particles also produced positive frequency shifts at concentrations > ~1.6 wt% [89]. Zhang et al. argued that this positive shift is because the overlaying particles that are detected by the QCM are clamped by inertia, making them stationary which therefore increases the contribution from elastic loading effects [89]. Interestingly, Zhang et al. also argued that the contact stiffness between the particles themselves contributed more to the positive frequency shift than the suspension solids concentration and suggested that the particle-particle contact stiffness plays a significant role [89]. Equation 2.14 does indeed show that $\Delta f \propto \kappa_S$, however $\kappa_S$ is the stiffness of the sphere-plate contact

and therefore does not take sphere-sphere contact stiffness into account. An increase in the particle-particle stiffness would however result in additional particles within the detectable range of the QCM to appear stationary since a greater force is present that holds the particles fixed in space. This will increase the overall contribution from elastic loading effects, increasing the frequency shift to more positive values.

If the particles remain within a sufficiently small size, and the solids concentration is low enough to ensure that a single layer of particles remain on the resonator surface after evaporation, the QCM response can also be used to track the solids concentration of the dilute suspensions [90, 91]. It should however be noted that the authors [90, 91] deposited a small known volume of suspension onto the resonator surface. If the resonator surface were to be exposed to an infinite volume of fluid instead, the particles may preferentially adsorb or remain away from the resonator surface, resulting resonance shifts that do not reflect the bulk suspension solids concentration.

Tellechea et al. [4] investigated the ratio between the QCM frequency shift and half-band-half-width shift ($\Delta\Gamma/-\Delta F$) during particle adsorption in an effectively infinite suspension volume. They found that the ratio increased with particle size (a greater contribution from the QCM dampening process), matching the observations from Pham et al. [88]. Tellechea et al. however takes this concept further and found that by plotting $\Delta\Gamma/-\Delta F$ against $-\Delta F/n$ as colloidal particles adsorb onto the resonator surface over time, you find a linear trend where you can estimate the film thickness if you extrapolate the plot to $\Delta\Gamma/-\Delta F = 0$ and using the obtained $-\Delta F/n$ in the Sauerbrey equation to find the Sauerbrey mass [4] (see Chapter 6 for a more in-depth description). If the density of the overlaying material is known, then the calculated Sauerbrey mass can be used to determine the thickness (or size) of the overlaying film.

Tellechea et al. used lipids and viruses in their experiments, making each individual colloid very small and therefore penetrable by the QCM sensor [4].

The work discussed here mainly focused on deposition rates and the evaporation of relatively dilute colloidal suspensions. The contact mechanics involving highly concentrated (networked) suspensions on a QCM resonator surface, where the QCM resonance shifts can be correlated to changes in the bulk suspension rheology is yet to be investigated. The focus of the work will therefore be broken down into 3 main areas of research:

1. Investigating how changes in the particle-particle contact strength affects suspension rheology and how these changes also affect the QCM response. The contact strength between the resonator surface and the particles will be constant.
2. Investigating the changes particle-sensor contact strength as the pH of a suspension is altered. The QCM response will be compared to bulk rheological changes of the suspension as well as models from the DLVO theory to investigate which interaction (particle-particle or particle-sensor) has the greatest influence on the QCM response.
3. Comparing bulk rheological changes of a suspension due to changes in its concentration to viscoelastic models using QCM data. The derived viscoelastic moduli at high frequencies will be compared to similar parameters at low frequency experiments that are used conventionally.

These 3 main areas of work would help address the current gap in literature and allow for the basics of using the QCM to measure the rheology of complex networked suspensions to be understood.

## 2.8. References


1. Johannsmann, D., *Viscoelastic, mechanical, and dielectric measurements on complex samples with the quartz crystal microbalance.* Physical Chemistry Chemical Physics, 2008. **10**(31): p. 4516-4534.
2. Johannsmann, D., *The Quartz Crystal Microbalance in Soft Matter Research*. 2015: Springer, Cham.
3. Sauerbrey, G., *Verwendung Von Schwingquarzen Zur Wagung Dunner Schichten Und Zur Mikrowagung.* Zeitschrift Fur Physik, 1959. **155**(2): p. 206-222.
4. Tellechea, E., et al., *Model-Independent Analysis of QCM Data on Colloidal Particle Adsorption.* Langmuir, 2009. **25**(9): p. 5177-5184.
5. Pomorska, A., et al., *Positive Frequency Shifts Observed Upon Adsorbing Micron-Sized Solid Objects to a Quartz Crystal Microbalance from the Liquid Phase.* Analytical Chemistry, 2010. **82**(6): p. 2237-2242.
6. Reviakine, I., D. Johannsmann, and R.P. Richter, *Hearing what you cannot see and visualizing what you hear: interpreting quartz crystal microbalance data from solvated interfaces*. 2011, ACS Publications.
7. Vogt, B.D., et al., *Effect of film thickness on the validity of the Sauerbrey equation for hydrated polyelectrolyte films.* The Journal of Physical Chemistry B, 2004. **108**(34): p. 12685-12690.
8. Kanazawa, K.K. and J.G. Gordon, *The Oscillation Frequency of a Quartz Resonator in Contact with a Liquid.* Analytica Chimica Acta, 1985. **175**(Sep): p. 99-105.
9. Martin, S.J., V.E. Granstaff, and G.C. Frye, *Characterization of a Quartz Crystal Microbalance with Simultaneous Mass and Liquid Loading.* Analytical Chemistry, 1991. **63**(20): p. 2272-2281.
10. Reviakine, I., D. Johannsmann, and R.P. Richter, *Hearing What You Cannot See and Visualizing What You Hear: Interpreting Quartz Crystal Microbalance Data from Solvated Interfaces.* Analytical Chemistry, 2011. **83**(23): p. 8838-8848.
11. Rodahl, M. and B. Kasemo, *A simple setup to simultaneously measure the resonant frequency and the absolute dissipation factor of a quartz crystal microbalance.* Review of Scientific Instruments, 1996. **67**(9): p. 3238-3241.
12. Sittel, K., P.E. Rouse Jr, and E.D. Bailey, *Method for Determining the Viscoelastic Properties of Dilute Polymer Solutions at Audio-Frequencies.* Journal of Applied Physics, 1954. **25**(10): p. 1312-1320.
13. Butterworth, S., *On electrically-maintained vibrations.* Proceedings of the Physical Society of London, 1914. **27**(1): p. 410.
14. Van Dyke, K., *The piezo-electric resonator and its equivalent network.* Proceedings of the Institute of Radio Engineers, 1928. **16**(6): p. 742-764.
15. Calvo, E., et al., *Quartz crystal impedance studies at 10 MHz of viscoelastic liquids and films.* Faraday Discussions, 1997. **107**: p. 141-157.
16. Wolff, O., E. Seydel, and D. Johannsmann, *Viscoelastic properties of thin films studied with quartz crystal resonators.* Faraday Discussions, 1997. **107**: p. 91-104.
17. Mason, W.P. and H. Baerwald, *Piezoelectric crystals and their applications to ultrasonics.* Physics Today, 1951. **4**: p. 23.
18. Rodahl, M., et al., *Quartz-Crystal Microbalance Setup for Frequency and Q-Factor Measurements in Gaseous and Liquid Environments.* Review of Scientific Instruments, 1995. **66**(7): p. 3924-3930.

19. Nandi, N., K. Bhattacharyya, and B. Bagchi, *Dielectric relaxation and solvation dynamics of water in complex chemical and biological systems.* Chemical Reviews, 2000. **100**(6): p. 2013-2046.
20. Voinova, M.V., et al., *Viscoelastic acoustic response of layered polymer films at fluid-solid interfaces: Continuum mechanics approach.* Physica Scripta, 1999. **59**(5): p. 391-396.
21. Domack, A., et al., *Swelling of a polymer brush probed with a quartz crystal resonator.* Physical Review E, 1997. **56**(1): p. 680.
22. Pakula, T., et al., *Relaxation and viscoelastic properties of complex polymer systems.* Rheologica acta, 1996. **35**(6): p. 631-644.
23. Dybwad, G.L., *A Sensitive New Method for the Determination of Adhesive Bonding between a Particle and a Substrate.* Journal of Applied Physics, 1985. **58**(7): p. 2789-2790.
24. D'amour, J., et al., *Capillary aging of the contacts between glass spheres and a quartz resonator surface.* Physical review letters, 2006. **96**(5): p. 058301.
25. Johnson, S.B., et al., *Surface chemistry-rheology relationships in concentrated mineral suspensions.* International Journal of Mineral Processing, 2000. **58**(1-4): p. 267-304.
26. Derjaguin, B.V., Landau, L., *Theory of the stability of strongly charged lyophobic sols and of the adhesion of strongly charged particles in solutions of electrolytes.* Acta Physicochim, 1941. **14**: p. 633-662.
27. Verwey, E.J.W., *Theory of the Stability of Lyophobic Colloids.* Journal of Physical and Colloid Chemistry, 1947. **51**(3): p. 631-636.
28. Pomorska, A., et al., *QCM study of the adsorption of polyelectrolyte covered mesoporous TiO2 nanocontainers on SAM modified Au surfaces.* Journal of colloid and interface science, 2011. **362**(1): p. 180-187.
29. Tombácz, E., *pH-dependent surface charging of metal oxides.* Periodica Polytechnica. Chemical Engineering, 2009. **53**(2): p. 77.
30. Welch, D.A., et al., *Using molecular dynamics to quantify the electrical double layer and examine the potential for its direct observation in the in-situ TEM.* Advanced Structural and Chemical Imaging, 2015. **1**(1): p. 1.
31. Du, H., et al., *Electric double-layer transistors: a review of recent progress.* Journal of materials science, 2015. **50**(17): p. 5641-5673.
32. Israelachvili, J. and H. Wennerström, *Role of hydration and water structure in biological and colloidal interactions.* Nature, 1996. **379**(6562): p. 219.
33. áO'Brien, R.W., *Electroacoustic studies of moderately concentrated colloidal suspensions.* Faraday Discussions of the Chemical Society, 1990. **90**: p. 301-312.
34. Lennard-Jones, J.E., *Cohesion.* Proceedings of the Physical Society, 1931. **43**(5): p. 461.
35. Hogg, R., T.W. Healy, and Fuersten.Dw, *Mutual Coagulation of Colloidal Dispersions.* Transactions of the Faraday Society, 1966. **62**(522P): p. 1638-&.
36. Israelachvili, J.N., *Adhesion Forces between Surfaces in Liquids and Condensable Vapors.* Surface Science Reports, 1992. **14**(3): p. 109-159.
37. Hamaker, H.C., *The London - Van Der Waals attraction between spherical particles.* Physica, 1937. **4**: p. 1058-1072.
38. Visser, J., *On Hamaker constants: A comparison between Hamaker constants and Lifshitz-van der Waals constants.* Advances in colloid and interface science, 1972. **3**(4): p. 331-363.

39. Lifshitz, E.M., *The Theory of Molecular Attractive Forces between Solids.* Soviet Physics Jetp-Ussr, 1956. **2**(1): p. 73-83.
40. Gomez-Merino, A.L., et al., *The Hamaker constant of anatase aqueous suspensions.* Journal of Colloid and Interface Science, 2007. **316**(2): p. 451-456.
41. Winterton, R., *The direct measurement of normal and retarded van der Waals forces.* Proc. R. Soc. Lond. A, 1969. **312**(1511): p. 435-450.
42. Ackler, H.D., R.H. French, and Y.-M. Chiang, *Comparisons of Hamaker constants for ceramic systems with intervening vacuum or water: From force laws and physical properties.* Journal of Colloid and Interface Science, 1996. **179**(2): p. 460-469.
43. Ducker, W.A., T.J. Senden, and R.M. Pashley, *Measurement of forces in liquids using a force microscope.* Langmuir, 1992. **8**(7): p. 1831-1836.
44. Larson, I., et al., *Direct force measurements between titanium dioxide surfaces.* Journal of the American Chemical Society, 1993. **115**(25): p. 11885-11890.
45. Hough, D.B. and L.R. White, *The calculation of Hamaker constants from Liftshitz theory with applications to wetting phenomena.* Advances in Colloid and Interface Science, 1980. **14**(1): p. 3-41.
46. Lennard-Jones, J.E., *Cohesion.* Proceedings of the Physical Society, 1931. **43**: p. 461-482.
47. Manciu, M. and E. Ruckenstein, *Role of the hydration force in the stability of colloids at high ionic strengths.* Langmuir, 2001. **17**(22): p. 7061-7070.
48. Hunter, R.J., *Foundations of colloid science*. 2001: Oxford university press.
49. Israelachvili, J.N. and R.M. Pashley, *Molecular Layering of Water at Surfaces and Origin of Repulsive Hydration Forces.* Nature, 1983. **306**(5940): p. 249-250.
50. Pashley, R., *Hydration forces between mica surfaces in aqueous electrolyte solutions.* Journal of Colloid and Interface Science, 1981. **80**(1): p. 153-162.
51. Pashley, R., *DLVO and hydration forces between mica surfaces in Li+, Na+, K+, and Cs+ electrolyte solutions: A correlation of double-layer and hydration forces with surface cation exchange properties.* Journal of Colloid and Interface Science, 1981. **83**(2): p. 531-546.
52. Israelachvili, J.N., *Forces between Surfaces in Liquids.* Advances in Colloid and Interface Science, 1982. **16**(Jul): p. 31-47.
53. Liddell, P.V. and D.V. Boger, *Yield stress measurements with the vane.* Journal of Non-Newtonian Fluid Mechanics, 1996. **63**(2-3): p. 235-261.
54. Dzuy, N.Q. and D.V. Boger, *Yield Stress Measurement for Concentrated Suspensions.* Journal of Rheology, 1983. **27**(4): p. 321-349.
55. Scales, P.J., et al., *Shear yield stress of partially flocculated colloidal suspensions.* AIChE Journal, 1998. **44**(3): p. 538-544.
56. Keentok, M., *The Measurement of the Yield Stress of Liquids.* Rheologica Acta, 1982. **21**(3): p. 325-332.
57. McDowell, C.M. and F.L. Ushep, *Viscosity and rigidity in suspensions of fine particles I - Aqueous suspensions.* Proceedings of the Royal Society of London Series a-Containing Papers of a Mathematical and Physical Character, 1931. **131**(817): p. 409-427.
58. Goodeve, C.F., *A general theory of thixotropy and viscosity.* Transactions of the Faraday Society, 1939. **35**(1): p. 0342-0357.

59. Chow, M.K. and C.F. Zukoski, *Nonequilibrium Behavior of Dense Suspensions of Uniform Particles - Volume Fraction and Size Dependence of Rheology and Microstructure.* Journal of Rheology, 1995. **39**(1): p. 33-59.
60. Dekee, D., P. Mohan, and D.S. Soong, *Yield Stress Determination of Styrene-Butadiene-Styrene Triblock Copolymer Solutions.* Journal of Macromolecular Science-Physics, 1986. **B25**(1-2): p. 153-169.
61. Dzuy, N.Q. and D.V. Boger, *Direct Yield Stress Measurement with the Vane Method.* Journal of Rheology, 1985. **29**(3): p. 335-347.
62. Alderman, N.J., G.H. Meeten, and J.D. Sherwood, *Vane Rheometry of Bentonite Gels.* Journal of Non-Newtonian Fluid Mechanics, 1991. **39**(3): p. 291-310.
63. Avramidis, K.S. and R.M. Turian, *Yield Stress of Laterite Suspensions.* Journal of Colloid and Interface Science, 1991. **143**(1): p. 54-68.
64. Chang, J.C., F.F. Lange, and D.S. Pearson, *Viscosity and Yield Stress of Alumina Slurries Containing Large Concentrations of Electrolyte.* Journal of the American Ceramic Society, 1994. **77**(1): p. 19-26.
65. Yoshimura, A.S., et al., *A Comparison of Techniques for Measuring Yield Stresses.* Journal of Rheology, 1987. **31**(8): p. 699-710.
66. Keentok, M., J.F. Milthorpe, and E. Odonovan, *On the Shearing Zone around Rotating Vanes in Plastic Liquids - Theory and Experiment.* Journal of Non-Newtonian Fluid Mechanics, 1985. **17**(1): p. 23-35.
67. National Research Council Canada. and American Society for Testing and Materials., *Laboratory shear testing of soils; a symposium*. ASTM special technical publication. 1964, Philadelphia,: American Society for Testing and Materials. vii, 505 p.
68. James, A.E., D.J.A. Williams, and P.R. Williams, *Direct Measurement of Static Yield Properties of Cohesive Suspensions.* Rheologica Acta, 1987. **26**(5): p. 437-446.
69. Yang, H.G., et al., *Rheological behavior of titanium dioxide suspensions.* Journal of Colloid and Interface Science, 2001. **236**(1): p. 96-103.
70. Mikulášek, P., R. Wakeman, and J. Marchant, *The influence of pH and temperature on the rheology and stability of aqueous titanium dioxide dispersions.* Chemical Engineering Journal, 1997. **67**(2): p. 97-102.
71. Leong, Y.-K., et al., *Control of the rheology of concentrated aqueous colloidal systems by steric and hydrophobic forces.* Journal of the Chemical Society, Chemical Communications, 1993(7): p. 639-641.
72. KwongáLeong, Y., *Rheological evidence of adsorbate-mediated short-range steric forces in concentrated dispersions.* Journal of the Chemical Society, Faraday Transactions, 1993. **89**(14): p. 2473-2478.
73. Leong, Y., *Interparticle forces arising from an adsorbed strong polyelectrolyte in colloidal dispersions: charged patch attraction.* Colloid and Polymer Science, 1999. **277**(4): p. 299-305.
74. Johnson, S.B., et al., *The binding of monovalent electrolyte ions on α-alumina. II. The shear yield stress of concentrated suspensions.* Langmuir, 1999. **15**(8): p. 2844-2853.
75. Johnson, S.B., P.J. Scales, and T.W. Healy, *The binding of monovalent electrolyte ions on α-alumina. I. Electroacoustic studies at high electrolyte concentrations.* Langmuir, 1999. **15**(8): p. 2836-2843.
76. Franks, G.V., et al., *Effect of interparticle forces on shear thickening of oxide suspensions.* Journal of Rheology, 2000. **44**(4): p. 759-779.

77. Barten, D., et al., *Double layer of a gold electrode probed by AFM force measurements.* Langmuir, 2003. **19**(4): p. 1133-1139.
78. Kasuya, M., et al., *Anion Adsorption on Gold Electrodes Studied by Electrochemical Surface Forces Measurement*. The Journal of Physical Chemistry C, 2016. **120**(29): p. 15986-15992.
79. Giesbers, M., J.M. Kleijn, and M.A.C. Stuart, *The electrical double layer on gold probed by electrokinetic and surface force measurements.* Journal of Colloid and Interface Science, 2002. **248**(1): p. 88-95.
80. Kapur, P.C., et al., *Yield stress of suspensions loaded with size distributed particles.* AIChE Journal, 1997. **43**(5): p. 1171-1179.
81. Shimura, K., N. Uchiyama, and K.i. Kasai, *Prevention of evaporation of small-volume sample solutions for capillary electrophoresis using a mineral-oil overlay*. Electrophoresis, 2001. **22**(16): p. 3471-3477.
82. Marxer, C.M., et al., *Cell spreading on quartz crystal microbalance elicits positive frequency shifts indicative of viscosity changes.* Analytical and Bioanalytical Chemistry, 2003. **377**(3): p. 578-586.
83. Lapidot, T., K.L. Sedransk Campbell, and J.Y. Heng, *Model for interpreting surface crystallization using Quartz Crystal Microbalance: Theory and experiments.* Analytical Chemistry, 2016. **88**(9): p. 4886-4893.
84. Johannsmann, D., I. Reviakine, and R.P. Richter, *Dissipation in Films of Adsorbed Nanospheres Studied by Quartz Crystal Microbalance (QCM).* Analytical Chemistry, 2009. **81**(19): p. 8167-8176.
85. Chen, K.L. and M. Elimelech, *Aggregation and deposition kinetics of fullerene (C60) nanoparticles.* Langmuir, 2006. **22**(26): p. 10994-11001.
86. Fatisson, J., et al., *Deposition of TiO2 nanoparticles onto silica measured using a quartz crystal microbalance with dissipation monitoring.* Langmuir, 2009. **25**(11): p. 6062-6069.
87. Gotoh, K., Y. Nakata, and M. Tagawa, *Evaluation of particle deposition in aqueous solutions by the quartz crystal microbalance method.* Colloids and Surfaces A: Physicochemical and Engineering Aspects, 2006. **272**(1-2): p. 117-123.
88. Pham, N., et al., *Application of the quartz crystal microbalance to the evaporation of colloidal suspension droplets.* Langmuir, 2004. **20**(3): p. 841-847.
89. Zhuang, H., et al., *Study of the evaporation of colloidal suspension droplets with the quartz crystal microbalance.* Langmuir, 2008. **24**(15): p. 8373-8378.
90. Reipa, V. and J.H. Choi, *Measurement of silicon nanoparticle concentration using quartz crystal microgravimetry.* ECS Transactions, 2009. **25**(9): p. 167-175.
91. Reipa, V., G. Purdum, and J. Choi, *Measurement of nanoparticle concentration using quartz crystal microgravimetry.* The Journal of Physical Chemistry B, 2010. **114**(49): p. 16112-16117.

# 3. Methodology

## 3.1. Scanning electron microscopy (SEM)

Electrons consist of smaller wavelengths ($10^{-2}$ – $10^{-3}$ nm) compared to visible light (400 – 700 nm), allowing for the detection of small objects at resolutions that can extend below that possible for light-based equipment [1]. Electrons are generated from tungsten filaments [1] within a thermionic emission or field emission electron (FEG) gun [2]. A series of electromagnetic lenses allows for the electrons to be focused before they interact with the presented sample. Images are taken inside a vacuum to reduce electron collision with gaseous atoms which will reduce image quality. Once the electron beam hits the sample surface, electrons may be backscattered (elastic scattering) or be reflected as secondary or auger electrons (inelastic scattering) with the excess energy being emitted in the form of X-ray radiation [3]. In SEM, the electron beam rasters over the sample surface and the reflected electrons are detected by surrounding detectors, which generates an image of the surface [4]. Secondary electrons are significantly more abundant due to the excitation of several atoms for each incident electron, however they are more surface sensitive due to their low kinetic energy. More energetic backscattered electrons allow for additional characterisation including the ability for distinctions of different elements of high atomic masses to be made. For analysis, powder samples were deposited onto a metal holder covered by a carbon tape and blown with compressed gas to remove any particles not stuck to the tape. The powder samples are then mounted into the SEM device, and air is pumped from the system to create a vacuum environment before imaging commences.

## 3.2. Thermo-gravimetric analysis and differential scanning calorimetry (TGA-DSC)

The TGA-DSC is a high sensitivity mass balance that allows for the quantification of chemical reactions or physical transformations in terms of mass change. A semi-sealed tube furnace (Fig. 3.1) allows for passage of the sample arm which is in turn connected to an ultra-balance in a separate chamber that is normally protected by an inert gas-flow such as $N_2$. TGA-DSC experiments in this project uses air instead of $N_2$ gas to allow for the sample to react with $O_2$, producing mass changes. The measurement sensitivity is limited by the sensitivity of the ultra-balance as well as the innate sensitivity of environmental effects such as external vibrations. Powder samples are loaded into alumina crucibles which is then placed onto the balance arm. An empty 'reference crucible' of the same material is also inserted to monitor for any significant mass changes that may result from the crucible itself and not the sample. A given heating rate and/or plateau temperature is selected and mass (TGA) and heat flow (DSC) data is continuously recorded. Data analysis is performed using StarE Evaluation software (Mettler-Toledo) and Microsoft Excel. The TGA-DSC was used to measure the change in mass when $Mg(OH)_2$ particles react with $O_2$ in the air to form MgO according to the following equation [5]: $Mg(OH)_2 \rightarrow MgO + H_2O$. The wt% concentration of the already existing MgO can therefore be inferred from mass loss data and compared to results from X-ray diffraction. Enthalpy change values can also be calculated by integrating the heat flow curves and compared to literature values for the dehydration of $Mg(OH)_2$ to MgO to help confirm that similar processes are taking place [5, 6].

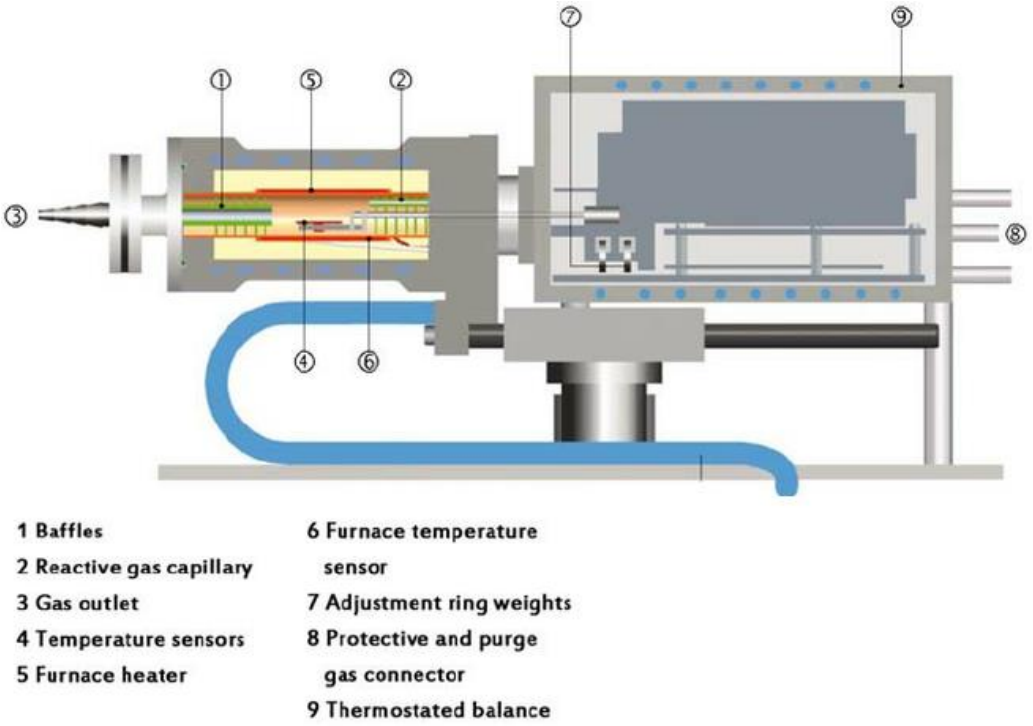


**Figure 3.1: Cross-sectional schematic of a Mettler Toledo TGA-DSC. Adapted from Ház et al. [7].**

## 3.3. X-ray diffraction (XRD)

An X-ray diffractometer is essentially composed of a cathode ray tube that emits electrons which are accelerated through an electrical potential of 40 kV [8]. The high energy electrons then collide with a copper plate that is maintained at a cool temperature [8]. The impinging electrons will excite inner electrons within the copper plate, eventually causing other electrons from elevated energy levels to transition down to more stable low energy levels, which cause the excess energy to be emitted as X-rays [8]. The energy of the X-ray radiation will be related to the electronic structure of the copper atoms, where the most intense so-called 'Kα radiation' is selected and the rest is filtered out using nickel foil [8]. The interaction between the Kα radiation of a very fine wavelength distribution and electron orbitals on a material surface results in elastic scattering behaviour [8]. The scattered waves will propagate outwards and undergo a series of constructive and destructive interferences with one-

another [8]. If the material is highly crystalline with distance $d$ in-between each layer of atoms (Fig. 3.2), additive constructive interferences will occur between these parallel planes of atoms [8]. When these conditions are met, the incident angle of X-rays (θ), the X-ray wavelength and the interplanar spacing $d$ can be related to the Bragg law: $n\lambda = 2d\sin\theta$, where $n$ is a positive integer [8]. Several maxima in diffracted X-ray intensities at specific d-spacing values (proportional to 2θ or '2theta') is therefore obtained that is unique to the crystalline phases of distinct materials which hallows for the 'fingerprinting' of specific crystalline phases within the sample [8]. To maximise data collection, the detector is rotated at varying angles around the sample, causing a 2-dimensional diffraction pattern to form with each diffraction peak corresponding to constructive interference from the crystal surface of a given $d$ spacing.

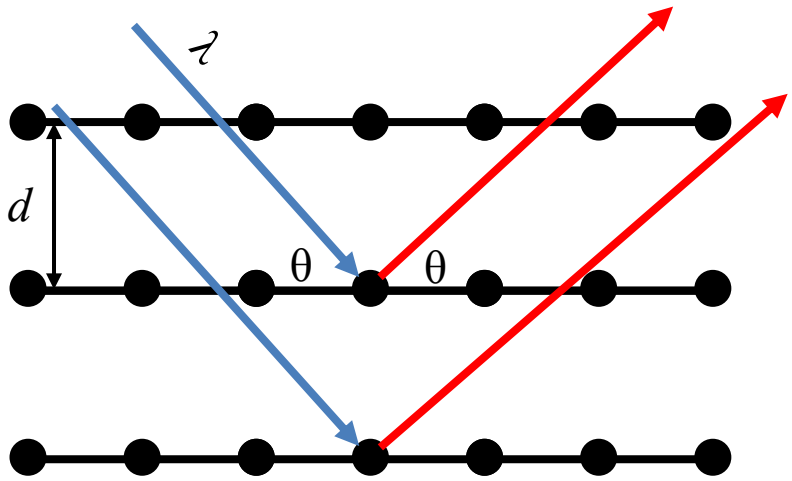


**Figure 3.2: Diffraction of monochromatic X-rays when it interacts with atoms located inside different crystal planes.**

Databases such as the International Centre of Diffraction Data (ICDD) contain powder diffraction filed (PDF) for known crystal phases from literature, allowing for comparisons to be made to help determine sample cell parameters.

The Bragg relationship assumes that the sample is perfect and infinite, and that the incident X-rays are perfectly parallel and monochromatic in nature [8]. This is of

course not the case, where samples may consist of several small crystals at different orientations, and imperfections in machine calibration is also present. These contributions result in a broadening of the X-ray diffraction peaks, enabling for full-width-half-maximum (FWHM) values to be obtained [8]. Using this information, the crystallite size of the sample can be determined (up to ~500 nm), where each XRD peak corresponds to a given direction within the crystal structure [8]. The following method is used to obtain crystallite size information. Firstly, a template file is created using a silicon standard to reveal Gaussian and Lorentzian broadening coefficients. The raw XRD pattern is then inserted to this template file and saved. The diffraction pattern is then clipped to only include the region of interest where significantly high or low 2θ values stemming from poorly-resolved data is removed. A polynomial background spline was then fitted to the diffraction pattern (granularity 11, bending factor 3, data smoothing is on) with a minimum of base points possible but with the fit still following the baseline. A peak search was then performed on the main peaks present, where default settings were allowed in automatic searching mode. A fit was sufficient when the goodness of fit factor was less than 5. The FWHM values are also checked for any outliers.

The maximum crystallite size (*D*) is approximated by applying the Scherrer equation (Equation 3.1) to the selected peaks [9].

$$D = \frac{k\lambda}{\beta_D cos\theta} \qquad \textbf{Equation 3.1}$$

Where β = the FWHM (rad), ${\beta_D}^2 = {\beta_{observed}}^2 - {\beta_{instrumental}}^2$, $k$ = shape factor (1 is normally used for round or complex samples [10]), $\lambda$ = wavelength of the X-ray, $\theta$ = Bragg angle of the analyte peak [11].

## 3.4. Zeta potential

Particles present within an ionic solution that exhibit a net charge will have a layer of ions bound to its surface that create an overall charge that is nearly as large but also of an opposite sign (Fig. 3.3A) [12, 13]. The ions within this so-called Stern layer are tightly bound to the particle surface [12]. To further cancel out the extra opposite charge from these tightly bound particles, a second 'diffuse layer' forms that comprises of ions that are more loosely associated [12]. These two layers are collectively named the electrical double layer of the particle [12]. As a particle moves through the solution either via Brownian motion or due to the attraction/repulsion of a nearby charged surface, the loosely bound ions from the diffuse layer will shed off, leaving only the tightly bound Stern layer behind (Fig. 3.3B) [12].

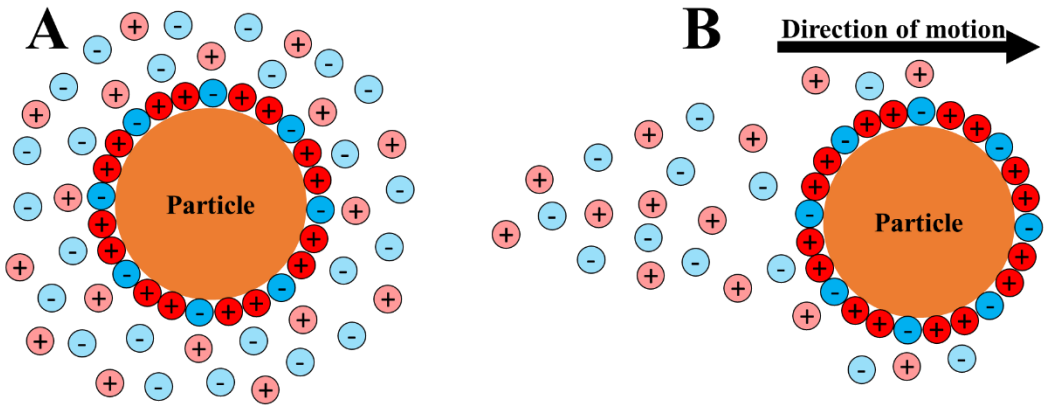


**Figure 3.3: (A) formation of the electrical double layer when a charged particle is present within an ionic solution and (B) the trail of loosely bound ions that are left behind when a particle moves within the solution [12].**

The boundary between the ions remaining with the particle and the ions being removed is termed the 'slipping plane', and the electrostatic potential between this point and the bulk solution is termed the particle zeta potential [12]. Equipment like the Malvern Zetasizer nano ZS can be used to obtain zeta potential values of particles in ionic solutions. During measurement, an electrical field is applied across a small

volume of suspension [12]. The particles will therefore begin to move at a given velocity (electrophoretic mobility), and their velocity is measured using laser Doppler velocimetry [12]. Laser Doppler velocimetry is essentially where a laser of a given wavelength hits the particle and is reflected. The reflected beam will have a slightly different wavelength, and based on the difference between the wavelengths of the two beams, the velocity and direction of the particle motion can be inferred [12]. The Henry equation in Equation 3.2 is then used to calculate the particle zeta potential, *z*:

$$U_e = \frac{2\varepsilon z f(\kappa a)}{3\eta} \qquad \textbf{Equation 3.2}$$

Where $U_e$ = the electrophoretic mobility, $\varepsilon$ = dielectric constant, $\eta$ = absolute zero-shear viscosity of the medium, $f(\kappa a)$ = Henry function where $\kappa a$ is a ratio of the particle radius to its Debye length.

For the Malvern zetasizer ZS, a small aliquot of suspension is pipetted into a clear plastic cell containing a gold electrode on either end. When a current is applied to the electrodes, they become charged, causing the particles to move towards either the positive or negative electrode depending on the particle charge. A higher particle charge results in a greater electrophoretic mobility (faster velocity) and therefore a greater particle zeta potential that is determined. The particle radius can be obtained via *in-situ* dynamic laser diffraction techniques (laser diffraction is described in more detail during particle size distribution methodology description).

## 3.5. Surface zeta potential

In a similar fashion to a colloidal particle, a large surface exposed to the solution will also form an electric double layer [14]. The surface in this case cannot be moved when an external potential difference is applied due to its size, however instruments like the Anton Paar SurPASS Electrokinetic Analyser (Anton Paar, USA) will instead pump

fluid past the sample surface (Fig. 3.4) [14]. Ions on the surface of the material will therefore be removed, depending on the charge difference between the material and the bulk solution as well as the relative rate the solution is moving past the sample surface [14]. The removed ions will cause a change in the potential difference between the points before and after the surface is exposed to the solution. This will in turn cause a change in the current acting across the circuit.

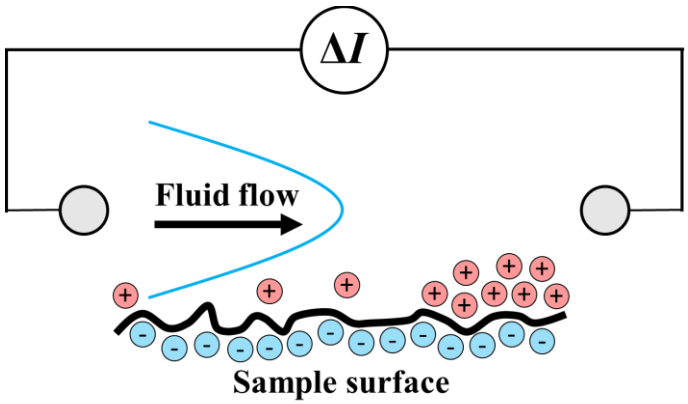


**Figure 3.4: Schematic illustrating the mechanism behind surface zeta potential measurement. A charge surface within a solution containing electrolyte ions will cause the build-up of an electrical double layer within the solution. When fluid flows past the surface, ions will be removed from the surface. The number of ions removed from the surface depends on the charge of the surface and the fluid velocity. The removed ions will change the electrical current (proportional to potential difference) between the points before and after the fluid had passed the surface. Adapted from Anton Paar, USA.**

By measuring the circuit current as a function of differential pressure, a linear trend is observed (Fig. 3.5) [14]. The gradient of this trend, $\frac{dI}{dP}$, can therefore be obtained (Fig. 3.5).

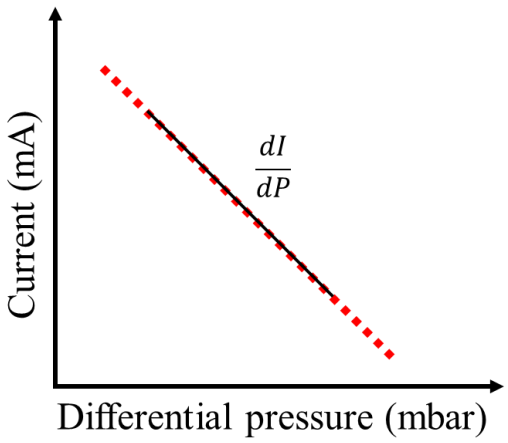


**Figure 3.5: Calculation of the change in electrical current with changing pressure from the electrokinetic analyser electrical current vs. differential pressure graph. Adapted from Anton Paar, USA.**

This obtained value can be used in the Hemholtz-Smoluchwoski relationship (Equation 3.3) to calculate the zeta potential of the surface [15].

$$\zeta = \frac{dI}{dP} \times \frac{\eta}{\varepsilon \times \varepsilon_0} \times \frac{L}{A} \qquad \textbf{Equation 3.3}$$

Where $\zeta$ = zeta potential of the sample, $\eta$ = fluid viscosity, $\varepsilon$ = dielectric constant of the medium, $\varepsilon_0$ = permittivity of free space, $L$ = exposed sample length and $A$ = cross-sectional area of the exposed sample surface.

## 3.6. Particle size distribution

Laser diffraction is the underlaying technique that was used to determine particle size distributions for this project. Laser diffraction is capable of measuring particle sizes that lie within the ~0.04 – 2000 µm range, which is ideal for simple characterisation of samples consisting of a wide range of different particle sizes [16]. For laser diffraction, an incoming laser beam of typically 750 nm wavelength is focused using a set of focusing lenses (Fig. 3.6A) before entering a sample containing a dilute concentration of the particles of interest. When the focused beam hits a spherical

particle of a given radius, the beam will be diffracted at an angle that is inversely proportional to the particle size [16] (Fig. 3.6B). A set of detectors surrounding the sample zone will detect the intensity of diffracted light at different detection points (Fig. 3.6A) [16]. The intensity of diffracted light can then be correlated to the relative concentration of particles present within the given diffraction angle range [16]. For the calculation of particle size distribution using refraction data, commonly used equipment like the Malvern Mastersizer 2000E use the Mie theory, which is essentially a solution of the Maxwell equations that governs the behaviour of electric and magnetic fields to describe the propagation of the electromagnetic waves in space [16]. The solution only works for spherical particles, however when particles of complex shapes are suspended in solution, they will begin to rotate, exposing different surface sites to the incoming laser (Fig. 3.6C). Several similar particles will also reflect light at different points along the particle's geometry at a given time, resulting in a broadening of the diffraction signal for particles of a given size (Fig. 3.6C) [16]. Rough surfaces may also contribute to this effect [17] where a combination of particle shape and roughness effects may lead to an overestimation in the volume fraction present for particles of a given size [17].

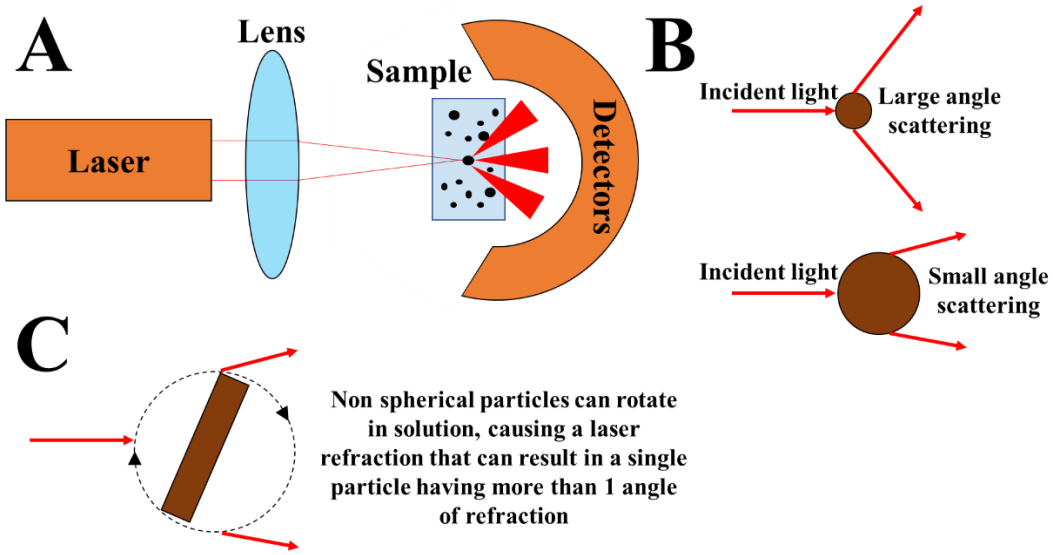


**Figure 3.6: (A) schematic showing the operation of typical equipment using laser diffraction for particle size distribution measurement. (B) laser beam refraction angle is proportional to particle size and (C) non-sphericity may lead to an overestimation in the volume concentration of particles of a given size within the sample. Adapted from Eshel et al. [16].**

This project will use particle size distribution data for simple characterisation and direct comparisons where particle shape effects are expected to be relatively similar. Calculations that include particle size distribution data will be used for qualitative comparisons only. The overestimation from laser diffraction data will therefore have no significant effect on the overall quality on this project.

## 3.7. Atomic force microscopy (AFM)

AFM is a technique that enables for the appearance (i.e. texture/roughness) of surfaces to be determined at a high resolution and accuracy [18]. The AFM operates differently from conventional imaging techniques like the SEM or light-based microscopy in that a cantilever with a small tip essentially 'feels' the surface of the material, allowing for a variation of different characterisation techniques to be employed [18]. The cantilever will have a given stiffness or 'spring force constant', and when the

cantilever experiences an external force, it will be deflected by a given amount that is proportional to the magnitude of the external force (Fig. 3.7) [18]. A laser source focussing on the cantilever will therefore also experience a slight shift in its angle of deflection (Fig. 3.7), and if a photodiode is placed at a sufficiently large distance away from the deflected beam, small changes in deflection angles can be detected, enabling for conventional AFM devices to easily detect forces in the nN – range [18]. For AFM cantilevers with a sharp tip at its end, forces acting on the tip can be measured, allowing for the roughness, stiffness and contours of surfaces to be measured with relative ease [18].

If a spherical colloidal particle is firmly attached to the end of the cantilever, forces acting on the particle can instead be measured [18, 19]. The direction of the cantilever deflection (and hence the scattered angle of the laser) will therefore also provide users with information regarding the direction of force (i.e. whether or not a given surface exerts an attractive of repulsive force to the colloidal particle, Fig. 3.7).

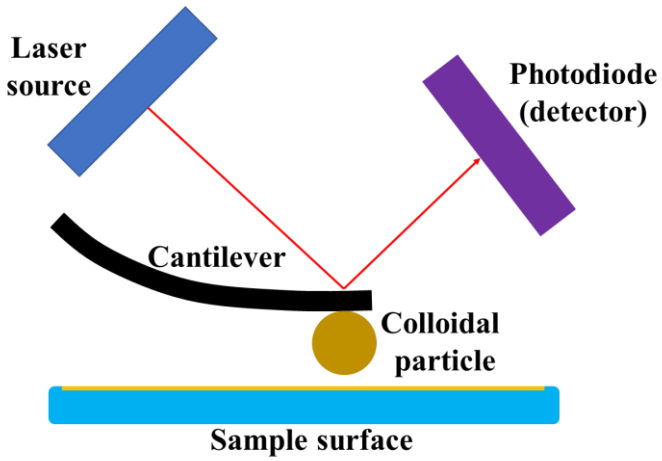


**Figure 3.7: Schematic showing the basic setup of the atomic force microscope. When a colloidal particle glued to a cantilever experiences a force from the sample surface, a deflection in the cantilever will occur. This deflection will change the angle of reflection from a laser that is focused on the cantilever, which allows for the distance of deflection to be inferred. If the force constant of the cantilever is known, the applied force to the colloidal particle can be calculated. Adapted from Eaton and West [18].**

## 3.8. Quartz crystal microbalance (QCM)

A significant portion of commercial QCM devices available use a 'flow cell' design where the suspension or fluid to be analysed is pumped through a chamber containing the resonator. This design will however not suffice for this project since suspensions containing yield stresses that therefore behave as soft solids will be used. A polypropylene dip-probe that forms a small cup where the resonator surface is located was instead purchased (Stanford Research Systems) (Fig. 3.8). The suspension can be pushed directly onto the resonator surface without the need for pumping. In all cases, the resonator was held in a vertical position (Fig. 3.8) to better represent the expected orientation that may be used once commissioned in industry.

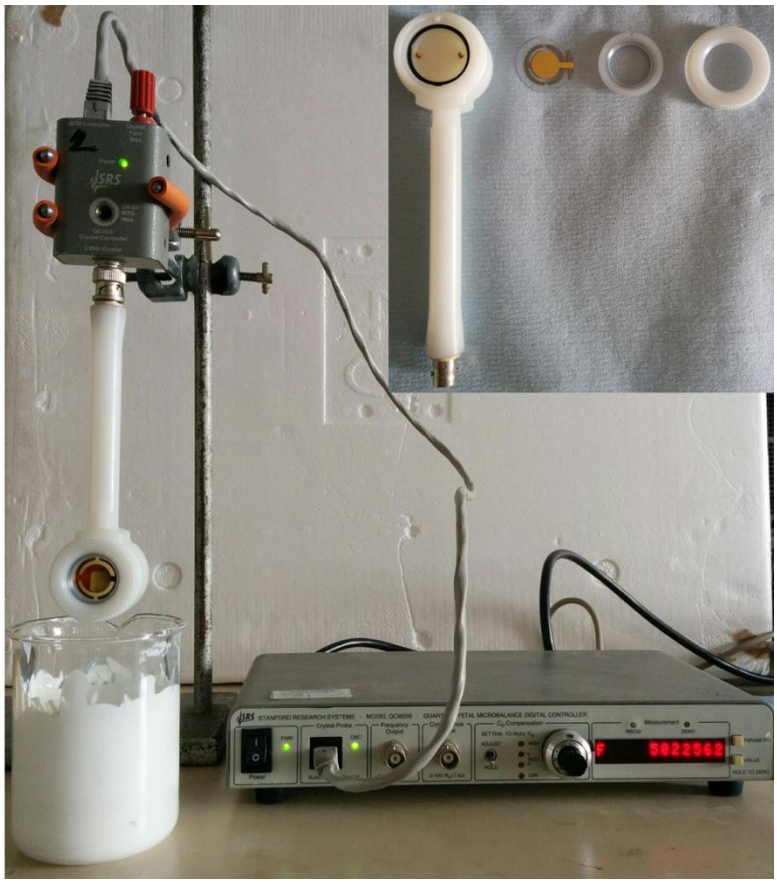

**Figure 3.8: QCM dip-probe design and experimental setup. The probe is maintained at a vertical position for all experiments to mimic the crystal orientation that would likely be used during industrial deployment.**

For high yield stress suspensions that do not flow easily, aliquots of the suspension were taken and pushed directly onto the resonator surface to fill the well and completely cover the resonator surface. The resulting resonance shifts were observed and recorded once stable. The suspension was re-mixed onto the resonator surface and the resulting stable shifts recorded once again. This process was repeated until no significant difference in stable shifts are observed after individual mixing events, which helps ensure that the resonator is in full contact with the overlaying suspension. A similar method was employed for low yield stress suspensions, however in this case the probe can easily be submerged into a beaker containing the suspension and mixed, allowing for the suspension to flow directly onto the resonator surface (Fig. 3.8).

Due to the high sensitivity of the QCM, air pockets present at the surface can easily be detected and will therefore provide different readings. The air pockets themselves may also create a strain within the suspension network surrounding it, potentially influencing QCM readings as well. Figure 3.9 shows comparison data between the method previously described (method 1) and a simpler method where the probe is submerged directly into the suspension and rotated at a 90° angle (method 2). Method 1 shows a much clearer trend (drops at ~ 1 – 5 vol% for method 1 are possibly due to suspension network breakdown) and has been used in further work to describe the QCM response during suspension concentration tests [20]. For this reason, method 1 was used at all times.

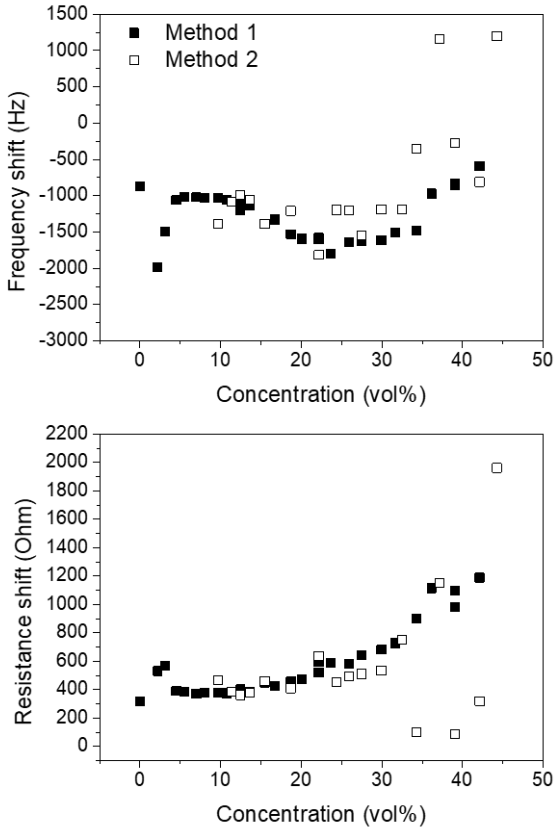


**Figure 3.9: Observed QCM200 response when two methods of mixing suspensions onto the resonator surface is compared. Method 1 involves manually pushing and re-mixing the suspension until no change in stable shifts are observed and method 2 involves submerging the probe into the suspension and rotating it at a 90° angle with no further mixing taking place.**

## 3.9. Yield stress

The yield stress of a material is defined as the minimum amount of stress that must be applied to a material to induce flow [21]. In this case it is the minimum stress required to break the particle-particle network structure down so that the suspension properties transitions from a solid-like behaviour (i.e. elastic deformation where complete strain recovery is present after the application of stress) to a fluid-like behaviour (i.e. the material becomes viscous where no strain recovery is present after the application of stress) [21]. A transition range from elastic to viscous behaviour is however present where the material exhibits viscoelasticity where plastic deformation occurs causing strain recovery to not be complete after the application of stress [21]. Two yield

stresses can therefore exist. If a 4-bladed cylindrical vane is submerged into a yield stress material, and it rotates at a fixed rate that is low enough for elastic deformation to occur, the applied stress required to maintain the rotating vane at its fixed velocity will increase linearly over time [21] (see Fig. 2.13 in Chapter 2). The transition point where linear deformation ends, and plastic deformation starts is the dynamic yield stress [21]. The maximum strain required to maintain the vane rotation occurs at the point in the viscoelastic region before the onset of viscous flow where the suspension network bonds begin to break [21]. This maximum strain value is termed the dynamic yield stress, and is the parameter that is measured in this study [21].

For this project, a Brookfield DV II+ vane viscometer is used. The vane shears the suspension similar to how a rotating cylinder would (Fig. 3.10), however unlike a cylinder, slip effects can be considered negligible as the vane entrains a large volume of sludge within its cylindrical volume, making it the preferred choice for yield stress measurements, especially for high yield stress suspensions [21]. The viscometer will measure the torque acting on the vane as it is being rotated at constant velocity [21]. The maximum registered torque can be converted to the dynamic yield stress according to Equation 3.4 [21, 22].

$$T_m = \frac{\pi D^3}{2}\left(\frac{H}{D} + \frac{1}{3}\right)\tau_0 \qquad \textbf{Equation 3.4}$$

Where $T_m$ = maximum torque value obtained from viscometry experiment, $D$ = vane diameter (Fig. 3.10), $H$ = vane height (Fig. 3.10) and $\tau_0$ = dynamic yield stress of the material.

Wall effects from the sample container may also affect the results obtained. Alderman et al. ensured that the sample container diameter was around 3 times greater than the vane diameter, and that the vane is submerged into the centre of the suspension by

lifting the suspension container using a laboratory jack to ensure horizontal movement is kept to a minimum during experimental setup [21].

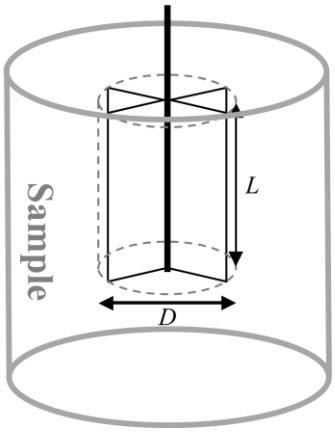


**Figure 3.10: Vane theoretical shear geometry when it is submerged into the sample. Ideally the vane should be completely submerged into the sample material (manufacturers would imprint a little 'notch' at the top of the vane as an indicator to ensure the vane is completely submerged). The sample container should also be of a length (*L*) and diameter (*D*) that is significantly larger than that of the vane to ensure that wall effects do not play a role in yield stress measurements. Adapted from Alderman et al. [23].**

The speed of rotation could also affect the maximum torque registered [21]. Figure 3.11 shows for faster rotational speeds, higher maximum torque values are registered by the vane, possibly due to the relaxation time of the material after the application of additional strain being longer than the experimental rate. Figure 3.11 shows that the torque becomes dependent on rotational speeds of > 1 rpm, which is in good agreement for other similar setups used to produce Figure 3.11 for bauxite slurries [22][24] and cements [25] instead. A rotational speed of 1 rpm was therefore chosen for concentrated suspensions used in this study.

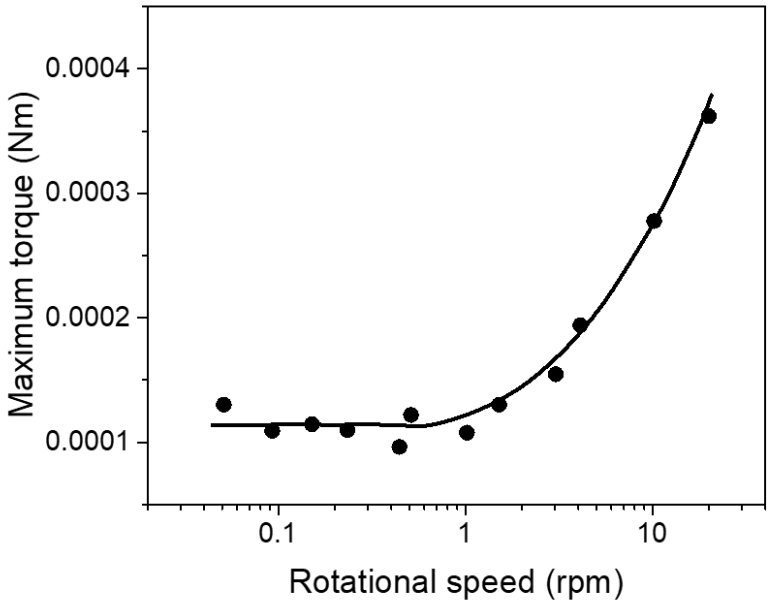


**Figure 3.11: Variation in maximum torque obtained when a vane is rotated at a fixed rpm in 7.81 wt% bentonite clay. Adapted from Alderman et al. [23].**

## 3.10. Suspension viscoelasticity

The rheometer is a device capable of measuring the viscosity and viscoelasticity of fluids, semi-solids and solid materials alike and has since become the conventional method used to characterise these rheological properties for a variation of different materials [26-28]. This project looks at the rheological behaviour of concentrated particulate suspensions at different experimental frequencies to allow for direct comparisons to be made with high frequency QCM experiments. The viscoelastic storage modulus (G') and loss modulus (G'') of soft materials have been shown to change over broad experimental frequency ranges [29], making it necessary to measure the frequency dependent behaviour of concentrated suspensions when comparisons are made.

Devices like the Discovery HR-2 rheometer (TA Instruments, UK) have in-built software to allow for the viscoelastic behaviour of concentrated suspensions to be

measured at different frequencies. Before 'frequency sweep' measurements can take place for a given sample, the region of linear viscoelasticity (LVR) has to be identified for the sample [26]. This is done by performing an 'amplitude sweep', where the viscoelastic properties of the material are measured with varying strain (amplitude of oscillation) (Fig. 3.12). The particulate suspension is firstly placed into a cup of diameter 30.4 mm, and a 4-bladed vane (length = 42 mm, diameter = 28 mm) is gently inserted into the suspension, forming a similar setup to that shown in Figure 3.10. The height of the vane from the bottom of the cup was set to a fixed height (9.6 mm for this work). The sample is then pre-sheared to allow for the suspension structure to re-form in experimental conditions to remove any history effects on the sample (i.e. thixotropy). The amplitude test is then performed at a sufficiently low fixed experimental frequency, where a response similar to that shown in Figure 3.12 is then obtained.

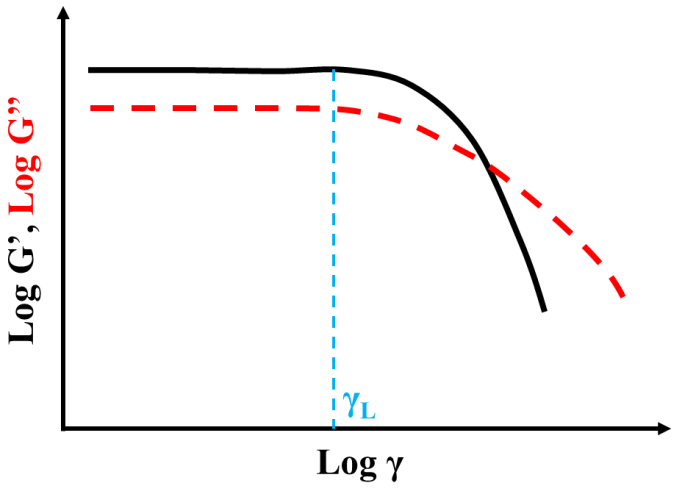


**Figure 3.12: Expected response observed when the storage modulus (G') and loss modulus (G'') of a concentrated suspension is measured with changing oscillation strain (γ). At strains below the limiting value of the region of linear viscoelasticity ($\gamma_L$), the viscoelastic properties of the material are independent of increasing strain (linear response). Adapted from Ferry and Ferry [30].**

When the experiment occurs within the LVR of the suspension, deformation is small enough for the change in the arrangement of the material to not be far from equilibrium, meaning that significant particle-particle link stretching and bond breaking does not occur within this region [30, 31]. The magnitudes of stress and strain are related linearly meaning that the behaviour of the material can be described by a single function of time [31].

The applied stress is in the form of an oscillatory (sinusoidal) deformation (Fig. 3.13A), which causes a delayed material response (Fig. 3.13B) [30]. The difference between the applied deformation and the material response is measured as a phase angle (δ) (Fig. 3.13C).

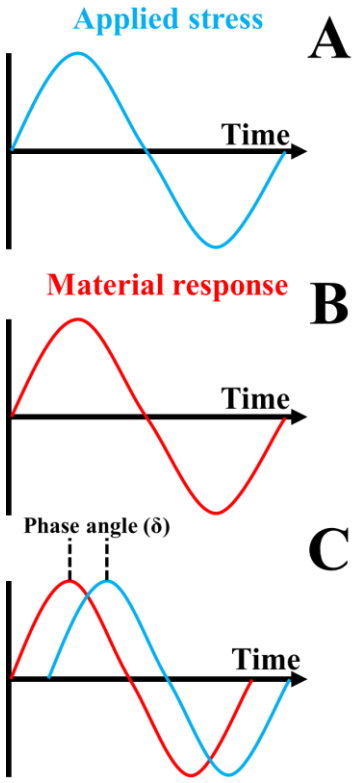


**Figure 3.13: Viscoelastic response (strain) (B) of a material when a sinusoidal stress (A) is applied to it. The difference between the applied stress curve and the material response curve is measured as a phase angle (δ) (C). Adapted from Ferry and Ferry [30].**

The viscoelastic properties (G' and G'') can then be represented as a vector diagram (Fig. 3.14), where the complex shear modulus is equivalent to the stress/strain ratio $\left(G^* = \frac{\tau}{\gamma}\right)$.

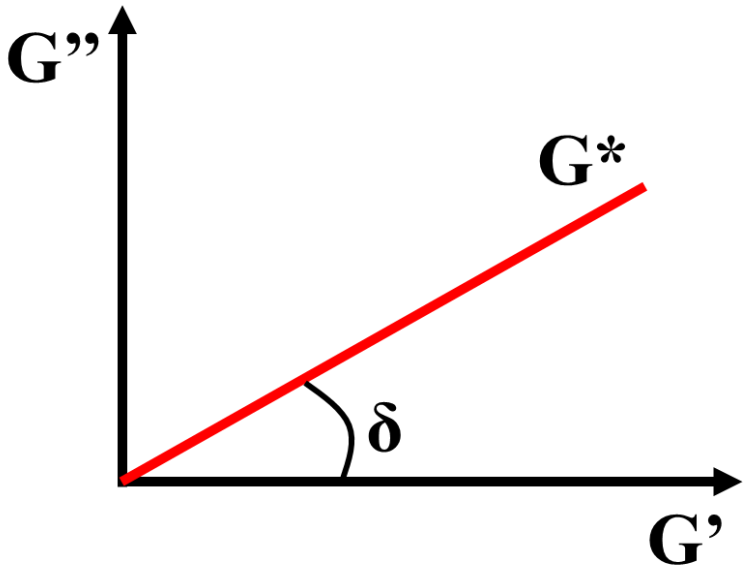


**Figure 3.14: Viscoelastic response of a material represented as a vector diagram. For a given strain (amplitude), the viscoelastic properties of the material can be derived using the previously obtained value of δ. Adapted from Ferry and Ferry [30].**

δ can also be represented as tan[δ], which is termed the loss factor or damping factor, where $\delta = 0^\circ$ represents an ideally elastic medium and $\delta = 90^\circ$ is an ideally viscous medium [30]. Once the viscoelastic properties at varying strains have been measured and obtained, a 'frequency sweep' can then be commenced. The strain on the material is kept constant and is within the suspension LVR, the frequency of the sinusoidal stress curve in Figure 3.13A is changed (typically from 100 – 0.1 rad/s) and the resulting G' and G'' values are obtained as described for every measured frequency point [30] (Fig. 3.15).

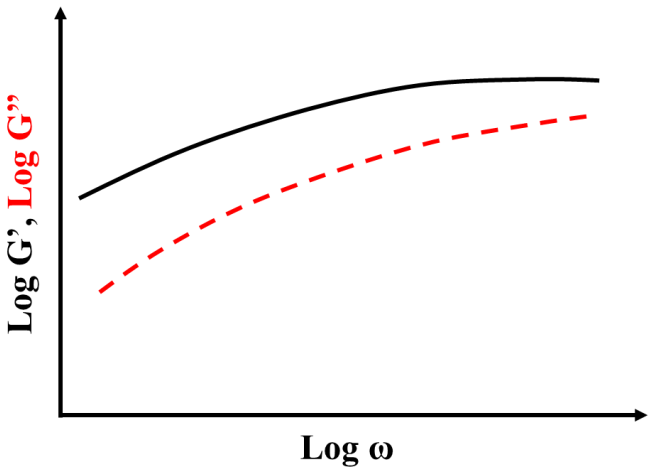


**Figure 3.15: Viscoelastic (G', G'') response of a material with changing experimental frequency. The sample viscoelasticity is expected to show a frequency dependence that span over several magnitudes [29]. Adapted from Rudraraju and Wyandt [26].**

The viscoelastic properties of suspensions at different experimental frequencies is therefore obtained, allowing for frequency comparisons to be made.

## 3.11. References

1. Watt, I.M., *The Principles and Practice of Electron Microscopy*. 1997: Cambridge University Press, Cambridge.
2. Goodhew, P.J., J. Humphreys, and R. Beanland, *Electron Microscopy and Analysis*. 2000: CRC Press, Boca Raton.
3. Goldstein, J., et al., *Scanning Electron Microscopy and X-ray Microanalysis: a Text for Biologists, Materials Scientists, and Geologists*. 2012: Springer Science & Business Media.
4. Postek, M.T., et al., *The Scanning Electron Microscope*. Handbook of Charged Particle Optics, 1997: p. 363-399.
5. Anderson, P.J. and R.F. Horlock, *Thermal Decomposition of Magnesium Hydroxide*. Transactions of the Faraday Society, 1962. **58**(478): p. 1993-&.
6. Halikia, I., P. Neou-Syngouna, and D. Kolitsa, *Isothermal Kinetic Analysis of the Thermal Decomposition of Magnesium Hydroxide using Thermogravimetric Data*. Thermochimica Acta, 1998. **320**(1-2): p. 75-88.
7. Ház, A., et al. *Determination of Temperature Regions in Thermal Degradation of Lignin*. in *4 th International Conference on Renewable Energy Source, High Tatras, Slovak Republic*. 2013.
8. Ladd, M.F.C., R.A. Palmer, and R.A. Palmer, *Structure Determination by X-ray Crystallography*. 1985: Springer, Berlin.
9. Patterson, A., *The Scherrer Formula for X-ray Particle Size Determination*. Physical Review, 1939. **56**(10): p. 978.

10. Langford, J.I. and A. Wilson, *Scherrer After Sixty Years: a Survey and some new Results in the Determination of Crystallite Size.* Journal of Applied Crystallography, 1978. **11**(2): p. 102-113.
11. Cullity, B.D. and J.W. Weymouth, *Elements of X-ray Diffraction.* American Journal of Physics, 1957. **25**(6): p. 394-395.
12. Clogston, J.D. and A.K. Patri, *Zeta Potential Measurement*, in *Characterization of Nanoparticles Intended for Drug Delivery*. 2011, Springer. p. 63-70.
13. Johnson, S.B., et al., *Surface Chemistry-Rheology Relationships in Concentrated Mineral Suspensions.* International Journal of Mineral Processing, 2000. **58**(1-4): p. 267-304.
14. Luxbacher, T., et al., *Zeta Potential Determination of Flat Solid Surfaces Using a SurPASS Electrokinetic Analyzer.* Tekstil: Journal of Textile & Clothing Technology, 2009. **58**(8).
15. Shapiro, A., P. Renaud, and R.F. Probstein, *Preliminary Studies on the Removal of Chemical-Species from Saturated Porous-Media by Electroosmosis.* Physicochemical Hydrodynamics, 1989. **11**(5-6): p. 785-802.
16. Eshel, G., et al., *Critical Evaluation of the use of Laser Diffraction for Particle-Size Distribution Analysis.* Soil Science Society of America Journal, 2004. **68**(3): p. 736-743.
17. Campbell, J.R. and I. Roach, *Limitations in the Laser Particle Sizing of Soils.* Advances in Regolith, 2003. **1**: p. 38-42.
18. Eaton, P. and P. West, *Atomic Force Microscopy*. 2010: Oxford University Press.
19. Ducker, W.A., T.J. Senden, and R.M. Pashley, *Direct Measurement of Colloidal Forces Using an Atomic Force Microscope.* Nature, 1991. **353**(6341): p. 239-241.
20. Botha, J.A., et al., *Quartz Crystal Microbalance as a Device to Measure the Yield Stress of Colloidal Suspensions.* Colloids and Surfaces A: Physicochemical and Engineering Aspects, 2018. **546**: p. 179-185.
21. Liddell, P.V. and D.V. Boger, *Yield Stress Measurements with the Vane.* Journal of Non-Newtonian Fluid Mechanics, 1996. **63**(2-3): p. 235-261.
22. Dzuy, N.Q. and D.V. Boger, *Yield Stress Measurement for Concentrated Suspensions.* Journal of Rheology, 1983. **27**(4): p. 321-349.
23. Alderman, N., G. Meeten, and J. Sherwood, *Vane Rheometry of Bentonite Gels.* Journal of non-newtonian fluid mechanics, 1991. **39**(3): p. 291-310.
24. Dzuy, N.Q. and D.V. Boger, *Direct Yield Stress Measurement with the Vane Method.* Journal of Rheology, 1985. **29**(3): p. 335-347.
25. Haimoni, A. and D. Hannant, *Developments in the Shear Vane test to Measure the Gel Strength of Oilwell Cement Slurry.* Advances in Cement Research, 1988. **1**(4): p. 221-229.
26. Rudraraju, V.S. and C.M. Wyandt, *Rheology of Microcrystalline Cellulose and Sodiumcarboxymethyl Cellulose Hydrogels Using a Controlled Stress Rheometer: part II.* International Journal of Pharmaceutics, 2005. **292**(1-2): p. 63-73.
27. Fisher, D.T., et al., *The Bucket Rheometer for Shear Stress-Shear Rate Measurement of Industrial Suspensions.* Journal of Rheology, 2007. **51**(5): p. 821-831.
28. Fischer, P. and E.J. Windhab, *Rheology of Food Materials.* Current Opinion in Colloid & Interface Science, 2011. **16**(1): p. 36-40.

29. Pakula, T., et al., *Relaxation and Viscoelastic Properties of Complex Polymer Systems.* Rheologica acta, 1996. **35**(6): p. 631-644.
30. Ferry, J.D. and J.D. Ferry, *Viscoelastic Properties of Polymers*. 1980: John Wiley & Sons.
31. Pryamitsyn, V. and V. Ganesan, *Origins of Linear Viscoelastic Behavior of Polymer− Nanoparticle Composites.* Macromolecules, 2006. **39**(2): p. 844-856.

# 4. Quartz crystal microbalance as a device to measure the yield stress of colloidal suspensions

The application of quartz crystal microbalance (QCM) as a device to measure the yield stress of colloidal suspensions has been studied. Using a commercial dip-probe QCM, the yield stress of magnesium hydroxide suspensions has been correlated to the resonance properties of a 5 MHz AT-cut quartz sensor. A stable resonance baseline was first established in air before submerging the sensor into the colloidal suspension. The response of the sensor resistance was shown to correlate to changes in the suspension yield stress, while the frequency response was found to result from more complex contact mechanics and possible suspension viscoelasticity contributions. Since the QCM is a relatively simple technique with no mechanically moving parts, this approach offers the potential for rapid *in-situ* rheology assessment.

This chapter is based on work from the following jointly authored publications:

Botha, Johannes A, Timothy N Hunter, Weixuan Ding, Simon Biggs, Graham A Mackay, Robin Cowley, Simon E Woodbury, and David Harbottle. A Novel Technology for Complex Rheological Measurements. WM2016 Conference Proceedings: WM Symposia, 2016.

Botha, Johannes A, Weixuan Ding, Timothy N Hunter, Simon Biggs, Graham A Mackay, Robin Cowley, Simon E Woodbury, and David Harbottle. "Quartz Crystal Microbalance as a Device to Measure the Yield Stress of Colloidal Suspensions." Colloids and Surfaces A: Physicochemical and Engineering Aspects 546 (2018): 179-85.

The author would like to thank Weixuan Ding for his support in helping the author operate the TGA-DSC as well as the X-ray diffractometer. His in-depth theoretical discussions are also greatly appreciated. The author would also like to thank Simon Biggs, Timothy Hunter and David Harbottle for their academic supervision and Graham A Mackay, Robin Cowley and Simon Woodbury for their supervision from an industrial point of view.

## 4.1. Introduction

The UK nuclear industry is currently entering a phase of post operational clean out (POCO) to safely remove and store legacy wastes which have accumulated over several decades of nuclear power generation. A particular concern for the UK is the legacy sludge waste which has been stored in open air ponds and silos and now needs to be retrieved for further interim storage or ultimate disposal. To ensure the safe recovery of the wastes, design guides for sludge retrieval will be proposed based on the physical and chemical properties of the materials to be recovered. Understanding the rheology of the legacy sludge, along with its modification during handling is therefore of great importance. However, conventional rheometer techniques are often unsuitable due to issues of sample handling (radioactivity and methods of extraction), and the requirement to frequently collect data in confined spaces. With its simple design, small size and no mechanical parts, a quartz crystal microbalance (QCM) has the potential to directly measure rheology in challenging environments.

In its standard configuration, a QCM consists of a piezoelectric AT-cut quartz sensor with electrodes coated on each surface. Applying an oscillating electric field across the piezoelectric sensor generates an internal mechanical stress that vibrates the sensor [1]. Interpretation of the vibrational motion reveals the viscosity-density product of the deposited material from which other physical properties such a deposited film thickness and viscoelasticity can be determined [2-6].

The baseline data includes QCM resonance frequency and motional resistance. The resonance frequency is often quoted due to the simplicity of the Sauerbrey equation (Eq. 4.1) which provides a simple conversion of resonance frequency shift to deposited mass:

$$\Delta f = -\frac{2f_0^2 \Delta m}{A\sqrt{\rho_q \mu_q}} \qquad \textbf{Equation 4.}$$

where $\Delta f$ is the measured frequency shift, $f_0$ is the fundamental frequency, $\Delta m$ is the mass change, $A$ is the sensor area, $\rho_q$ is the density of quartz sensor (2.648 g cm$^{-3}$), and $\mu_q$ is the shear modulus of quartz sensor (2.947 x 10$^{11}$ g cm.s$^{-2}$).

While a Sauerbrey conversion is often useful, the underlying principle as an extension of the resonating sensor is only truly valid when the added mass satisfies: i) no slip, ii) rigid deposition, and iii) even deposition on the sensor surface [2].

Nomura and Bruckenstein demonstrated the stable resonance of QCM when one surface of the sensor was intimately in contact with a bulk liquid [7-9]. Gordon-Kanazawa-Mason [3, 10, 11] derived a simple relationship correlating the change in resonance frequency to changes in the density and viscosity of a non-adsorbing fluid (Eq. 4.2):

$$\Delta f = -f_{0*}^{\frac{3}{2}}\left(\frac{\rho_L \mu_L}{\pi \rho_q \mu_q}\right)^{\frac{1}{2}} \qquad \textbf{Equation 4.2}$$

where $f_{0*}$ is the fundamental resonance frequency, and $\rho_L$ and $\mu_L$ are the absolute density and viscosity of the fluid, respectively. More recently, studies based on the Mason equivalent circuit theory [12] or the Voigt-Voinova theory [13] have demonstrated the applicability of QCM to measure the viscoelastic properties of bulk fluids and deposited layers on the sensor surface.

While those fundamental studies highlight the great potential of QCM when investigating solid, liquid and gaseous systems, until recently solid-liquid systems had received very little attention; in particular particle suspensions. The interaction of particles and the QCM sensor has been considered in detail by Johannsmann and co-workers [6, 14], where the Mason model has been suitably modified to include point-contact loads that are relevant to non-uniform loads such as deposited particles on the resonating sensor. Of the few studies considering QCM and particles, other applications include i) measuring the particle concentration by drying suspensions onto the sensor [15] and ii) detecting particle deposition onto a heterogeneous surface [16, 17], with the resonance properties correlated to the colloidal forces acting between the resonating sensor and suspension. When studying particle systems, researchers have reported positive frequency shifts during mass deposition, which is contrary to the mass deposition theories described by Sauerbrey and Voigt-Voinova [18-20].

Dybwad and Pomorksa [20, 21] developed a model termed the 'coupled resonance model' to account for such interesting behaviour. The model states that for a sphere in contact with a resonating sensor of angular frequency, $\omega$, the sphere will adopt its own resonance of angular frequency, $\omega_s = (\kappa/m)^{1/2}$, where κ is the contact stiffness and $m$ the particle mass [20, 21]. The contact stiffness is a function of both tangential and normal load contributions, although for a 5 MHz sensor the contact stiffness is strongly influenced by the normal oscillatory load due to the flexural contributions to the displacement pattern. If the sphere is small and the particle contact with the resonating sensor is sufficiently stiff, the condition $\omega_s >> \omega$ holds true and 'inertial loading' occurs where the mass of the sphere reduces the sensor resonance frequency, i.e. Sauerbrey behavior [2, 20, 21]. If the sphere is large however (typically > 1 μm)

and is weakly bound to the sensor, the condition $\omega_s << \omega$ holds true and the resonance frequency of the sensor increases, described as 'elastic loading' [20, 21]. Pomorska et al. performed finite element calculations on relevant systems and concluded that this phenomena is plausable in liquid phase media, where the resonance frequency of the sensor is dependent on the strength of the sphere-sensor contact rather than the adsorbed mass [20].

The objective of the current study is to extend the application of QCM and correlate the frequency and resistance responses to changes in the rheology of particle suspensions, i.e. the shear yield stress. The measurement approach is quite simple and involves measuring the frequency shift and resistance from the baseline resonance in air to the steady-state values once submerged into the test material. In particular, samples of two different types of magnesium hydroxide were investigated, as similar materials are thought to represent the major fractions of corroded fuel canister wastes, present in various nuclear legacy ponds and silos in the UK [22].

## 4.2. Materials and Methods

### 4.2.1. Materials

Two magnesium hydroxide ($Mg(OH)_2$) samples were used as model test materials relevant to legacy nuclear waste in the UK. The first test material Versamag A was supplied by Rohm and Hass and the second test material Versamag B (sample labelling used throughout) was supplied by Martin Marietta. Both samples were chosen due to their varied magnesium oxide (MgO) contents leading to differences in aging behaviour, see discussion below. The pH of all suspensions was maintained at pH 10.2 due to the natural buffering of the system, which corresponded to conditions close to the particle isoelectric point ($pH$ 10.2, $\zeta = -7 \pm 4\ mV$). Both particle types

were used as received and dispersed in deionised water with a resistivity of 18 MΩ cm.

### 4.2.2. Sample gel point determination

The suspension gel-point was determined by the method outlined in de Krester et al. [23]. In brief, a 7 vol% suspension of Versamag B was prepared following the method described and poured into 400 mL graduated cylinders of varying suspension height between 45 mL and 230 mL. The graduated cylinders were then sealed with Parafilm and left un-disturbed for 72 h. The final sediment bed height was measured and the gel-point determined from $\emptyset = \frac{\partial(\emptyset_0 h_0)}{\partial h_\infty}$, where $\emptyset_0$ is the suspension volume fraction at t = 0, $h_0$ is the initial suspension height, and $h_\infty$ is the final sediment height. Fig. 4.1 illustrates the relationship used to determine the gel point for Versamag B.

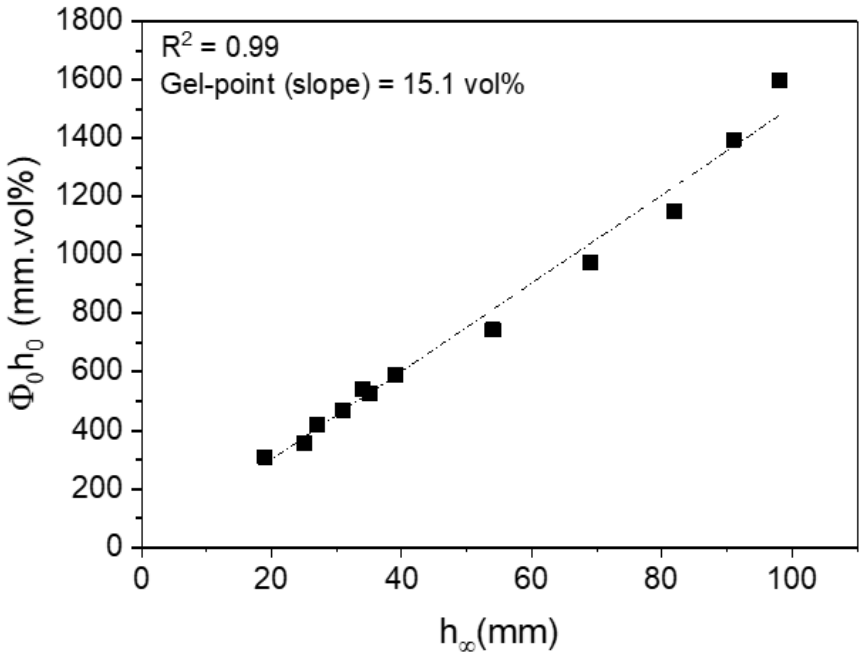


**Figure 4.1: Gel-point determination of Versamag B.**

### 4.2.3. Sample aging

80 g Versamag (A or B) was added to 120 g deionised water (solid content = 22 vol%) in a 250 mL glass beaker and hand mixed for 15 min until the suspension resembled a smooth paste. The suspension was left undisturbed for 5 min before measuring the yield stress and QCM response (separate samples). The objective of the aging tests was to measure the time-dependent changes in the suspension yield stress between 0 and 70 h. The suspension volume fraction was chosen such that the particle concentration exceeded the gelling concentration [23, 24] (Fig. 4.1), hence no suspension sedimentation would occur during sample aging. To avoid yield stress changes due to sample drying, a thin layer of mineral oil ($\rho$ = 0.84 g/cm$^3$) was gently pipetted onto the suspension (following immersion of the QCM sensor), before finally sealing the glass beaker with Parafilm.

The shear yield stress was measured using an AMETEK Brookfield DV-II+ Pro Viscometer with a four blade vane ($H$ = 43.33 mm, $D$ = 21.67 mm). The vane was gently lowered into the sediment to a pre-determined height and rotated at 1 rpm for 2 min, with the motor torque continuously measured. At the yield point the suspension begins to flow and the measured torque decreases. The shear yield stress ($\tau_y$) can be calculated from the maximum torque and vane dimensions via Equation 4.3 [25, 26]:

$$\tau_y = {2T_{(\max)}}\Big/{\pi D^3 \left(\frac{H}{D} + \frac{1}{6}\right)} \qquad \textbf{Equation 4.3}$$

where $T_{(max)}$ is the maximum torque, $D$ is the vane diameter, and $H$ is the vane height. To minimize any wall effects, the vane-to-cylinder ratio equalled 1:3.5, and the glass beaker was held in place using a clamp to ensure no sample rotation during the measurement.

Equivalent time-dependent studies were completed using a Stanford Research Systems (SRS) QCM 200, see Fig. 4.2.

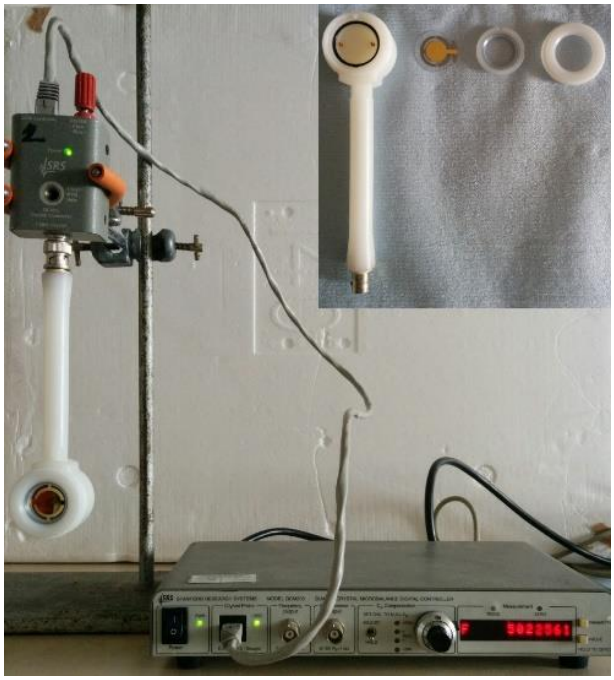

**Figure 4.2: QCM experimental set-up – Stanford Research System QCM200. The gold-coated QCM sensor had a fundamental resonance frequency of 5 MHz.**

A 5 MHz AT-cut gold coated quartz sensor (d = 25.4 mm) was cleaned by sonication in 2 vol% Decon-90 solution for 5 min and rinsed thoroughly with deionised water prior to drying under a stream of $N_2$ gas. The cleaned sensor was then mounted in the QCM holder and left to resonate in air for approximately 30 min. The QCM compensation was adjusted to null the capacitance ensuring that the frequency and resistance values reflected the true resonant properties of the sensor. A stable resonance frequency and resistance was achieved when the sensor responses were within the limits of 2 Hz/h and 0.5 Ohm/h, respectively.

With a stable baseline the QCM probe was gently submerged into the suspension and agitated to enhance the sensor-suspension contact. The QCM probe was repeatedly agitated until the frequency and resistance values of the sensor stabilized, thus

confirming good contact between the QCM sensor and particle suspension. The QCM compensation was then re-adjusted to null the capacitance. To avoid any sensor drift due to thermal fluctuation, the sample beaker was submerged in a water bath that was heated using a hot plate. A temperature probe was immersed in the suspension to maintain the temperature at 30 °C. Long term (70 h) stability of the QCM sensor was first verified by conducting a time-dependent measurement in water, see Fig. 4.7.

### 4.2.4. Solids concentration

With minimal time-dependent aging, Versamag B was chosen to study the effect of solids concentration on the shear yield stress and QCM response. A stock suspension of 44.2 vol% Versamag B was prepared and left to hydrate for two weeks. The stock suspension was prepared in a sealed container and periodically agitated (hand stirring) before diluting the suspension to the desired solids concentration for testing. All test samples were mixed until homogenous and used within three days following hydration.

The same method for measuring the shear yield stress was followed. However, the range of shear yield stresses was broad, and thus to ensure that the maximum torque of the viscometer was not exceeded, two vane geometries of different dimensions were used: Vane 72 ($H$ = 43.33 mm, $D$ = 21.67 mm) for yield stresses between 0 Pa to ~ 40 Pa, and Vane 73 ($H$ = 12.70 mm, $D$ = 12.50 mm) for yield stresses > 45 Pa. Previous research has shown good agreement between shear yield stresses measured using different sized geometries in the crossover region [25, 27-29].

The QCM measurement protocol followed the method previously described. Since all measurements were completed within 30 min, sample drying was considered negligible in the absence of a thin oil layer.

### 4.2.5. Particle size distribution

A Malvern Mastersizer 2000 E (Malvern Instruments, UK) was used to measure the particle size distribution of both Versamag samples. Particle suspensions were prepared to 0.9 vol% and sonicated for 10 min. The particle size distribution and Scanning Electron Microscopy (SEM) images of Versamag A and B are shown in Fig. 4.3. The $d_{50}$ for both samples is almost equivalent (~ 4 µm), although the Versamag B sample showed an observable shoulder towards the larger particle fraction leading to a $d_{90}$ ~ 20 µm compared with $d_{90}$ ~ 15 µm for Versamag A. Both samples had a $d_{10}$ equal to 1.5 µm. SEM images of the two particles revealed a tabular plate-like crystal formation common to the Brucite crystal structure [30].

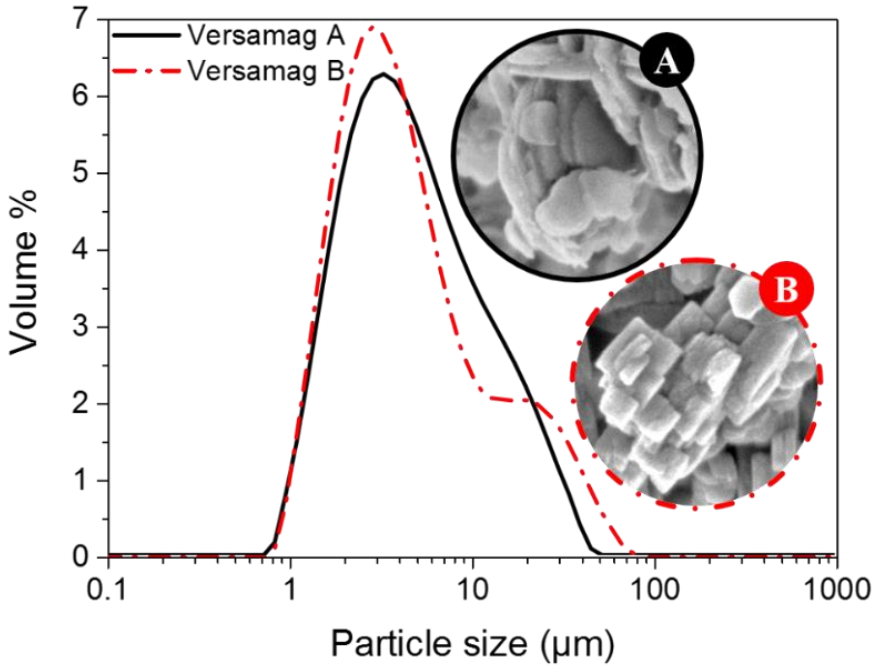


**Figure 4.3: Particle size distribution and SEM images showing the physical appearance of aggregated (A) Versamag A and (B) Versamag B (circlet scale is 500 nm in diameter).**

### 4.2.6. X-ray diffraction (XRD)

Dried samples were disaggregated using a mortar and pestle and mounted in a PANalytical X'pert$^3$ Powder X-ray diffractometer (pXRD), with Cu-Kα radiation (λ = 0.15418 nm) in the 2θ range of 10º - 65º with step size of 0.01˚. Lattice parameters

for MgO (Periclase) (ICDD: 04-014-7440) and $Mg(OH)_2$ (Brucite) (ICDD: 04-011-5938) were obtained from the International Centre for Diffraction Data – Powder Diffraction File database (ICDD-PDF4+).

Intensity-normalised X-ray diffraction patterns for Versamag A and B are shown in Fig. 4.4. Both Versamag samples were predominantly composed of a crystalline hydrated $Mg(OH)_2$ phase (Brucite, ICDD 04-011-5938), comprising infinite stacked layers of Mg-O-Mg sheets. Some minor MgO-content (Periclase, ICDD 04-014-7440), a by-product of the manufacturing process, was also present in both samples, where the higher intensity-maxima of the Periclase [002]-reflection at ~ 43° 2theta (Fig. 4.4. inset) indicates a higher apparent oxide content for Versamag A.

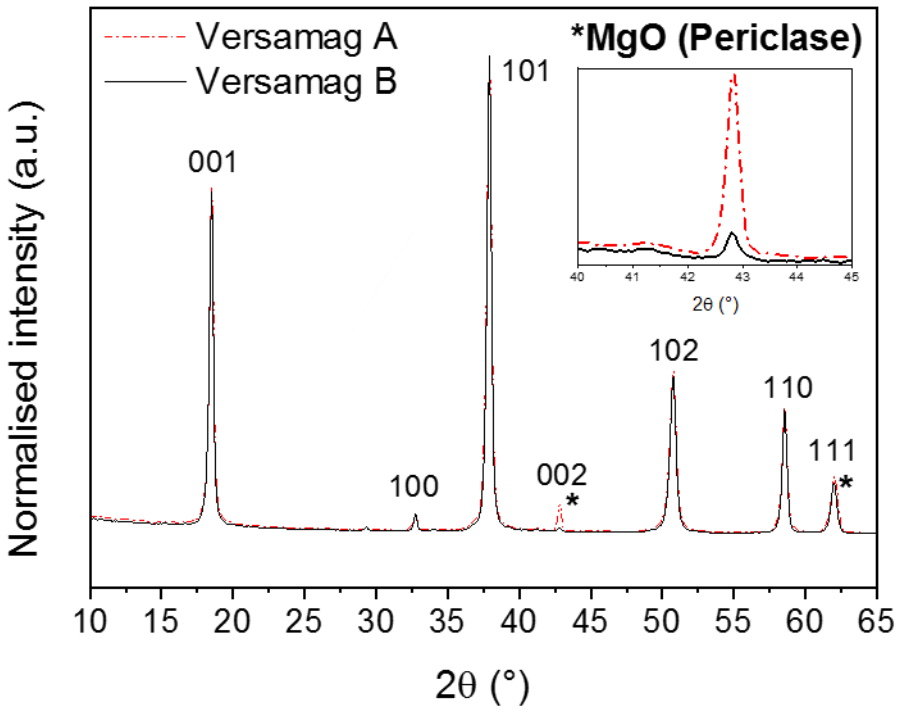


**Figure 4.4: Intensity normalised X-ray diffraction patterns for Versamag A and B.**

### 4.2.7. Thermogravimetric-Differential Scanning Calorimetry (TGA-DSC)

Aliquots of the aged Versamag samples were extracted and quenched using propan-2-ol and allowed to dry. Samples were subsequently pulverised and inserted into 70 µL alumina crucibles (Mettler Toledo) of known mass and weighed. Dynamic thermogravimetric and calometric analyses were carried out using a TGA-DSC 1 (Mettler Toledo) under dry air (70:30 $N_2$:$O_2$ mix) at a flow-rate of 50 mL/s. The heating rate was set at 10 ºC/min and data was recorded between 250 ºC and 450 ºC. Background scans using spent samples (pure MgO) were subtracted from mass loss data to account for air buoyancy effects.

The MgO content was determined by firstly calculating the molar amount of water lost between 250 – 450 °C. The mass of $Mg(OH)_2$ was then calculated through the degradation reaction $Mg(OH)_2 \rightarrow MgO + H_2O$ [31], with the theoretical $Mg(OH)_2$ mass then subtracted from the original sample mass to yield the MgO content. In addition, the enthalpy change per mole of $Mg(OH)_2$ was determined by integrating the peak obtained in the heat flow as the $Mg(OH)_2$ thermally decomposes. Typical TGA-DSC curves for the samples are shown in Fig. 4.5.

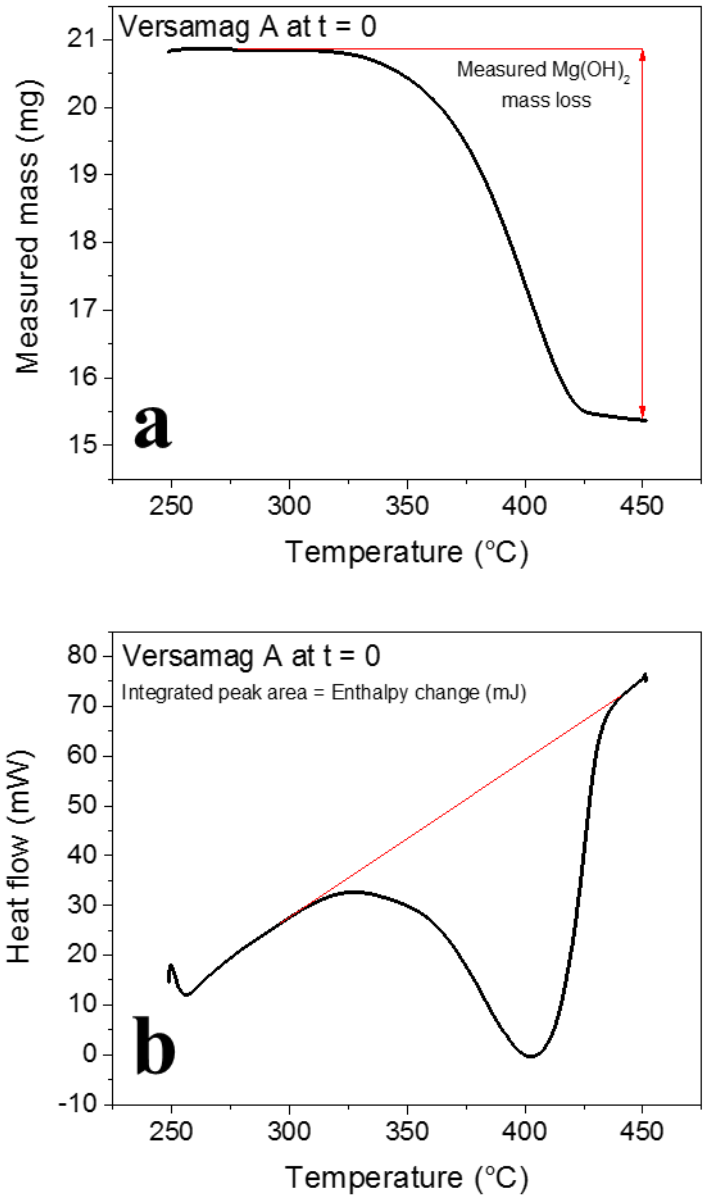


**Figure 4.5: Typical TGA (a) and DSC (b) data for the thermal decomposition of dried (no aging) Versamag A.**

## 4.3. Results and Discussion

### 4.3.1. Sample aging

Vane viscometry was used to assess the time-dependent shear yield stress of Versamag A and B. The two Versamag samples exhibited different aging behaviour (Fig. 4.6) with the yield stress of Versamag A significantly increasing from ~50 Pa to ~300 Pa (~ 490% increase), showing rapid strengthening between t = 6 and 21 h,

while Versamag B attained a maximum yield stress of ~73.5 Pa (~ 46% increase from ~50 Pa at t = 0) at 70 h aging. As previously discussed, aging effects due to sediment sedimentation and/or sample drying can be considered negligible, with the sample aging dynamics more associated to the physicochemical properties of the two particle types, see discussion below.

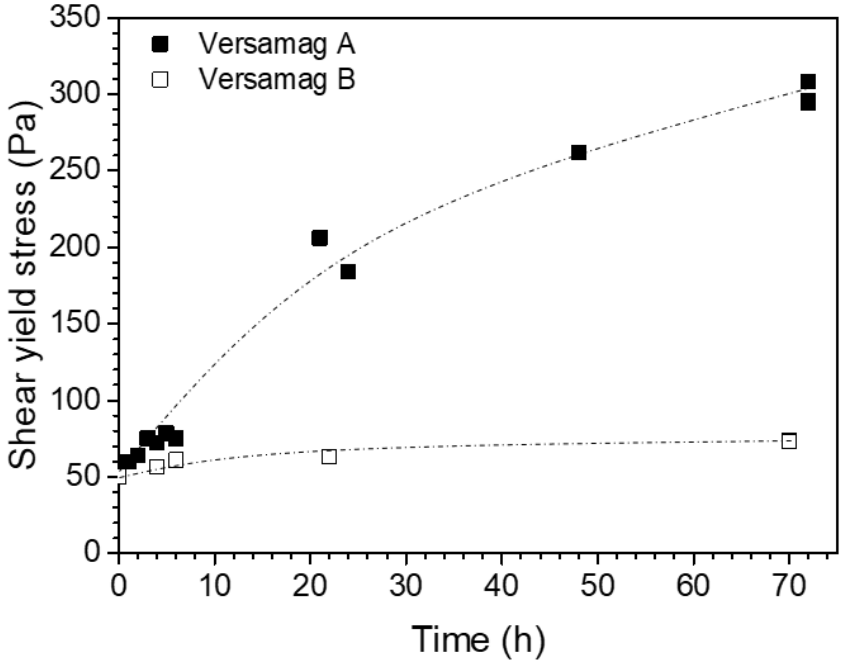


**Figure 4.6: Time-dependent shear yield stress of 22 vol% Versamag A and B.**

*In-situ* QCM measurements confirmed the contrasting aging behaviour of Versamag A and B. The sensor resonance frequency (Hz) and resistance (Ohm) were measured (Fig. 4.7) with the QCM submerged in both Versamag suspensions. At t = 0, the measured frequency and resistance for both Versamag samples were almost equivalent, confirming comparable rheology for the freshly prepared samples (Fig. 4.6). However, during sample aging the sensor resonance frequency and resistance for Versamag A increased, with the sensor frequency eventually exceeding the stable resonance frequency in air (i.e. when $\Delta F = 0$ Hz). This behaviour is in contrast with the QCM response when submerged in Versamag B, where measured changes were significantly smaller. To verify that these changes in resonance frequency and

resistance were not due to instabilities of the QCM sensor, we have also included a 70 h aging test for water only. With good temperature control (T = 30°C) throughout the experiment, neither the sensor resonance frequency nor resistance fluctuated, thus confirming the stability of the QCM sensor. The QCM responses were in good agreement with shear yield stress trends (Fig. 4.6), i.e. the QCM frequency and resistance were responsive to the increasing suspension yield stress.

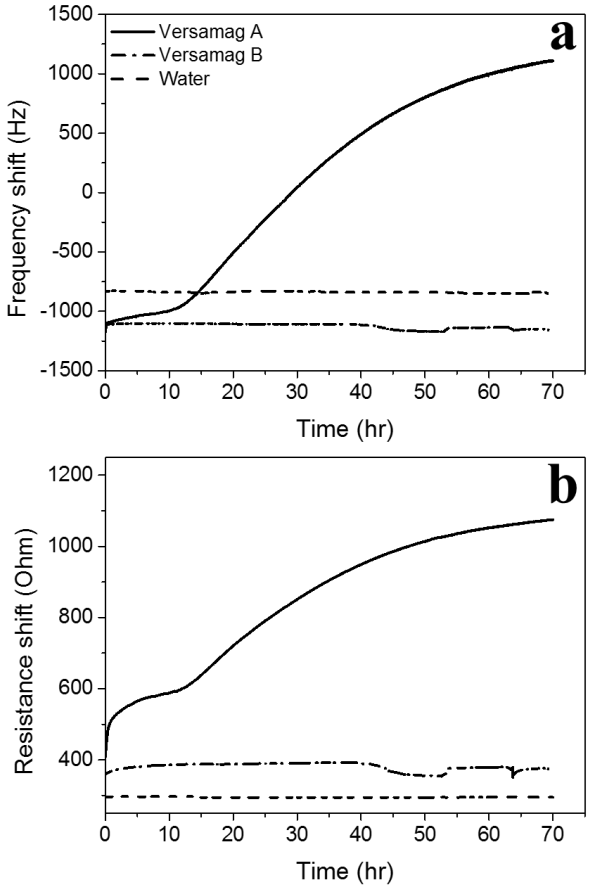


**Figure 4.7: Time-dependent QCM air-to-sample (a) ΔF and (b) ΔR responses for Versamag A (solid line), Versamag B (dash-dot line), and water only (dashed line).**

Further analysis of the Versamag A QCM data revealed a time-dependent response characterized by an approximately bilinear trend (Fig. 4.8).

The resistance shift $\Delta R_1$ (Ohm) can be transformed to a shift in half-bandwidth $\Delta\Gamma$ (Hz) using Eq. 4.4 [32]:

$$\Delta R + i\Delta f = \frac{A}{4\phi^2}\tilde{Z}_L = -i\frac{\pi}{16}\frac{Z_q^3}{Ae_{26}^2\rho_q^2 f_0^3}(\Delta f + i\Delta\Gamma) \qquad \textbf{Equation 4.4}$$

where A is the active sensor area ($m^2$), $Z_q$ the acoustic wave impedance ($8.8 \times 10^6$ kg $m^{-2}$ $s^{-1}$), $e_{26}$ the piezoelectric stress coefficient ($9.65 \times 10^{-2}$ C $m^{-2}$), $\rho_q$ the density of crystalline quartz (2.65 g $cm^{-3}$) and $f_0$ the fundamental resonance frequency (5 MHz). Solving Eq. 4.4 leads to a simple conversion of $\Delta\Gamma \sim 2\Delta R_1$. The apparent differential loss tangent $\frac{\Delta\Gamma}{\Delta F}$ for Region I (t = 1 h to ~8.6 h) was 1.992 and for Region II (t = ~8.6 h to ~13 h) $\frac{\Delta\Gamma}{\Delta F}$ = 0.445. A higher apparent differential loss tangent in Region I suggests that the measured mass is more 'lossy' (i.e. more energy from the oscillating resonator is lost), since $\Delta\Gamma$ measures losses, while $\Delta F$ measures stiffness. Thus, the stiffness contribution dominates Region II as the suspension yield stress increases. Some non-linearity lies at the threshold between the two regions (Fig. 4.8, $\Delta F$ = ~-1000 to -750 Hz at ~16 h), indicating a non-steady-state transition from Region I to Region II. Since the particle and sensor zeta potentials were expected to remain constant (no change in pH or electrolyte concentration), these two regions highlight a two-stage aging process which most likely contributes to the increased suspension yield stress.

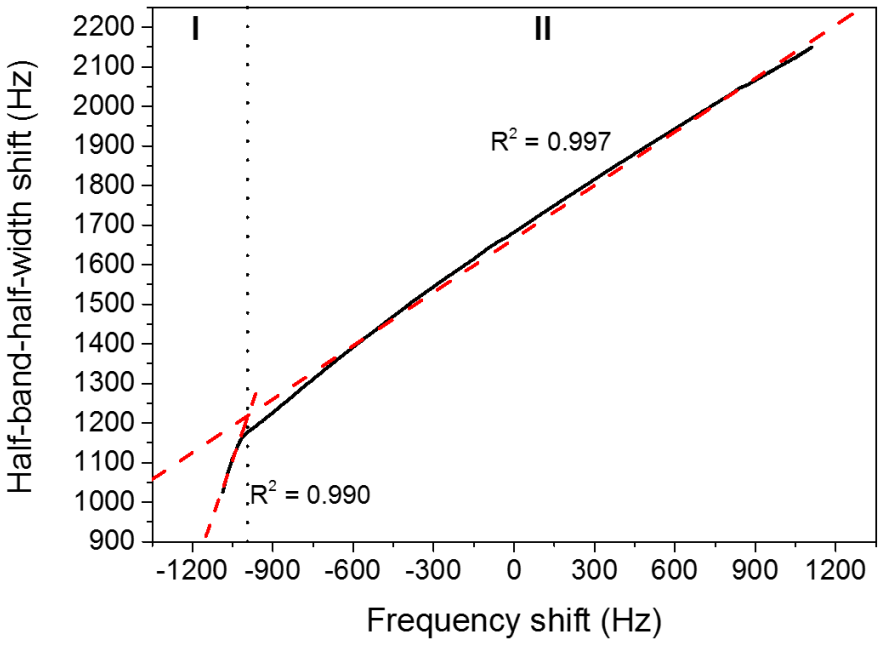


**Figure 4.8: Apparent differential loss tangent (ΔΓ/ΔF) as a function of sample aging, suggesting the occurrence of a 2-stage aging process (sample: Versamag A).**

XRD analysis (as previously shown in Fig. 4.4) revealed measurable differences in MgO content between Versamag A and B prior to aging. As MgO hydration to form $Mg(OH)_2$ is expected to occur in water, *ex situ* time-dependent-XRD was performed to verify this conversion with the aging of Versamag A (Fig. 4.9a). To this end, 7 g samples of Versamag A were hydrated sacrificially for 0, 24, 48 and 70 h, before reactions were quenched by rinsing in 20 mL propan-2-ol, followed by air-drying for 12 h. X-ray diffractograms revealed a progressive reduction in the Periclase [002]-peak with increasing aging time (Fig. 4.9b), indicating significant dissolution, or conversion of Periclase (MgO) into Brucite ($Mg(OH)_2$). Using the Scherrer equation (K = 1) [33] to approximate the crystallite size for Brucite across multiple reflection peaks ([001], [100], [101], [102], [110], [111]), Versamag A showed little variation and the crystallite size was substantially smaller than that measured for Versamag B (Fig. 4.9c). Such small changes in crystalline size may preclude direct MgO to $Mg(OH)_2$ conversion from influencing the QCM response, instead an aggregation-

dominated mechanism akin to oriented attachment or Ostwald ripening effects could be more influential [34].

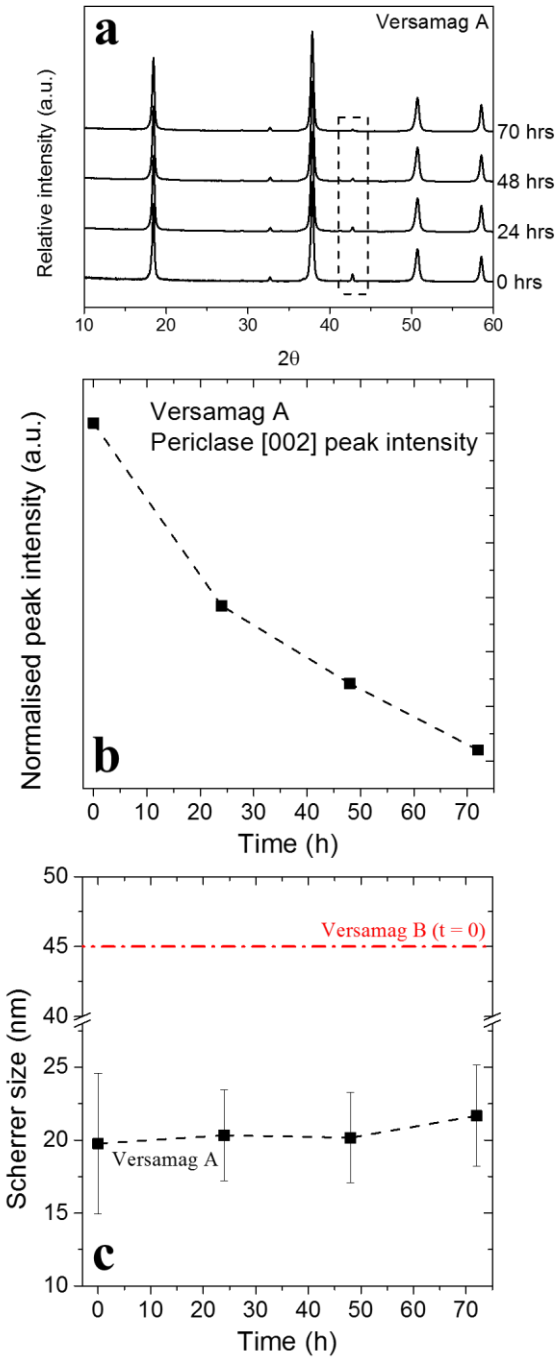


**Figure 4.9: (a) X-ray diffraction patterns of Versamag A after sample aging for 0, 24, 48 and 70 h – shaded region represents the Periclase [002] peak. The Periclase [002]-peak intensity was normalized to the Brucite [101] maximum peak and plotted as a function of aging time (b). The calculated Scherrer crystallite size as a function of sample aging was compared with Versamag B at t=0 (c).**

The apparent two-stage hydration of Versamag A (Fig. 4.8) via the aggregation mechanism was further explored using *ex situ* thermal analysis of samples aged for t = 0, 4, 16, 24, 31, 48 and 72 h. The MgO contents for the fresh Versamag A and B samples were ~16.6 wt% and ~11.5 wt%, respectively, in good agreement with the qualitative assessment by XRD, see Fig. 4.4. The enthalpy associated with the decomposition ($\Delta H_d$) of $Mg(OH)_2$ was determined from integrating the DSC heat-flux peaks, see Fig. 4.5. $\Delta H_d$ ranged between -45 and -80 kJ/mol of $Mg(OH)_2$ (Fig. 4.10), smaller than previously reported activation energies ($E_a$) for the dehydroxylation of $Mg(OH)_2$ (-80.75 to -98.74 kJ/mol [31, 35]), but larger than the dissociation enthalpy of sorbed water (-40.92 kJ/mol [36]), indicating that both hydrate-dissociation and dehydroxylation processes contribute to the dehydration of Versamag A and B.

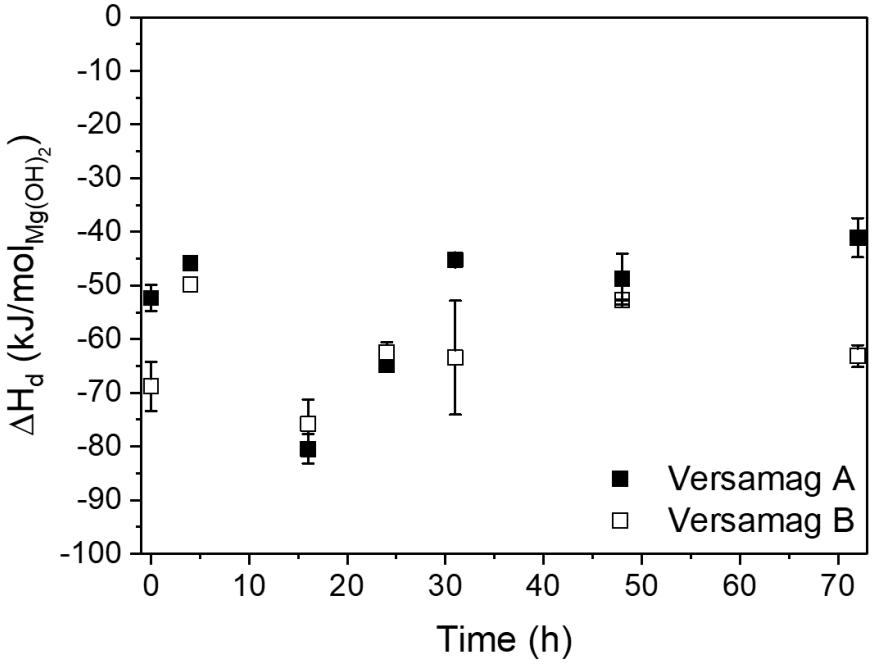


**Figure 4.10: Calculated enthalpy change per mole of $Mg(OH)_2$ based on the thermogravimetric mass loss and differential scanning calorimetry data.**

Hence, the observed two-stage aging (Fig. 4.8) may suggest a dissolution-precipitation reaction of $Mg(OH)_2$. When dispersed in water, MgO and smaller $Mg(OH)_2$ particles undergo increased rates of dissolution. As the aqueous solution

becomes more saturated, precipitated $Mg(OH)_2$ may coat the MgO reactant, thus precipitation will exceed dissolution [37, 38]. This enhances the number of bonds between particles, which stiffens the overall particle-particle network and increases the suspension yield stress (Fig. 4.6) [39, 40].

### 4.3.2. Suspension concentration

The suspension shear yield stress can be varied over several orders of magnitude by increasing the solids concentration. The shear yield stress of Versamag B was firstly measured using the vane viscometer and corresponding measurements completed using the QCM. Fig. 4.11 confirms the exponential increase in shear yield stress with increasing solids concentration [29].

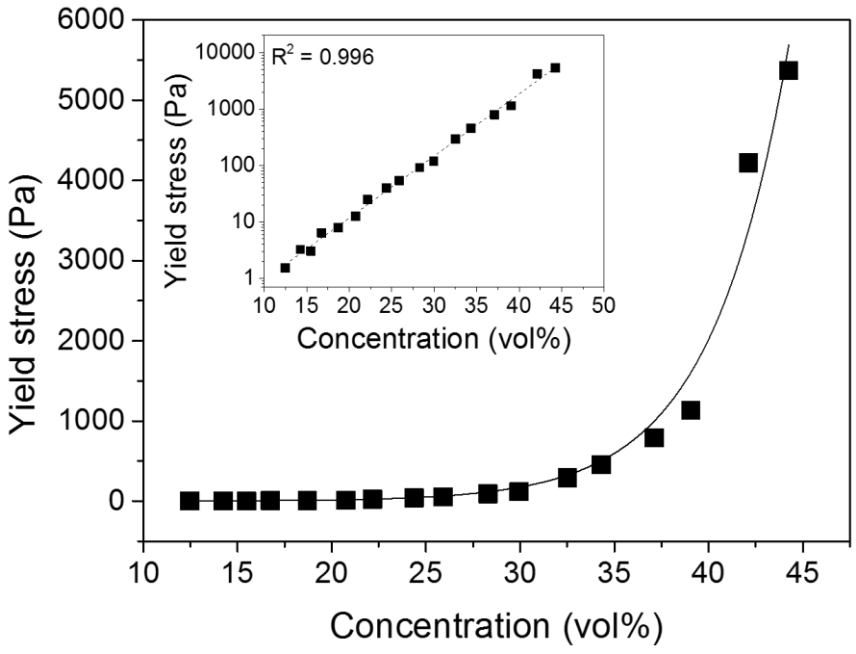


**Figure 4.11: Shear yield stress of Versamag B suspensions as a function of the solids concentration. Data collected using the vane viscometer.**

Complementary QCM tests were conducted (Fig. 4.12) to determine the QCM response as the suspension yield stress increased. The measured ΔR (Fig. 4.12a) also exhibited an apparently exponential response to changes in the suspension yield stress (Fig. 4.11), with the two data sets showing excellent agreement with a correlation coefficient $R^2 = 0.993$, see Fig. 4.12b. The motional resistance across the QCM circuit is a measure of the amount of energy required to oscillate the sensor. Therefore, as the suspension concentration is increased, the number of particle-particle and particle-sensor point contacts is also thought to increase, thus providing greater resistance to the oscillating sensor. Such an effect may also be enhanced by the 'caging' of particles due to restrictions from their closest neighbours [41].

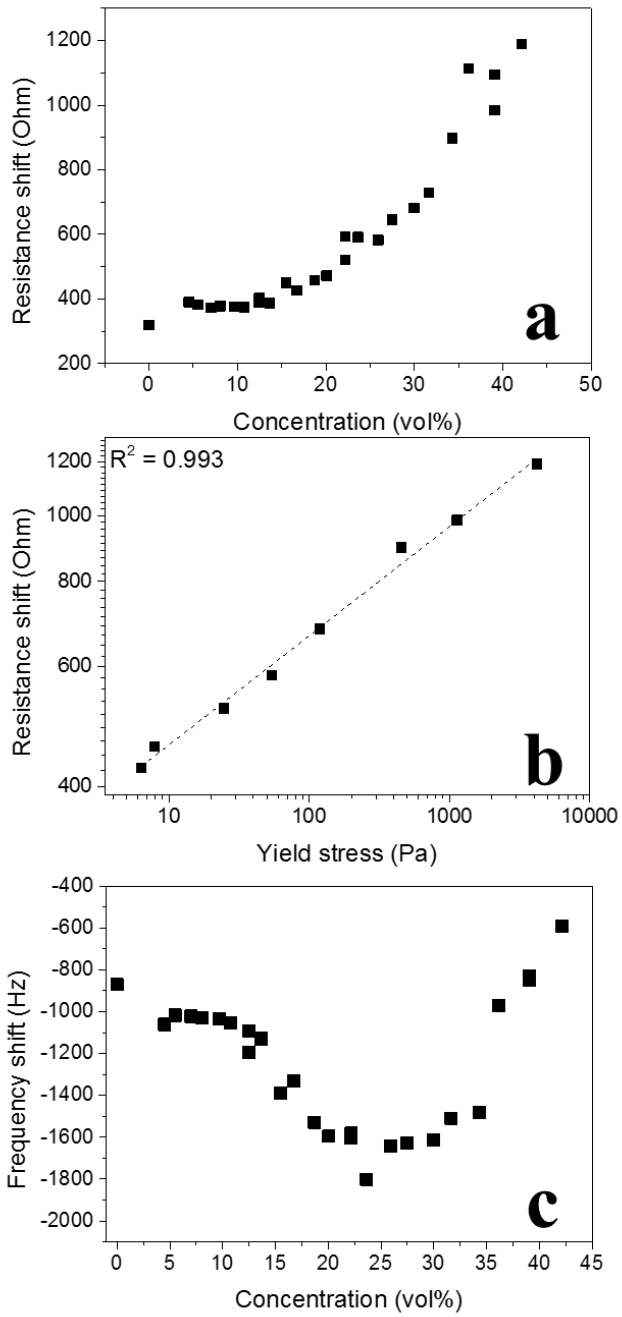


**Figure 4.12: QCM ΔR (a), its correlation to suspension yield stress (b) and ΔF (c) responses for Versamag B as a function of solids concentration.**

In the solids concentration range 5 – 43 vol%, the frequency response was less characteristic of the exponential increase in suspension shear yield stress. At lower solid concentrations (5 – 12 vol%), the measured $-\Delta F$ was shown to be almost independent of the increasing solids concentration. At these low concentrations, the suspension was below the gel point (Fig. 4.1), hence, a contiguous particle network

throughout the suspension had not formed, and particles remained mobile relative to one-another. As such, the suspension loading on the resonating sensor remained constant due to the negligible suspension yield stress. The small decrease in frequency (~ 70 Hz) over the solids concentration range likely resulted from changes in the bulk fluid properties, i.e. small changes in the suspension density and viscosity.

In the solids concentration range ~12 to ~23 vol%, the QCM -ΔF response increased with increasing solids content. The solids concentration was now beyond the suspension gel point, hence a 3D contiguous network had formed, restricting particle mobility, and inducing an intermediary suspension yield stress (~2 – 30 Pa). As the particle network in contact with the QCM sensor stiffens (i.e. increased yield stress), the QCM may detect the associated stiffening as an increase in the apparent mass loaded on the sensor [2], or as a stiffening viscoelastic medium [6]. Another factor that has not yet been explored, is the influence of the contiguous particle network on the shear wave penetration depth. For a 5 MHz sensor, the shear wave penetration depth (or viscous penetration depth) in water is ~ 250 nm (penetration depth $\delta = \left(\frac{2\mu_L}{\omega\rho_L}\right)^{1/2}$), with the penetration depth forming the measurement region [6]. With contacts between the sensor-particle and particle-particle, the pathway for dissipating energy is likely to vary from a simple viscous decay. As such, an increase in the shear wave penetration depth would result in increased 'mass sensing' and an overall increase in the air-sample $-\Delta F$.

With further increases in solids concentration ($>$ 23 vol%) the suspension yield stress was observed to increase to several thousand Pa. In response, the air-to-sample frequency shift of the QCM sensor decreased, eventually measuring frequency shifts below $\Delta F_{solution}$ = -825 Hz (i.e. no particles). At such high yield stresses the apparent mass detected by the QCM may now become large enough for the condition $\omega_S \ll \omega$

to be satisfied, resulting in a transition from inertial to elastic loading [2, 20, 21]. Alternatively, we could also consider the frequency response to be governed by changes in the suspension viscoelasticity. Hence, an increase in the viscoelastic ratio of the suspension, storage modulus (elastic component) to loss modulus (viscous component), may lead to changes in the sensor resonance frequency (i.e. less negative shift) [6]. At present, it is not possible to exactly describe the mechanism(s) governing the measured frequency shifts, further work is ongoing.

## 4.4. Conclusions

A new technique to characterize the rheology of colloidal suspensions has been demonstrated. QCM is ubiquitously used to study kinetics, adsorbed/deposited film and bulk fluid properties, yet the technique has not been extensively utilized to probe colloidal suspensions. Two $Mg(OH)_2$ suspensions were considered due to their considerable differences in sample aging, influenced by dissolution-precipitation mechanisms of MgO conversion to $Mg(OH)_2$ and Ostwald ripening of smaller $Mg(OH)_2$ crystallites. As a result, the Versamag sample with the higher MgO content (Versamag A) exhibited yield stress aging, with the yield stress of a 22 vol% suspension increasing to ~300 Pa in 70 h, while Versamag B showed minimal yield stress aging and a maximum yield stress of 73.5 Pa. When the QCM sensor was submerged in equivalent suspensions, the sensor resonance properties, frequency and resistance, were able to monitor those differences in yield stress aging, with the resonance frequency and resistance increasing as the particle network stiffened (increased yield stress).

In the absence of sample aging, the solids concentration was increased to enhance suspension yield stress. The air-to-sample responses of the QCM sensor were recorded and the shift in resonance resistance shown to correlate with the suspension

yield stress. The frequency response was shown to be more complex and probably influenced by multiple factors such as: i) contact mechanics, ii) suspension viscoelasticity and iii) shear wave penetration depth. Since this is the first study of its kind, the present understanding of the resonance frequency remains poorly understood and is the focus of ongoing research. The research has however demonstrated the applicability of QCM to monitor changes in suspension yield stress, which can be of great value, although the full potential of QCM in characterizing colloidal suspensions is yet to be realized.

## 4.5. References


1. O'Sullivan, C.K. and G.G. Guilbault, *Commercial Quartz Crystal Microbalances - Theory and Applications.* Biosensors & Bioelectronics, 1999. **14**: p. 663-670.
2. Sauerbrey, G., *Verwendung Von Schwingquarzen Zur Wagung Dunner Schichten Und Zur Mikrowagung.* Zeitschrift Fur Physik, 1959. **155**(2): p. 206-222.
3. Kanazawa, K.K. and J.G. Gordon, II, *Frequency of a Quartz Microbalance in Contact with Liquid.* Analytical Chemistry, 1985. **57**(8): p. 1770-1.
4. Denolf, G.C., et al., *High Frequency Rheometry of Viscoelastic Coatings with the Quartz Crystal Microbalance.* Langmuir : the ACS journal of surfaces and colloids. **27**(16): p. 9873-9.
5. Martin, S.J., V.E. Granstaff, and G.C. Frye, *Characterization of a Quartz Crystal Microbalance with Simultaneous Mass and Liquid Loading.* Analytical Chemistry, 1991. **63**(20): p. 2272-2281.
6. Johannsmann, D., *Viscoelastic, Mechanical, and Dielectric Measurements on Complex Samples with the Quartz Crystal Microbalance.* Physical Chemistry Chemical Physics, 2008. **10**(31): p. 4516-4534.
7. Bruckenstein, S. and M. Shay, *Experimental Aspects of use of the Quartz Crystal Microbalance in Solution.* Electrochimica Acta, 1985. **30**(10): p. 1295-300.
8. Nomura, T. and O. Hattori, *Determination of Micromolar Concentrations of Cyanide in Solution with a Piezoelectric Detector.* Analytica Chimica Acta, 1980. **115**(Mar): p. 323-326.
9. Nomura, T. and M. Okuhara, *Frequency Shifts of Piezoelectric Quartz Crystals Immersed in Organic Liquids.* Analytica Chimica Acta, 1982. **142**: p. 281-284.
10. Kanazawa, K.K. and J.G. Gordon, II, *The Oscillation Frequency of a Quartz Resonator in Contact with a Liquid.* Analytica Chimica Acta, 1985. **175**: p. 99-105.
11. Mason, W.P. and H. Baerwald, *Piezoelectric Crystals and Their Applications to Ultrasonics.* Physics Today, 1951. **4**: p. 23.

12. Nakamoto, T. and T. Moriizumi, *A Theory of a Quartz Crystal Microbalance Based Upon a Mason Equivalent-Circuit*. Japanese Journal of Applied Physics Part 1-Regular Papers Short Notes & Review Papers, 1990. **29**(5): p. 963-969.
13. Voinova, M.V., et al., *Viscoelastic Acoustic Response of Layered Polymer Films at Fluid-Solid Interfaces: Continuum Mechanics Approach*. Physica Scripta, 1999. **59**(5): p. 391-396.
14. Johannsmann, D., I. Reviakine, and R.P. Richter, *Dissipation in Films of Adsorbed Nanospheres Studied by Quartz Crystal Microbalance (QCM)*. Analytical Chemistry, 2009. **81**(19): p. 8167-8176.
15. Reipa, V., G. Purdum, and J. Choi, *Measurement of Nanoparticle Concentration Using Quartz Crystal Microgravimetry*. The Journal of Physical Chemistry B, 2010. **114**(49): p. 16112-16117.
16. Fatisson, J., et al., *Deposition of TiO2 Nanoparticles Onto Silica Measured Using a Quartz Crystal Microbalance with Dissipation Monitoring*. Langmuir, 2009. **25**(11): p. 6062-6069.
17. Gotoh, K., Y. Nakata, and M. Tagawa, *Evaluation of Particle Deposition in Aqueous Solutions by the Quartz Crystal Microbalance Method*. Colloids and Surfaces A: Physicochemical and Engineering Aspects, 2006. **272**(1-2): p. 117-123.
18. Marxer, C.M., et al., *Cell Spreading on Quartz Crystal Microbalance Elicits Positive Frequency Shifts Indicative of Viscosity Changes*. Analytical and Bioanalytical Chemistry, 2003. **377**(3): p. 578-586.
19. Tellechea, E., et al., *Model-Independent Analysis of QCM Data on Colloidal Particle Adsorption*. Langmuir, 2009. **25**(9): p. 5177-5184.
20. Pomorska, A., et al., *Positive Frequency Shifts Observed Upon Adsorbing Micron-Sized Solid Objects to a Quartz Crystal Microbalance from the Liquid Phase*. Analytical Chemistry, 2010. **82**(6): p. 2237-2242.
21. Dybwad, G.L., *A Sensitive New Method for the Determination of Adhesive Bonding between a Particle and a Substrate*. Journal of Applied Physics, 1985. **58**(7): p. 2789-2790.
22. Johnson, M., et al., *Characterization of Multiple Hindered Settling Regimes in Aggregated Mineral Suspensions*. Industrial & Engineering Chemistry Research, 2016. **55**(37): p. 9983-9993.
23. De Kretser, R.G., D.V. Boger, and P.J. Scales, *Compressive Rheology: an Overview*. Rheology Reviews, 2003: p. 125-166.
24. Franks, G.V., et al., *Effect of Aggregate Size on Sediment Bed Rheological Properties*. Physical Chemistry Chemical Physics, 2004. **6**(18): p. 4490-4498.
25. Liddell, P.V. and D.V. Boger, *Yield Stress Measurements with the Vane*. Journal of Non-Newtonian Fluid Mechanics, 1996. **63**(2-3): p. 235-261.
26. Dzuy, N.Q. and D.V. Boger, *Yield Stress Measurement for Concentrated Suspensions*. Journal of Rheology, 1983. **27**(4): p. 321-349.
27. Alderman, N.J., G.H. Meeten, and J.D. Sherwood, *Vane Rheometry of Bentonite Gels*. Journal of Non-Newtonian Fluid Mechanics, 1991. **39**(3): p. 291-310.
28. Dzuy, N.Q. and D.V. Boger, *Direct Yield Stress Measurement with the Vane Method*. Journal of Rheology, 1985. **29**(3): p. 335-347.
29. Johnson, S.B., et al., *Surface Chemistry-Rheology Relationships in Concentrated Mineral Suspensions*. International Journal of Mineral Processing, 2000. **58**(1-4): p. 267-304.

30. Zigan, F. and R. Rothbauer, *Neutronenbeugungsmessungen am Brucit*. Neues Jahrbuch für Mineralogie Monatshefte, 1967. **1967**: p. 137À143.
31. Anderson, P.J. and R.F. Horlock, *Thermal Decomposition of Magnesium Hydroxide*. Transactions of the Faraday Society, 1962. **58**(478): p. 1993-&.
32. Johannsmann, D., *The Quartz Crystal Microbalance in Soft Matter Research*. 2014: Springer, Cham.
33. Langford, J.I. and A. Wilson, *Scherrer After Sixty Years: a Survey and Some New Results in the Determination of Crystallite Size*. Journal of Applied Crystallography, 1978. **11**(2): p. 102-113.
34. Mullin, J.W., et al., *Aging of Precipitated Magnesium-Hydroxide*. Industrial & Engineering Chemistry Research, 1989. **28**(11): p. 1725-1730.
35. Halikia, I., P. Neou-Syngouna, and D. Kolitsa, *Isothermal Kinetic Analysis of the Thermal Decomposition of Magnesium Hydroxide Using Thermogravimetric Data*. Thermochimica Acta, 1998. **320**(1-2): p. 75-88.
36. Sinelnikov, S. and V. Gropyanov, *Kinetics of Non-Isothermal Decomposition of Magnesium-Hydroxide*. Journal of Applied Chemistry of the USSR, 1982. **55**(3): p. 461-463.
37. Thomas, J.J., S. Musso, and I. Prestini, *Kinetics and Activation Energy of Magnesium Oxide Hydration*. Journal of the American Ceramic Society, 2014. **97**(1): p. 275-282.
38. Gursky, J.A., et al., *Particle−Particle Interactions between Layered Double Hydroxide Nanoparticles*. Journal of the American Chemical Society, 2006. **128**(26): p. 8376-8377.
39. Stumm, W. and J. Morgan, *The Surface Chemistry of Oxides, Hydroxides, and Oxide Mineral*. Aquatic Chemistry, 1981: p. 625-640.
40. Rahnemaie, R., T. Hiemstra, and W.H. van Riemsdijk, *Inner-and Outer-Sphere Complexation of Ions at the Goethite–Solution Interface*. Journal of Colloid and Interface Science, 2006. **297**(2): p. 379-388.
41. Zhang, H., et al., *Interfacial Particle Dynamics: One and Two Step Yielding in Colloidal Glass*. Langmuir, 2016. **32**(50): p. 13472-13481.

# 5. Particle-Substrate Force Interactions Measured by Quartz Crystal Microbalance

The application of quartz crystal microbalance (QCM) to measure relative changes in colloidal forces between a gold-coated sensor and a concentrated (16.2 vol%) suspension of $TiO_2$ has been considered. The interaction between a single $TiO_2$ sphere (representative particle) and gold-coated sensor measured by atomic force microscopy confirmed the colloidal forces act over a few tens of nanometres with the strongest attraction between the two surfaces measured at pH 4 – 5.5 and purely repulsive interactions measured when pH $\geq$ 6.5. QCM provides both a measure of frequency and dissipative processes (half-band-half-width) with the resonance properties of the sensor shown to be strongly influenced by the interaction forces between the sensor and overlying particle layer. Due to the chosen system these interaction forces (sensor-suspension) dominated compared the weaker interaction forces between the $TiO_2$ particles, hence changes in the suspension rheology had a negligible effect on the sensor response. The sensor resonance properties as the QCM was submerged in the test sample were measured, i.e. air-to-sample shifts. Both frequency and half-band-half-width responses were sensitive to the changing colloidal forces between gold and $TiO_2$ and were shown to be in good agreement with the Hogg, Healy and Fuerstenau (HHF) theory which describes the interaction strength between two dissimilar charged surfaces.

## 5.1. Introduction

The interaction between particles in concentrated suspensions has traditionally been shown to significantly affect its bulk rheological behaviour [1-8]. The strength of the particle-particle interactions in a suspension can be manipulated by altering the solution pH and electrolyte concentration [1-6, 8-10] and has been shown to correlate well to the Derjaguin, Landau, Verwey and Overbeek (DLVO) theory [1, 11, 12]. The DLVO theory describes the stability of a colloidal system and is the sum of the London van der Waals forces of attraction and electrical double layer forces of repulsion [1, 11-13]. The theory has been used to compare the stability of colloidal dispersions across a multitude of different systems [1-6, 8-10]. Extra non-DLVO forces including hydration forces, hydrophobic forces, steric and electrosteric forces including other polymer-based interactions have shown to cause deviations from predicted behaviour [1, 14-17]. For hard metal oxide particles in monovalent electrolyte solutions at concentrations at or below 10 mMol/L for $Na^+$ [18], the effect from these non-DLVO forces is very small.

In recent years, the quartz crystal microbalance (QCM) has become a useful tool for measuring the behaviour of colloidal systems [19]. The QCM is traditionally used to measure the areal mass density of thin, firm, tightly bound uniform films in the $ng/cm^2$ range [20, 21]. Applications of its use have extended to include measurements in liquids, with changes in the sensor air-to-sample resonance frequency ($\Delta F$) and half-band-half-width ($\Delta\Gamma$) being correlated to the density-viscosity product of non-adsorbing Newtonian liquids [22-25].

Several authors have since performed particle adsorption studies onto oscillating QCM resonator surfaces to obtain highly sensitive and rapid information on the adsorption behaviour of colloidal systems in a convenient manner [19, 26]. Chen et

al. [27] showed that the deposition rate of montmorillonite clays onto QCM resonators coated with carbon and asphaltene increased with an increasing electrolyte concentration and cationic valency [27]. Gotoh et al. [28] performed similar experiments where they investigated the adsorption behaviour of spherical polyethylene or nylon particles onto polyethylene, Nylon 6 and cellulose acetate coated resonator surfaces, as well as an uncoated gold surface. They found that upon mixing ethanol into the solution, a reduction in the rate of adsorption is observed due to changes in background fluid properties [28]. In addition to *in-situ* adsorption kinetic experiments, the QCM can be used to monitor changes in the physical properties of the adsorbed particles themselves [26, 29]. Tellechea et al. [26] revealed that the adsorption of discrete particles in solution produces a QCM response that differs to that expected for homogenous layers. The liposomes and viruses examined may be referred to as non-rigid (soft) colloidal particles that can accommodate external stress by changing its shape, producing QCM resonance shifts that can be used to calculate the thickness of an adsorbed layer over time [26]. The dependency of the QCM response with particle size was exploited by Lapidot et al. [29] where they grew calcium sulphate crystals onto the QCM resonator surface directly, and showed that the extent of crystallisation of these crystals is proportional to the QCM frequency and dissipation response [29].

Zhuang et al. [30] revealed that the QCM response is sensitive to particle size and concentration effects when studying the evaporation of colloidal suspension droplets from the resonator surface [30]. Their results showed similarities to Lapidot et al. [29] in that the particle-sensor loading behaviour changes as the particle size is increased [30]. Upon complete evaporation of concentrated suspensions, Zhang et al reported positive $\Delta F$ values. Larger (1 μm) particles produced significantly larger $+\Delta F$ responses compared to smaller (50 nm) particles (~1200 Hz vs ~490 Hz at a maximum

concentration of 5 wt%) [30]. Pham et al. [31] also reported positive ΔF values coupled with a drastic increase in ΔΓ upon complete evaporation of suspension droplets containing 1 wt% 5 – 10 μm latex particles. A clear size-dependency is therefore observed, with larger particles producing a more positive ΔF response [30, 31]. Zhuang et al. [30] also reported that for the same particles, a more positive ΔF response is also observed at higher solids concentrations after complete evaporation of the droplet [30]. Initially a more negative shift is observed at initial solids concentrations of < 0.6 wt% 50 nm alumina, which then became more positive with increasing initial solids concentration [30]. The authors suggest that the particles no longer form a single uniform layer on the sensor, and that the interaction between the individual particles may play a role where detected particles are clamped in space by overlaying particles, creating frequency shifts in a similar manner than if the particles were of a larger size [30]. For small particle sizes (< 1 μm) [30, 32] and low concentrations (< 0.6 wt% ) [30], the QCM response can be correlated to the concentration of colloidal suspensions during evaporation studies [33]. Reipa et al. also reported no positive shifts at these low concentrations of nm-sized particles [33]. Gotoh et al., Tellechea et al., Zhuang et al. and Pham et al. have all found that changes in the QCM signal during particle adsorption can be correlated to the DLVO theory [26, 28, 30, 31]; changes in the intensity of the repulsive electrical double layer forces and attractive London van der Waals forces would produce a comparable QCM response in that a stronger interaction between particles results in larger QCM resonance shifts [19, 26-28, 30, 33].

D'Amour et al. [34] and Pomorska et al. [32] revealed that if the colloidal particle-QCM sensor is modelled as a sphere-plate coupled resonance system, where both the sphere and the sensor each have their own frequency of oscillation, properties relating to the mass of the sphere and the sphere-plate contact stiffness can be inferred [32,

35], which can then be related back to DLVO theory. A numerical representation of the coupled resonance theory is shown in Equation 5.1 [32, 35].

$$\frac{\Delta f + i\Delta\Gamma}{f_F} \approx \frac{-N_S m_S \omega}{\pi Z_q} \frac{1}{1 - \frac{\omega^2}{\omega_S^2}} \qquad \textbf{Equation 5.1}$$

Where $\Delta f$ = air-to-sample frequency shift (Hz), $\Delta\Gamma$ = air-to-sample half-band-half-width shift (Hz), $f_F$ = fundamental mode resonance frequency (Hz), $N_S$ = number of spheres ($cm^{-2}$), $m_S$ = mass of spheres (g), $Z_q$ = impedance of AT-cut quartz ($8.8 \times 10^6$ kg $m^{-2}$ $s^{-1}$), $\omega$ = angular frequency of the sensor (rad/s), $\omega_S$ = angular frequency of the sphere (rad/s), where smaller (lighter) spheres resonate at larger angular frequencies.

By comparing the angular frequency of the particle to that of the sensor, two loading regimes can be inferred: inertial loading and elastic loading.

If $\omega \ll \omega_s$ (inertial loading – negative $\Delta f$):

$$\frac{\Delta f + i\Delta\Gamma}{f_F} \approx \frac{-2 f N_S m_S}{Z_q} \qquad \textbf{Equation 5.2}$$

The result in Equation 5.2 is termed inertial loading and is the Sauerbrey equation [20, 21, 32, 35, 36] where $N_S m_S = \frac{m}{A}$, $m$ = detected mass (g), $A$ = piezoelectrically active area of the sensor ($cm^2$) and $f$ = resonance frequency of the sensor ($\omega = 2\pi f$) (rad $s^{-1}$).

An increase in the amount of detected mass will result in a more negative $\Delta f$ response. This limit applies to small (typically <1 µm) particles that are tightly bound to the sensor surface where they behave as a film [21, 32, 34, 36]. When the strength of the particle-sensor link increases, a larger mass is detected by the particles, resulting in a more negative $\Delta f$ response [32]. The monolayer mass (< 0.6 wt% for 50 nm alumina)

detected by Zhuang et al. [30] initially follow the inertial loading response. If $\omega \gg \omega_s$ (elastic loading – positive $\Delta f$):

$$\frac{\Delta f + i\Delta\Gamma}{f_F} \approx \frac{1}{\pi Z_q}\frac{N_S \kappa_S}{\omega} \qquad \textbf{Equation 5.3}$$

Where $\omega_S = \sqrt{\frac{\kappa_S}{m_S}}$ and $\kappa_S$ = stiffness of the sphere-plate contact.

Equation 5.3 is the Dybwad case where an increase in the number of linked particles result in a positive $\Delta f$ response [21, 32, 34, 36, 37]. The limit applies to large particles that are bound weakly enough to the sensor for them to be clamped by inertia [21, 32, 34, 36, 37]. The changes in loading behaviour experienced by Zhuang et al. [30] and Lapidot et al. [29] correlates to the coupled resonance model in that a $+\Delta f$ response is observed when particles become large enough for the bulk of their mass to no longer follow the sensor oscillation (i.e. a phase lag occurs between the oscillating particle and sensor due to a significantly lower $\omega_S$). An increased solids concentration (> 0.6 wt% for 50 nm alumina in the case of Zhuang et al. [30]) that result in several layers of particles to form on the resonator surface will produce inertial forces on the initial detected layer of particles, causing them to behave as larger entities.

It should be noted however that in some cases the QCM may not detect the entire adsorbed particle mass. Tellechea et al. [26] has shown that an increased surface area in contact with the QCM resonator (i.e. stronger adsorption) resulted in a more efficient transfer of vibrational energy (a reduction in the $\Delta\Gamma/-\Delta f$ response), which also coincided with larger $-\Delta f$ responses.

The QCM penetration depth may also play a significant role. The QCM shear wave penetration depth, $\delta = (2\eta_{liq}/(\rho_{liq}\omega))^{1/2}$, ($\eta_{liq}$ = liquid viscosity, ($\rho_{liq}$ = liquid density) is estimated to be ~250 nm in water at 5 MHz, but reduces exponentially with

increasing resonance frequency [21, 26]. By increasing the resonance overtone order $n$ (i.e. for conventional QCM devices, $n$ = 1, 3, 5 is equivalent to 5, 15, 25 MHz resonance frequency), the QCM penetration depth can be altered [21], potentially allowing for surface-specific interactions such as the particle-sensor interaction strengths to be distinguished from other bulk effects such as neighbouring particle-particle interactions.

When studying concentrated $Mg(OH)_2$ suspensions, our recent publication showed that the air-to-sample QCM resistance shift (a parameter that is directly proportional to half-band-half-width) [25] was in good agreement with the suspension yield stress, i.e. the resistance shift increased with increasing suspension yield stress. In that study the suspension yield stress was varied by altering the particle concentration with all other parameters kept constant. The QCM frequency response was found to be more complex and thought to be sensitive to the suspension properties (gel point onset and viscoelasticity) and the suspension-sensor loading mechanics (inertial and elastic loading). Since the colloid interaction forces between the suspension and sensor was constant (pH and ionic concentration were fixed), the observed changes in the sensor resonance was dependent on the suspension properties. However, in the current study we explore the importance of the suspension-sensor interaction on the overall sensor response. By varying the pH of a 16.2 vol% $TiO_2$ suspension, the interaction forces between $TiO_2$-$TiO_2$ and $TiO_2$-gold (QCM sensor) can be modulated with the relative contributions of each interaction type dependent on the surface potentials and system Hamaker constants: $TiO_2$-$H_2O$-$TiO_2$ ($A_{131} = 0.00278 \times 10^{-20}$ J) being orders of magnitude smaller than $TiO_2$-$H_2O$-gold ($A_{132} = -0.253 \times 10^{-20}$ J).

## 5.2. Materials and Methods

### 5.2.1. Materials

Hombitan S141 (Venator) is an anatase grade of $TiO_2$ with a d50 of 0.664 µm (see Fig. S5.3). The sample was used as received. 16.2 vol% $TiO_2$ suspensions were prepared in $10^{-2}$ M NaCl background electrolyte (analytical grade, Fisher Scientific). The samples were mixed for 5 min until the suspension resembled a smooth paste. Samples were then pH adjusted using either finely crushed NaOH pellets (ACS reagent, Sigma Aldrich) or 5 M HCl (AnalaR-grade, VWR International), mixed for 5 min, sealed and left overnight (minimum 15 h) to equilibrate. For testing, the suspension pH was checked and readjusted to the desired pH if needed. All sample pHs were adjusted from the natural pH condition (pH = 5.3).

### 5.2.2. Zeta potential

A Zetasizer Nano ZS (Malvern, UK) was used to measure the pH dependent particle zeta potential. Dilute suspensions (0.25 vol%) of $TiO_2$ were prepared in $10^{-2}$ M NaCl background electrolyte and left overnight on a carousel to equilibrate. The pH was either adjusted to acidic or basic conditions from the natural pH of the dilute suspension. A SurPASS Electrokinetic Analyser (Anton Paar, USA) was used to measure the streaming potential on the gold-coated QCM sensor (Stanford Research Systems). The 25.4 mm diameter 5 MHz AT-cut gold coated sensor was first cut to size (d = 14 mm) by laser ablation. The cut sensor was then cleaned in 2 vol% Decon solution, sonicated for 10 min and rinsed thoroughly with deionized water, before being dried using $N_2$ gas. To be consistent, $10^{-2}$ M NaCl was used as the background electrolyte and the pH adjusted from pH 3.5 – 9.5. The gold-coated sensor was clamped in the instrument flow cell sample holder and connected to two electrodes. The background electrolyte of desired pH was then pumped through the flow cell

where electrolyte ions would preferentially adsorb onto the sensor surface, depending on its charge relative to the bulk solution. A potential difference in the solution before and after it flowed past the sample is measured, allowing for the zeta potential to be derived using the Helmholtz-Smoluchowski approach [38].

### 5.2.3. X-ray diffraction (XRD)

Dry powder samples of $TiO_2$ were mounted into a D8 XRD (Bruker, US), with Cu-K$\alpha$ radiation ($\lambda$ = 0.15418 nm) in the 2$\theta$ range of 20º - 80º with step size of 0.016˚. Lattice parameters were obtained from the International Centre for Diffraction Data – Powder Diffraction File database (ICDD-PDF4+).

### 5.2.4. Atomic force microscopy (AFM)

The pH-dependent interaction forces between a single $TiO_2$ sphere (Sachtopore NP, Sachtleben Chemie) and the gold-coated QCM sensor was studied by AFM. To prepare the colloidal probe, a tipless silicon-coated cantilever (Nanosensors, USA. Supplied by NanoAndMore, Germany) with a spring constant of 0.2 N/m was gently dipped into a thin line of Araldite rapid epoxy resin (Huntsman Advanced Materials) to wet the cantilever with a small drop of the epoxy resin. The cantilever was then immediately withdrawn and positioned over the centre of a 20 µm sphere (see Supporting Information Fig. S5.1 for SEM image of sample particles) and lowered into contact with the single particle. The cantilever-particle were held in contact for 10 min to ensure the epoxy resin had partially set before retracting the colloidal probe from the substrate. The colloidal probe was left overnight in the BioScope II AFM cantilever holder (Veeco, USA). Before measurement, the colloidal probe was washed by submerging it into deionised water followed by the background electrolyte solution and calibrated using the X-Y calibration function in the NanoScope V710 software.

The gold-coated QCM sensor was mounted on a glass slide using the same epoxy resin and left overnight for the epoxy resin to set. The sensor was washed in 2% Decon-90 solution for 5 min, rinsed thoroughly with deionised water, and dried with $N_2$ gas, The sensor was mounted on the AFM stage and submerged in $10^{-2}$ M NaCl electrolyte solution of adjusted pH. The AFM was set to 'tapping mode' to allow the colloidal probe to approach the gold surface laterally while measuring the amount of deflection in the cantilever. The deflection is proportional to the force acting on the adsorbed colloidal particle and can be obtained by multiplying the cantilever force constant by the deflected distance. The colloidal probe approach and retract speed was kept constant at 150 nm/s and multiple force curves (minimum 60) were collected at several different locations on the gold-coated sensor. A minimum of 10 force curves were analysed to provide a reasonable statistical assessment of the particle-sensor attraction force on approach. Before each pH condition the gold-coated sensor and colloidal probe were cleaned following the previously described methods.

### 5.2.5. Yield stress

The pH-dependent yield stress of the 16.2 vol% $TiO_2$ suspension was measured using a viscometer (Brookfield DV-II+ Pro Viscometer, UK) with a 4-blade vane of dimensions: H = 43.33 mm and D = 21.67 mm. A detailed explanation of the measurement setup has been provided in our previous study [39]. Briefly, the vane was lowered below the suspension interface to a constant height identified by a 'notch' on the geometry. With the vane fully submerged, the vane was rotated at 1 rpm for 2 min with the viscometer torque continuously measured. The suspension yield stress was then determined from the maximum torque measured. To minimize wall effects, the vane-to-cylinder ratio was 1:3.5 and the sample beaker was clamped to avoid sample rotation during the measurement.

### 5.2.6. Quartz crystal microbalance (QCM)

An impedance monitoring QCM (Clausthal University of Technology, Germany) operating in 'reflection mode' (enhance the sensitivity of the sensor in liquid environments) was used to measure the air-to-sample sensor resonance frequency and half-band-half-width shifts. The QCM dip probe (Stanford Research Systems, USA) housed a 25.4 mm, 5 MHz gold-coated sensor which was cleaned following the method previously described. The QCM was first calibrated in air by locating and fitting the peak obtained when the electrical admittance of the resonator as a function of oscillation frequency is mapped [25], and the resonance properties of overtones 1, 3, 5, 7, 9, 11 (n = 1, 3, 5, etc. is equivalent to 5, 15, 25, etc. MHz) were recorded until a stable baseline had been established (~30 min). The QCM dip probe was then submerged in the 16.2 vol% $TiO_2$ suspension of known pH and rotated several times. With the sensor fully submerged, the QCM was re-calibrated by refitting the electrical admittance peaks and the resonance frequency and half-band-half-width measured until a new baseline was established, which typically took 45 min to achieve a steady signal (i.e. drift in resonance frequency < 5 Hz/h). The air-to-sample resonance frequency ($\Delta F$) and half-band-half-width ($\Delta \Gamma$) were determined from the shift in steady-state signals.

## 5.3. Results and Discussion

### 5.3.1. Particle and Sensor Characterization

Background subtracted X-ray diffraction analysis of dried Hombitan powder (Fig. 5.1) revealed the sample to be composed predominantly of a crystalline $TiO_2$ phase identified as Anatase (ICDD: 01-075-2546). Comparing the peak positions with an anatase reference taken from the American Mineralogist Crystal Structure Database Record (RRUFF: R060277.9) revealed a significant degree of peak broadening,

indicating small crystallite sizes and/or the presence of amorphous material within the sample matrix [40]. SEM imaging using a Hitachi SU8230 SEM on dry sample powder prepared the same way for X-ray diffraction experiments (inset Fig. 5.1) showed small crystallites typically ranging from ~50 to 80 nm. The sample crystallites shown in Figure 5.1 do not show well-defined features that are expected for highly crystalline samples [41], which suggests the presence of amorphous material. This amorphous material is likely composed of titanic acid ($[Ti_x(OH)_{4-2x}]_n$) that is a result of the particle manufacturing process which may also cause the relatively low equilibrium pH of the saturated suspension (pH ~5.3), a condition below the suspension isoelectric point (Fig. 5.2) [41].

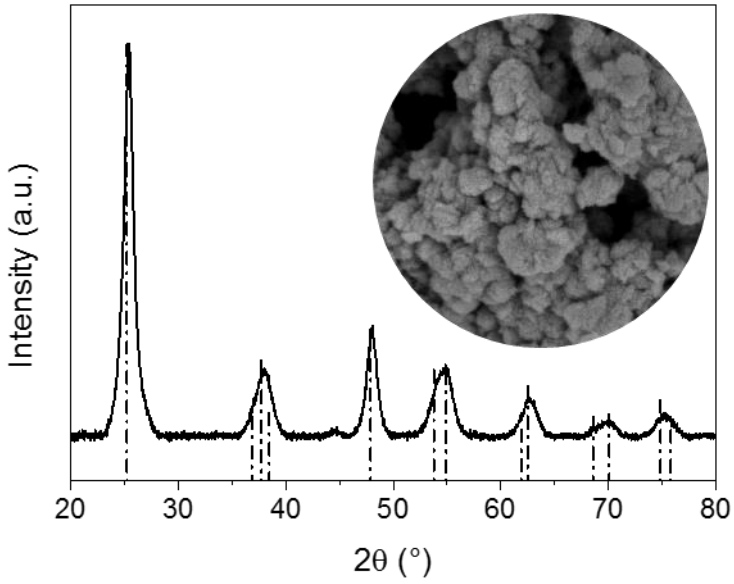


**Figure 5.1: Hombitan S141 X-ray diffraction spectra (solid lines) and physical appearance of dry Hombitan S141 powder measured using a Hitachi SU 8230 SEM. Inset diameter = 1 µm. Dash-dot lines represent the reference peaks for anatase, taken from the American Mineralologist Crystal Structure Database Record (RRUFF: R060277.9).**

The zeta potentials of the hydrated $TiO_2$ particles (Fig. 5.2) showed a pH dependence typical of anatase [42], with an isoelectric point of pH 6.62, hence the contribution of any small impurities on the measured particle zeta potential was considered to be

negligible. In addition, the zeta potential of the gold-coated QCM sensor (determined from measuring the streaming potential) was negative over the pH range of interest, with an isoelectric point below pH 3.5. These values were in reasonable agreement with published data [43, 44] confirming the deposited gold layer on the QCM sensor was suitably thick to screen any contribution from the underlying chrome layer.

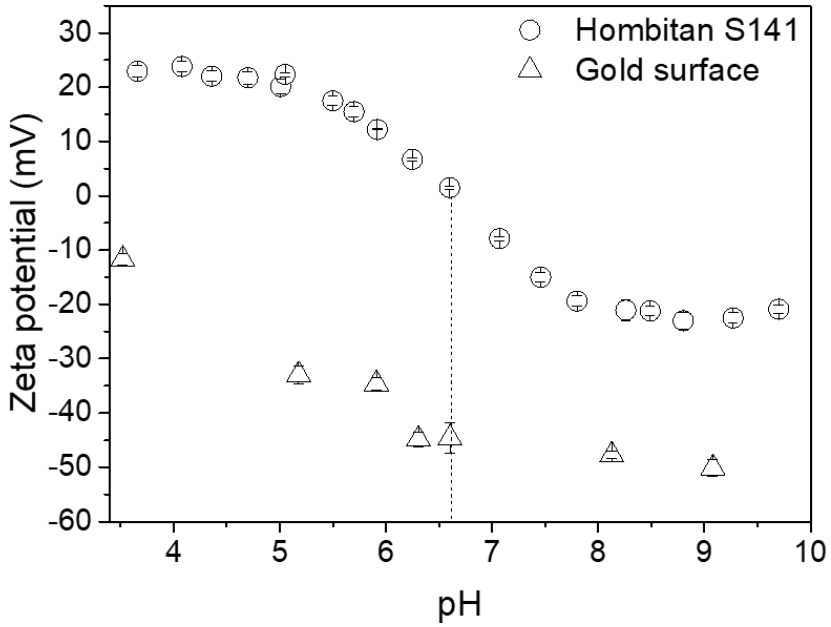


**Figure 5.2: Zeta potentials of Hombitan S141 and the gold-coated QCM sensor as a function of pH in 10 mM NaCl background electrolyte. Dashed line represents the isoelectric point of Hombitan S141 measured using electrophoresis (pH 6.64).**

### 5.3.2. Particle-QCM sensor and particle-particle interactions

The colloidal interaction forces between the gold-coated QCM sensor and a spherical $TiO_2$ particle, analogue for the Hombitan S141 particles, was measured by AFM, see Fig. 5.3. In acidic conditions (pH 4.0) when the $TiO_2$ particle was positively charged, inferred from Fig. 5.2, the colloid probe experiences an attraction at distances less than ~15 nm from the gold-coated sensor (Fig. 5.3A). Conversely, when the pH of the background electrolyte was adjusted to pH 8.3, a purely repulsive interaction was

measured. With the negative zeta potential of the gold-coated sensor, the change from attraction to repulsion is consistent with the zeta potential trend shown in Fig. 5.2 and charge reversal of the $TiO_2$ particle.

The maximum attractive force, F/R (nN/μm), taken to be the most negative force measured on approach, was plotted as a function of pH, see Fig. 5.3B. The experimental variability is clearly shown to depend on the strength of the attractive force, which is not unreasonable and may result from slight variability, possibly influenced by local surface contaminants including sorbed oxide, hydroxide and chloride species [43, 45]. However, there is a clear pH dependence on the attractive force with the maximum attraction measured in the pH range 4 to 4.5. Thereafter, as the pH increased, the attractive force weakens, eventually becoming unmeasurable when the pH $\geq$ 6.6. Interestingly, the isoelectric point for the Hombitan S141 particles was between pH 6.5 and 7.0, thus the AFM colloidal probe study is a good analogue to describe the interaction force between the Hombitan S141 particles and the gold-coated QCM sensor.

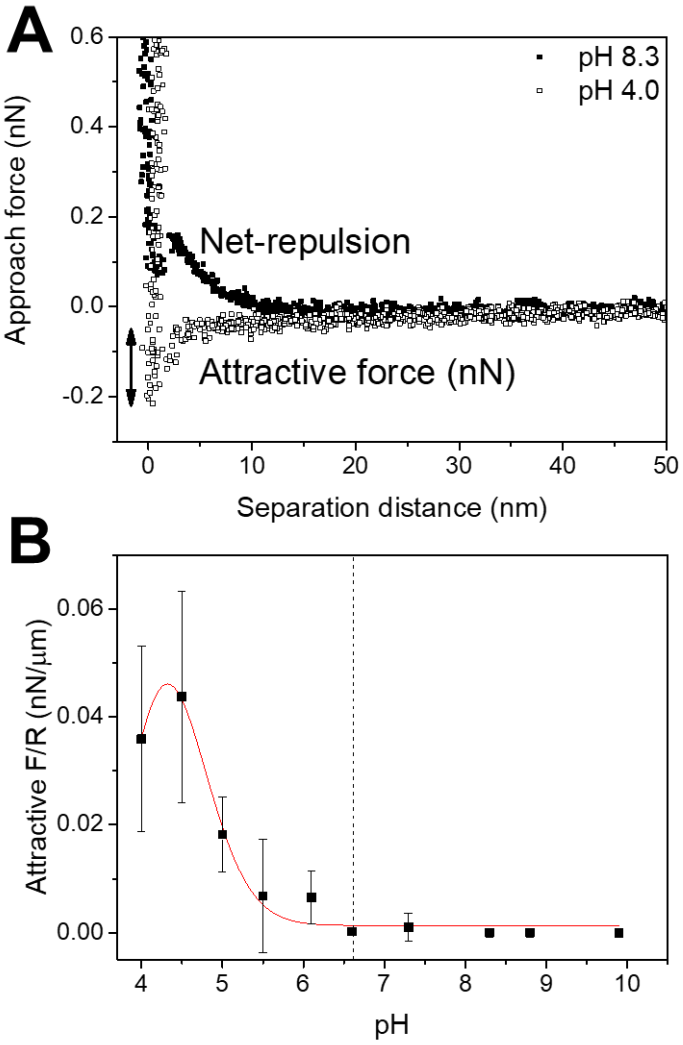


**Figure 5.3: (A) Representative AFM approach force curves obtained to produce (B) a plot of the spherical $TiO_2$ attractive force/radius to the QCM resonator gold surface with changing pH in 10 mMol NaCl solution. Inset figure shows the physical appearance of the spherical $TiO_2$ used where the inset diameter = 50 µm. Sphere radius used = 6.5 µm. Dashed line represents the isoelectric point of Hombitan S141 measured using electrophoresis.**

With a pH dependent zeta potential, the particle-particle interaction strength and hence the rheology of the concentrated particle suspension can be varied significantly [3]. Fig. 5.4 shows the pH dependent yield stress of a 16.2 vol% Hombitan S141 suspension. At low pH (pH 4.3) the suspension appears 'milky' with no measurable yield stress. As the pH was increased towards the isoelectric point the particle zeta potential reduced and the suspension yield stress increased. Such behaviour is common and is a consequence of increasing attraction between particles, forming

aggregates and clusters which network, forming a material with a solid-like behaviour which results in the suspension having a finite yield stress [4, 5, 46]. The maximum yield stress was measured at pH 5.9 which is approximately one pH unit below the measured isoelectric point. The cause of this difference is not entirely understood but has been reported previously for anatase suspensions and attributed to the rheology and electrokinetic techniques responding to electric potentials at two different distances from the surface [47]. Beyond pH 5.9 the suspension yield stress decreased linearly with pH, responding to the increased negative zeta potential of the $TiO_2$ particles. The suspension yield stress increase (pHs below the isoelectric point) and decrease (pHs above the isoelectric point) showed an asymmetry around the maximum yield stress. Such asymmetry has been reported for anatase suspensions [47] and is caused by differences in the pH of the point of zero charge (PZC) and isoelectric point in the presence of electrolyte [47].

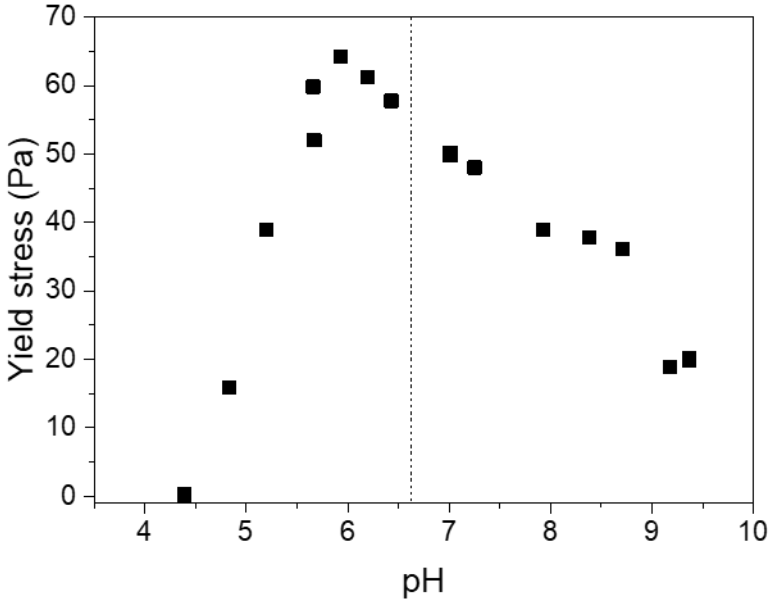


**Figure 5.4: pH-dependent yield stress of 16.2 vol% Hombitan S141 suspensions in 10 mM NaCl. Dashed line corresponds to the isoelectric point of Hombitan S141 measured using electrophoresis.**

Using the measured zeta potential values (Fig. 5.2), the Hogg, Healy and Fuerstenau (HHF) equation was used to calculate the total potential energy of interaction ($V_T$) between Au-$TiO_2$ (QCM sensor – suspension anatase particles) and compared to $V_T$ of $TiO_2$-$TiO_2$ (anatase) calculated using DLVO theory. The HHF theory describes the potential energy of interaction (contribution of van der Waals attraction and electrical double layer repulsive forces) between two dissimilar surfaces. The attractive and repulsive forces between a sphere and flat plate are given by Equations 5.4 and 5.5, respectively, with the total potential energy of interaction given by the sum of the repulsive electrical double layer interaction ($V_R$) and the attractive London van der Waals interaction ($V_A$) ($V_T = V_A + V_R$) [48, 49].

$$V_R = 2\pi\varepsilon_r\varepsilon_0 a_p \zeta_p \zeta_c \left\{ \ln\left[\frac{1+\mathrm{e}^{-\kappa a_p H}}{1-\mathrm{e}^{-\kappa a_p H}}\right] + \frac{\left(\zeta_p^2+\zeta_c^2\right)}{2\zeta_p\zeta_c}\ln[1-\mathrm{e}^{-2\kappa a_p H}] \right\} \quad \textbf{Equation 5.4}$$

$$V_A = -\frac{A_{132}\,a_p}{6H} \quad \textbf{Equation 5.5}$$

Where $\varepsilon_r$ = permittivity of the medium ($JV^{-2}$), $\varepsilon_0$ = permittivity of free space ($JV^{-2}$), $a$ = radius (m), $\zeta$ = zeta potential (V), $\tau$ = inverse Debye length ($m^{-1}$), where $\tau^{-1} = \frac{0.304\times10^{-9}}{\sqrt{M}}$ at 25 ℃, $M$ = molar concentration of electrolyte in solution, $H$ = separation distance (m) and $A_{132}$ = $TiO_2$-water-Au Hamaker constant (= $-0.2534\times10^{-20}$ J) [50-52]. Subscripts $p$ and $c$ denotes the spherical particle and the flat plate collector, respectively.

Fig. 5.5 compares the minimum total potential energy of interaction ($V_{Tmin}$) for similar (particle-particle) and dissimilar (particle-sensor) surfaces. To better compare the two systems over the pH range ~3.6 to 9.8, a Boltzmann fit ($R^2$ 0.9774, Fig. S5.2) of the measured zeta potentials of the gold-coated sensor was made to determine zeta potential values at pH values equivalent to those measured for $TiO_2$. In the calculation

of the electrical double layer force, the particle radius was taken to be 0.3075 µm, representing the modal particle size as measured by the Zetasizer Nano ZS (S5.3).

Comparing the two interactions, $V_{Tmin}$ for anatase-anatase is significantly weaker than $V_{Tmin}$ anatase-gold when the pH is $\leq 7$. The strongest attraction between anatase-anatase is calculated at $pH_{iep}$, with the total interaction potential ~3 orders of magnitude weaker than anatase-gold at the equivalent pH. The maximum $|V_{Tmin}|$ for anatase-gold is at pH 5 and is in reasonable agreement with the AFM measurements (Fig. 5.3B) which showed the maximum attractive force between the $TiO_2$ sphere and gold-coated QCM sensor to be pH 4.5. As expected, $V_{Tmin}$ for anatase-gold diminishes when the two surfaces are both negatively charged.

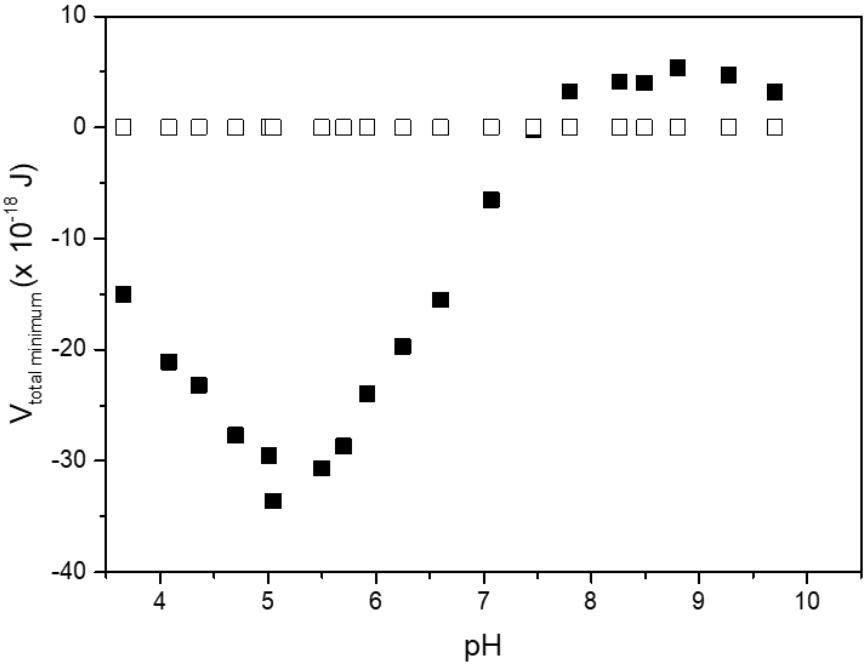


**Figure 5.5: The minimum (most attractive) total potential energy of interaction ($V_{Tmin}$) between anatase-gold (black squares) and anatase-anatase (white squares) as calculated using the HHF theory. For the electrical double layer interaction, the following parameters and values were used: $\varepsilon_r = 80.3\ \mathrm{J/V^2}$, $\varepsilon_0 = 8.854 \times 10^{-12}\ \mathrm{J/V^2}$, $a_p = 0.3075\ \mu\mathrm{m}$, $\zeta_p$ = values from Figure 5.2, $\zeta_c$ = calculated using a Boltzmann fit on data from Figure 5.2 (see Fig. S5.2), $M = 0.01$ M NaCl and $H = 0.01 - 10$ nm (the peak of strongest attraction had already occurred at 10 nm, as seen from Fig. 5.3A).**

### 5.3.3. QCM response

When studying $Mg(OH)_2$ suspensions, our previous publication showed the QCM technique to be sensitive to changes in suspension yield stress. The pH of the suspension remained constant near the isoelectric point of the suspension (zeta potential was found to be -7 $\pm$ 4 mV at pH 10.2) and the yield stress was varied by increasing the solids concentration. Using the HHF theory, the total potential energy of interaction between $Mg(OH)_2$ and the gold sensor in water is $-1547.90 \times 10^{-18}$ J, confirming a significantly stronger attraction between the QCM sensor and suspension due to a low contribution from the electrical double layer effects and a

relatively large Hamaker constant [39, 53]. In the current study, the suspension yield stress was adjusted by controlling the colloidal interaction strength between neighbouring particles (pH controlled). At the same time the interaction potential between the QCM sensor and suspension is also adjusted, with the magnitude of the QCM sensor-suspension interaction potential substantially greater than the particle-particle interaction potential (see Fig. 5.5). The influence of changing two parameters simultaneously, yield stress and QCM sensor-suspension interaction potential, has not yet been considered.

The $\Delta F$ and $\Delta \Gamma$ responses of the i-QCM when submerged in 16.2 vol% $TiO_2$ suspensions of varying pH are shown in Figs. 5.6A and B. The sensor overtones (n = 1 to 11) showed the same general trend with changing pH, with smaller overtones measuring larger values in $\Delta F$ and $\Delta \Gamma$, as expected (larger piezoelectrically active surface area) [21]. The fundamental overtone is typically prone to signal-to-noise error, which may account for the increased instability observed for $\Delta \Gamma$, n = 1 [25].

As the suspension pH was adjusted from acidic to basic conditions, both $\Delta F$ and $\Delta \Gamma$ responses fluctuated at lower pH values before becoming almost independent of the suspension pH when the pH $>$ 6.6 - 7. Starting at pH 3.7, $\Delta F$ becomes more negative, with the maximum $\Delta F$ measured at pH 4.55. $\Delta F$ gradually decreased as the pH was adjusted between pH 4.55 and pH 7.0, with the QCM response independent of the suspension pH at higher pH values. The responses of $\Delta \Gamma$ were shown to be nearly the inverse of those observed for $\Delta F$. A slight pH deviation is observed between the most negative $\Delta F$ (pH 4.55) and largest $\Delta \Gamma$ (pH 4.95), indicating that the differences observed for electrokinetic (zeta potential) and rheological (yield stress) measurements may also have an effect on the differences observed between the $\Delta F$ and $\Delta \Gamma$ response (i.e. the QCM F and $\Gamma$ behaviour may also respond to electric

potentials at two different distances from the surface in addition to other currently unknown effects).

The pH dependent ΔF and ΔΓ responses do not completely follow the changes in suspension yield stress (Fig. 5.4). Both ΔF and ΔΓ increase with increasing suspension yield stress (low pH), consistent with our previous observations [39], however the ΔF and ΔΓ values begin to reduce before the maximum yield stress is reached (pH 5.9). At higher pH values (pH 7 – 9.4) the ΔF and ΔΓ responses are independent of any changes in suspension yield stress; a 30 Pa decrease in suspension yield stress is measured for the same pH range. Poor agreement between QCM responses and suspension yield stress suggest that the resonance properties of the QCM sensor are influenced greater by additional factor(s). In the pH range 3.7 – 5.7, a significant pH dependency on the QCM ΔF and ΔΓ response is observed at all overtones. This implies that the mechanism responsible for this shift is surface specific since the penetration depth of the sensor is expected to decrease significantly with increasing overtone order, which would result in a significantly smaller pH dependency in this region [21].

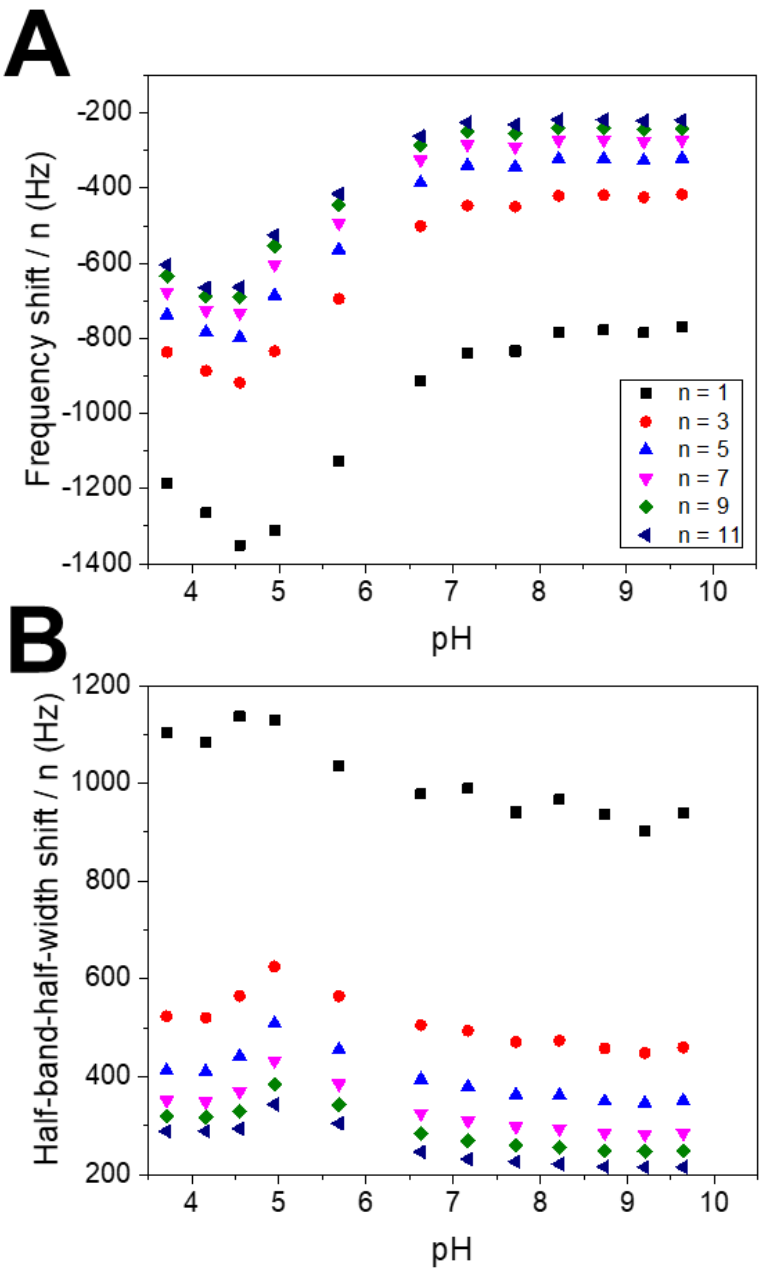


**Figure 5.6: 16.2 vol% Hombitan S141 in 10 mM NaCl i-QCM (A) ΔF and (B) ΔΓ response at overtones n = 1 – 11. At pH values above the isoelectric point of Hombitan S141 (pH 6.6), the QCM response shows an independency to the suspension pH. To confirm the robustness of the technique, measurements were performed using the QCM200 on both Hombitan and a different anatase-grade $TiO_2$ suspension. See Figs S5.3-S5.6 for more information.**

Figure 5.7A and B shows a comparison between the HHF sphere-plate model and the QCM response at the 3rd overtone. The QCM response correlates well with the model, particularly the $\Delta\Gamma$ response which shows a maximum at the most attractive theoretical interaction potential (pH ~5). A good fit between the QCM $\Delta\Gamma_{n=3}$ response and the HHF model was found ($R^2$ = 0.9193) (Fig. 5.7B) where deviations may primarily be due to variations in particle shapes/sizes (the model considers only 1 spherical particle of a given size) and surface roughness effects as well as any anisotropic surface properties that may stem from these effects. The HHF model can therefore be used as a guide to explain the QCM response for concentrated suspensions of changing pH.

At pH < 6.6, the particles are attracted to the resonator surface and will therefore adsorb (Figs. 5.3B, 5.5 and 5.7A). This results in a Sauerbrey-like response which causes the sensor to oscillate at a more negative frequency as the sensor detects more of the adsorbed particles' mass [32]. The adsorbed particles are however not an ideal Sauerbrey case in that they are not firmly linked to the sensor surface and therefore do not behave as a complete extension to the resonator's mass (i.e. a corresponding increase in $\Delta\Gamma$ is also observed, which is a measure of oscillation dampening [21, 54]). The particles will therefore still behave as discrete entities and withstand motion from the resonator. As the particle-sensor link strengthens (i.e. at pH 4.5), the stronger links will result in a greater amount of the particles' mass to be detected, increasing the contribution from the Sauerbrey effect to a greater extent [32], resulting in a larger $\Delta$F. The stronger particle-sensor links may also cause a more efficient energy transfer from the sensor to the particles where fewer links are also broken (more energy is required to break stronger links). This will result in an increase in the detected $\Delta\Gamma$ response as more energy transfer increases oscillation dampening.

At pH > 6.6 – 7.5, the particles are no longer attracted to the resonator surface (Fig. 5.3B, 5.5 and 5.7A), causing the particles to no longer form links to the gold surface. The QCM ΔF response therefore tends towards the Gordon-Kanazawa-Mason limit of -750 Hz to -830 Hz, depending on crystal roughness [22, 23, 39, 55] (Fig. 5.6 for n = 1). Particles however may still be entrained within the rough edges in the sensor surface, resulting in a slightly more negative ΔF due to Sauerbrey-like effects. Despite no significant amount of particle-sensor links being formed, the particles may remain near the surface of the resonating crystal. The resonator surface may therefore collide with nearby particles and transfer some of its kinetic energy to the particles, resulting in higher ΔΓ values compared to -ΔF in this region (-ΔF = ΔΓ for Newtonian fluids [21], however for the suspension at pH ~9.2, $-\Delta F_{n=3}/\Delta\Gamma_{n=3} = 0.95$ despite a possible larger ΔF due to particle entrainment). The reduction in ΔΓ with increasing pH beyond pH 7 (Figs. 5.6 and 5.7) suggests that as the Hombitan particles become more negative (gold negative charge remains constant) (Fig. 5.2), the particles experience an increased repulsive interaction (Fig. 5.5 and 5.7A) and are therefore more likely to remain further away from the resonator surface, reducing the amount of kinetic energy transfer as the number of collisions reduce, further reducing ΔΓ. The difference in the ΔΓ and ΔF trend observed in this pH region also indicate that ΔF is less sensitive to particle-sensor collisions that do not result in link formation.

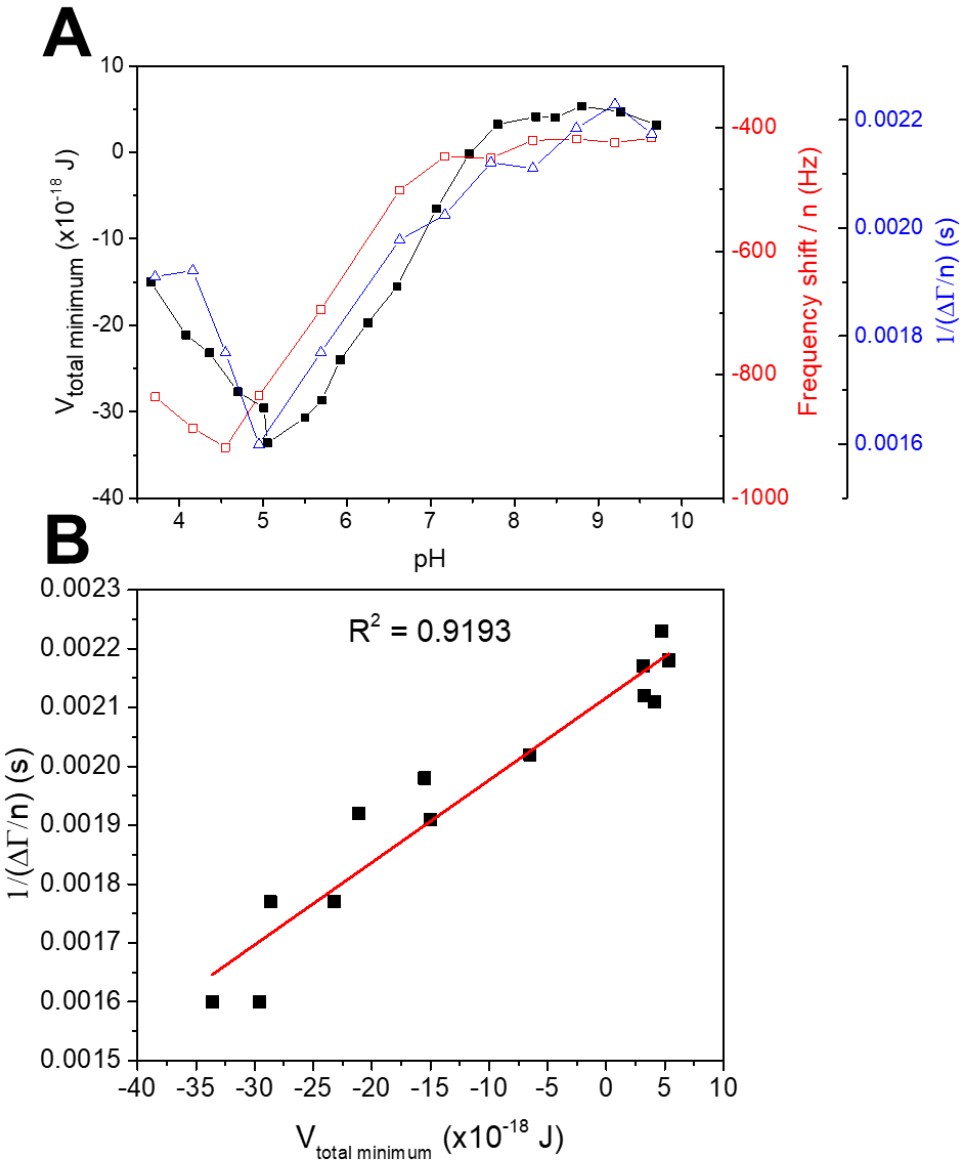


**Figure 5.7: (A) comparison between the Hogg, Healy and Fuerstenau minimum total interaction potential curve (black squares, left axis) and the iQCM ΔF (red open squares, inner right axis) and ΔΓ (blue open triangles, outer right axis) response at n = 3 for 16.2 vol% Hombitan S141 in 10 mMol/L NaCl. (B) by plotting the $1/\Delta\Gamma_{n=3}$ as a function of the minimum total interaction potential, a linear trend is observed ($R^2$ = 0.9193).**

These findings indicate that the QCM response in its MHz range is surface-specific and can therefore be used as a tool to measure the relative particle-sensor interaction forces, allowing for the charging behaviour of concentrated suspensions to be inferred.

## 5.4. Conclusions

Previous work has demonstrated that the quartz crystal microbalance (QCM) is a tool that is sensitive to changes in particle-sensor interaction strengths for dilute colloidal suspensions as well as changes in the strength of the particle-particle interactions for more concentrated sludges. To investigate the effect that changes in the particle-sensor interaction strength for concentrated sludges have on the QCM, pH tests using concentrated (16.2 vol%) $TiO_2$-based suspensions were performed. Changes in the particle-sensor interactions between $TiO_2$ and gold were measured using atomic force microscopy (AFM) and modelled using the Hogg, Healy and Fuerstenau (HHF) model and compared to changes in the QCM resonance and the bulk suspension yield stress. The QCM response was found to follow AFM data and the HHF model more closely, indicating that changes in the particle-resonator contacts play a significant role when using the QCM to measure suspension rheology. The QCM in its MHz frequency range may therefore have a sufficiently low penetration depth where the changes in particle-sensor interaction forces for a concentrated suspension dominates its response, allowing for potential deployment in systems where the charge behaviour of colloidal suspensions need to be known and understood.

## 5.5. References


1. Johnson, S.B., et al., *Surface Chemistry-Rheology Relationships in Concentrated Mineral Suspensions.* International Journal of Mineral Processing, 2000. **58**(1-4): p. 267-304.
2. Mikulášek, P., R. Wakeman, and J. Marchant, *The Influence of pH and Temperature on the Rheology and Stability of Aqueous Titanium Dioxide Dispersions.* Chemical Engineering Journal, 1997. **67**(2): p. 97-102.
3. Scales, P.J., et al., *Shear Yield Stress of Partially Flocculated Colloidal Suspensions.* AIChE Journal, 1998. **44**(3): p. 538-544.
4. Leong, Y.-K., et al., *Control of the Rheology of Concentrated Aqueous Colloidal Systems by Steric and Hydrophobic Forces.* Journal of the Chemical Society, Chemical Communications, 1993(7): p. 639-641.
5. KwongáLeong, Y., *Rheological Evidence of Adsorbate-Mediated Short-Range Steric Forces in Concentrated Dispersions.* Journal of the Chemical Society, Faraday Transactions, 1993. **89**(14): p. 2473-2478.
6. Leong, Y., *Interparticle Forces Arising From an Adsorbed Strong Polyelectrolyte in Colloidal Dispersions: Charged Patch Attraction.* Colloid and Polymer Science, 1999. **277**(4): p. 299-305.
7. Yang, H.G., et al., *Rheological Behavior of Titanium Dioxide Suspensions.* Journal of Colloid and Interface Science, 2001. **236**(1): p. 96-103.
8. Franks, G.V., et al., *Effect of Interparticle Forces on Shear Thickening of Oxide Suspensions.* Journal of Rheology, 2000. **44**(4): p. 759-779.
9. Johnson, S.B., et al., *The Binding of Monovalent Electrolyte Ions on α-Alumina. II. The Shear Yield Stress of Concentrated Suspensions.* Langmuir, 1999. **15**(8): p. 2844-2853.
10. Johnson, S.B., P.J. Scales, and T.W. Healy, *The Binding of Monovalent Electrolyte Ions on α-Alumina. I. Electroacoustic Studies at High Electrolyte Concentrations.* Langmuir, 1999. **15**(8): p. 2836-2843.
11. Derjaguin, B.V., Landau, L., *Theory of the Stability of Strongly Charged Lyophobic Sols and of the Adhesion of Strongly Charged Particles in Solutions of Electrolytes.* Acta Physicochim, 1941. **14**: p. 633-662.
12. Verwey, E.J.W., *Theory of the Stability of Lyophobic Colloids.* Journal of Physical and Colloid Chemistry, 1947. **51**(3): p. 631-636.
13. Hogg, R., T.W. Healy, and Fuersten.Dw, *Mutual Coagulation of Colloidal Dispersions.* Transactions of the Faraday Society, 1966. **62**(522P): p. 1638-&.
14. Israelachvili, J.N., *Forces between Surfaces in Liquids.* Advances in Colloid and Interface Science, 1982. **16**(Jul): p. 31-47.
15. Pashley, R., *Hydration Forces between Mica Surfaces in Aqueous Electrolyte Solutions.* Journal of Colloid and Interface Science, 1981. **80**(1): p. 153-162.
16. Biggs, S., *Steric and Bridging Forces Between Surfaces Bearing Adsorbed Polymer: an Atomic Force Microscopy Study.* Langmuir, 1995. **11**(1): p. 156-162.
17. Biggs, S., *Non-Equilibrium Interaction Forces Between Adsorbed Polymer Layers.* Journal of the Chemical Society, Faraday Transactions, 1996. **92**(15): p. 2783-2789.
18. Pashley, R., *DLVO and Hydration Forces Between Mica Surfaces in Li+, Na+, K+, and Cs+ Electrolyte Solutions: A Correlation of Double-Layer*

*and Hydration Forces with Surface Cation Exchange Properties.* Journal of Colloid and Interface Science, 1981. **83**(2): p. 531-546.

19. Chen, Q., et al., *QCM-D Study of Nanoparticle Interactions.* Adv Colloid Interface Sci, 2015.
20. Sauerbrey, G., *Verwendung Von Schwingquarzen Zur Wagung Dunner Schichten Und Zur Mikrowagung.* Zeitschrift Fur Physik, 1959. **155**(2): p. 206-222.
21. Johannsmann, D., *Viscoelastic, Mechanical, and Dielectric Measurements on Complex Samples with the Quartz Crystal Microbalance.* Physical Chemistry Chemical Physics, 2008. **10**(31): p. 4516-4534.
22. Kanazawa, K.K. and J.G. Gordon, *The Oscillation Frequency of a Quartz Resonator in Contact with a Liquid.* Analytica Chimica Acta, 1985. **175**(Sep): p. 99-105.
23. Mason, W.P. and H. Baerwald, *Piezoelectric Crystals and Their Applications to Ultrasonics.* Physics Today, 1951. **4**: p. 23.
24. Martin, S.J., V.E. Granstaff, and G.C. Frye, *Characterization of a Quartz Crystal Microbalance with Simultaneous Mass and Liquid Loading.* Analytical Chemistry, 1991. **63**(20): p. 2272-2281.
25. Johannsmann, D., *The Quartz Crystal Microbalance in Soft Matter Research*. 2014: Springer, Cham.
26. Tellechea, E., et al., *Model-Independent Analysis of QCM Data on Colloidal Particle Adsorption.* Langmuir, 2009. **25**(9): p. 5177-5184.
27. Chen, Q., et al., *Understanding Interactions Between Clay and Model Coal Surfaces in Electrolyte Solutions by a Quartz Crystal Microbalance with Dissipation Study.* Energy & Fuels, 2017. **32**(1): p. 233-240.
28. Gotoh, K., Y. Nakata, and M. Tagawa, *Evaluation of Particle Deposition in Aqueous Solutions by the Quartz Crystal Microbalance Method.* Colloids and Surfaces A: Physicochemical and Engineering Aspects, 2006. **272**(1-2): p. 117-123.
29. Lapidot, T., K.L. Sedransk Campbell, and J.Y. Heng, *Model for Interpreting Surface Crystallization Using Quartz Crystal Microbalance: Theory and Experiments.* Analytical Chemistry, 2016. **88**(9): p. 4886-4893.
30. Zhuang, H., et al., *Study of the Evaporation of Colloidal Suspension Droplets with the Quartz Crystal Microbalance.* Langmuir, 2008. **24**(15): p. 8373-8378.
31. Pham, N., et al., *Application of the Quartz Crystal Microbalance to the Evaporation of Colloidal Suspension Droplets.* Langmuir, 2004. **20**(3): p. 841-847.
32. Pomorska, A., et al., *Positive Frequency Shifts Observed Upon Adsorbing Micron-Sized Solid Objects to a Quartz Crystal Microbalance from the Liquid Phase.* Analytical Chemistry, 2010. **82**(6): p. 2237-2242.
33. Reipa, V., G. Purdum, and J. Choi, *Measurement of Nanoparticle Concentration Using Quartz Crystal Microgravimetry.* The Journal of Physical Chemistry B, 2010. **114**(49): p. 16112-16117.
34. D'Amour, J.N., et al., *Capillary Aging of the Contacts Between Glass Spheres and a Quartz Resonator Surface.* Physical Review Letters, 2006. **96**(5).
35. D'amour, J., et al., *Capillary Aging of the Contacts Between Glass Spheres and a Quartz Resonator Surface.* Physical Review Letters, 2006. **96**(5): p. 058301.

36. Vittorias, E., et al., *Studying Mechanical Microcontacts of fine Particles with the Quartz Crystal Microbalance.* Powder Technology, 2010. **203**(3): p. 489-502.
37. Dybwad, G.L., *A Sensitive New Method for the Determination of Adhesive Bonding between a Particle and a Substrate.* Journal of Applied Physics, 1985. **58**(7): p. 2789-2790.
38. Shapiro, A., P. Renaud, and R.F. Probstein, *Preliminary Studies on the Removal of Chemical-Species from Saturated Porous-Media by Electroosmosis.* Physicochemical Hydrodynamics, 1989. **11**(5-6): p. 785-802.
39. Botha, J.A., et al., *Quartz Crystal Microbalance as a Device to Measure the Yield Stress of Colloidal Suspensions.* Colloids and Surfaces A: Physicochemical and Engineering Aspects, 2018. **546**: p. 179-185.
40. Bates, S., et al., *Analysis of Amorphous and Nanocrystalline Solids from their X-ray Diffraction Patterns.* Pharmaceutical Research, 2006. **23**(10): p. 2333-2349.
41. Murakami, N., et al., *Shape-Controlled Anatase Titanium (IV) Oxide Particles Prepared by Hydrothermal Treatment of Peroxo Titanic Acid in the Presence of Polyvinyl Alcohol.* The Journal of Physical Chemistry C, 2009. **113**(8): p. 3062-3069.
42. Gustafsson, J., et al., *The Influence of pH and NaCl on the Zeta Potential and Rheology of Anatase Dispersions.* Colloids and Surfaces A: Physicochemical and Engineering Aspects, 2000. **175**(3): p. 349-359.
43. Giesbers, M., J.M. Kleijn, and M.A.C. Stuart, *The Electrical Double Layer on Gold Probed by Electrokinetic and Surface Force Measurements.* Journal of Colloid and Interface Science, 2002. **248**(1): p. 88-95.
44. Sylvestre, J.P., et al., *Surface Chemistry of Gold Nanoparticles Produced by Laser Ablation in Aqueous Media.* Journal of Physical Chemistry B, 2004. **108**(43): p. 16864-16869.
45. Barten, D., et al., *Double Layer of a Gold Electrode Probed by AFM Force Measurements.* Langmuir, 2003. **19**(4): p. 1133-1139.
46. Leong, Y.K., et al., *Effect of Particle Size on Colloidal Zirconia Rheology at the Isoelectric Point*. Journal of the American Ceramic Society, 1995. **78**(8): p. 2209-2212.
47. Kosmulski, M., J. Gustafsson, and J.B. Rosenholm, *Correlation Between the zeta Potential and Rheological Properties of Anatase Dispersions.* Journal of Colloid and Interface Science, 1999. **209**(1): p. 200-206.
48. Israelachvili, J.N., *Intermolecular and Surface Forces*. 2011: Academic Press.
49. Gu, Y., *The Electrical Double-Layer Interaction Between a Spherical Particle and a Cylinder.* Journal of Colloid and Interface Science, 2000. **231**(1): p. 199-203.
50. Gómez-Merino, A., et al., *The Hamaker Constant of Anatase Aqueous Suspensions.* Journal of Colloid and Interface Science, 2007. **316**(2): p. 451-456.
51. Kim, T., et al., *Control of Gold Nanoparticle Aggregates by Manipulation of Interparticle Interaction.* Langmuir, 2005. **21**(21): p. 9524-9528.
52. Gregory, J., *Particles in Water: Properties and Processes*. 2005: CRC Press.
53. Li, W., et al., *The Influencing Mechanisms of Sodium Hexametaphosphate on Chalcopyrite Flotation in the Presence of MgCl2 and CaCl2.* Minerals, 2018. **8**(4): p. 150.

54. Calvo, E., et al., *Quartz Crystal Impedance Studies at 10 MHz of Viscoelastic Liquids and Films.* Faraday Discussions, 1997. **107**: p. 141-157.
55. Martin, S.J., et al., *Effect of Surface Roughness on the Response of Thickness-Shear Mode Resonators in Liquids.* Analytical Chemistry, 1993. **65**(20): p. 2910-2922.

## 5.6. Supplementary Information

A Scanning electron microscope (SEM) image of the $TiO_2$ spheres used to produce the colloid AFM cantilever is shown in Figure S5.1. The image was taken using a Hitachi TM3030Plus SEM.

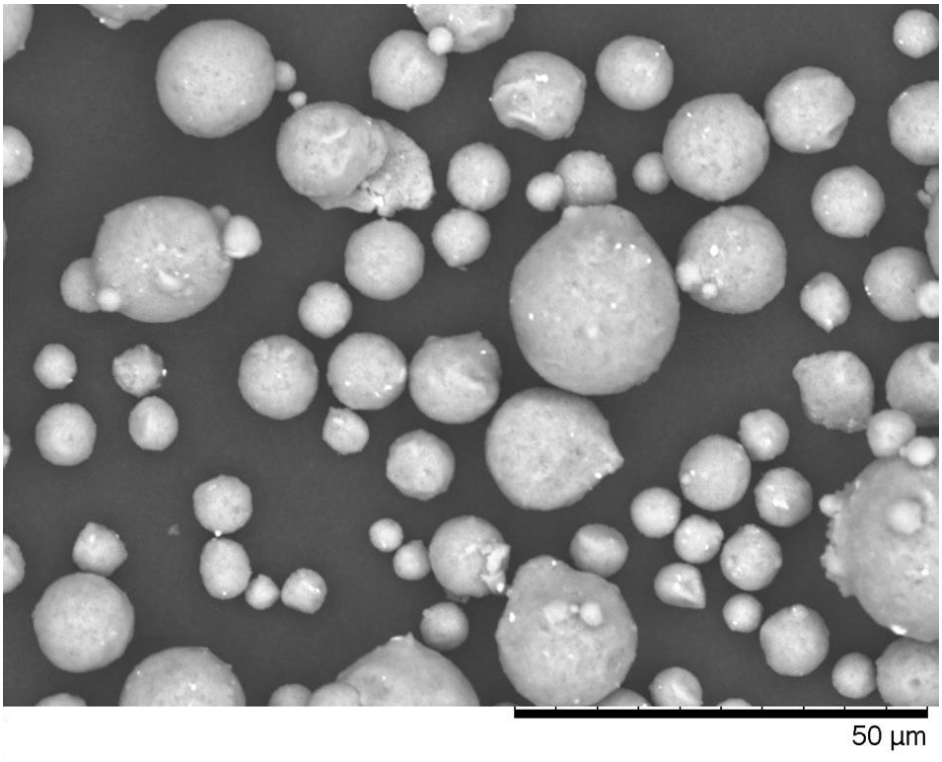


**Figure S5.1: SEM image showing the physical appearance of the $TiO_2$ spheres used to produce the colloid AFM probe.**

A Boltzmann fit of the gold surface zeta potential was made to allow for both gold and Hombitan S141 zeta potential values can be obtained at the same pH.

$$y = -50.58272 + (-0.28223 + 50.58272)/\left(1 + e^{((x-4.69721)/1.01129)}\right)$$

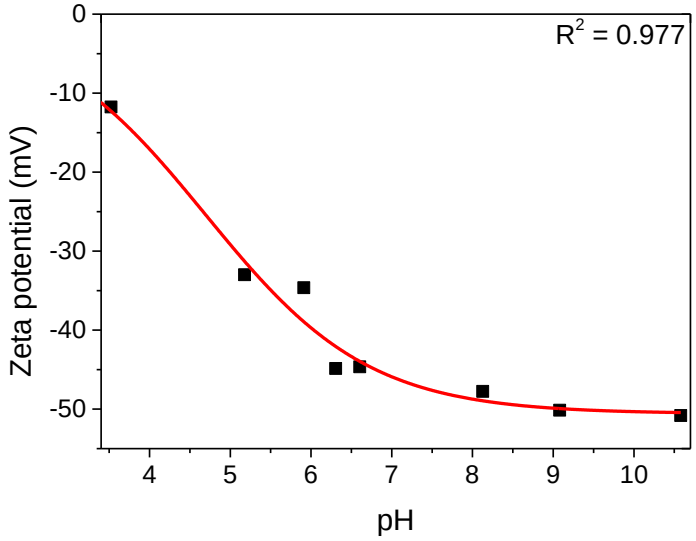


**Figure S5.2: Boltzmann fit of the gold-coated QCM resonator surface seta potential data.**

A particle size of 0.615 µm was used when modelling the interaction behaviour between anatase and gold using the Hogg, Healy and Fuerstenau relationship. 0.615 µm represented the maximum volume % in the suspension, see Fig. S5.3.

The pH dependent response of additional anatase-grade $TiO_2$ suspensions at 16.2 vol% were tested using the QCM200 to test the robustness of the technique. ANX-Type N titanium dioxide (Huntsman, UK) was compared with Hombitan S141 to investigate if a similar pH dependence is observed. ANX type-N composed of particles of a larger size distribution than Hombitan S141 (Fig. S5.3).

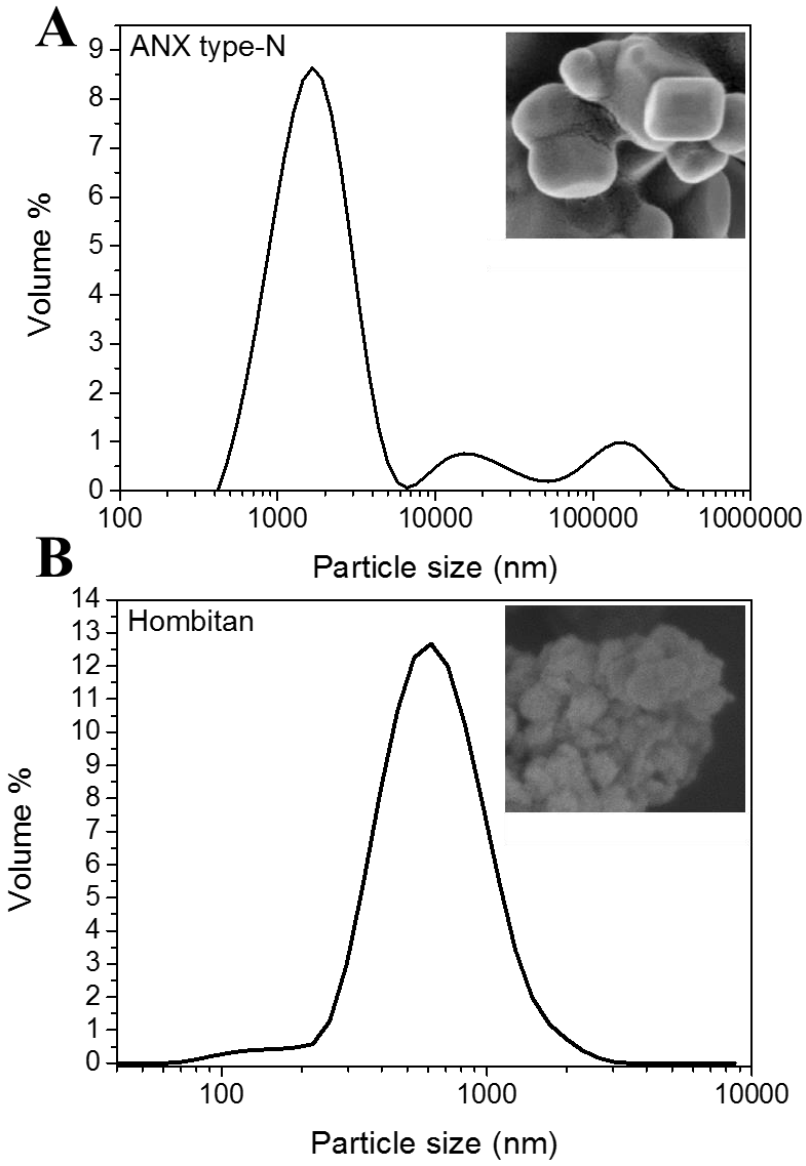


**Figure S5.3: Comparison between the physical appearance and particle size distribution of (A) ANX type-N and (B) Hombitan S141. Image horizontal width = 500 nm.**

Both ANX type-N and Hombitan S141 were synthesised using similar methods, resulting in a high surface area to volume ratio anatase mixed with amorphous titanium hydroxides to be formed (see Results and Discussion section for more information). Figure S5.4 shows a comparison between the XRD spectra for both ANX type-N and Hombiotan S141 showing significant peak broadening for both samples.

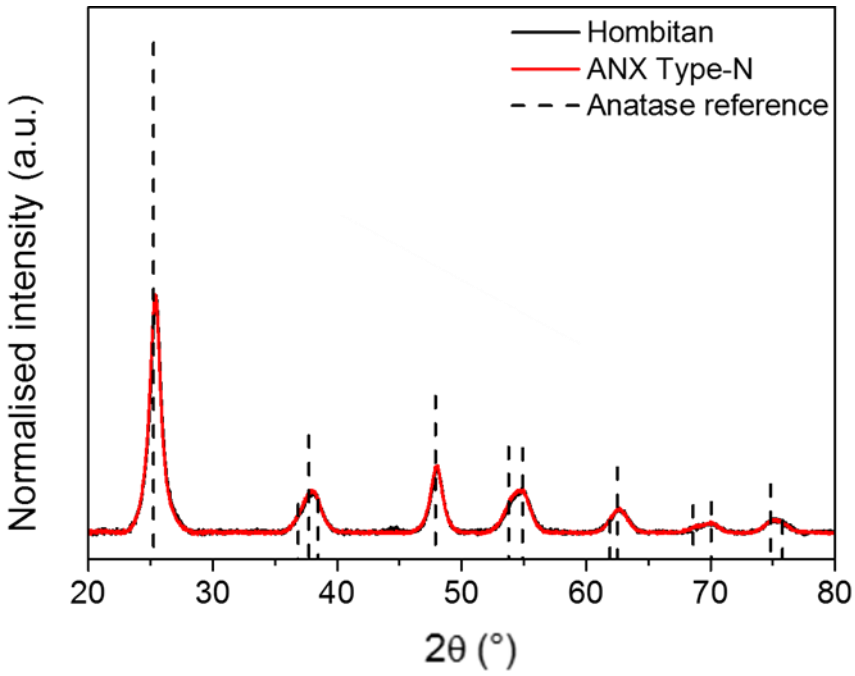


**Figure S5.4: Comparison between the X-ray diffraction patterns for Hombitan S141 (solid black) and ANX type-N (solid red). A comparison to an anatase reference taken from the American Mineralologist Crystal Structure Database Record (RRUFF: R060277.9) (vertical dashed black line) shows that both samples exhibit a significant amount of peak broadening possibly due to the presence of amorphous Ti-hydroxides.**

Due to the similar processes used in synthesising both samples, the charging behaviour of both Hombitan S141 and ANX-type N are expected to be similar. Figure S5.5 shows that ANX type-N exhibits a similar charging behaviour to Hombitan S141 with varying pH, however ANX type-N experiences a greater change in its zeta potential with pH, possibly due to the relatively larger anatase crystallites present within the sample (Fig. S5.3) that will contribute to the overall charge of the particles.

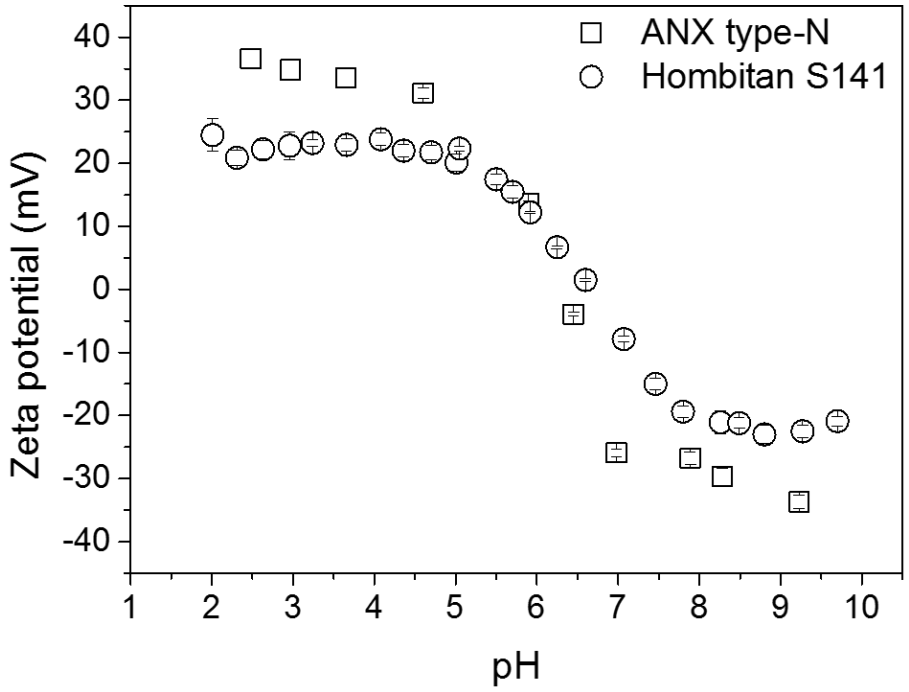


**Figure S5.5: Zeta potentials of Hombitan S141 (circles) and ANX type-N (squares) with pH in 10 mMol/L NaCl electrolyte.**

QCM pH tests were performed on both samples at 16.2 vol% in 10 mMol/L NaCl (Fig. S5.6). A QCM200 was used instead. A similar trend was observed for both samples, with ANX type N showing larger ΔF and ΔR shifts, possibly due to the greater charge dependency ANX type-N has with changing pH (Fig. S5.5). The response for both samples compare well with the iQCM data in Figure 5.6. Interestingly, a larger ΔF response is observed for the QCM200 data. When the iQCM suddenly changes its frequency of oscillation when it measures samples at different overtones, a disturbance in the nearby suspension network may occur, breaking the network down, causing the QCM to detect less of the overlaying suspension (Chapter 6 investigates this effect in greater detail).

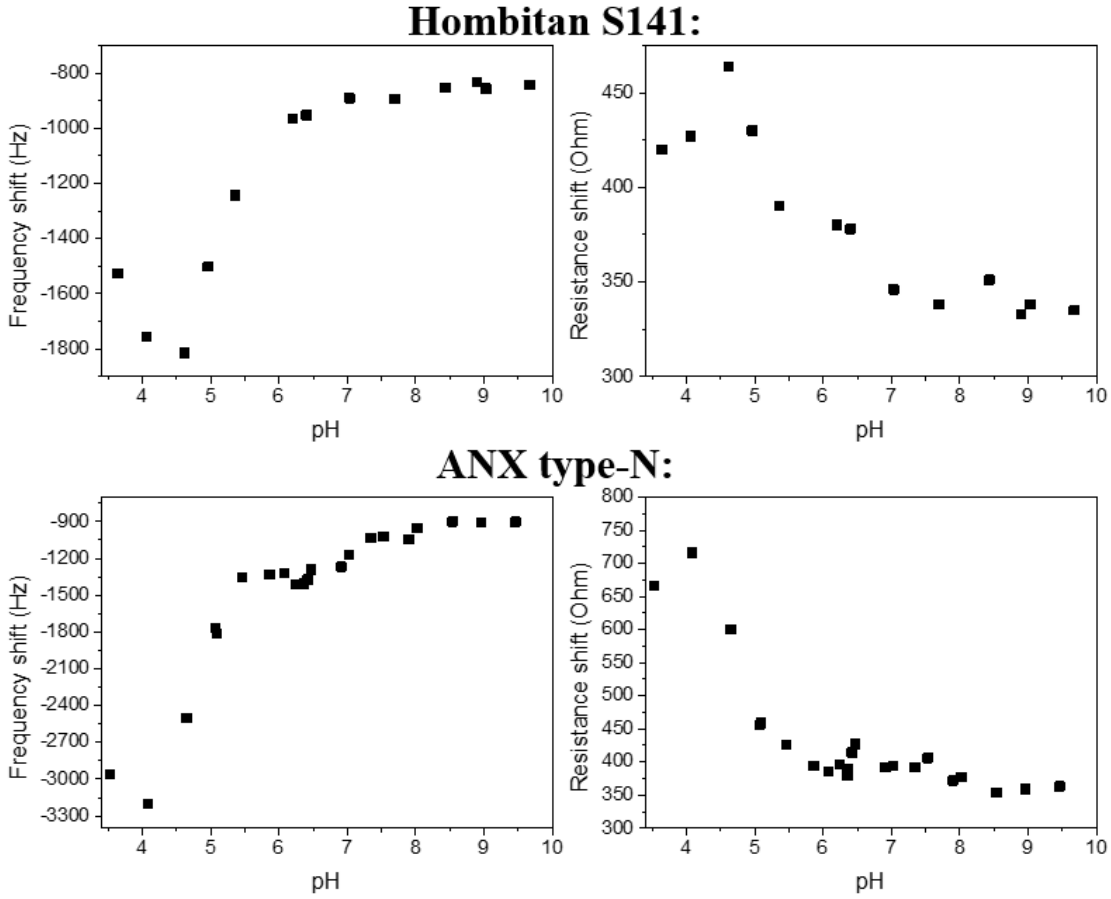


**Figure S5.6: QCM200 pH ΔF and ΔR data for 16.2 vol% Hombitan S141 (top) and 16.2 vol% ANX type-N (bottom) in 10 mMol/L NaCl.**

# 6. Measuring the Viscoelasticity of Concentrated Particulate Suspensions using Quartz Crystal Microbalance

The application of quartz crystal microbalance (QCM) to measure the viscoelastic properties of concentrated (> 10 vol%) ZnO suspensions has been considered. The viscoelasticity and bulk shear yield stress of ZnO at varying solids concentrations were firstly measured using a conventional rheometer (rotational and oscillatory rheology). The QCM air-to-sample frequency and half-band-half-width shifts ($\Delta F$ and $\Delta\Gamma$, respectively) were influenced by changes in the solids concentration, with the point contact load model first considered to describe the changes in resonance properties. However, the resonance properties at different overtones revealed a dependency that could not be described via the point contact model alone, but rather showed a response more representative of a viscoelastic model. By fitting the QCM data, the high frequency storage modulus (G') and loss modulus (G'') of the suspensions were determined using acoustic multilayer formalism. This data was then compared to the data obtained using rotational/oscillatory rheology. The calculated G' values (QCM) directly correlated to the elastic modulus measured by oscillatory rheology (frequency range 0.16 - 16 Hz), while the $\Delta\Gamma$ response correlated to the bulk shear yield stress, demonstrating the capability of the QCM to measure bulk rheological properties of concentrated suspensions. The relatively high G'' and low G' measured by QCM could be due to suspension network disturbance when the sensor changes its oscillation frequency and an inefficient transfer of vibrational energy from the resonator to the adsorbed particles, which has been confirmed by measuring the QCM response with changes in oscillation amplitude. In summary, the QCM can be used to measure the viscoelastic properties of concentrated particle suspensions, with the resonance properties interpreted using both the point contact load model and viscoelastic model.

## 6.1. Introduction

### 6.1.1. Point contact loads

The quartz crystal microbalance (QCM) has been used to measure colloidal particles in aqueous media, probing the physical and chemical characteristics of the system. Chowdhury et al. [1], Krozer et al. [2], Mihut et al. [3] and Chen et al. [4] for example have all studied the deposition behaviour of colloidal particles onto QCM sensors. These studies have shown that the changes in QCM resonance properties during particle deposition can be compared to the classic Derjaguin, Landau, Verwey and Overbeek (DLVO) theory [5-7] which describes the colloidal interaction potential acting between two surfaces. In those studies mentioned, colloidal particles included graphene oxide [1], silica [2], soft colloids onto biomembranes [3], and kaolinite particles (particles which exhibit anisotropic surface properties) [4]. In addition to monitoring particle deposition, QCMs have also be used to dynamically study the evaporation process of particle-laden droplets [8-11]. Reipa et al. [9] performed evaporation studies on the QCM resonator surface using methanol droplets containing colloidal Ag and Si nanoparticles ($\leq$ 20 nm). Figure 6.1 shows the QCM frequency response obtained.

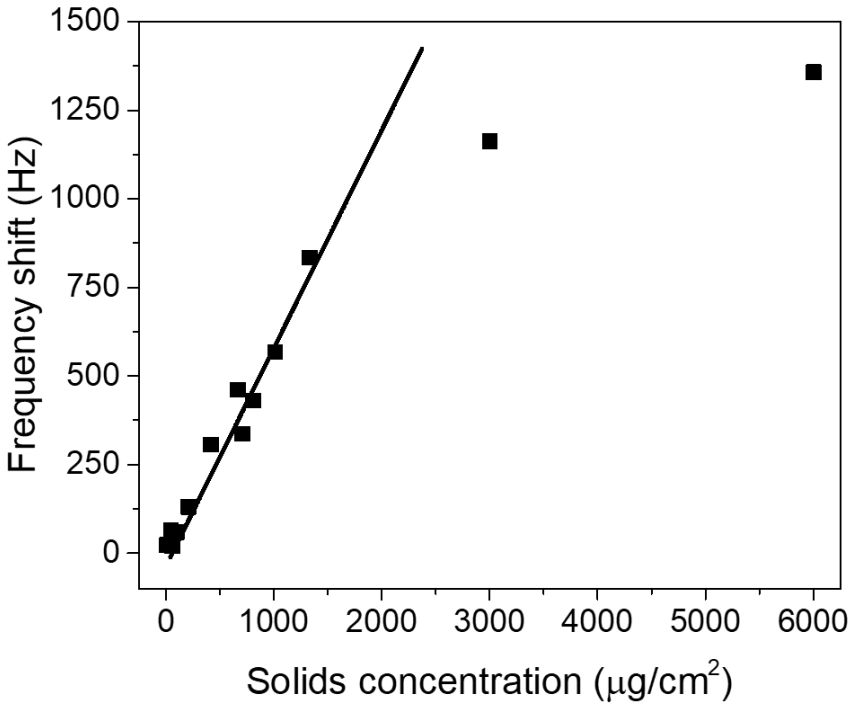


**Figure 6.1: QCM frequency response obtained when 20 µL methanol droplets containing Ag and Si nanoparticles (≤ 20 nm) have been evaporated from the resonator surface. The solid line represents a Sauerbrey frequency response estimate. Error bars have been omitted from the adapted data. Adapted from Reipa et al. [9].**

Reipa et al. discussed the contact mechanics of their particles after evaporation in terms of the Sauerbrey relationship [9]. The Sauerbrey relationship, shown in Equation 6.1, relates the QCM air-to-sample frequency shift to the added mass loading on the sensor, allowing for an average mass over the piezoelectrically active area of the resonator to be calculated [12].

$$\Delta f = -2\Delta m n f_0^2 / \left(A\sqrt{\mu_q \rho_q}\right) \qquad \textbf{Equation 6.1}$$

Where $\Delta f$ = change in frequency of oscillation (Hz), $\Delta m$ = area-averaged change in mass of the system (typically quoted as ng/cm$^2$), $n$ = overtone order (related to the initial frequency of operation), $f_0$ = fundamental mode oscillation frequency (Hz), $A$ = piezoelectrically active area of contact on the resonator surface (= 30 mm$^2$ for 5

MHz AT-cut quartz), $\mu_q$ = shear modulus of quartz ($29 \times 10^9$ Pa) and $\rho_q$ = density of quartz (2.65 g/cm$^3$).

The Sauerbrey model assumes that the added mass is rigid, small and evenly distributed, resulting in no dampening effect on the oscillating surface [12]. When an increase in sensor dampening is detected (i.e. an increase in the measured sensor impedance curve half-band-half-width response ($\Delta\Gamma$) [13], then the Sauerbrey model is no longer valid and more complex particle-sensor contact models are required.

Reipa et al. [9] found that at sufficiently low initial particle concentrations, the QCM response closely follows the Sauerbrey relationship (Fig. 6.1), however at initial concentrations of > 3000 µg/cm$^2$ the QCM response no longer follows the model where smaller $\Delta F$ values were obtained experimentally [9]. They argued that at low particle concentrations, a single layer of particles is present on the resonator surface, allowing for them to be tightly bound to the resonator surface and act as an extension of the sensor's mass [9]. At concentrations above the critical limit of ~ 3000 µg/cm$^2$, additional layers of particles begin to form [9]. The particles are therefore no longer tightly bound to the resonator surface, causing their own inertia to affect the QCM response, resulting in deviations from the Sauerbrey relationship [9]. Tellechea et al. [14] found similar behaviour where more loosely bound particles in solution would deviate from the Sauerbrey prediction in which case large $\Delta\Gamma$ responses are also observed (Fig. 6.2), further showing that loosely bound particles will exert inertial forces on the resonator surface which creates increased resistance to motion and reduces the amount of adsorbed mass the QCM detects (Fig. 6.2) [14]. The colloids investigated by Tellechea et al. are soft colloids which adsorb more strongly to the sensor surface over time [14]. They found that the ratio ($\Delta\Gamma$/-$\Delta$F) decreases over time as the particles adsorb more firmly onto the resonator surface (i.e. the contribution $\Delta\Gamma$

has on the overall response become less over time) [14]. They discovered that if you extrapolate the data back to where there is zero contribution from ΔΓ, the adsorbed particle size can be determined by calculating the change in mass on the resonator using the extrapolated -ΔF/n value via the Sauerbrey relationship (Equation 6.1) and dividing this mass by the density of the adsorbed particles [14].

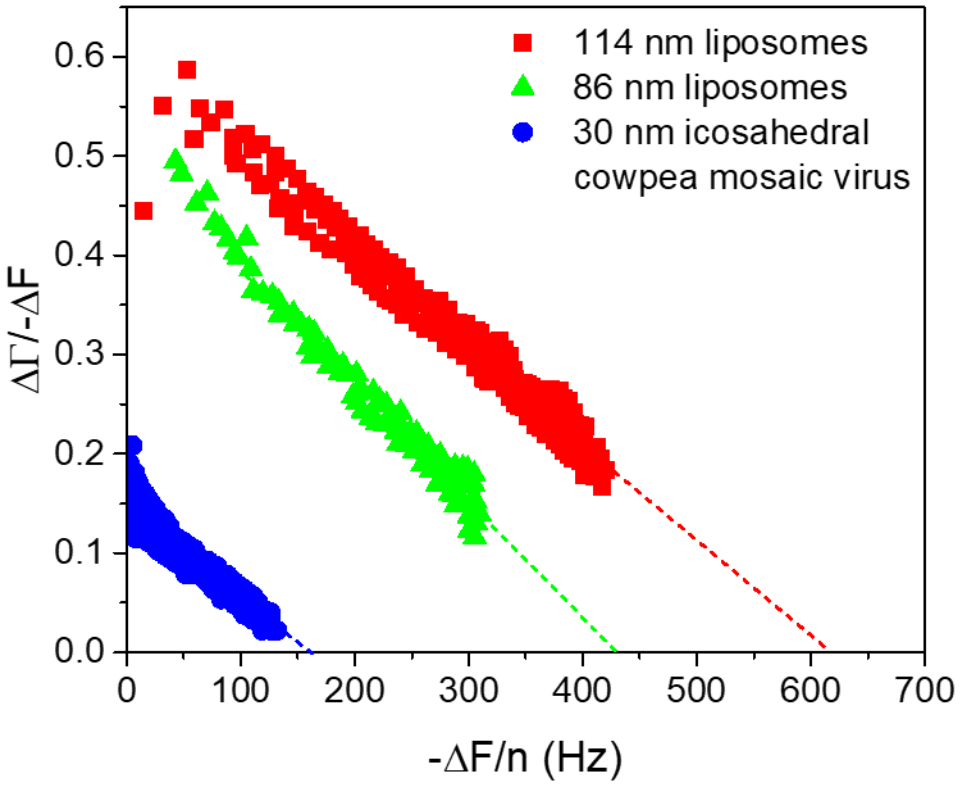


**Figure 6.2: Dependence the ratio ΔΓ/-ΔF have on soft colloids of different sizes that adsorb more firmly onto the resonator surface over time. The data can be extrapolated to zero contribution from ΔΓ where the Sauerbrey model can then be used to infer the physical properties of the adsorbed particles. Adapted from Tellechea et al. [14].**

Tellechea et al. and other authors [15-17] prefer to refer to the deposited particles as point contact loads rather than simply a tightly bound film. Point contact loads are non-uniform loads acting on the sensor surface, therefore accounting for the inhomogeneity resulting from particles depositing onto a QCM resonator surface [15-17].

If an external object such as a particle (sphere) contacts the QCM sensor, the area of contact would be significantly smaller than the particle diameter and the wavelength of sound [16, 18] (Fig. 6.3). When these conditions are met, the stiffness of the particle-sensor contact can be inferred from the QCM frequency response [16, 17, 19]. A stiffer contact would allow for a greater amount of the vibrational energy from the resonator to transfer across the particle-sensor link (Fig. 6.3). This contact stiffness has been shown to correlate with the colloidal interaction strength as described by DLVO theory [8, 11, 14, 20, 21], enabling authors to determine the surface charge of the deposited particles (see Chapter 5).

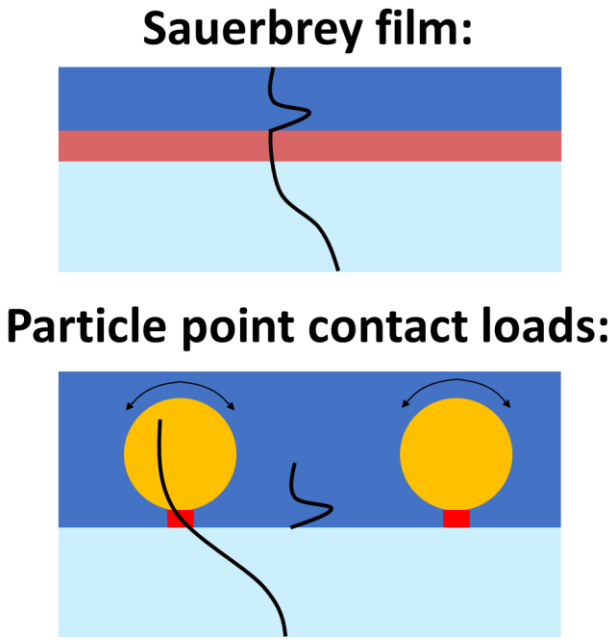


**Figure 6.3: Schematic showing the difference in nature between a Sauerbrey film and a point contact load on the resonator surface. The Sauerbrey film (top, dark red) acts as an extension of the resonating crystal's (light blue) thickness. A reduction in oscillation frequency occurs since the standing shear wave (black lines) now travels through the sensor and the adsorbed layer as if it is one medium. When particles (orange) are linked (bottom, bright red) to the resonator surface, the standing shear wave may travel through this link to the particles. The stiffness of the particle-sensor link can therefore be correlated to the QCM response. A significant portion of the dissipation (energy loss) occurs at the particle-liquid boundary. Particle motion could also exert external forces on the resonator, affecting the QCM response. Adapted from Reviakine et al. [13].**

Particles which form point contacts on the resonator surface are discrete entities and do not form an extension of the resonator's mass (Fig. 6.3). The particle will therefore have its own natural frequency of vibration which depends on the particle size [15, 17]. As such, the coupled-resonance model (Equation 6.2) can be used to describe the deposition of point contact loads on a QCM sensor [15, 17, 22]

$$\frac{\Delta f^*}{f_F} \approx \frac{-N_S m_S \omega}{\pi Z_q} \frac{1}{1 - \frac{\omega^2}{\omega_S^2}} \qquad \textbf{Equation 6.2}$$

where $\Delta f^*$ is the complex resonance frequency shift ($\Delta f^* = \Delta f + \mathrm{i}\Delta\Gamma$), $\Delta f$ is the air-to-sample resonance frequency shift (Hz), $\Delta\Gamma$ the air-to-sample electrical impedance curve half-band-half-width shift (a measure of the dissipative processes of the resonating sensor) (Hz), $f_F$ the fundamental mode frequency (Hz), $m_S$ the mass of the sphere (particle) (typically ng), $N_S$ the number of spheres (particles), $Z_q$ the acoustic wave impedance of AT-cut quartz ($8.8 \times 10^6$ kg m$^{-2}$ s$^{-1}$), $\omega$ the angular frequency of the sensor (rad) and $\omega_S$ the angular frequency of the sphere (particle) (rad).

Changing the size of the particle will change the ratio between its own angular frequency of vibration ($\omega_S$) and the angular frequency of vibration of the sensor ($\omega$) [15, 17, 22]. Two cases can therefore exist: i) inertial loading and ii) elastic loading.

If $\omega \ll \omega_s$

$$\frac{\Delta f + \mathrm{i}\Delta\Gamma}{f_F} \approx \frac{-2\omega N_S m_S}{Z_q} \qquad \textbf{Equation 6.3}$$

Equation 6.3 describes inertial loading and is numerically the same as the Sauerbrey result where $N_S m_S = \frac{\text{particle mass}}{\text{sensor active area}}$ [12, 17]. If the particles are sufficiently small to have a high frequency of vibration and are not clamped by inertia (i.e. they oscillate

in phase with the resonator), an increase in adsorbed mass and/or number of particles will result in a more negative $\Delta f$ response.

However, adsorbed particles may not form links that cause the particles to be bound firmly to the resonator surface (Fig. 6.3). As such, an inefficient transfer of vibrational energy from the resonator to the adsorbed particles is likely to influence F and Γ. Vittorias et al. [23] has shown that particles adsorbed to a vibrating QCM sensor can cause a particle motion that is governed by a balance between inertial and contact forces [23] (Fig. 6.3). Johannsmann et al. [24] termed these two modes 'rocking' and 'slipping' [24]. In the slipping mode, the sphere rotates about its centre, causing a tangential force to be exerted onto the resonator surface at the point of contact [24]. During rocking, the adsorbed sphere will rotate about its point of contact instead, exerting a torque on the QCM sensor [24]. The axis of rotation during both rocking and slipping was found to be slightly displaced from their ideal positions in liquid environments, meaning that during slipping some of the tangential force may also cause small amounts of torque on the resonator [24]. A common way to interpret the particle contact is to change the QCM amplitude of oscillation and to monitor the resulting F and Γ response (Fig. 6.4), potentially exciting the particle through different regimes of partial slip, gross slip, rocking or coulomb friction effects, which allows particle contacts to be discerned from other forms of contact such as viscoelastic behaviour or simple behaviour as a Hookean spring (i.e. a Sauerbrey film) (Fig. 6.4) [23-25].

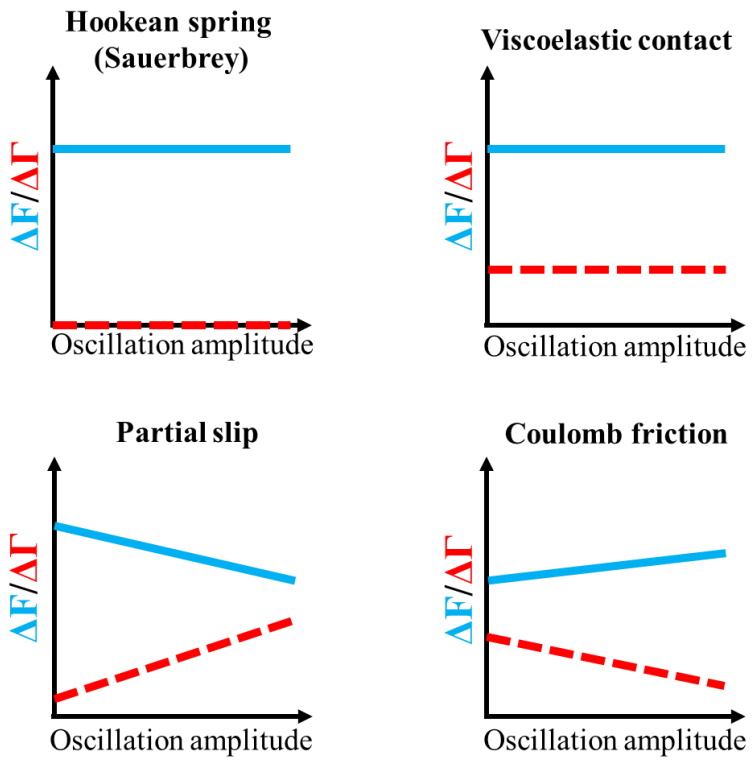


**Figure 6.4: Expected QCM frequency shift (ΔF, solid blue line) and half-band-half-width shift (ΔΓ, dashed red line) with changing oscillation amplitude. Sauerbrey films and viscoelastic media do not show any dependence on oscillation amplitude. Adapted from Vittorias et al. [23].**

A strong particle-sensor link can result in more of the particle's mass being in phase with the sensor oscillation, thus a larger $-\Delta f$ response is measured, which based on Equations 6.1 and 6.3 equates to more added mass [12, 15, 17, 26]. Chapter 5 showed that this relationship holds true even for concentrated particle suspensions, where a direct comparison between the QCM response and the DLVO theory has been made.

From Equation 6.2, if $\omega \gg \omega_S$

$$\frac{\Delta f + i\Delta\Gamma}{f_F} \approx \frac{1}{\pi Z_q}\frac{N_S \kappa_S}{\omega} \qquad \textbf{Equation 6.4}$$

The condition $\omega \gg \omega_S$ (Equation 6.4) is reached when particles become sufficiently large (i.e. > ~1 μm) that the particles' frequency of vibration is reduced and the particles do not move with the oscillating resonator, i.e. they are clamped by inertia

[15, 17, 22]. This mode of contact is termed elastic loading. The oscillating sensor no longer measures sphere mass, but the strength of the particle-sensor interaction [12, 15, 17]. Our earlier results have shown that if the links between neighbouring particles in concentrated particle suspensions become strengthened via precipitation reactions, the particles detected by the QCM are essentially "clamped" in place, hence a large $+\Delta f$ response is observed [27] (Chapter 4).

### 6.1.2. QCM viscoelasticity

Palmqvist et al. [28] considered a different approach when describing the adsorption behaviour of materials. The authors compared QCM resonance shifts to the viscoelastic properties of adsorbed polymers [28]. The mass adsorbed onto the QCM resonator surface was calculated using both the Sauerbrey relationship (Equation 6.1) and the viscoelastic Voigt model [28, 29]. By comparing the calculated adsorbed masses using these two models, the relative stiffness of the particle layer can be inferred (i.e. if the Voigt mass is close to the Sauerbrey mass, then the particles can be considered to be firmly attached and stiff) [28]. Short chain polymers (stiffer particles) showed an adsorbed mass that are more comparable to the Sauerbrey case (i.e. a short chain comb copolymer investigated showed a $\frac{m_{Sauerbrey}}{m_{Voigt}}$ ratio of ~0.88, whereas that for a long chain comb copolymer was found to be ~0.77) indicating that particle viscoelasticity affects the relative QCM response [28]. Palmqvist et al. [28] obtained the QCM dissipation shift (ΔD) vs. frequency shift (ΔF) response for the long chain comb copolymer (Fig. 6.5B) and found that the QCM response correlates with changes in the material viscoelasticity measured using conventional oscillatory rheometry (Fig. 6.5A) [28]. A reduction in the gradient, $\frac{\Delta D}{-\Delta F}$, indicates that there is a reduction in the amount of viscous dampening taking place as the particles adsorb onto the QCM resonator surface (Fig. 6.5), indicating that the polymers behave more

elastically which correlates to the measured increase in the polymer storage modulus (G') using conventional rotary rheometry.

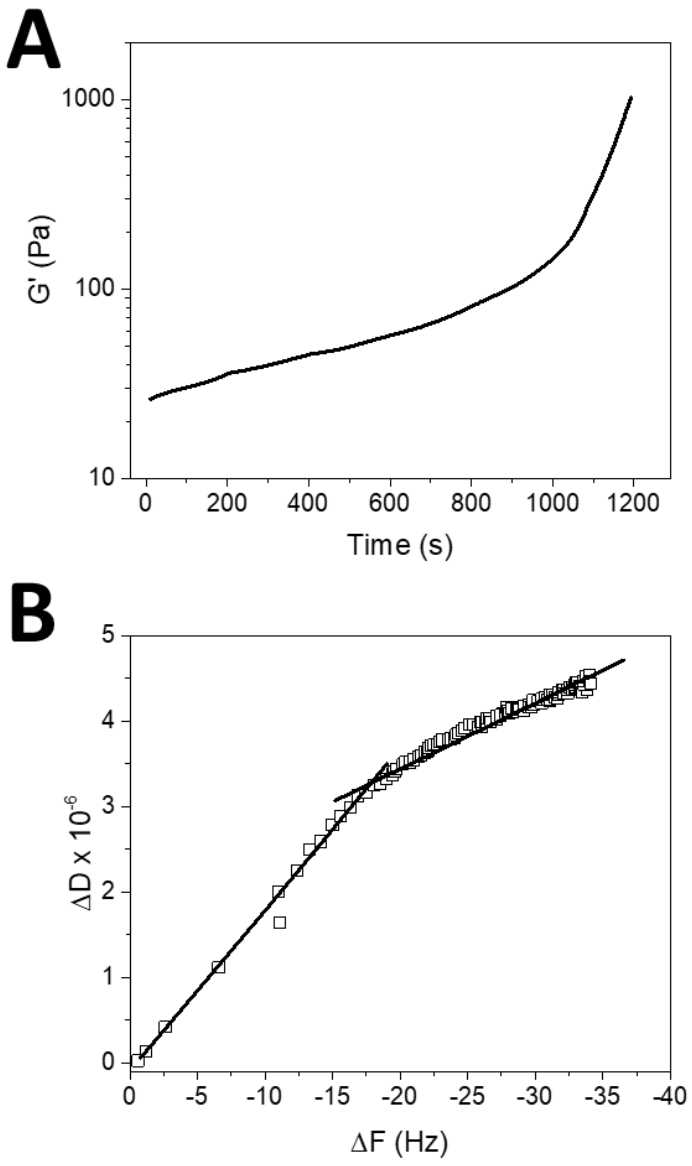


**Figure 6.5: (A) increase in the storage modulus (G') of a long chain comb copolymer during *in-situ* slip casting. (B) the QCM dissipation shift (ΔD, proportional to ΔΓ) vs. frequency shift (ΔF) response correlates with viscoelasticity changes in that the increase in sensor dissipation with frequency reduces after the initial stages of adsorption, indicating that the material behaves more elastically (i.e. increased G') as less energy is lost due to viscous dampening. Experimental time frame = 1200 s. Adapted from Palmqvist et al. [28].**

Previous work has shown that concentrated particle suspensions follow a QCM response that can be explained using the point contact load model. For example, positive air-to-sample ΔF values were obtained as the suspension networked stiffened, matching the conditions for elastic loading behaviour to occur (Equation 6.4) [27]. The QCM resistance shift (ΔR, proportional to ΔΓ) however showed good correlation to changes in the bulk suspension yield stress [27], indicating that the QCM response may be sensitive to the behaviour of the suspended particle network structure if the particles are strongly linked to the QCM resonator surface.

To investigate if the QCM response is sensitive to the stiffness of the bulk suspension network, the QCM response will be compared to the viscoelasticity of the network at different suspension solids concentrations (i.e. changing viscoelastic behaviour). Viscoelastic parameters can be obtained from QCM data by using viscoelastic models such as the Voigt model used by Palmqvist et al. [28]. The Voigt model [29] considers the QCM response in terms of ΔF and ΔD, however the parameter used to measure dampening for this study is the ΔΓ response, simply because both ΔΓ and ΔF share the same units (Hz) and can therefore be compared more easily. Johannsmann et al. [16] proposed a QCM viscoelastic model that is numerically equivalent to the Voigt model [16, 18, 29], and uses ΔΓ as the parameter for oscillation dampening [16]. For this reason, the viscoelastic model derived by Johannsmann et al. [16] will be used for this study, and compared with the measured viscoelasticity of the suspension at low frequencies measured using conventional rheometry.

For a viscoelastic film in a liquid environment, the QCM response can be correlated to the physical properties of the overlaying medium according to the relationship in Equation 6.5 [16]

$$\frac{\Delta f^*}{f_F} = \frac{-Z_\mathrm{f}}{\pi Z_q} \frac{\tan(k_\mathrm{f} d_\mathrm{f}) - \mathrm{i}Z_\mathrm{liq}}{Z_\mathrm{f} + \mathrm{i}Z_\mathrm{liq} \tan(k_\mathrm{f} d_\mathrm{f})} \qquad \textbf{Equation 6.5}$$

where $Z_\mathrm{f}$ is the acoustic impedance of the film (kg.m$^{-2}$s$^{-1}$), $k_\mathrm{f}$ the wave vector, $d_\mathrm{f}$ the film thickness (nm) and $Z_\mathrm{liq}$ the acoustic impedance of the liquid (kg.m$^{-2}$s$^{-1}$).

For sufficiently thin films, Equation 6.5 can be Taylor expanded to the first order in $d_\mathrm{f}$, which yields [16]

$$\frac{\Delta f^*}{f_F} \approx \frac{-\omega m_f}{\pi Z_q} \left(1 - \frac{Z_{liq}^2}{Z_f^2}\right) \qquad \textbf{Equation 6.6}$$

where $m_f$ = mass of the overlaying film (ng). Equation 6.6 is essentially the Sauerbrey relationship shown in Equation 6.1, but with an added scaling factor in brackets to account for the viscoelasticity of the film [16].

For the functions $\rho(z)$ (density), $G'(z)$ (storage modulus) and $G''(z)$ (loss modulus), the displacement (amplitude), $\hat{\mu}(z)$ ($z$ = distance) can be calculated, and the stress-velocity ratio $\left(\frac{\widehat{\sigma_S}}{\widehat{v_S}}\right)$ at $\hat{u}(z=0)$ and $\frac{d\hat{u}}{dz}(z=0)$ can be inferred by approximating the viscoelastic profiles as several thin layers and using advanced mathematical software packages (Fig. 6.6) [16].

The load impedance, $Z_L$, can be calculated for a displacement at the surface of the sensor, i.e. when $\hat{u}(z=0)$ [16]:

$$Z_L = \frac{\widehat{\sigma_S}}{\widehat{v_S}} = \frac{-\tilde{G} \frac{d}{dz} \hat{u}(z)\Big|_{z=0}}{\mathrm{i}\omega \hat{u}(z)|_{z=0}} \qquad \textbf{Equation 6.7}$$

where $\tilde{G}$ is the film shear modulus ($\tilde{G} = G' + \mathrm{i}G''$), $G'$ the storage modulus and $G''$ the loss modulus. $Z_L$ is the acoustic impedance of the film evaluated at the resonator surface ($z=0$) ($Z_f$ at $z=0$ is equivalent to $Z_L$). $\hat{u}(z)$ is the solution to the wave equation, which is [16, 18]

$$-\rho(z)\omega^2\hat{u}(z) = \frac{d\hat{\sigma}}{dz} = \frac{d}{dz}\left(\tilde{G}(z)\frac{d\hat{u}(z)}{dz}\right). \qquad \textbf{Equation 6.8}$$

The initial condition, $\hat{u}_\infty$, and its derivative, $\left.\frac{d\hat{u}}{dz}\right|_{z=\infty}$, occurs at distance $z$ outside the region of interest (i.e. well beyond the zone that the QCM penetrates) (Fig. 6.6) [16, 18]. The integration then occurs from this point down to $z = 0$. The derivative at $z = \infty$ is inferred from the viscosity of the bulk solution where it is homogenous, and $\hat{u}_\infty$ can be chosen arbitrarily since it cancels out in the calculation of $Z_L$ [16, 18].

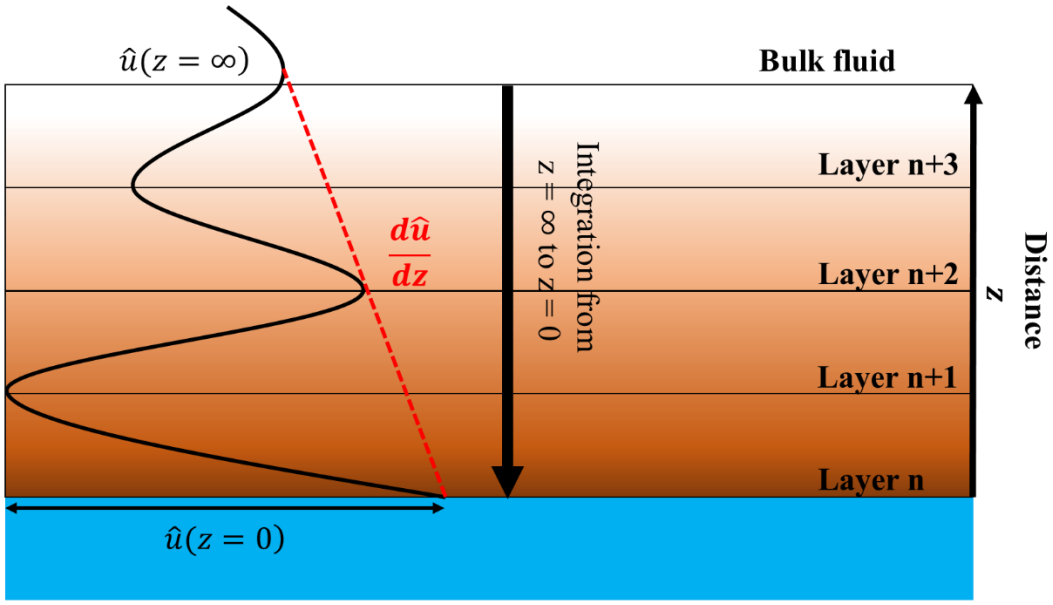


**Figure 6.6: Schematic showing a description of how $Z_L$ on the resonator can be calculated using acoustic multilayer formalism. $\hat{u}(z)$ is firstly calculated via Equation 6.8 for each thin layer, starting where the layer properties are the same as the bulk fluid ($z = \infty$) until $z = 0$ is reached. The obtained value of $\hat{u}(z = 0)$ can then be used to calculate $\tilde{G}$ and hence $Z_L$ (Equation 6.7), allowing for Equation 6.6 to be used to calculate the layer thickness if the film density is known and hence the QCM response.**

By performing the steps described in Equations 6.6 to 6.8, G' and G'' can be calculated at a reference frequency ($f_{ref}$ or $f_F$ in Equation 6.6) [16, 18]. Other authors have shown that a material's viscoelastic behaviour follows broad changes over several orders of magnitude in experimental frequency [30]. We can therefore assume

that the QCM, which operates across slightly over a single magnitude in frequency (5 – 55 MHz), the G' and G'' response can be fitted as a power law of the form $y = mx^c$, where $y =$ G' or G'', $m = G'_{\omega_{ref}}$ or $G''_{\omega_{ref}}$, $x = \frac{f}{f_{ref}}$ and $c$ is the fitting parameter, ranging between $0 < c < 2$ for G' and $-1 < c < 1$ for G'' [16, 18]. The viscoelastic properties of a material can now be determined at any frequency excited by the QCM.

By comparing the QCM viscoelasticity data for high solids concentration zinc oxide (ZnO) suspensions to that measured using conventional rheometry, the relative contributions of the QCM viscoelastic model and the point contact model can be compared to conventional (lower frequency) rheometer data. As such, the applicability of the QCM to measure the viscoelasticity of concentrated particle suspensions is to be considered.

## 6.2. Materials and Methods

### 6.2.1. Materials

RM1321 zinc oxide (Scarva, UK) was used for this study. The sample was used as received. 26.5 vol% ZnO suspensions were prepared in deionised water with a resistivity of 18.2 MΩ.cm. The samples were mixed thoroughly for 20 min using a metal spatula until the suspension appearance was uniform throughout. The suspension container was sealed using parafilm (VWR International) and left to fully hydrate for 1 week. For solids concentration-based testing, the stock suspension of 26.5 vol% suspension was taken, and a known volume of deionised water was added to the sample diluting the sample to the desired solids concentration. The diluted sample was mixed using a metal spatula for 5-10 min until it resembled a smooth paste before being sealed and left for 20 min to equilibrate before experimentation.

### 6.2.2. X-ray diffraction (XRD)

~50 mg dry powder samples of ZnO were mounted into a D8 XRD (Bruker, US), with Cu-Kα radiation (λ = 0.15418 nm) in the 2θ range of 10º - 80º with step size of 0.016˚. Lattice parameters were obtained from the International Centre for Diffraction Data – Powder Diffraction File database (ICDD-PDF4+). The experimental operation followed the standard method provided by the instrument manufacturer.

### 6.2.3. Gel point determination

The gel point of ZnO, defined as the critical solids concentration when particles form a complete three-dimensional continuous network and the individual particles no longer move relative to one-another, was determined by the method outlined by de Krester et al. [31, 32]. In brief, a 3 vol% suspension of ZnO was prepared using the sample preparation method described above. The suspension was poured into 400 mL graduated cylinders of varying suspension volumes ranging from 45 mL to 230 mL, thus varying the overall suspension height. The graduated cylinders were sealed with parafilm and left undisturbed for 3 days. After consolidation the final sediment bed height was measured and the gel point determined from the relationship $\emptyset = \frac{\partial(\emptyset_0 h_0)}{\partial h_\infty}$, where $\emptyset_0$ is the suspension volume fraction at t = 0, $h_0$ is the initial suspension height, and $h_\infty$ is the final sediment height.

### 6.2.4. Yield stress

The solids concentration-dependent yield stress of ZnO suspensions was measured using a Brookfield DV-II+ Pro Viscometer with a 4-blade vane of dimensions: H = 12.50 mm and D = 12.67 mm was used for higher yield stress suspensions (~ 140 Pa – 2000 Pa) and a vane of dimensions H = 43.33 mm and D = 21.67 mm was used for lower yield stress suspensions ($<$ 130 Pa). The largest geometry for each yield stress range was used to minimize experimental error. It should be noted from previous work

that the variability introduced from using vanes of different dimensions is minimal, hence the intermediate yield stresses measured using either geometry was reliable [33-36]. Our previous study [27] provided a more in-depth description of our measurement setup. Briefly, the suspension was firstly prepared using the method outlined above. The suspension was then mixed using a metal spatula, air bubbles were removed by tapping the cylindrical beaker and the suspension was left for 10 min to equilibrate. The viscometer was calibrated, and the beaker clamped in place to avoid beaker rotation during the measurement. The vane was gently lowered below the suspension interface to a known depth. The vane was then rotated at 1 rpm for 2 min with the viscometer torque continuously measured. The suspension yield stress was measured from the maximum torque obtained. To minimise wall effects, the vane-to-cylinder ratio was 1:3.5.

### 6.2.5. Rheometer measurements

Suspension oscillatory rheology was measured using a Discovery HR-2 Rheometer (TA Instruments, UK) using a concentric cylinder Peltier steel vane of dimensions H = 42 and D = 28 mm. The geometry inertia of the concentric cylinder vane was firstly calibrated using the TA Instrument software. The magnetic bearing that is used to provide near friction free torque to the sample is then calibrated. The suspensions were prepared using the same method described for the yield stress measurements. With the suspension (~200 mL) loaded into the stainless-steel rheometer cup (D = 30.4 mm), the vane was gently lowered (controlled by the instrument software) to a gap setting of 9.6 mm. The suspension was first pre-sheared by rotating the vane at 400 rpm for 5 min, before being left for 3 min to equilibrate. The pre-shear was essential to remove any sample history effects which may have occurred during sample loading in the rheometer cup. An oscillation ‘strain sweep’ was first performed to determine the yield strain of the suspension. The oscillation frequency was fixed at 10 rad/s

(determined to be within the linear viscoelastic regime) and the strain amplitude increased beyond the critical condition when the storage modulus (G') was no longer measurable and the loss modulus (G'') decreased to a new lower limit where G'' ≫ G'. The region of linear viscoelasticity (LVR) is then determined by taking the applied strain value where G' and G'' behave linearly with increasing strain. A strain of 6% was found to be well within the LVR for the suspension at each concentration and was selected. Following the strain sweep measurement, the suspension was once again pre-sheared following the same protocol previously described. A 'frequency sweep' was then performed at the selected constant strain. The experimental frequency commenced at 100 rad/s and reduced to 0.1 rad/s over a period of 17 min with G' and G'' recorded at 5 data points per frequency decade. The high-to-low experimental frequency was chosen since the experimental time would be significantly shorter due to a shorter adjustment time for the frequency controller. This would reduce time-dependent effects such as sample drying from potentially influencing the experiment.

### 6.2.6. Quartz crystal microbalance (QCM)

A QCM with impedance monitoring (Clausthal University of Technology, Germany) operating in reflection mode, to provide enhanced sensitivity in liquid environments, was used to measure the air-to-sample sensor resonance frequency and half-band-half-width shifts, $\Delta F$ and $\Delta \Gamma$, respectively. The QCM sensor holder was a probe made of PTFE (Stanford Research Systems, USA) housing a 25.4 mm, 5 MHz gold-coated sensor clamped in place and sealed by two o-rings. The QCM sensor was cleaned by washing in 2% Decon-90 solution for 5 min followed by rinsing with deionised water (continuous flow for 5 min) and dried using $N_2$ gas. The QCM sensor was first calibrated in air by manually locating and fitting the peak obtained when the electrical admittance (y) vs. resonance frequency (x) is plotted for each sensor overtone. Prior

to measurement, resonance properties at sensor overtones 1, 3, 5, 7, 9, 11 were continuously recorded until stable F and Γ baselines were observed in air (i.e. less than 5 Hz/hr drift in both responses which normally required ~30 min in air). With stable baselines established, the QCM sensor was submerged (dipped) in the suspension and mixed (high volume fraction suspensions were deposited directly onto the sensor surface). With the sensor fully submerged, the QCM resonance properties were re-calibrated by re-fitting the electrical admittance peaks. The sensor-suspension environment was then sealed using parafilm and the suspension gently re-agitated to achieve stable ΔF and ΔΓ values. The resonance properties were then continuously measured for up to 1 hr. The air-to-suspension resonance shifts was then determined by the difference between the two baseline signals prior to and following submerging the probe in the suspension.

QTM modelling software, developed by Diethelm Johannsmann from Clausthal University of Technology (the author acknowledges the support from Prof. Diethelm Johannsmann for the development of the software and his technical input when modelling the QCM data), was used to numerically model the viscoelastic behaviour of the overlaying suspensions using QCM data. Firstly, a set of limits are introduced to ensure the system behaves realistically (i.e. a sample cannot have a negative thickness for example). The limits are shown in Figure 6.7.

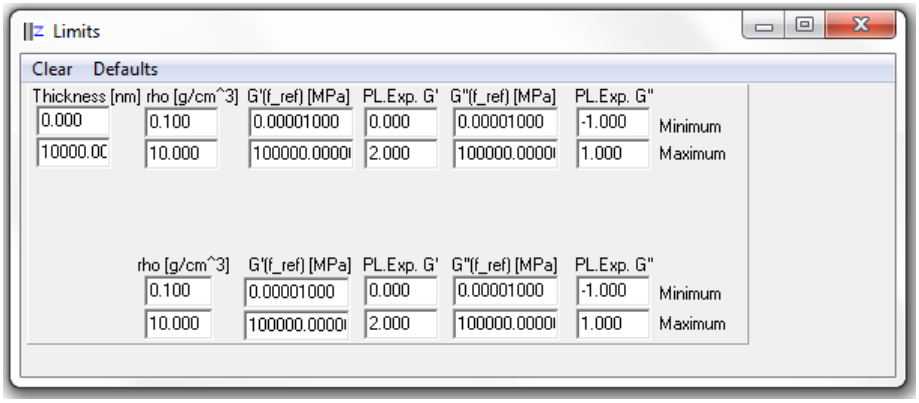


**Figure 6.7: Limits introduced for the viscoelastic layer (top values) and the bulk liquid (bottom values) when their properties are used when calculating the viscoelastic properties of the overlaying suspension. Thickness is the viscoelastic overlayer thickness ($d_f$) (the parameter is used in Equation 6.6 to fit the viscoelastic properties of the material to the QCM response via the film density), rho is the density of the medium in g/cm$^3$, G'(f_ref) and G''(f_ref) is the G' and G'' of the viscoelastic medium at the selected reference frequency. PLExp.G' is the power law fit coefficient for G' data and PLExp.G'' is the power law fit coefficient for G'' data.**

The suspension is treated as a viscoelastic layer within a bulk fluid. The properties of both the viscoelastic layer and the bulk fluid are therefore considered. It should be noted that the viscoelastic properties of the medium were found to not change significantly when the properties of the bulk fluid were excluded from the calculation (the fluid properties are then taken to be a part of the medium). The QCM $\Delta F$ and $\Delta \Gamma$ response is then inserted. Example values for 15.1 vol% ZnO are used for the fits shown in Figure 6.8. Note that the values are $\Delta F$ and $\Delta \Gamma$ at different overtones (n) and not $\Delta F/n$ or $\Delta \Gamma/n$ values. The 1$^{st}$ overtone was excluded for all calculations since the QCM response at the first overtone is traditionally known to cause deviations from model predictions [18]. A reference frequency (e.g. 25 MHz) was selected, a density of 1 g/cm$^3$ was inserted for the bulk liquid (water), and the suspension bulk density was inserted for the layer (i.e. 1.69 g/cm$^3$ for 15.1 vol% ZnO). The model was then fitted to the raw data using a Fresnel-type calculation by following the numerical methods previously outlined (Fig. 6.8).

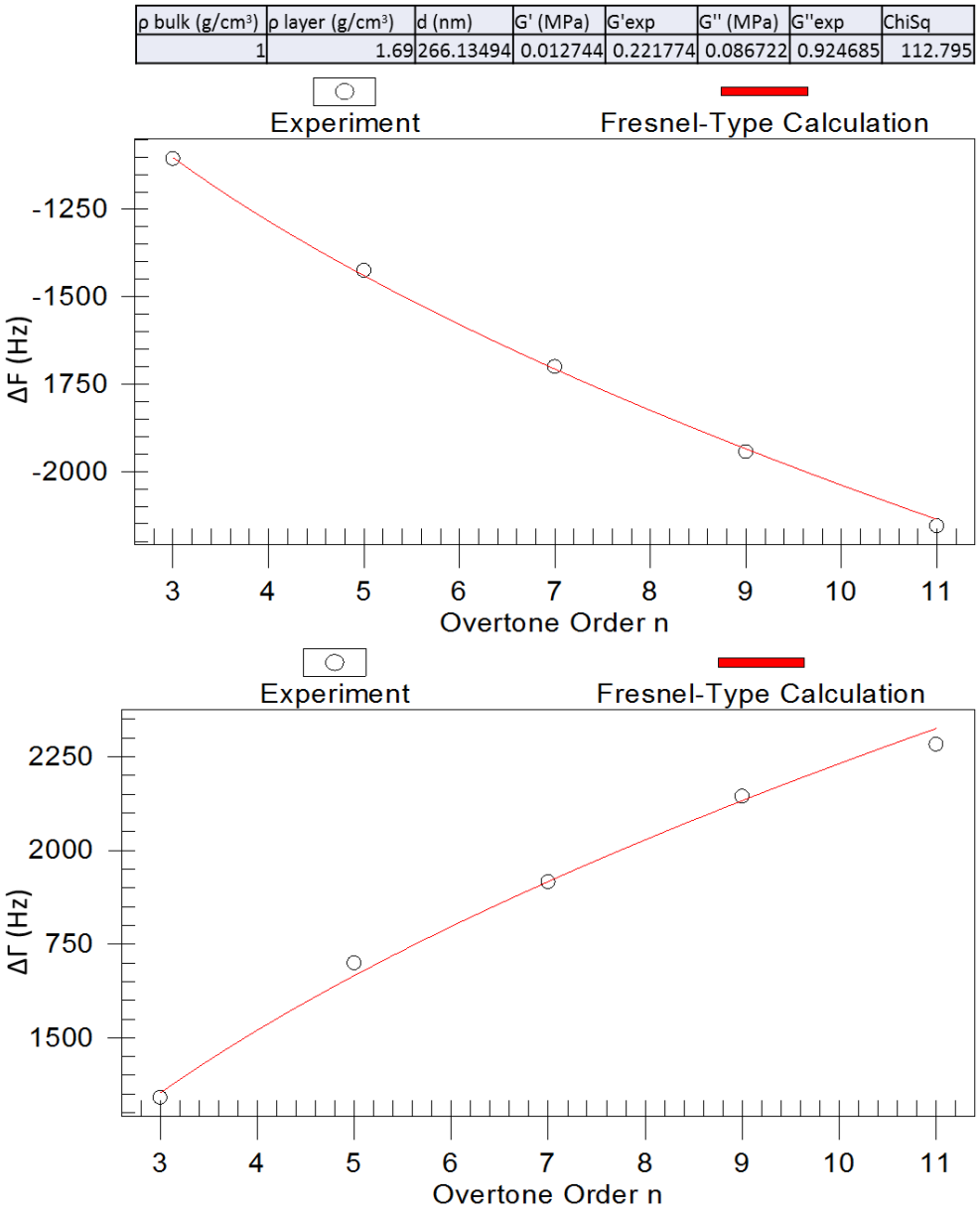


**Figure 6.8: Fitting of raw QCM data for 15.1 vol% ZnO to the acoustic multilayer formalism model using a Fresnel type calculation.**

The viscoelastic parameters of the suspension at 25 MHz reference frequency ($f_{ref}$) is then obtained. If G' and G'' values at different frequencies are required, then the aforementioned power law relationship can be used, e.g. for G': $G' = G'_{\omega_{ref}} \left(\frac{f}{f_{ref}}\right)^c$, where $c$ = G'exp (or PLExp.G'), $G'_{\omega_{ref}}$ is the obtained G' value at the 25 MHz reference frequency and $G'$ is the new G' value obtained where the sensor oscillates at a new frequency $f$.

### 6.2.7. Amplitude tests

The QCM sensor frequency and half-band-half-width response with changing resonator amplitude was determined using conventional impedance analysis [37] (courtesy of Frederick Sebastian Meyer and Prof. Diethelm Johannsmann for assistance in obtaining the impedance analysis amplitude data). The amplitude of oscillation, $\mu_0$, is related to the supplied current, $I$, according to the relationship (Equation 6.9) [25, 38, 39]

$$\mu_0 = \alpha \frac{d_q}{2\omega e_{26} A_{eff}} I = \alpha \frac{d_q}{2\omega e_{26} A_{eff}} \frac{U}{(R_{out} - R_1)}$$

$$\approx \alpha \frac{d_q}{2\omega e_{26} A_{eff}} \frac{U}{R_{out}} \qquad \textbf{Equation 6.9}$$

where $\alpha$ is the numerical factor equal to 1 if the resonator is modelled as a parallel plate, $e_{26} = 9.26 \times 10^{-2}$ C/m$^2$ is the piezoelectric stress coefficient, $U$ the nominal output voltage of the impedance analyser (V), $d_q$ the sensor plate thickness (m), $A_{eff}$ the piezoelectrically effective area (m$^2$), $R_{out}$ the output resistance of the impedance analyser (Ohm) and $R_1$ the motional resistance of the crystal (Ohm).

The apparent amplitude can be modified by altering the supplied voltage (which is proportional to the supplied current) to the sensor. The ZnO suspension of desired solids concentration was prepared and the QCM sensor surface was submerged in the suspension before sealing the test cell with Parafilm as previously described. The submerged QCM was left to equilibrate for 3 hrs. The supplied voltage was then altered in the following range: (0.3 V to 1.95 V, then 1.95 V back to 0.3 V) × 2 over a period of 6 hrs (i.e. a total of 4 steps, meaning each step took 1.5 hrs to complete). 68 frequency and half-band-half-width data points were collected across the voltage range for each step, making the average step increment every ~0.024 V.

## 6.3. Results and Discussion

### 6.3.1. Zinc oxide particle/suspension characterisation

X-ray diffraction of dried ZnO powder revealed the sample to be predominantly composed of Wurtzite (ICDD: 04-008-7254), with the crystal orientation labelled in Fig. 6.9 [40]. A small amount of an unknown impurity was detected, shown by a weak but broader peak measured at 2θ = 59.5°, Fig. 6.9. Based on further particle characterization data (see below), the effect of the minor impurity on the overall particle properties was considered to be negligible.

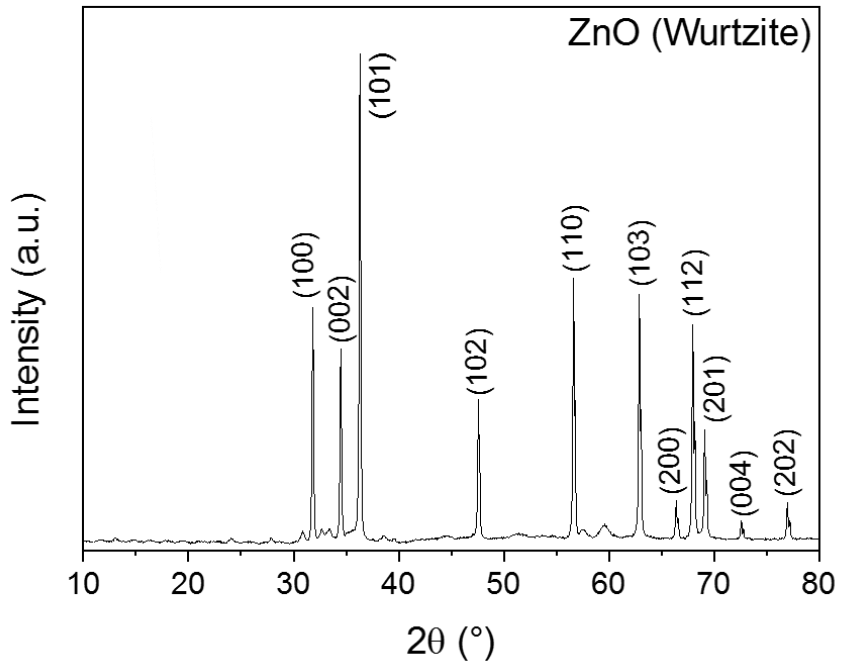


**Figure 6.9: X-ray diffraction pattern of the zinc oxide particles. The associated crystallite orientations for each major peak is included [40]. A weak but broader peak is observed at 2θ = 59.5°, indicating trace amounts of an unknown impurity.**

With the ZnO particles hydrated for one week (extended time to avoid effects of partial hydration), the zeta potential of the particles was measured to be $23 \pm 0.5$ mV at pH 6.5 – 6.6. Obtaining the Hamaker constants for gold ($45.3 \times 10^{-20}$ J) [41], zinc oxide ($9.1 \times 10^{-20}$ J) [42], and water ($3.7 \times 10^{-20}$ J) [43] in air (vacuum), the

minimum total potential energy of interaction (strongest attraction) between ZnO and gold in water was calculated to be $-546 \times 10^{-18}$ J using the sphere-plate HHF theory (see Chapter 5 for a more detailed description) [41-45]. A representative particle radius of 500 nm was used (particle radius does not affect whether the system is attractive or repulsive, but only the magnitude of the value). Therefore, the positively charged ZnO particles will strongly interact with the negatively charged gold sensor [5]. It should be noted that the streaming potential of the gold sensor was measured in 10 mM NaCl electrolyte solution and used for the HHF calculation, whereas the particle suspension and the resultant QCM studies were conducted in deionised water. This difference is not thought to be significant since the streaming potential of gold is likely to be more negative when in a lower concentration electrolyte medium (deionised water), thus resulting in a greater strength of interaction between the particles and sensor [36].

Due to the strong interaction between the particles and sensor, the shear wave decay length, which describes the measurement (sensitivity) zone of the QCM, should be significant ($\gg$ decay length in water), although the exact decay length has not been calculated due to difficulties in modelling the energy transfer through complex solid-pathways within the particle suspension network. As such, the measured response of the QCM will be sensitive to changes in the bulk properties of the particle suspension, as previously shown when measuring $Mg(OH)_2$ suspensions (Chapter 4).

The gel point of ZnO suspensions (pH = 6.5 – 6.6, no background electrolyte) was found to be 7.4 vol% (Fig. 6.10). Even though the particle zeta potential is 23 mV, a low gel point concentration would indicate the particle tendency to aggregate, forming low volume fraction, voluminous aggregates. Our interest was to probe the viscoelastic properties of ZnO suspensions in the Hz and MHz range, with particle

concentration increased to modify the rheology of the suspension. A suspension below its gel point would not behave as a viscoelastic solid (G'' is expected to be larger than G') and there would be no continuous three-dimensional particle network that extend across the volume of the suspension (i.e. particles can still move relative to one-another and are not held in place). By performing tests above this minimum limit, the viscoelastic properties of the particle network will therefore be probed, enabling for direct comparisons to QCM data to be made. The ability of the QCM to measure these bulk particle network viscoelastic changes can therefore be determined.

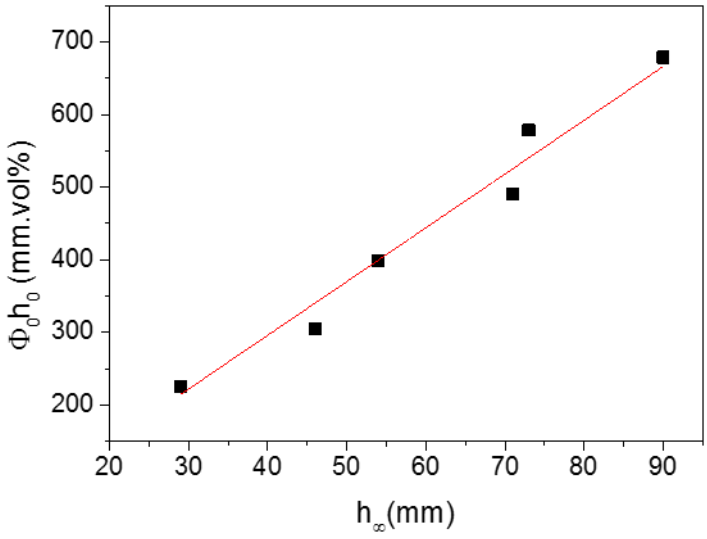


**Figure 6.10: Determination of the gel point of the ZnO via cylinder settling tests using 3 vol% initial suspension concentrations. The linear regression (solid red line) goodness of fit was $R^2 = 0.996$. The gradient of the line of best fit is based on the relationship $\emptyset = \frac{\partial(\emptyset_0 h_0)}{\partial h_\infty}$ and is equivalent to the gel point of the suspension (7.4 vol%).**

### 6.3.2. Solids concentration effects – vane viscometry

The shear yield stress of ZnO suspensions was shown to increase when the solids concentration was greater than the gel point concentration, and followed an expected power law relationship with increasing solids concentration [36, 46-49], see Fig. 6.11.

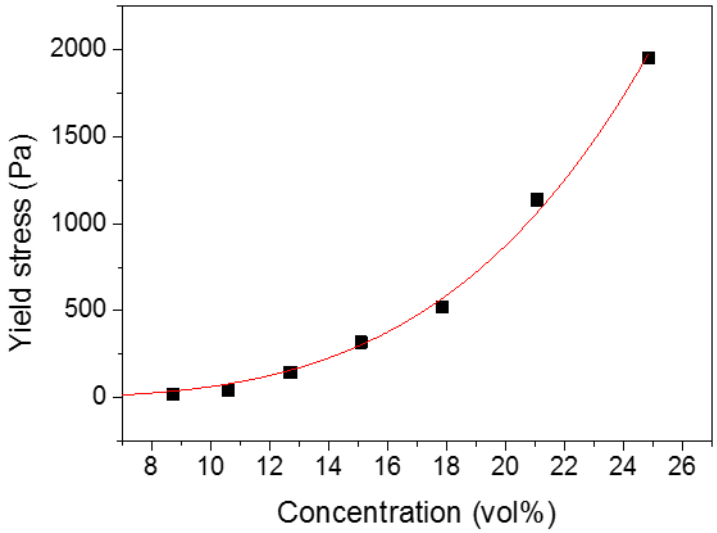


**Figure 6.11: Shear yield stress of ZnO suspensions with increasing solids concentration using vane viscometry. An allometric fit of the data (solid red line) has an equation of $y = 0.01127x^{3.75848}$ , with R2 = 0.996 and has been extrapolated to 0 Pa yield stress at 0 vol%.**

The viscoelastic properties of the yield stress ZnO suspensions were studied using the TA Instrument DHR-II rheometer. Oscillating the vane geometry ($\gamma = 6\%$), the elastic modulus (G') was greater than the viscous modulus (G'') at all solids concentrations (Fig. 6.12A and B), with the difference between the two moduli increasing with increased solids concentration as expected (Fig. 6.12B) [18, 50, 51]. An increase in the solids concentration results in a greater number of particle-particle contacts forming a space-filling three-dimensional network which absorbs stresses at deformations below the yield stress [50]. For the solids concentrations studied, G'' appears to be independent of the oscillation frequency, while G' shows a weak dependence. It does not appear that the solidification process follows the conventional

transition to $G'(\omega) \sim \omega^0, G''(\omega) \sim \omega^0$, but the distribution in G' and G" gradually widens with solidification possibly influenced by growing fractal flocs. For comparison, the suspension viscoelastic properties G' and G" were considered at a constant frequency, 10 rad/s, see Fig. 6.12B.

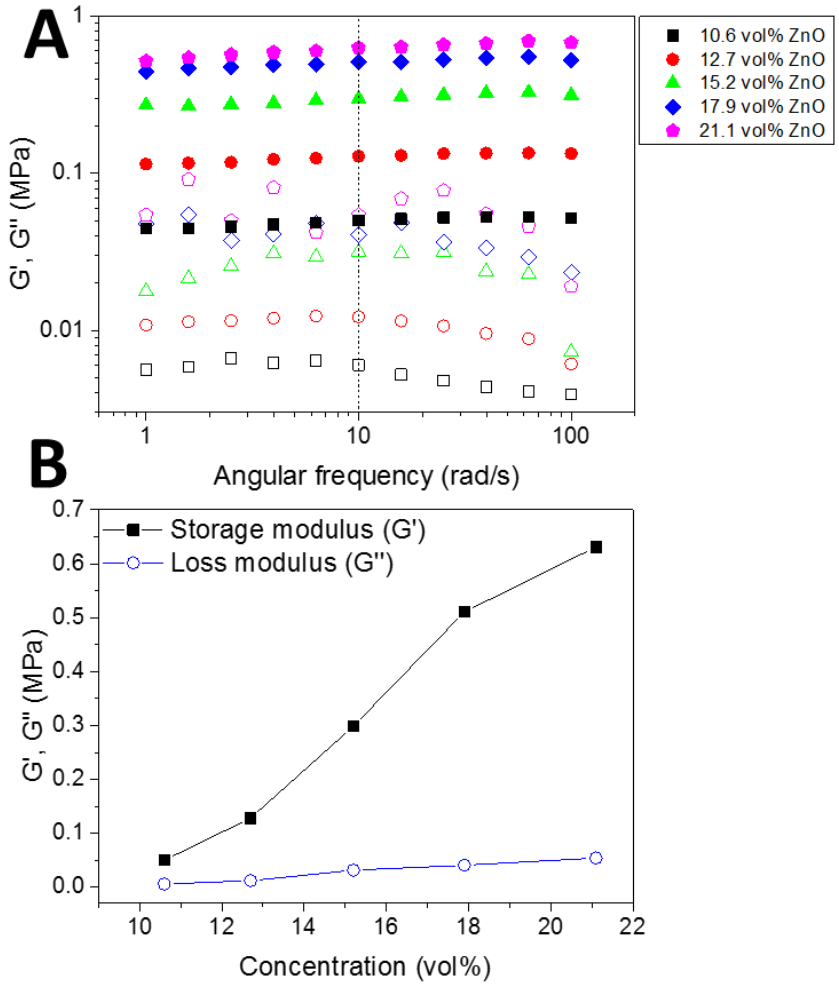


**Figure 6.12: (A) storage moduli (G', closed symbols) and loss moduli (G'', open symbols) for ZnO suspensions at different concentrations with changing measurement angular frequency. (B) by selecting the G' and G'' values at 10 rad/s, the viscoelastic behaviour of ZnO at different solids concentrations for this experimental frequency is obtained. All strains used were within the linear viscoelastic regime for the suspension.**

### 6.3.3. Quartz crystal microbalance – solids concentration

Studying the same ZnO suspensions, the QCM responses (air-to-sample, ΔF and ΔΓ) were measured, see Fig. 6.13. The QCM responses were very similar to those observed in our previous study when submerging the QCM into $Mg(OH)_2$ suspensions [27]. The response in -ΔF, first increasing before decreasing with increasing solids concentration, exhibited a transition near to the suspension gel point (~10.6 vol%), with the transition observed to occur at the same solids concentration for all overtones. Thus, the mechanism for this transition is unlikely related to a transition from inertial to elastic loading stemming from a difference in sensor-to-particle oscillation frequencies [15-17], but rather due to effects unrelated to the resonator oscillation frequency. It is worth noting the magnitude in frequency and half-band-half-width shifts scale with the overtone number, and hence the likely measured response is a function of the shear wave decay length (penetration depth) [16]. At $\theta > 23$ vol%, the 5 MHz response (frequency shift) no longer follows the trend of the higher order overtones, and the measured frequency shift for n = 1 becomes positive. Such behaviour is not currently understood but may have contributions from poor energy trapping and electric fringe field effects that currently do not have trust-worthy models to describe the effects [18]. Also, as previously described the positive ΔF may result from elastic loading with a higher resonance frequency ($\omega$) induced by the resonance ($\omega_S$) of the elastically loaded particle network, satisfying the condition $\omega \gg \omega_S$ [17, 22], although this effect is not observed for all overtones.

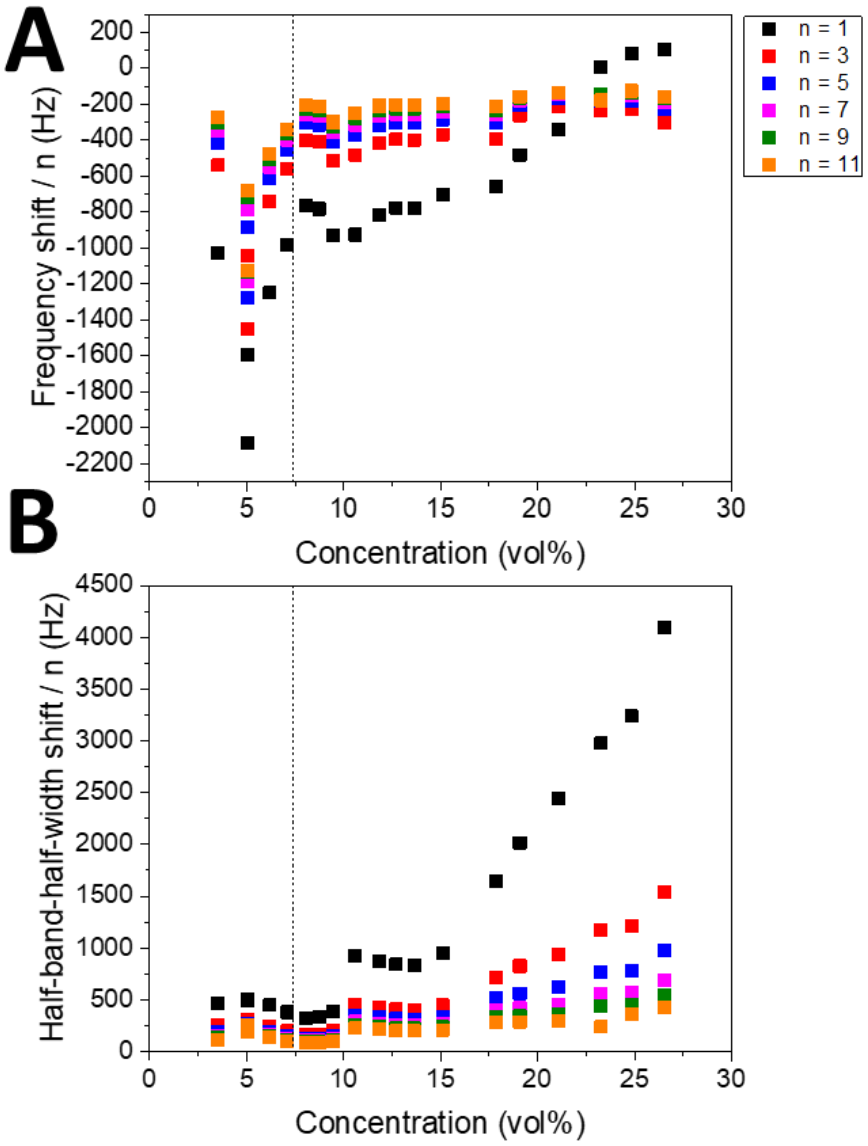


**Figure 6.13: i-QCM ΔF and ΔΓ response with changing ZnO solids concentration. Vertical dashed line corresponds to the gel point concentration of the suspension. The experiment was performed at a constant apparent amplitude of ~ 0.5 nm.**

Fig. 6.14C shows a direct correlation between the shift in half-band-half-width (ΔΓ) and the suspension yield stress, confirming our earlier finding when studying $Mg(OH)_2$ [27]. Such good agreement between ΔΓ and $\tau_y$ relates to the particles in contact with the sensor being clamped by inertia, resisting the motion of the oscillating sensor. The data shown in Fig. 6.14 demonstrates that independent of the particle-

type, and with a positive particle-sensor interaction (attraction), the QCM technique can be used to infer values of suspension yield stress.

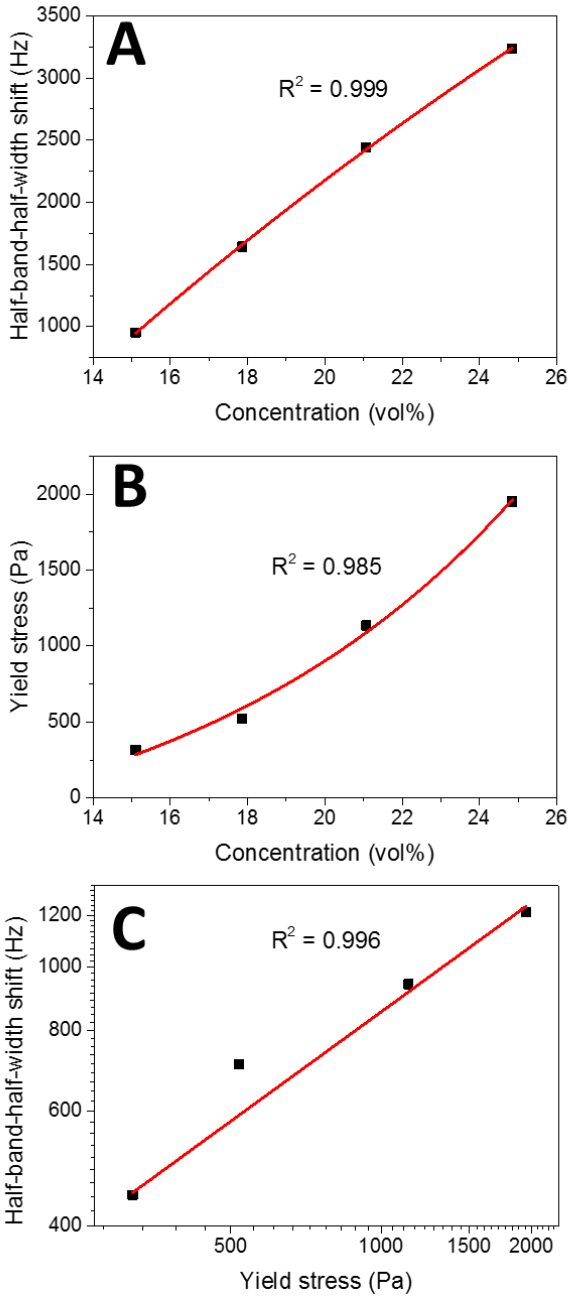


**Figure 6.14: (A) QCM ΔΓ response at the 3rd overtone for the ZnO suspension as a function of concentration. Data was taken from Figure 6.13. (B) the yield stress of the suspension was measured within the same concentration range. (C) a log-log plot of the QCM ΔΓ response and the suspension yield stress is performed. The final plot in part C showed an anomalous result near ~500 Pa and was excluded from the linear fit (red line) that otherwise showed $R^2$ = 0.996.**

### 6.3.4. Quartz crystal microbalance – viscoelastic modelling

Since the QCM cannot be completely described by inertial to elastic loading as described by the point contact load model, it may be better to consider the overlaying sludge as a viscoelastic medium with the suspension storage modulus increasing with solids concentration. The load impedance on the sensor ($Z_L$) will change with the apparent stiffness of the overlying suspension, resulting in characteristic shifts in -ΔF and ΔΓ [16]. Fits of the QCM -ΔF and ΔΓ (Fig. 6.15; 5 MHz [n = 1] data excluded; raw data shown rather than –ΔF/n and ΔΓ/n) to the acoustic multilayer formalism, revealed that the measured QCM -ΔF and ΔΓ responses were in good agreement with the overtone dependent shifts calculated using Equations 6.6 – 6.8 and thus the ZnO suspension overlying the QCM sensor behaved as a viscoelastic fluid (Fig. 6.15). As such, the QCM is responsive to changes in the viscoelastic properties of concentrated suspensions in contact with the QCM sensor. While this finding is new, it does contradict our earlier finding when studying $Mg(OH)_2$ suspensions (findings were solely described using the point contact load model, however this new information shows that both point contact load and viscoelastic behaviour is observed), although the $Mg(OH)_2$ suspensions were only investigated for n = 1 with no higher order overtones measured. When n = 1 is considered for the ZnO suspensions, positive air-to-suspension ΔF values are observed at concentrations $\theta > 23$ vol%, implying that elastic loading effects (Equation 6.4) from the point contact load model are still present. The relative contributions from both the point contact load and viscoelastic models is not trivial and may depend on the physicochemical properties of the suspension and QCM sensor, along with the physicomechanical properties of the particle suspension. Further work is needed to better understand the relative contributions of each loading mechanics on the overall QCM response.

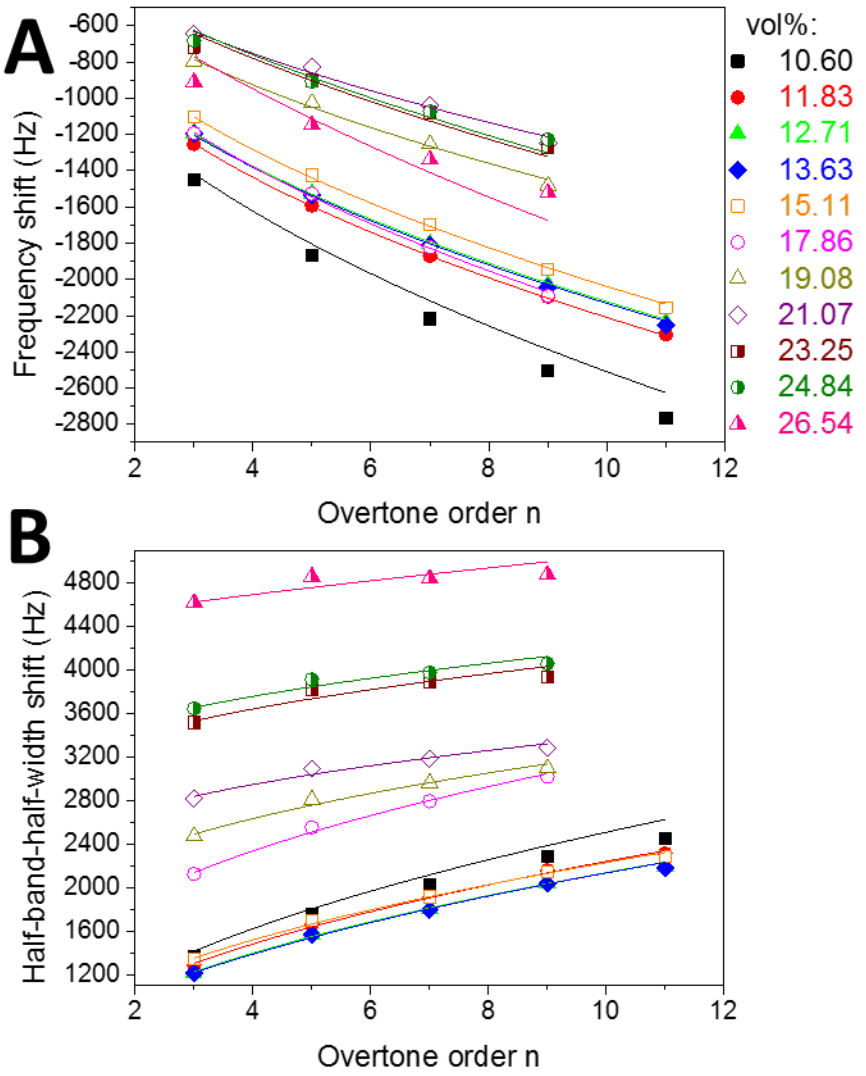


**Figure 6.15: Fit of raw QCM data from Fig. 6.13 to QCM viscoelastic models using acoustic multilayer formalism (Equations 6.6 – 6.8). Symbols = raw data and lines = fitted data. The fitted data is then used to calculate the viscoelastic properties of the suspension. Overtone order n = 3, 5, 7, etc. is equivalent to approximately 15, 25, 35, etc. MHz fundamental frequency. Data at the fundamental overtone (n = 1) is excluded for all concentrations since it is well-known to deviate from expected results, possibly due to poor energy trapping and electric fringe field effects [18]. Overtone n = 11 has been excluded for higher concentration fits where the QCM penetration depth is lower, resulting in a greater particle-sensor contact load contribution. The calculated viscoelastic parameters will be statistically relevant if 3 or more overtones are used to fit the data [18].**

Selecting a reference frequency (25 MHz which is equivalent to $\sim 157 \times 10^6$ rad/s), G' and G'' of the ZnO suspensions can be calculated using Equations 6.6 – 6.8. Fig. 6.16A and B shows the calculated viscoelastic moduli obtained from the acoustic multilayer formalism.

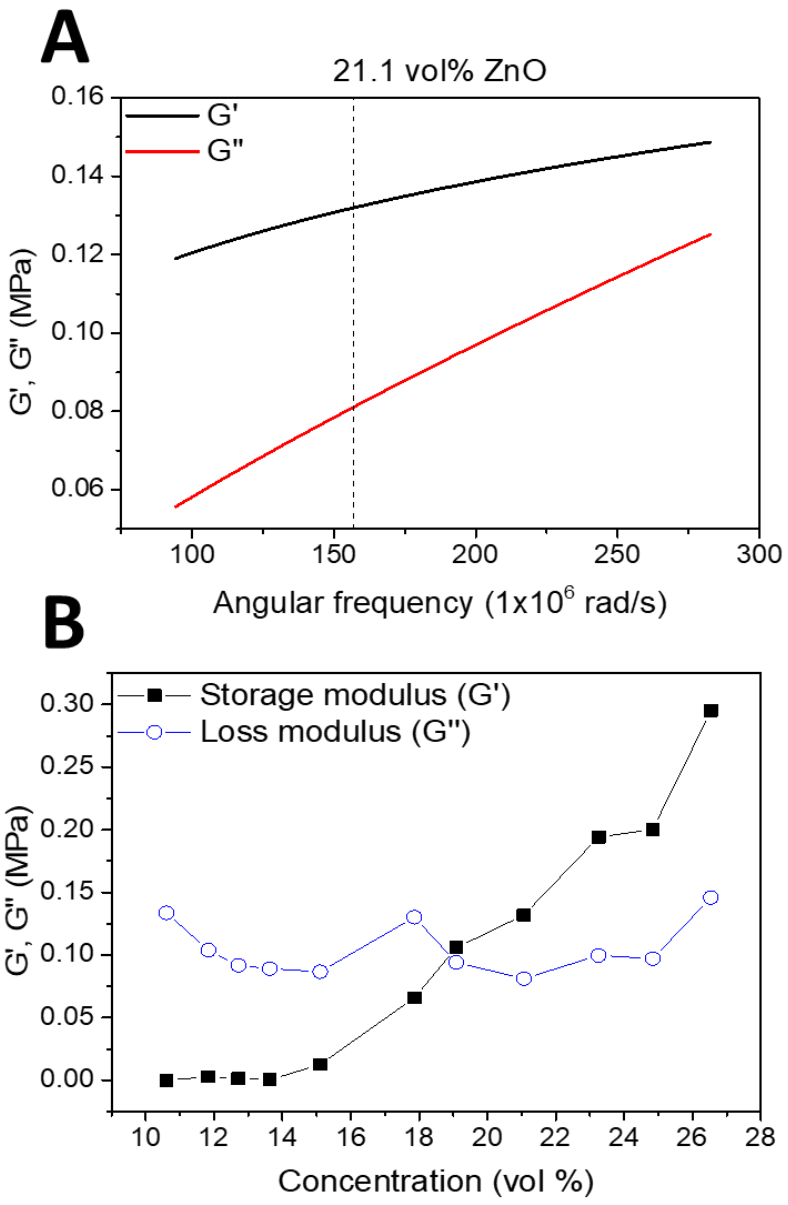


**Figure 6.16: (A) G' and G'' of a 21.1 vol% ZnO suspension as a function of the angular frequency (sensor overtones) calculated by fitting a power law relationship $y = mx^c$ (see Introduction and Experimental Methodology section) to the viscoelastic moduli calculated using the acoustic multilayer formalism. (B) G' and G'' of ZnO suspensions at a constant experimental frequency of $157.08 \times 10^6$ rad/s (25 MHz) as a function of solids concentration, derived using acoustic multilayer formalism.**

The calculated viscoelastic moduli (at 25 MHz) revealed that the ZnO suspensions exhibited a loss modulus (G") almost independent of the solids concentration, while the storage modulus (G') showed a gradual increase above a critical concentration of 13.6 vol%. As such, the ZnO suspension exhibited a liquid-like to solid-like transition (G' > G") at $\theta$ ~19.1 vol%. This transition was shown to be weakly sensitive to the chosen reference frequency, see Fig. S6.2. As previously shown in Figure 6.12, when measuring the viscoelastic properties at low frequencies (< 100 rad/s), G' exceeded G" at all ZnO solid concentrations, which is reasonable since all solids concentrations were above the suspension gel point. Despite those differences in viscoelastic moduli, Fig. 6.17 compares G' measured by QCM and rotational rheometer as a function of solids concentrations (12.7, 15.2, 17.9 and 21.1 vol%), with good agreement observed between the two data sets.

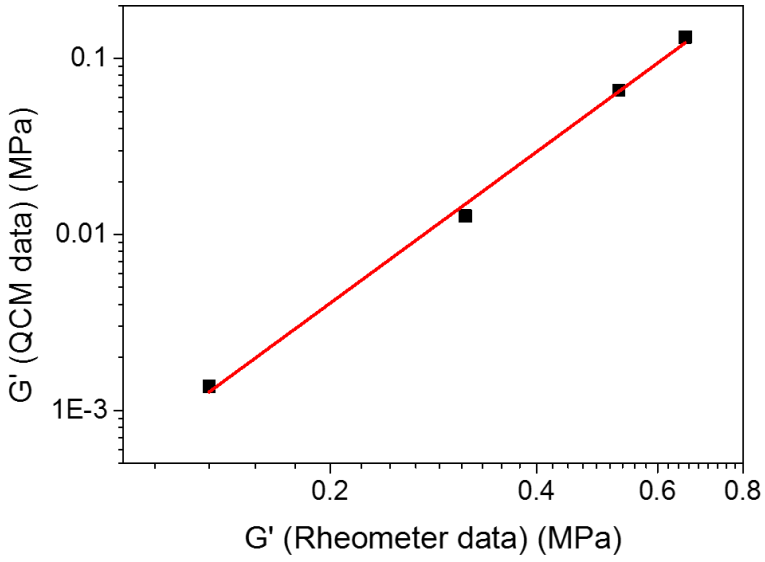


**Figure 6.17: Comparison between QCM and rheometer data for the measurement of the elastic modulus of ZnO suspensions at different solids concentrations. The QCM data reference angular frequency was at $157.08 \times 10^6$ rad/s while the rheometer data at 10 rad/s was used in this comparison. The comparison was made at concentrations of 12.7, 15.2, 17.9 and 21.1 vol% since the QCM viscoelastic data in Figure 6.16 started to show a detectable increase in G' values after 12.7 vol%. Linear regression (red line) $R^2 = 0.996$.**

The higher frequency of the experiment may play a role in the difference in ZnO viscoelastic behaviour [30, 52]. Typically, the suspension storage modulus (G') is expected to increase with increasing experimental frequency [30], however the yield strain of the suspension also reduces with increasing experimental frequency [52], resulting in potential structural breakdown due to relatively high experimental strains at MHz frequencies, causing the suspension G' to reduce [52]. For QCM devices, the amplitude of sensor oscillation could in this case be equivalent to the applied strain to the system, which may cause suspension structural breakdown.

The QCM detects the ZnO suspension as a Newtonian fluid at $\theta < 13$ vol%; with G' = 0 (Fig. 6.16), $-\Delta F$ shown as a linear correlation of $n^{1/2}$ (Fig. 6.18A), and $-\Delta F/\Delta\Gamma \approx 1$ (Fig. 6.18B), all indicators of Newtonian fluid behaviour [16, 18].

When the sensor changes its oscillation frequency for measurement at different overtones, the abrupt change in oscillation frequencies coupled with the relatively low yield strain of the suspension at high frequencies may cause the QCM resonance to produce strains that are above the suspension yield strain, causing a disturbance in the particle-sensor and nearby particle-particle links [52]. Evidence for this disturbance is shown in Figure S6.1 where i-QCM data were compared to QCM200 data [27] (the QCM200 oscillates the sensor at a constant 5 MHz frequency). A low concentration deviation is observed where the i-QCM loses sensitivity compared to the QCM200, indicating that structural disturbance may have taken place. This disturbance may cause link breakage for sludge consisting of overall weaker networks (i.e. low solids concentrations).

At low solids concentrations (< 10.6 vol% ZnO), the overall strength of the particle network structure is weaker (i.e. lower yield stress, see Fig. 6.11). Disruption caused by changes in the resonator oscillation frequency will cause strains that exceed the

yield strain of the network, causing link breakage (see Fig. S6.1). A $-\Delta F/\Delta\Gamma$ ratio of > 1 is observed (Fig. 6.18B), indicating a response expected for point-contact loads of a relatively stiff particle-sensor link [17, 20]. The particle network will therefore break, causing a reduction in the $\Delta\Gamma$ contribution, and leaving particles linked to the resonator surface (Fig. 6.20). The remaining particles will also carry a significant amount of entrained fluid [16] (Fig. 6.20) and possibly also a small amount of remaining intact particle-particle links, causing a QCM $n^{1/2}$ response expected for 'thicker' fluids (eg. 10 wt% glucose) (Fig. 6.18A).

At intermediate concentrations, (11.8 – 13.6 vol% ZnO), the particle network links become relatively stronger. When this network is disturbed due to sudden changes in sensor oscillation frequency, particle links will still be broken in this concentrated region. In this case however, the overall particle-particle links are sufficiently strong such that most of the particle-sensor links are now broken instead (i.e. particles will move to accommodate the increased stress, causing link breakage at the sensor surface) (Fig. 6.20). The QCM will no longer detect the particles, resulting the QCM to only detect the fluid (water) surrounding the particles, resulting in a similar QCM behaviour to that expected for water (Fig. 6.18A and B). A $-\Delta F/\Delta\Gamma$ ratio of < 1 at lower overtones (Fig. 6.18B) may be due to the QCM detecting a small number of particles that have not completely broken their network bonds, due to increased penetration depths at lower overtones [16].

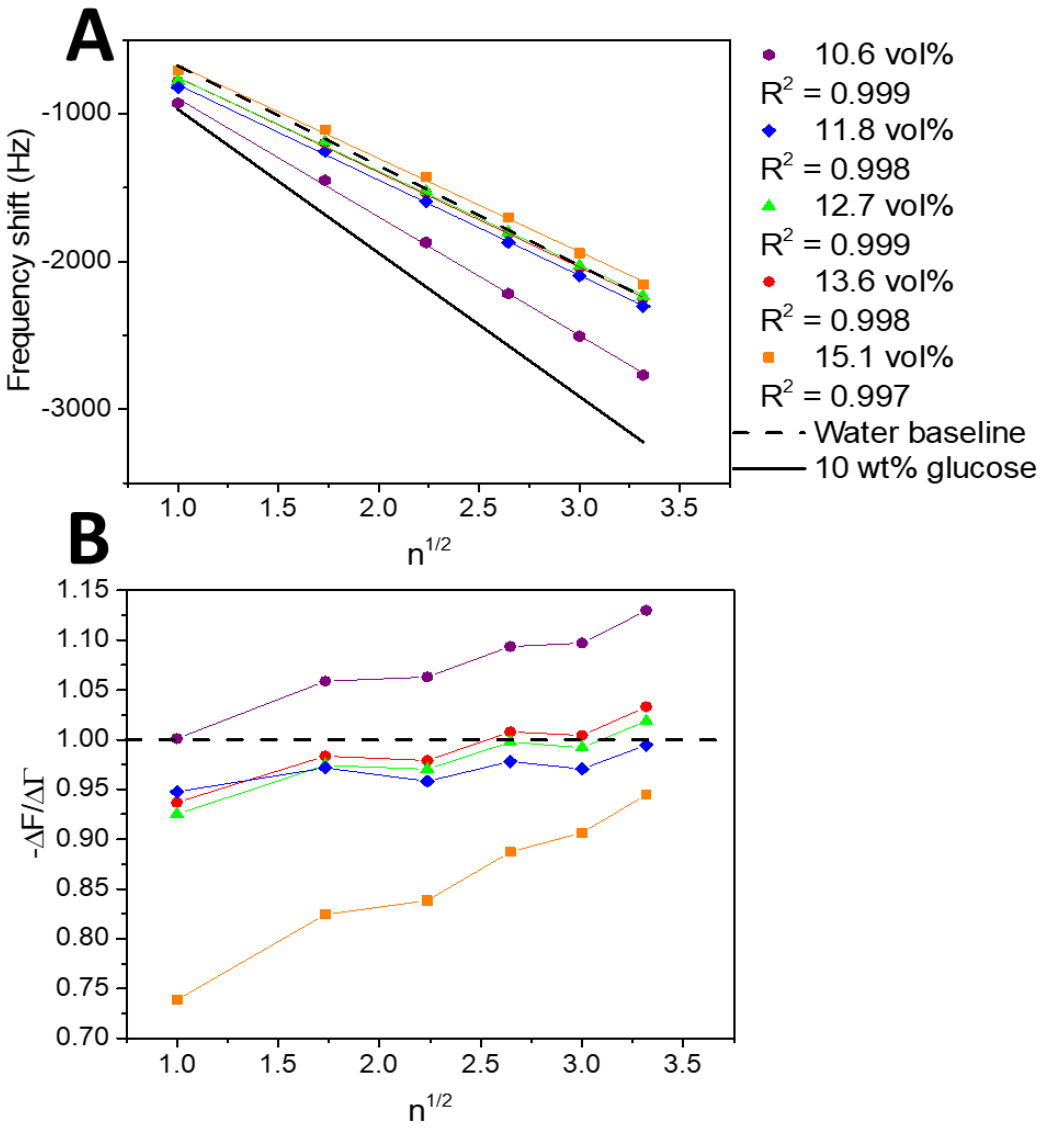


**Figure 6.18: (A) relationship between the QCM frequency response and the square root of the frequency overtone ($n^{1/2}$) for ZnO suspensions at low ZnO solids concentrations. The values are compared to the theoretical frequency response for water and 10 wt% glucose using the Kanazawa relationship (Equation S6.1). (B) the -ΔF/ΔΓ ratios are also compared to that expected for water.**

At high concentrations (> 17.9 vol% ZnO), the QCM response no longer follows the response for water, but instead for a fluid of a lower density-viscosity product (Fig. 6.19A and B). There is therefore a reduction in the overall viscous contribution to the QCM signal (i.e. a significant increase in the suspension storage modulus is observed at this concentration, see Fig. 6.16). The particle network is now strong and

concentrated enough where the particles are effectively held firmly in position when disruption occurs due to sudden changes in sensor frequencies; i.e. particles no longer move to accommodate this increased stress, keeping links intact (Fig. 6.20). The disruption caused by the sensor when it changes its oscillation frequency therefore no longer affects the overall QCM response (i.e. Fig. S6.1, at > 21 vol%, no significant deviation in QCM responses are observed).

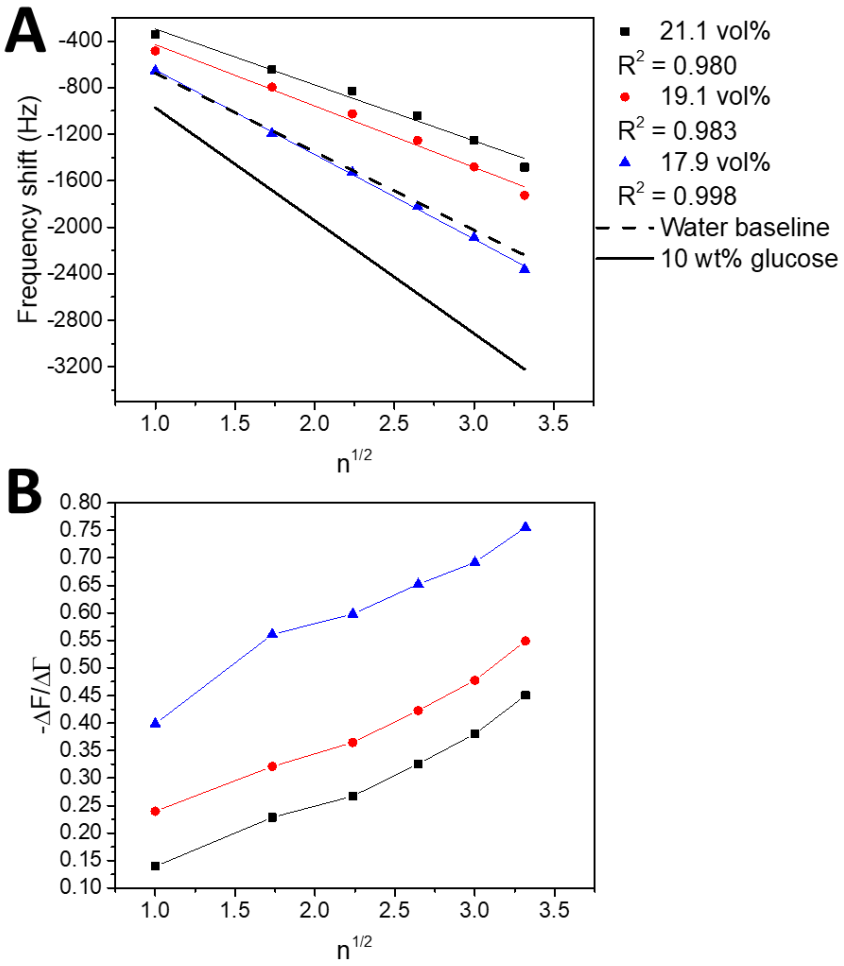


**Figure 6.19: Relationship between the QCM frequency response and $n^{1/2}$ for ZnO suspensions at high ZnO solids concentrations. The values are compared to the theoretical frequency response for water and 10 wt% glucose using the Kanazawa relationship (Equation S6.1). (B) the $-\Delta F/\Delta\Gamma$ ratios are significantly less than 1, indicating non-Newtonian fluid behaviour.**

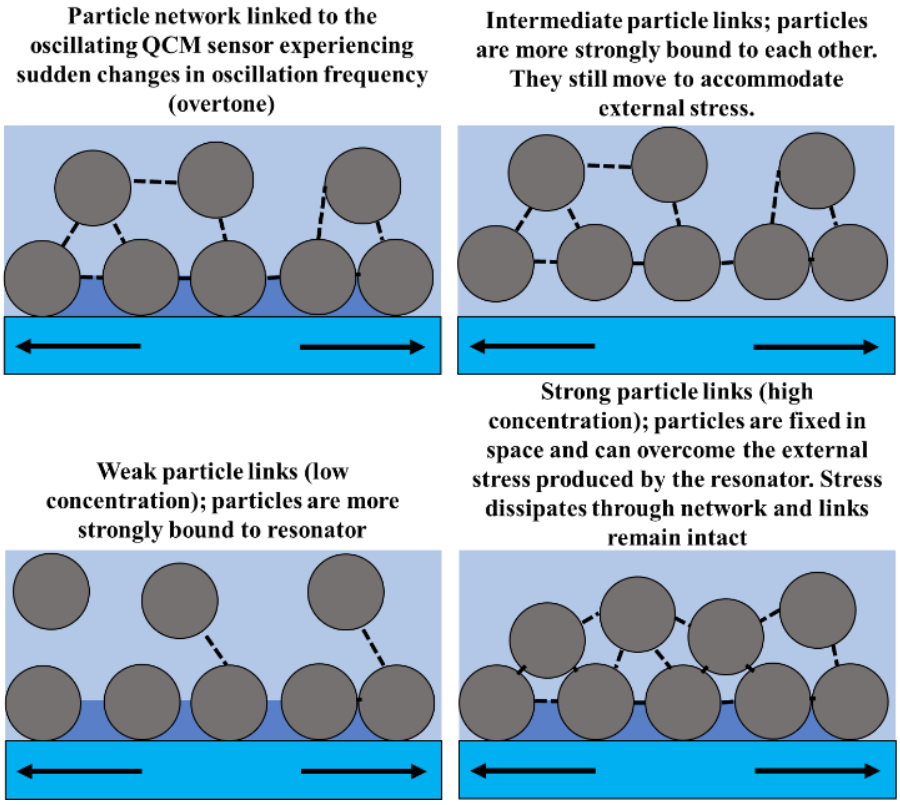


**Figure 6.20: Proposed networked suspension breakdown mechanism during QCM oscillation when oscillation frequencies are changed abruptly. At low concentrations (< 10.6 vol% ZnO), the overall particle-particle links are weaker, causing particles to remain on the sensor surface and act as point contact loads with water entrainment [16]. An intermediate particle network (11.8 – 13.6 vol% ZnO) will result in more links at the resonator surface to be broken (stronger overall particle-particle links), causing the QCM to detect the background medium instead (i.e. water). Strong links will clamp particles in place where they can resist the external stress from the sensor, meaning links are not broken.**

### 6.3.5. Quartz crystal microbalance – amplitude tests

When the sensor oscillates at a constant frequency (i.e. no abrupt changes), inefficient transfer of vibrational energy from the oscillating sensor to the linked particles may also reduce G' and increase G'' (i.e. particle link deformation expend energy from the resonator, causing energy that could be stored in the bulk particle network to be used up instead). Chapter 5 showed that a stiffer particle-sensor link resulted in greater QCM shifts, also indicating that the efficiency of energy transfer from the QCM

sensor to the linked particles was dependent on the particle-sensor interaction strength.

Slipping effects may induce an inefficient transfer of vibrational energy from the QCM sensor to the particle network since deformation of the particle-sensor link costs additional energy. QCM oscillation amplitude tests were performed to investigate potential slipping effects, see Figure 6.21. When a particle forms a link with the QCM sensor, deformation of the link may occur if the sensor moves from the original position. By investigating the resulting sample-sample (i.e. the QCM sensor remained fully submerged in the sample during amplitude sweep testing) $\Delta F$ and $\Delta \Gamma$ responses, the influence of resonator amplitude on the particle-sensor contact can be inferred. It should be noted that the $\Delta F$ and $\Delta \Gamma$ responses are shifts relative to $\Delta F_0$, $\Delta \Gamma_0$, the initial suspension conditions at ~ 0.1 nm apparent amplitude. The shifts result purely from changes in the oscillation amplitude, which in the previous experiments described throughout the thesis the oscillation amplitude was kept constant.

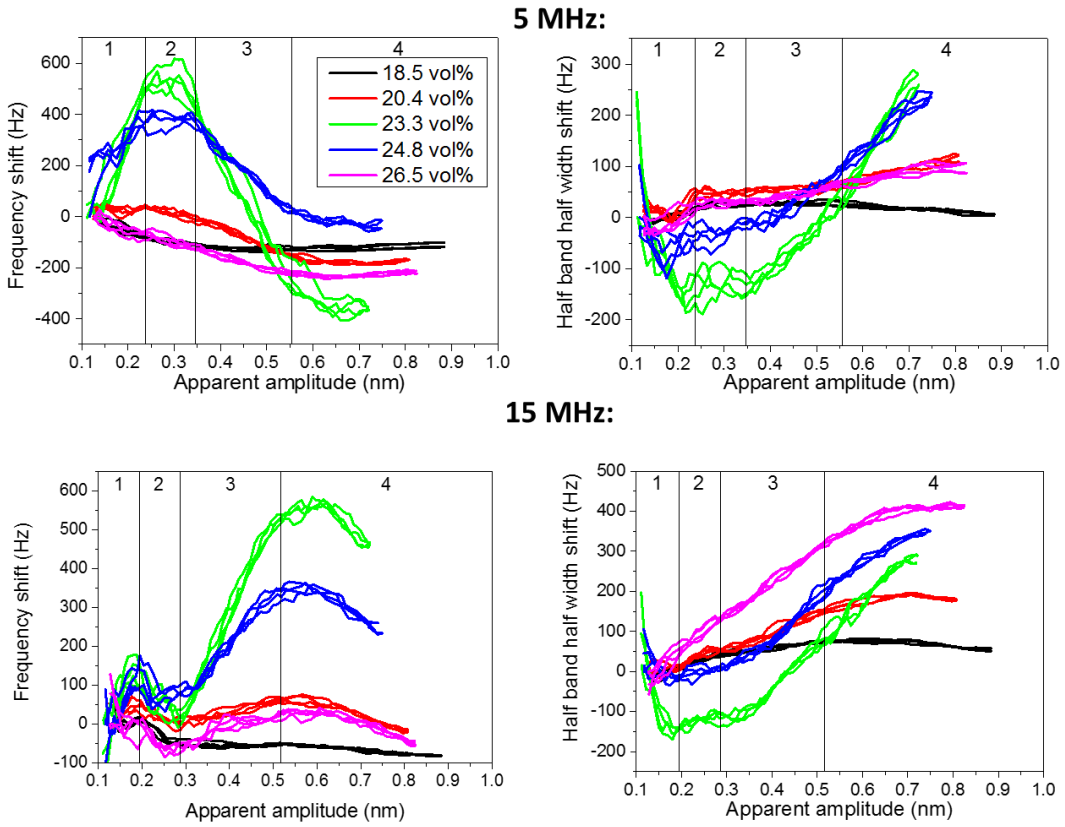


**Figure 6.21: QCM amplitude tests at 5 MHz and 15 MHz on ZnO suspensions at varying bulk concentrations. The initial QCM F and Γ value at ~0.1 nm was taken to be zero, making ΔF and ΔΓ relative to this initial value. The experiment was performed to completion at 5 MHz before data at 15 MHz was taken to account for potential disturbance during frequency changes. Four zones can be identified (separated by black vertical lines); 1 – coloumb friction, 2 – onset of partial slip, 3 – partial slip and 4 – onset of gross slip.**

Fig. 6.21 shows the ZnO suspensions exhibit a strong dependency on the apparent amplitude of the oscillating sensor. Purely viscoelastic media have been known to not show a change in ΔF and ΔΓ responses with increasing amplitude of oscillation (see Fig. 6.4) [23, 25]; revealing further evidence that the networked particle suspension interacting with the QCM sensor cannot be treated as a purely viscoelastic fluid. The largest fluctuations in ΔF and ΔΓ correspond to the 23.3 vol% ZnO suspension, with the magnitude of fluctuations reducing in the order: 24.8 vol%, 20.4 vol%, 26.5 vol% and 18.5 vol%.

Increasing the suspension concentration should lead to greater ΔF and ΔΓ due to more particle-sensor links and additional particle-particle links that dampen oscillation and make the particles appear larger, increasing the effective mass on the resonator [12, 17]. Beyond a critical concentration (i.e. at 23.3 vol%), the suspension may become too stiff to properly flow when it is pushed onto the resonator surface during experimental preparation, reducing the overall shifts observed which reduces further as the sludge becomes stiffer.

Four different regions have been identified from the data in Figure 6.21. By investigating the overall ΔF and ΔΓ trends in each region and comparing them to findings from Vittorias et al. [23] and Hanke et al. [25] (see Fig. 6.4 for the general trends that the data is compared to), changes in the properties of the particle-sensor contact for each region can be described:

*Coulomb friction* – At low amplitudes, the particle-sensor contact remains intact and purely elastic since point contact displacement is low. The positive ΔF and negative ΔΓ response shows evidence that coulomb friction effects may be taking place [23]. As the displacement increases, the particle-sensor van der Waals forces of attraction reduces in magnitude [5, 36]. The link would therefore weaken, reducing the overall QCM shifts, producing a +ΔF and –ΔΓ response.

*Onset of partial slip* – As the amplitude increases, a greater portion of the particles may begin to move to accommodate the increased stress which may produce a residual strain on the overlaying network structure. Due to this increased strain, particles may no longer move to accommodate further increased stress, causing the particle-sensor link to slip, resulting in a –ΔF and +ΔΓ trend [23, 25].

*Partial slip* – Eventually the displacement would become large enough where the bulk of the detected suspension particles can no longer move to accommodate the increased

stress, causing them to slip. Interestingly, at this point the 15 MHz response switches from -ve to +ve trend at ~0.3 nm. This may be a transition from inertial loading to elastic loading behaviour because as additional particles become unable to move due to the high strain environment, they become clamped by these inertial forces, satisfying the conditions required for elastic loading effects to occur where the sensor frequency is much greater than the linked particles (i.e. 15 MHz) [17, 22].

*Onset of gross slip* – The displacement becomes large enough for the particle-sensor link to break completely; this results in fewer links producing a $\Delta F$ and $\Delta \Gamma$ response, causing the overall trend to level off. A bulk gross slip would produce no shifts with increasing amplitude as most of the particles no longer have a link to the sensor. Shifts similar to the high pH conditions (repulsive particle-sensor interaction) in Chapter 5 would be expected. Interestingly, the onset of gross slip appears to be more prominent in the 15 MHz response, possibly because the yield strain of the suspension may decrease due to the increased experimental frequency [52].

The amplitude tests therefore show that there is evidence of an inefficient transfer of vibrational energy from the QCM resonator to the networked particles, which may in turn change its derived viscoelastic properties and hence help explain the reduced G' and higher G'' values that have been obtained.

## 6.4. Conclusions

This chapter investigated the ability of the QCM to detect changes in bulk concentrated suspension rheology. The QCM response in previous work (Chapters 4 and 5) have been described in terms of the point contact load model which in turn describes the mechanics involved when single spheres meet an oscillating resonator surface.

This work, in conjunction with work from Chapter 4 has shown that changes in the sensor oscillation dampening is proportional to changes in the bulk suspension yield stress during concentration tests (i.e. the particle-sensor interaction remains constant). The QCM may therefore be sensitive to changes in particle-particle links within the near vicinity of the resonator surface. Zinc oxide (ZnO) concentration tests at varying QCM frequency overtones (5 MHz, 15 MHz, etc. initial frequencies) also revealed a response that cannot be explained using the point contact model alone, further indicating that a new approach is required to describe QCM data.

The QCM ZnO concentration data showed good agreement to viscoelastic models, indicating that the viscoelasticity of the particle-particle networks may also play a role in the overall QCM response in addition to effects stemming from particle adsorption. The QCM is therefore capable of probing the bulk viscoelasticity of concentrated particulate suspensions, however this may only occur when there is a significantly strong particle-sensor interaction (see Chapter 5) and when this interaction strength is kept constant.

The QCM point contact load and viscoelastic models contradict one-another by nature; the first describes single particle adsorption whereas the latter describes the behaviour of a smooth homogenous film exposed to the resonator surface. By having a networked particle suspension, the data may deviate from either model depending on the physical and chemical nature of the particles and the type of experiment involved. For example, sudden changes in sensor oscillation frequency resulted in suspension structural breakdown at lower concentrations (overall weaker links), resulting in a reduction in the sensitivity of the QCM to measure changes in suspension viscoelasticity at lower concentrations.

The ZnO suspension also showed to be sensitive to changes in oscillation amplitude, which is expected from point contact loads. This would however result in an inefficient transfer of vibrational energy, resulting in the elasticity of the suspension network to potentially be underestimated.

Despite these setbacks, the QCM storage modulus (G') data correlated well with changes in the G' of ZnO with increasing solids concentration using conventional vane rheometry. The QCM can therefore be used as an instrument to probe the high frequency viscoelastic properties of concentrated suspensions.

## 6.5. References


1. Chowdhury, I., et al., *Deposition and Release of Graphene Oxide Nanomaterials Using a Quartz Crystal Microbalance.* Environmental Science & Technology, 2014. **48**(2): p. 961-969.
2. Krozer, A., S.-A. Nordin, and B. Kasemo, *Layer by Layer Deposition of 5–50-nm Colloidal Silica Particles Studied by Quartz Microbalance.* Journal of Colloid and Interface Ccience, 1995. **176**(2): p. 479-484.
3. Mihut, A.M., et al., *Tunable adsorption of soft colloids on model biomembranes.* Acs Nano, 2013. **7**(12): p. 10752-10763.
4. Chen, Q., et al., *QCM-D study of nanoparticle interactions.* Advances in Colloid Interface Science, 2015.
5. Hogg, R., T.W. Healy, and Fuersten.Dw, *Mutual Coagulation of Colloidal Dispersions.* Transactions of the Faraday Society, 1966. **62**(522P): p. 1638-&.
6. Derjaguin, B.V., Landau, L., *Theory of the Stability of Strongly Charged Lyophobic Sols and of the Adhesion of Strongly Charged Particles in Solutions of Electrolytes.* Acta Physicochim, 1941. **14**: p. 633-662.
7. Verwey, E.J.W., *Theory of the Stability of Lyophobic Colloids.* Journal of Physical and Colloid Chemistry, 1947. **51**(3): p. 631-636.
8. Zhuang, H., et al., *Study of the Evaporation of Colloidal Suspension Droplets with the Quartz Crystal Microbalance.* Langmuir, 2008. **24**(15): p. 8373-8378.
9. Reipa, V., G. Purdum, and J. Choi, *Measurement of Nanoparticle Concentration using Quartz Crystal Microgravimetry.* The Journal of Physical Chemistry B, 2010. **114**(49): p. 16112-16117.
10. Reipa, V. and J.H. Choi, *Measurement of Silicon Nanoparticle Concentration using Quartz Crystal Microgravimetry.* ECS Transactions, 2009. **25**(9): p. 167-175.
11. Pham, N., et al., *Application of the Quartz Crystal Microbalance to the Evaporation of Colloidal Suspension Droplets.* Langmuir, 2004. **20**(3): p. 841-847.

12. Sauerbrey, G., *Verwendung Von Schwingquarzen Zur Wagung Dunner Schichten Und Zur Mikrowagung*. Zeitschrift Fur Physik, 1959. **155**(2): p. 206-222.
13. Reviakine, I., D. Johannsmann, and R.P. Richter, *Hearing What You Cannot See and Visualizing What You Hear: Interpreting Quartz Crystal Microbalance Data from Solvated Interfaces*. Analytical Chemistry, 2011. **83**(23): p. 8838-8848.
14. Tellechea, E., et al., *Model-Independent Analysis of QCM Data on Colloidal Particle Adsorption*. Langmuir, 2009. **25**(9): p. 5177-5184.
15. D'Amour, J.N., et al., *Capillary Aging of the Contacts Between Glass Spheres and a Quartz Resonator Surface*. Physical Review Letters, 2006. **96**(5).
16. Johannsmann, D., *Viscoelastic, Mechanical, and Dielectric Measurements on Complex Samples with the Quartz Crystal Microbalance*. Physical Chemistry Chemical Physics, 2008. **10**(31): p. 4516-4534.
17. Pomorska, A., et al., *Positive Frequency Shifts Observed Upon Adsorbing Micron-Sized Solid Objects to a Quartz Crystal Microbalance from the Liquid Phase*. Analytical Chemistry, 2010. **82**(6): p. 2237-2242.
18. Johannsmann, D., *The Quartz Crystal Microbalance in Soft Matter Research*. 2014: Springer, Cham.
19. Johannsmann, D., I. Reviakine, and R.P. Richter, *Dissipation in Films of Adsorbed Nanospheres Studied by Quartz Crystal Microbalance (QCM)*. Analytical Chemistry, 2009. **81**(19): p. 8167-8176.
20. Pomorska, A., et al., *QCM Study of the Adsorption of Polyelectrolyte Covered Mesoporous TiO2 Nanocontainers on SAM Modified Au Surfaces*. Journal of Colloid and Interface Ccience, 2011. **362**(1): p. 180-187.
21. Gotoh, K., Y. Nakata, and M. Tagawa, *Evaluation of Particle Deposition in Aqueous Solutions by the Quartz Crystal Microbalance Method*. Colloids and Surfaces A: Physicochemical and Engineering Aspects, 2006. **272**(1-2): p. 117-123.
22. Dybwad, G.L., *A Sensitive New Method for the Determination of Adhesive Bonding between a Particle and a Substrate*. Journal of Applied Physics, 1985. **58**(7): p. 2789-2790.
23. Vittorias, E., et al., *Studying Mechanical Microcontacts of Fine Particles with the Quartz Crystal Microbalance*. Powder Technology, 2010. **203**(3): p. 489-502.
24. Johannsmann, D., *Towards Vibrational Spectroscopy on Surface-Attached Colloids Performed with a Quartz Crystal Microbalance*. Sensing and Bio-Sensing Research, 2016. **11**: p. 86-93.
25. Hanke, S., J. Petri, and D. Johannsmann, *Partial Slip in Mesoscale Contacts: Dependence on Contact Size*. Physical Review E, 2013. **88**(3): p. 032408.
26. Kanazawa, K.K. and J.G. Gordon, *The Oscillation Frequency of a Quartz Resonator in Contact with a Liquid*. Analytica Chimica Acta, 1985. **175**(Sep): p. 99-105.
27. Botha, J.A., et al., *Quartz Crystal Microbalance as a Device to Measure the Yield Stress of Colloidal Suspensions*. Colloids and Surfaces A: Physicochemical and Engineering Aspects, 2018. **546**: p. 179-185.
28. Palmqvist, L. and K. Holmberg, *Dispersant Adsorption and Viscoelasticity of Alumina Suspensions Measured by Quartz Crystal Microbalance with Dissipation Monitoring and in situ Dynamic Rheology*. Langmuir, 2008. **24**(18): p. 9989-9996.

29. Voinova, M.V., et al., *Viscoelastic Acoustic Response of Layered Polymer Films at Fluid-Solid Interfaces: Continuum Mechanics Approach.* Physica Scripta, 1999. **59**(5): p. 391-396.
30. Pakula, T., et al., *Relaxation and Viscoelastic Properties of Complex Polymer Systems.* Rheologica acta, 1996. **35**(6): p. 631-644.
31. De Kretser, R.G., D.V. Boger, and P.J. Scales, *Compressive Rheology: an Overview*. Rheology Reviews, 2003: p. 125-166.
32. Franks, G.V., et al., *Effect of Aggregate Size on Sediment Bed Rheological Properties.* Physical Chemistry Chemical Physics, 2004. **6**(18): p. 4490-4498.
33. Alderman, N.J., G.H. Meeten, and J.D. Sherwood, *Vane Rheometry of Bentonite Gels.* Journal of Non-Newtonian Fluid Mechanics, 1991. **39**(3): p. 291-310.
34. Dzuy, N.Q. and D.V. Boger, *Direct Yield Stress Measurement with the Vane Method.* Journal of Rheology, 1985. **29**(3): p. 335-347.
35. Liddell, P.V. and D.V. Boger, *Yield Stress Measurements with the Vane.* Journal of Non-Newtonian Fluid Mechanics, 1996. **63**(2-3): p. 235-261.
36. Johnson, S.B., et al., *Surface Chemistry-Rheology Relationships in Concentrated Mineral Suspensions.* International Journal of Mineral Processing, 2000. **58**(1-4): p. 267-304.
37. Beck, R., U. Pittermann, and K.G. Weil, *Impedance Analysis of Quartz Oscillators, Contacted on one Side with a Liquid.* Berichte der Bunsengesellschaft für physikalische Chemie, 1988. **92**(11): p. 1363-1368.
38. Johannsmann, D. and L.-O. Heim, *A Simple Equation Predicting the Amplitude of Motion of Quartz Crystal Resonators.* Journal of Applied Physics, 2006. **100**(9): p. 094505.
39. Martin, B.A. and H.E. Hager, *Velocity Profile on Quartz Crystals Oscillating in Liquids.* Journal of Applied Physics, 1989. **65**(7): p. 2630-2635.
40. Aimable, A., et al., *Polymer-Assisted Precipitation of ZnO Nanoparticles with Narrow Particle Size Distribution.* Journal of the European Ceramic Society, 2010. **30**(2): p. 591-598.
41. Kim, T., et al., *Control of Gold Nanoparticle Aggregates by Manipulation of Interparticle Interaction.* Langmuir, 2005. **21**(21): p. 9524-9528.
42. Bergström, L., *Hamaker Constants of Inorganic Materials.* Advances in Colloid and Interface Science, 1997. **70**: p. 125-169.
43. Gregory, J., *Particles in Water: Properties and Processes*. 2005: CRC Press.
44. Israelachvili, J.N., *Intermolecular and Surface Forces*. 2011: Academic press, Massachusetts.
45. Gu, Y., *The Electrical Double-layer Interaction Between a Spherical Particle and a Cylinder.* Journal of Colloid and Interface Science, 2000. **231**(1): p. 199-203.
46. Scales, P.J., et al., *Shear Yield Stress of Partially Flocculated Colloidal Suspensions.* AIChE Journal, 1998. **44**(3): p. 538-544.
47. Leong, Y.-K., et al., *Control of the Rheology of Concentrated Aqueous Colloidal Systems by Steric and Hydrophobic Forces.* Journal of the Chemical Society, Chemical Communications, 1993(7): p. 639-641.
48. KwongáLeong, Y., *Rheological Evidence of Adsorbate-Mediated Short-Range Steric Forces in Concentrated Dispersions.* Journal of the Chemical Society, Faraday Transactions, 1993. **89**(14): p. 2473-2478.

49. Leong, Y., *Interparticle Forces Arising from an Adsorbed Strong Polyelectrolyte in Colloidal Dispersions: Charged Patch Attraction.* Colloid and Polymer Science, 1999. **277**(4): p. 299-305.
50. Yanez, J.A., et al., *Shear Modulus and Yield Stress Measurements of Attractive Alumina Particle Networks in Aqueous Slurries.* Journal of the American Ceramic Society, 1996. **79**(11): p. 2917-2917.
51. Alderman, N., G. Meeten, and J. Sherwood, *Vane Rheometry of Bentonite Gels.* Journal of non-Newtonian Fluid Mechanics, 1991. **39**(3): p. 291-310.
52. Liu, C., et al., *Rheological Properties of Concentrated Aqueous Injectable Calcium Phosphate Cement Slurry.* Biomaterials, 2006. **27**(29): p. 5003-5013.

## 6.6. Supplementary Information

The i-QCM response was compared to that of the QCM200 to determine if changes in the oscillation frequency can affect the networking behaviour of the suspension near the resonator surface. The same magnesium hydroxide (Versamag) sample was used from our previous study [27] for comparison. Significant differences are observed at concentrations below 20 vol% where i-QCM resistance shift data becomes independent of concentration sooner than QCM200 data, implying network structure breakdown may begin to occur. At ~13 vol%, the i-QCM frequency response drops whereas this only occurs at ~3 vol% for QCM200 data; further evidence that the suspension network may be disturbed due to changes in oscillation amplitude.

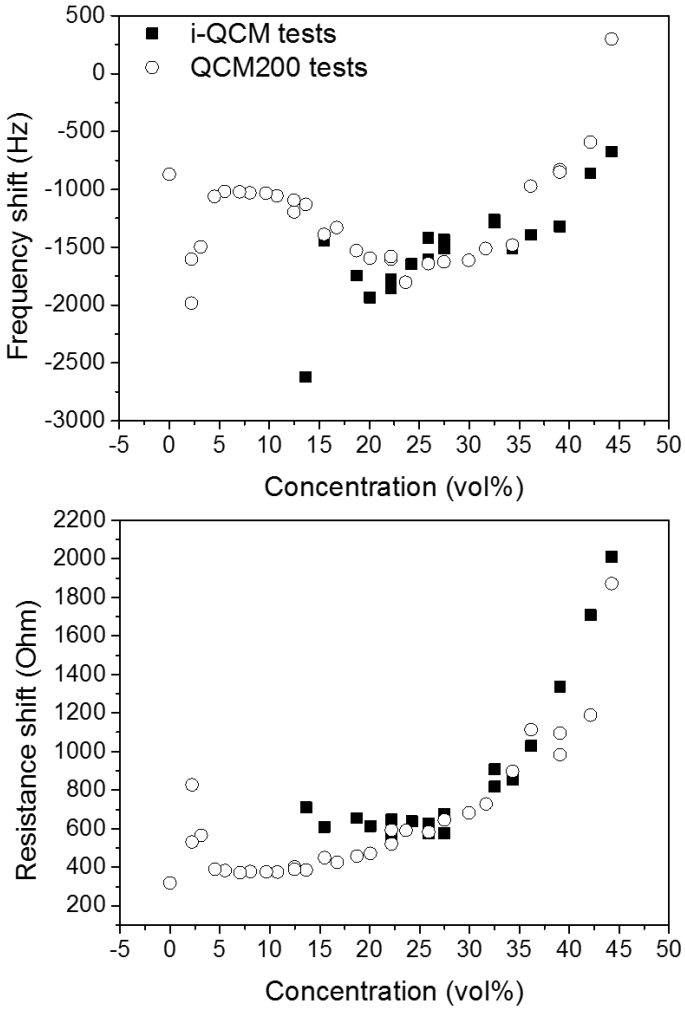


**Figure S6.1: Comparison between i-QCM concentration data and QCM200 concentration data for $Mg(OH)_2$ suspensions.**

The i-QCM ZnO data at low concentrations has been compared to theoretical predictions for water and 10 wt% glucose using the Kanazawa relationship which is shown in Equation S6.1 [18, 26].

$$\Delta f = \frac{f_0 (\rho_L \mu_L f)^{1/2}}{\sqrt{\pi} Z_q} \qquad \textbf{Equation S6.1}$$

Where $\Delta f$ = air-to-sample resonance frequency shift (Hz), $f_0$ = unloaded sensor frequency at the fundamental mode ($5 \times 10^6$ Hz), $\rho_L$ = fluid density (997 kg/m$^3$ for water and 1037.5 kg/m$^3$ for 10 wt% glucose), $\mu_L$ = absolute viscosity of the fluid (0.00089 Pa.s for water and 0.00177 Pa.s for 10wt% glucose), $f$ = unloaded sensor

frequency (Hz) (this value is directly proportional to the sensor overtone), $Z_q$ = acoustic wave impedance of AT-cut quartz ($8.8 \times 10^6$ kg m$^{-2}$ s$^{-1}$).

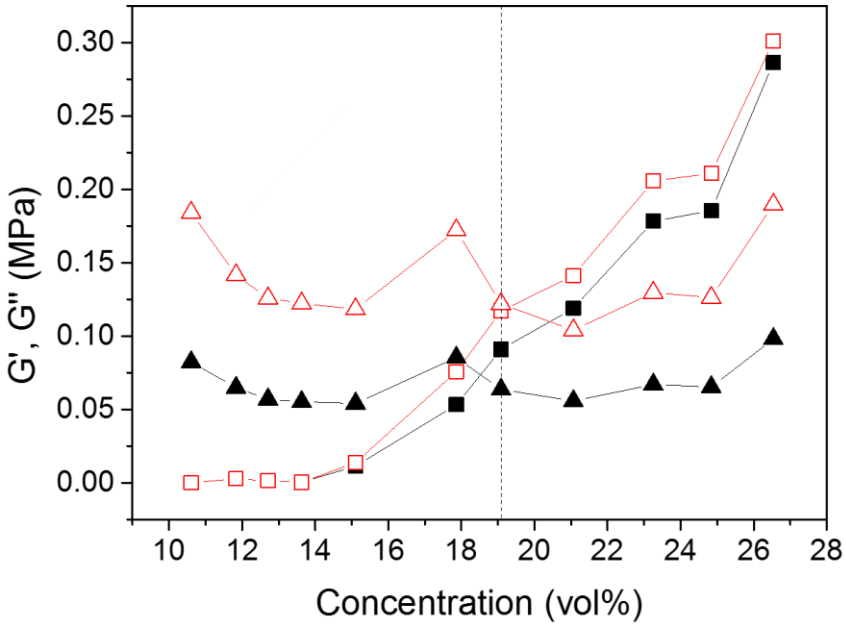


**Figure S6.2: Calculated QCM storage modilu (G', squares) and loss moduli (G'', triangles) as a function of ZnO suspension solids concentration. The viscoelastic parameters at 15 MHz (~95.25 $\times 10^6$ rad/s, black closed symbols) and 35 MHz (~219.91 $\times 10^6$ rad/s, red open symbols) are compared. The transition point from viscous dominated to elastic dominated behaviour is shown as a dashed line.**

There is an expected frequency dependence on the viscoelastic properties of the suspension present, however the transition from G' to G'' dominated behaviour occurs at the same concentration throughout the different frequency ranges considered (the transition point however does appear to reduce to lower solids concentrations with reducing frequency). Both G' and G'' appear to increase with increasing experimental frequency. The suspension may appear stiffer as its network is probed at higher frequencies, however there may also be an increase in energy loss present. Figure 6.21 for example showed that the possible onset of gross particle slip is significantly more apparent, indicating that particle links may be broken more easily at higher experimental frequencies due to a possible lower suspension yield strain [52].

# 7. Conclusions

This project investigated the hypothesis that changes in the quartz crystal microbalance (QCM) sensor frequency and dissipative response can be correlated to changes in the bulk rheology of concentrated suspensions.

Initial tests were performed on two comparable $Mg(OH)_2$-based systems: Versamag A and Versamag B. Versamag A contained a significantly greater apparent MgO (periclase) content (~16.6 wt% for Versamag A vs. ~11.5 wt% for Versamag B) that decreased when it was left over a period of 70 hrs as a 22 vol% suspension in water. The Versamag A particles were also predominantly composed of $Mg(OH)_2$ (Brucite) crystallites that were significantly thinner than those from Versmag B (Scherrer crystallite size = ~20 nm for versamag A and ~45 nm for Versamag B before hydration commenced). The reduction in apparent MgO content correlated with an increase in the bulk shear yield stress of the suspension using conventional vane viscometry, where Versamag A showed a significantly greater increase in yield stress over time compared to Versamag B (~490% vs. ~46%, respectively). Comparable QCM measurements were performed where significantly larger air-to-sample frequency shifts ($\Delta F$) and dissipation shifts ($\Delta R$ or $\Delta \Gamma$) were also observed for Versamag A, which correlated well with the increase in suspension shear yield stress. The QCM data revealed that a 2-phase reaction process could be present indicating a possible dissolution followed by precipitation process. The QCM $\Delta F$ response also showed large positive shifts (+1000 Hz after 70 hrs) indicating that a frequency enhancing force is present. The rate of change of $\Delta F$ was also greater in the precipitation stage of the hydration reaction. The QCM point contact load mechanics described by Dybwad, Pomorska et al. and D'amour et al. [1-3] suggests that a frequency restoring force is possible when the particles linked to the sensor is fixed in space and vibrate

at a significantly lower frequency compared to the QCM frequency of oscillation. The suspension network may therefore stiffen through the chemical dissolution of MgO, where it then reacts with $H_2O$ to form $Mg(OH)_2$ that will make the solution supersaturated, causing $Mg(OH)_2$ precipitation on already existing surface sites which binds neighbouring particles together. Small $Mg(OH)_2$ crystallites may also preferentially undergo dissolution and subsequent precipitation onto larger sites due to Ostwald ripening effects. The stiffer particle clusters will therefore appear larger and therefore have a lower frequency of vibration. The stiffer links will cause them to also remain fixed in space, causing more positive $\Delta F$ and $\Delta R$ values as the particles also resist motion from the resonator to a greater extent.

Bulk solids concentration tests on hydrated Versamag B have also been performed. The suspension followed an expected exponential increase in shear yield stress with increasing concentration. QCM $\Delta R$ shifts have also shown similar trends where a log-log plot of $\Delta R$ vs. yield stress revealed a straight-line fit. An increased number of particles will also increase the number of particle-particle links, which stiffens the suspension network structure (increased yield stress) causing particles linked to the sensor to resist a greater amount of impeded motion from the sensor. The QCM $\Delta F$ response however showed a 'more negative' followed by a 'more positive' trend transition that cannot be explained using the current information available. The response may be due to a combination between the point contact load mechanics of the suspension, how the QCM signal could potentially travel across particle networks that now include additional particles or even the viscoelasticity of the suspension itself. The QCM has nevertheless shown that its sensor oscillation dampening response can be correlated to the bulk suspension yield stress when the overall

particle-particle interaction strengths are altered and that the $\Delta F$ and $\Delta R/\Delta\Gamma$ responses appear to be independent from one-another.

These initial tests only investigated changes in particle-particle interaction strengths. The $Mg(OH)_2$ suspensions are self-buffering meaning that the charge characteristics of both the gold coated QCM sensor and suspension particles always remained constant. To investigate whether changes in the particle-sensor interactions could play a role in the overall QCM response, pH tests on high surface area to volume ratio $TiO_2$ (anatase) suspensions were performed. A 16.2 vol% suspension of these particles showed significant changes in its shear yield stress with suspension pH (64 Pa at pH 6 vs. 0 Pa at pH 4.4). A peak of greatest yield stress was observed near the isoelectric point of the suspension (pH 6 – 6.6). Atomic force microscopy (AFM) experiments were performed using a cantilever mounted with a spherical $TiO_2$ particle to represent the suspension particles. The 'attractive force' was obtained by measuring the cantilever deflection obtained when the particle approaches the sensor gold surface within a pH-adjusted solution. The observed trends were similar to calculations made using the Hogg, Healey and Fuerstenau model (HHF model), which is based on DLVO theory. The QCM $\Delta F$ and $\Delta R/\Delta\Gamma$ response showed to correlate more closely with the AFM data and the HHF model than changes in its bulk shear yield stress. The significantly stronger $TiO_2$-gold interaction compared to $TiO_2$-$TiO_2$ interactions may therefore result in the $TiO_2$-gold interaction behaviour to dominate the QCM response. The QCM response has therefore shown to be sensitive to changes in the particle-sensor interaction strength, with stronger interactions resulting in a more negative $\Delta F$ due to more of the particle's mass being detected and a larger $\Delta R/\Delta\Gamma$ response is measured since a stronger link will result in a greater amount of transfer of vibrational energy from the sensor to the particles.

The majority of these tests have revealed that the QCM response can mostly be explained by making use of the 'point contact load model' described by Johannsmann, D. [4], and D'amour et al. [3]. The correlation the QCM response has to the bulk shear yield stress for Versamag B suspensions indicates that the QCM response may also be sensitive to the bulk viscoelasticity of the suspension network which does not form a part of the point contact load model [4]. QCM and vane viscometry concentration tests were performed on zinc oxide suspensions that are expected to be strongly attracted to the QCM resonator surface. The QCM dissipation response once again correlated well to the bulk shear yield stress of the suspension, confirming that the correlation is present for other suspensions of differing chemical and physical nature. The QCM $\Delta F$ transition point also occurred at a much lower solids concentration than Versamag B, where the ZnO suspension showed a more positive $\Delta F$ and $\Delta\Gamma$ response within the concentration range of interest. The QCM data was then compared to the viscoelastic model described by Johannsmann, D. [4] using acoustic multilayer formalism to obtain high frequency storage moduli (G') and loss moduli (G'') values for the suspension at different solids concentrations. These calculated viscoelastic parameters were compared to those obtained using conventional rheometry experiments for the same suspension of varying concentration. A direct correlation was observed between the calculated high frequency QCM G' and the low frequency rheometer G', indicating that both instruments detect a similar change in the viscoelasticity of the suspension as its concentration is increased. The QCM is therefore capable of measuring the viscoelastic changes of the ZnO suspension as its bulk solid concentration changes.

The QCM however detects the suspension as behaving more as a fluid than an elastic solid when it's data is compared to rheometer experiments (i.e. lower G' and higher

G" values are obtained for QCM experiments). This response may be due to three following factors. It was firstly revealed that when the QCM resonance frequency is automatically changed for measurements at different overtones, disruption in the suspension network occurs, potentially causing the suspension network to be broken down near the resonator surface. This effect was found to be more significant at lower solids concentrations where the particle networks are weaker. The QCM will therefore detect the suspension as being less elastic and more fluid-like in behaviour as a result. An increase in experimental frequency (i.e. ~1.6 Hz for rheometer data vs. 5 MHz for QCM data) may result in a reduction in the yield strain of the suspension, causing the strain from the QCM oscillation to cause network breakdown, resulting in the suspension behaving more fluid-like as a result. There is also be an inefficient transfer of vibrational energy from the sensor to the particles, where the findings from the $TiO_2$ pH tests have shown this effect to be possible. Amplitude tests on the ZnO suspension further revealed that there are significant changes in the QCM response when the nature of the particle-sensor interaction is changed, and that there is evidence of partial or gross slip behaviour where the particles do not follow the sensor oscillation entirely. This effect will result in less of the vibrational energy from the QCM to be stored in the particle-particle networks, but will instead be lost when it is spent during particle link deformation, resulting in lower G' values and higher G" values. Despite these effects, the close correlation of QCM data to other conventional methods of rheology measurements have shown that the QCM response when it is submerged into concentrated particulate suspensions can therefore be correlated to these conventional bulk rheological parameters which can be described by both the point contact load model and the QCM viscoelastic model. The relative contribution from each depends on the chemical and physical properties of the suspension and the nature of the experiment involved.

## 7.1. References


1. Dybwad, G.L., *A Sensitive New Method for the Determination of Adhesive Bonding between a Particle and a Substrate.* Journal of Applied Physics, 1985. **58**(7): p. 2789-2790.
2. Pomorska, A., et al., *Positive Frequency Shifts Observed Upon Adsorbing Micron-Sized Solid Objects to a Quartz Crystal Microbalance from the Liquid Phase.* Analytical Chemistry, 2010. **82**(6): p. 2237-2242.
3. D'amour, J., et al., *Capillary Aging of the Contacts Between Glass Spheres and a Quartz Resonator Surface.* Physical Review Letters, 2006. **96**(5): p. 058301.
4. Johannsmann, D., *Viscoelastic, Mechanical, and Dielectric Measurements on Complex Samples with the Quartz Crystal Microbalance.* Physical Chemistry Chemical Physics, 2008. **10**(31): p. 4516-4534.

# 8. Future Recommendations

Chapter 5 has shown that the QCM response for concentrated suspensions is dependent on the strength of the particle-sensor interaction. The QCM has shown to be promising for measuring bulk rheological effects when the charge of the particles remained the same (i.e. the sensor surface/particle zeta potential ratio, $\frac{\zeta_S}{\zeta_P}$, remained the same). When $\frac{\zeta_S}{\zeta_P}$ changes, the QCM response will change, where a change in response due to changes in interaction strength can be significantly larger than viscoelastic or yield stress changes from the bulk suspension itself. If the bulk suspension effects are therefore to be known during pH testing, $\frac{\zeta_S}{\zeta_P}$ needs to be kept the same across the pH range. There are 2 main ways of keeping $\frac{\zeta_S}{\zeta_P}$ the same during pH testing, firstly by coating the resonator surface with a different material (i.e. $TiO_2$ coating for $TiO_2$ particles) and to control the charge of the sensor surface by applying an electrical potential through the sensor surface to control its charge. The two methods will briefly be described.

## 8.1. QCM sensor coating

The sensor can be coated manually by following the method outlined by Ichinose et al. [1]. The method is basically as follows. The QCM gold surface is firstly modified by immersing it into 10 mM mercaptoethanol in ethanol for 12 hrs [1]. This functionalises the gold surface where a large number of hydroxide species adsorb firmly to its surface as illustrated in Figure 8.1 [1]. The sensor is then immersed into 100 mM Ti-alkoxide in 1:1 toluene/ethanol solution [1]. The immersion took place for ~20 min at 20℃ before being immersed into deionised water for 1 min [1]. The

crystal is then dried using $N_2$ gas. The process is then repeated for thicker films to develop (Fig. 8.1) [1].

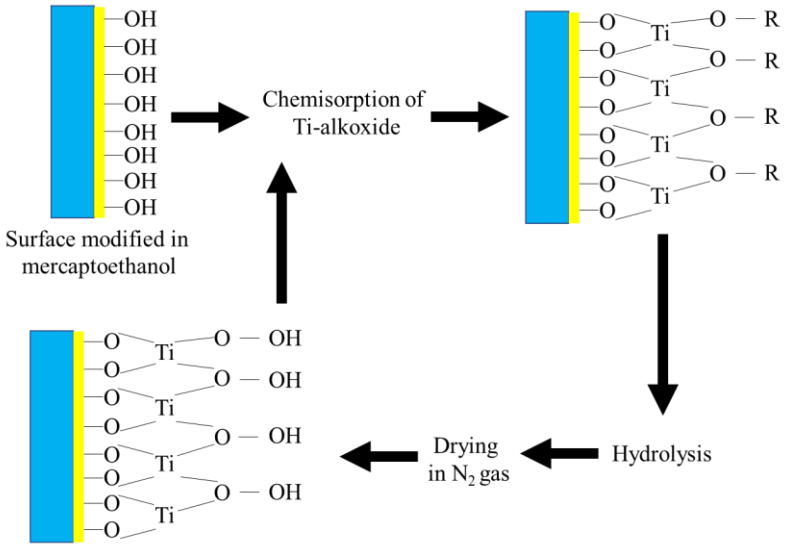


**Figure 8.1: $TiO_2$ sol-gel surface coating experimental procedure.**

Figure 8.2 shows the physical appearance of a QCM surface prepared in this way. It can however be seen that exposed gold may still be visible from in-between the cracks on the surface, and due to concerns with low penetration depths of the resonator, thin films that completely coat the resonator surface is preferred.

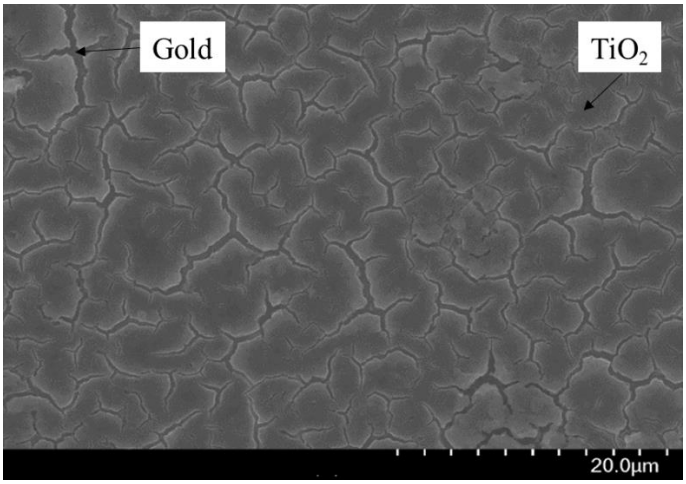


**Figure 8.2: Scanning electron microscopy (SEM) image showing the physical appearance of a $TiO_2$ coated QCM resonator surface using the sol-gel process.**

Alternatively, the $TiO_2$ layer can be sputter-coated onto the resonator surface where $TiO_2$ vapour hits the gold surface target, producing thin, evenly dispersed films. Crystals with a sputter coated $TiO_2$ layer was purchased from Renlux Crystals, China. An EDX-mapping was performed on the crystal cross-section at the centre of the crystal, showing the presence of $TiO_2$ on the sensor surface (Fig. 8.3).

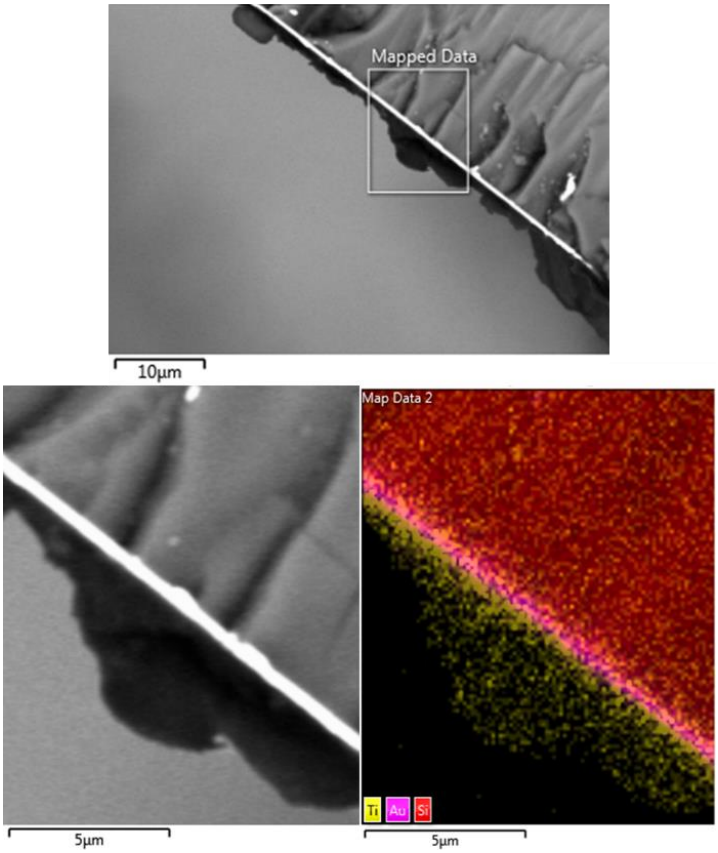


**Figure 8.3: SEM-EDX image showing the chemical composition across the central cross section of the sputter coated $TiO_2$ sensors. A small layer of gold (violet0 is seen coating the top of the Si-based (red) sensor. A layer of Ti (yellow) is present on top of the gold layer. The apparent non-uniformity of this layer is flaking from when the sensor was broken to provide access to its central cross-section.**

An X-ray diffraction analysis of the crystals revealed a single peak for gold in the (111) crystal orientation (Fig. 8.4). The sputter coating process may heat the gold surface up to temperatures where sintering is possible, causing the formation of crystals at a single orientation on the resonator surface. No anatase or rutile peaks were observed, suggesting that the surface may be amorphous, or contain small

crystallites where the diffraction pattern for the gold overshadowed any smaller patterns that could be obtained from the $TiO_2$ surface (it is worth noting that the gold (111) peak was at an extremely high intensity, which would result in lower intensity diffraction patterns to be overshadowed).

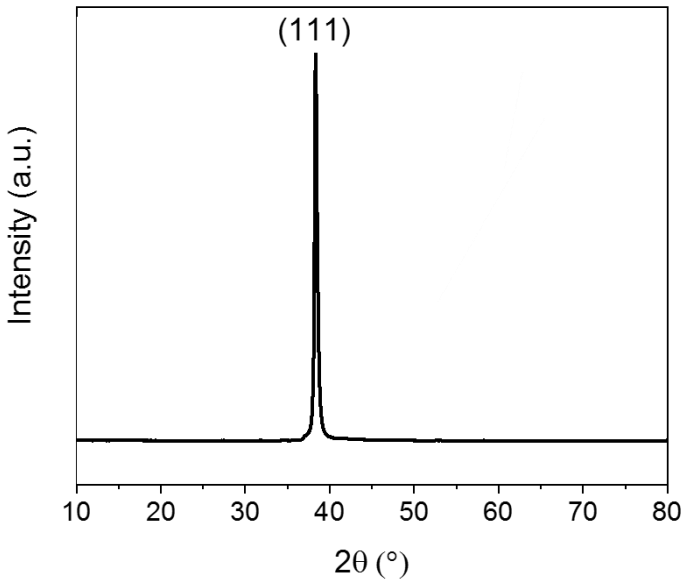


**Figure 8.4: X-ray diffraction pattern of the $TiO_2$ sputter coated gold QCM sensor. Only a gold (111) peak is observed suggesting that the process may cause sintering and that there is no clear crystal structure for the adsorbed $TiO_2$ layer.**

Surface zeta potential measurements of the $TiO_2$ sensors revealed a bulk surface charging behaviour similar to the gold sensors (Fig. 8.5) implying that either the highly charged gold affects the charging behaviour of the overlaying $TiO_2$ or the $TiO_2$ follows the charging behaviour of its rutile phase, with an isoelectric point at near pH ~3.5 [2].

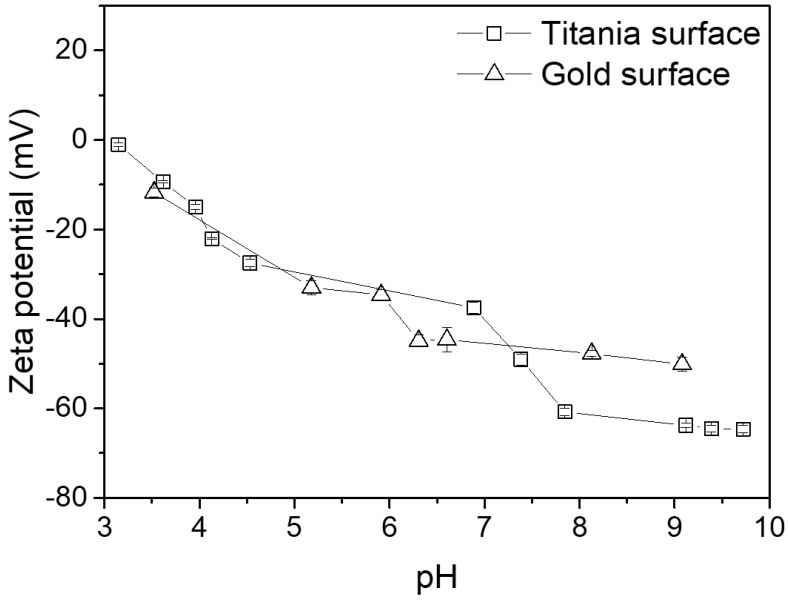


**Figure 8.5: Comparison between the charging behaviour of the $TiO_2$ sputter coated sensor (open squares) to its uncoated gold sensor counterpart (open triangles).**

By investigating the QCM response on pure rutile $TiO_2$ particles, $\frac{\zeta_S}{\zeta_P}$ should be relatively constant, allowing potentially for non-surface specific bulk rheological characterisations to be made. Unfortunately, due to time constraints and the inability to source high surface-area-to-volume ratio rutile phase $TiO_2$ suspension particles, this experiment could not be performed. Instead, QCM200 experiments were performed on Hombitan S141 and ANX Type-N, both of which are high surface area anatase suspensions with a similar charge behaviour (see Chapter 5). Interestingly, from Figure 8.6, the QCM resistance shift ($\Delta R$) response (proportional to $\Delta\Gamma$) shows a peak at the isoelectric point for the two anatase-based suspensions. No significant corresponding change in the $\Delta F$ response is observed. Apart from this peak at pH ~6.6, the QCM response is similar to the data described in Chapter 5.

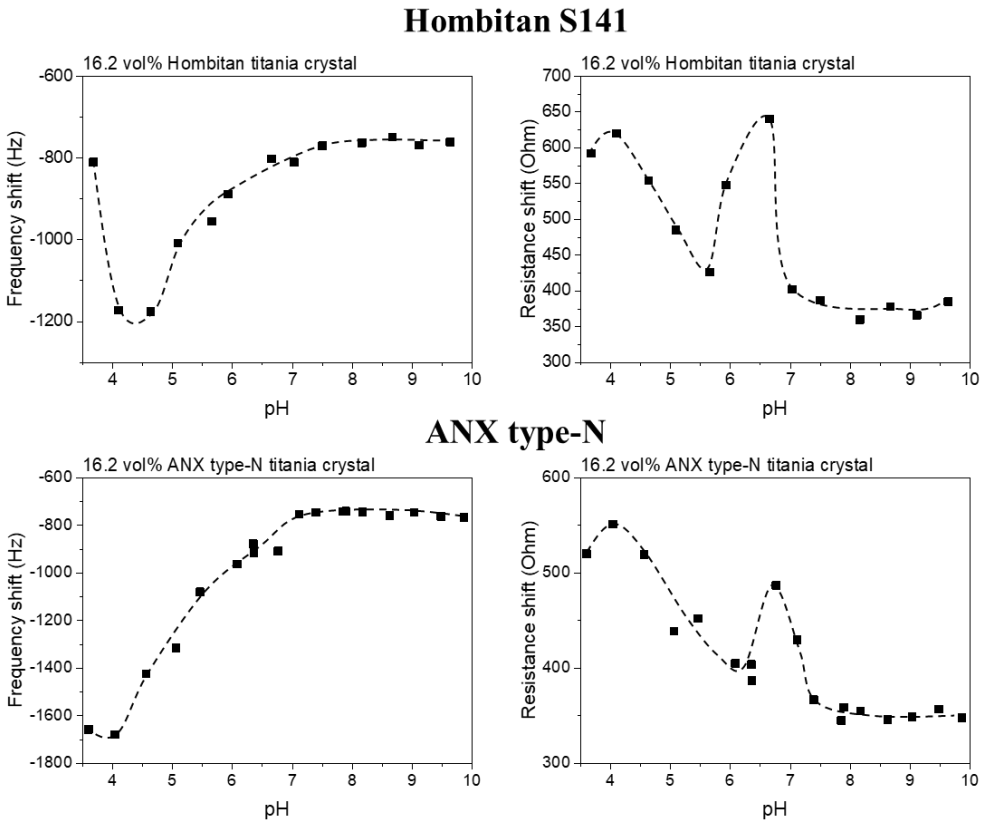


**Figure 8.6: QCM200 tests on 16.2 vol% Hombitan S141 (top) and ANX type_N (bottom) using the $TiO_2$ coated sensor. Dashed lines are to guide the eye only.**

The $TiO_2$ phase may therefore not be dominated by a rutile phase alone, but some anatase may be present, causing anisotropic surface properties. At pH ~6.6, both the particles and a few small areas on the sensor may be at its isoelectric points, causing a significant reduction in the intensity of the electrical double layer surrounding its surfaces. The particles will therefore come into a closer proximity, however due to the strong overall charge of the sensor, no significantly strong links are formed across the sensor surface. The close proximity of the particles may however still cause an increased amount of collisions at this pH (see Chapter 5 for a more in-depth explanation on the potential effects of particles in close proximity).

Additional characterisation on sputter coated surfaces (i.e. their crystal structure) and the QCM behaviour when the resonator is submerged into single-crystal phase isotropic suspensions with a similar charge behaviour to the sensor would be advised.

This could potentially allow for differences in the QCM frequency and dissipation signal to be measured which would help confirm the idea that particle proximity without link formation may affect QCM dissipation but not oscillation frequency.

## 8.2. Electrochemical quartz crystal microbalance (EQCM)

The QCM sensor surface charge can be controlled by maintaining an electrical potential through its surface. In addition, if the electrical circuit passes through a suspension containing a sufficient amount of background electrolyte, the local pH of the suspension will be altered as well, allowing for pH tests of the sludge to be performed without the need to manually add additional acid or base. This would also enable for pH tests to be performed during industrial application on samples that are not easily accessible.

The EQCM is essentially comprised of a metallic conductor that is placed in-between the resonator surface and the bulk sample (Fig. 8.7). An electrical circuit is formed by connecting both the resonator surface and the metallic conductor to a potentiostat (e.g. Potentiostat/Galvanostat from Gamry Instruments) which allows for the potential difference across the two surfaces to be controlled (Fig. 8.7). If a negative potential of -X volts is applied, the surface charge will become negative relative to the metallic conductor. From DLVO theory we know that for a negative surface charge to form, negative ions will be present on the resonator surface (i.e. the resonator surface is actually positive, but strongly adsorbed counterions makes it negative). This results in ions leaving the bulk sludge. The pH of the sludge will therefore reduce by a fixed amount due to an excess in positively charged ions (+Y). In the opposite case, a +X change in voltage would result in a -Y pH change in the sludge. The change in interaction between the sludge and sensor surface would therefore be the same amount

since $\frac{\zeta_S}{\zeta_P}$ will remain the same. The only parameter that therefore changes is the bulk particle-particle interactions resulting from local pH changes. This would theoretically allow for bulk rheological changes to be measured with changing suspension pH.

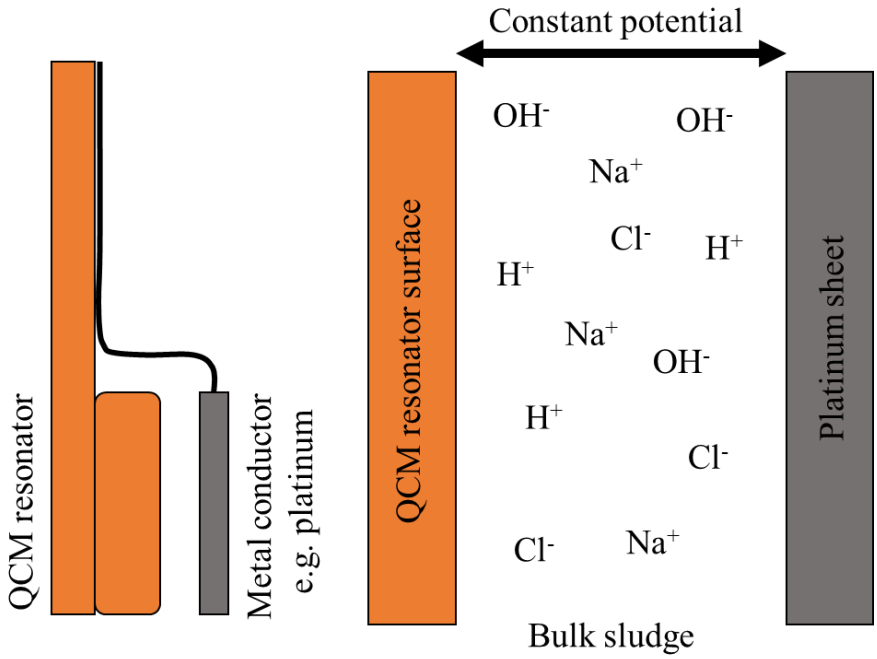


**Figure 8.7: Schematic showing the concepts behind an electrochemical QCM when it is submerged into a sludge with NaCl background electrolyte. A constant potential is applied between the QCM surface and platinum sheet, allowing for the particle-sensor interaction to be controlled which would also result in bulk suspension rheological changes as its pH is altered as a result as well. The pH of the sludge can be estimated by using the Nernst equation: $E = E_0 - 15.1\ \text{mV} \times \text{pH}$, where $E$ = measured voltage (mV) and $E_0$ = open circuit potential (mV) [3].**

Initial proof of concept tests was performed using an EQCM setup (many thanks to professor Diethelm Johannsmann, Judith Petri and Astrid Peschel from the Technical University of Clausthal for their support and technical input). A 16.2 vol% Hombitan S141 suspension was firstly left to equilibrate for 1 month (final pH = 4.7, initial pH adjustments were made). The suspension had to be left for a long period of time due to the high sensitivity of the experiment. The EQCM was submerged into the suspension using the same method throughout this study. The potential difference

across the sensor was then slowly changed from 0.5 V to -1 V over 2 hours, then from -1 V back to 0.5 V over 2 hours. This process repeated automatically over a period of 36 hrs where eventually the QCM response became stable (Fig. 8.8). Care was taken to not go beyond this range since the gold coating on the sensor may then be destroyed.

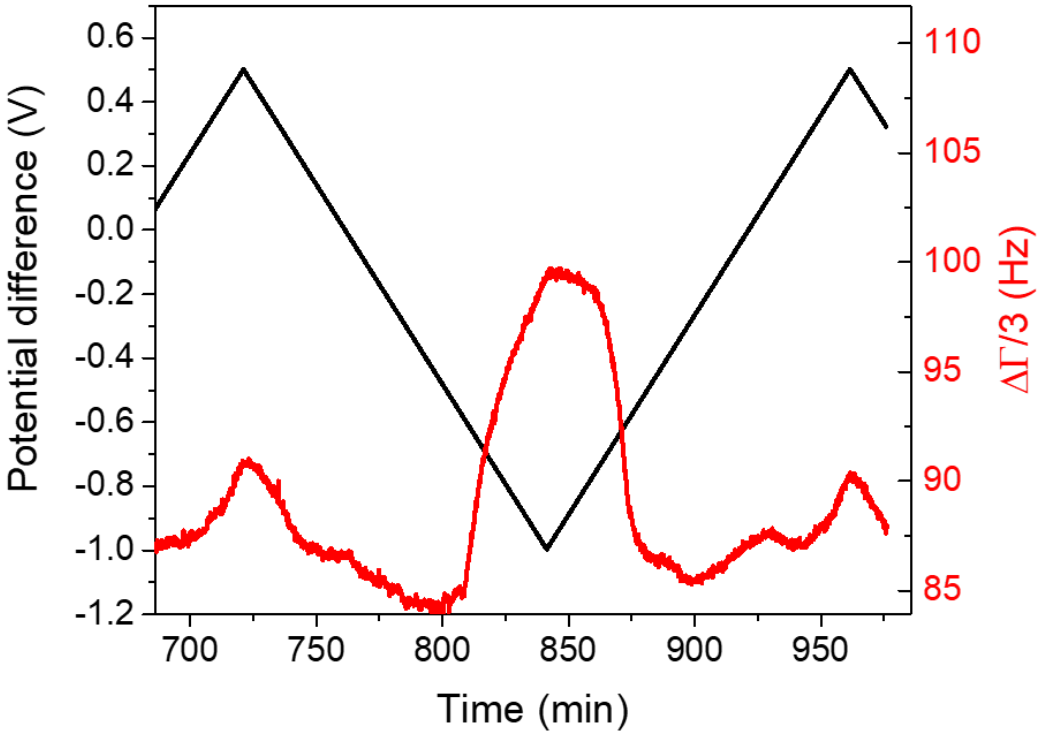


**Figure 8.8: 16.2 vol% Hombitan S141 in 10 mMol NaCl electrolyte EQCM stable ΔΓ/n response at n = 3 (red line, right axis) during changes in potential difference across the circuit (black triangular line, left axis).**

The QCM showed clear changes in its response. By plotting the obtained ΔΓ response as a function of the applied potential difference (time difference between the applied potential difference and the sludge response is considered) from Figure 8.8, the trend shown in Figure 8.9 is obtained.

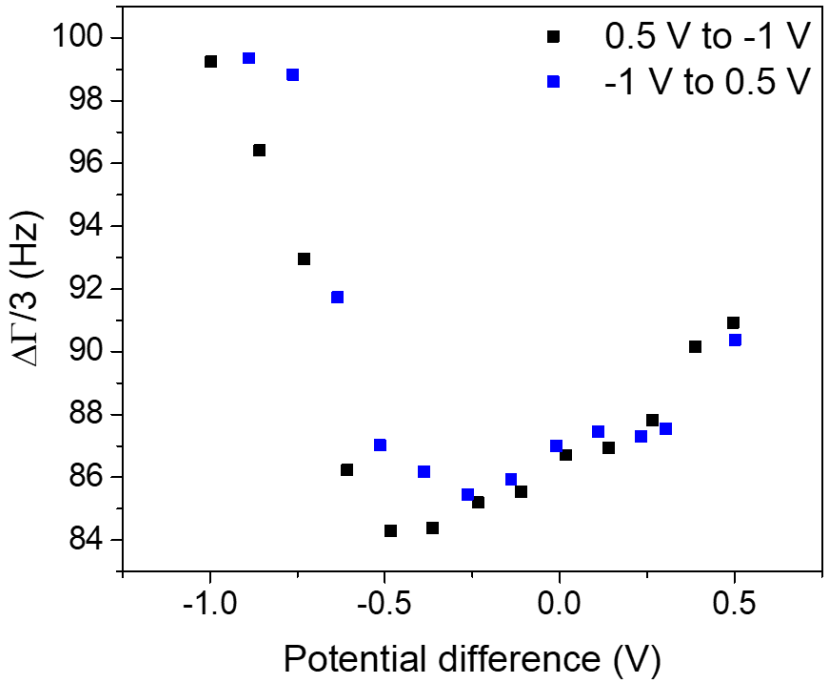


**Figure 8.9: Obtained QCM ΔΓ/n response at n = 3 as a function of applied potential. The 0.5 V to -1 V cycle (black squares) show a similar trend to the -1 V to 0.5 V cycle apart from the region near -0.5 V, which may suggest that the system may not have fully equilibrated despite the experiment continuing for over 36 hrs at this point.**

The response in Figure 8.9 represents the inverse of the Hombitan S141 bulk suspension yield stress (see Chapter 5). A comparison between the suspension yield stress and $1/\Delta\Gamma_{n=3}$ is shown in Figure 8.10. A close comparison is observed, indicating that it could be possible for *in-situ* bulk suspension tests to be performed without the need for operator sampling.

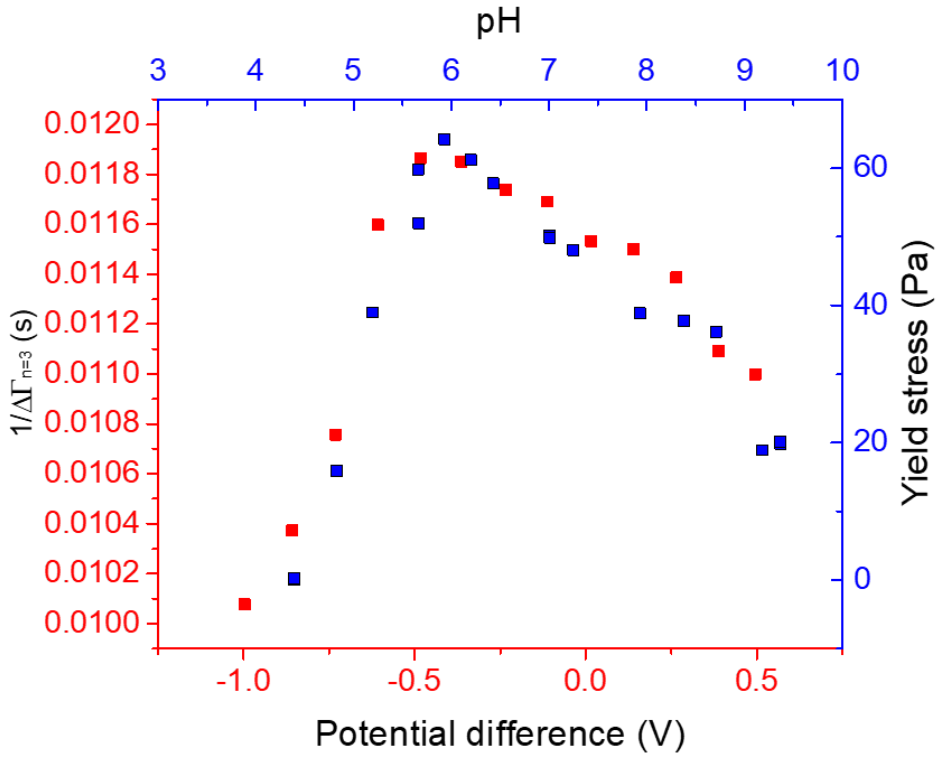


**Figure 8.10: Comparison between the EQCM ΔΓ/n response at n = 3 (red squares) for 16.2 vol% Hombitan S141 to its bulk shear yield stress with changing suspension pH (blue squares).**

More tests are however required (i.e. repetitive results across different experiments) and additional tests that focus on improving the stability of the system (i.e. effect of electrolyte concentrations). EQCM tests on bulk concentrated suspensions could however show interesting results that may add to the usability of the device for on-site deployment.

## 8.3. pH measurements on suspension particles consisting of anisotropic surface properties

The pH response of 22.5 vol% kaolinite was investigated to observe how the QCM response compares to conventional vane viscometry for more complex systems. The yield stress response of the kaolinite with changing suspension pH was found to compare well with literature data [4] (Fig. 8.11).

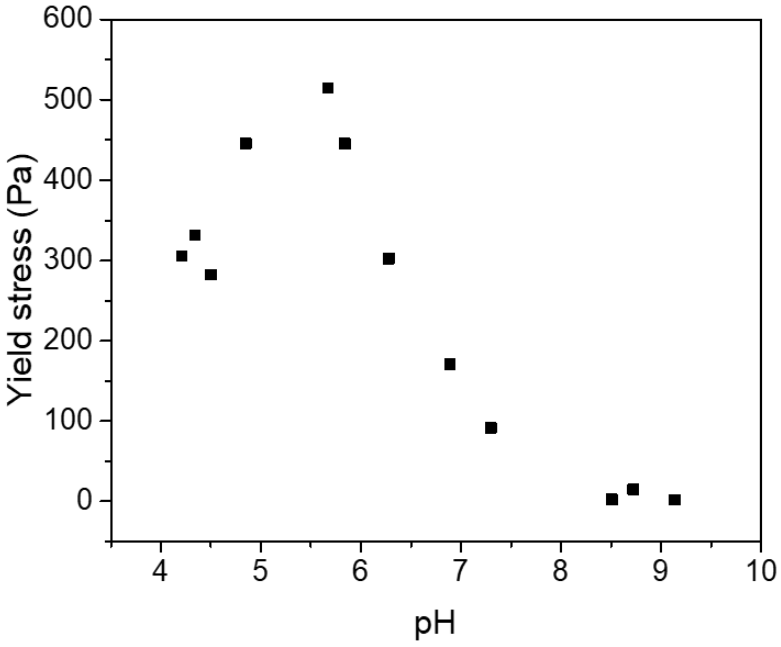


**Figure 8.11: Yield stress measurements on 22.5 vol% kaolinite in 10 mMol NaCl electrolyte. The experimental procedure was the same as that for Hombitan S141 outlined in Chapter 5.**

QCM200 measurements have been performed on similar suspensions of the same composition (Fig. 8.12A and B). The ΔR response (Fig. 8.12B) appears to follow the suspension yield stress behaviour closely, where both the yield stress (Fig. 8.11) and ΔR response (Fig. 8.12B) increases from pH ~4 to a maximum value at pH 5.5. Both the yield stress and ΔR then decrease from pH 5.5 to pH ~7.5. The yield stress then reaches a minimum value, however the QCM ΔR response still experiences a

decrease, possibly due to a relatively weaker interaction strength that also result in lower ΔF shifts (Fig. 8.12A).

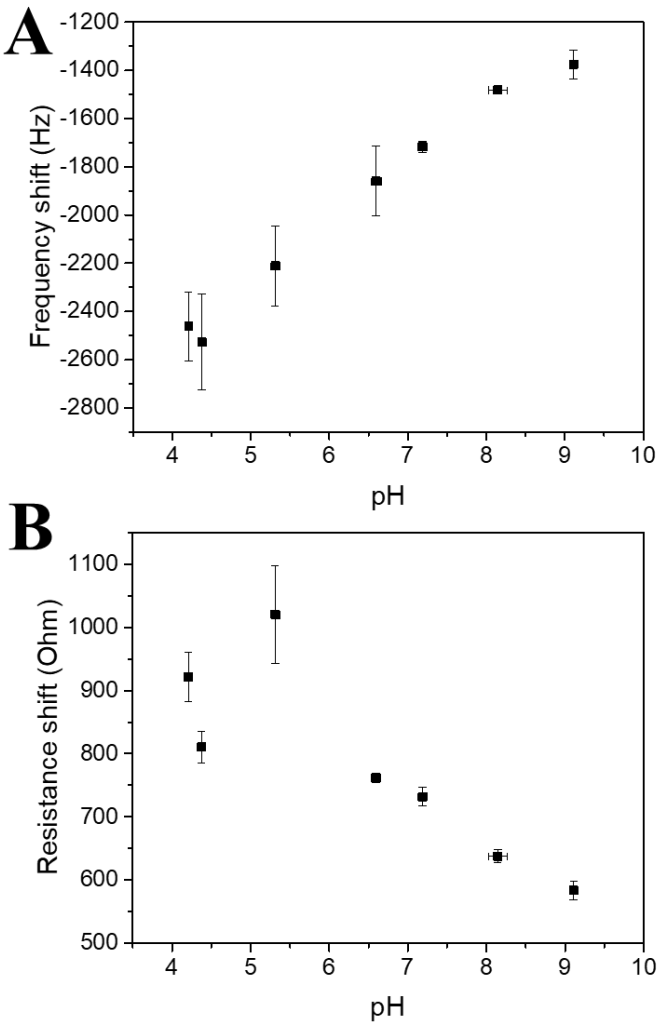


**Figure 8.12: QCM200 Frequency (A) and resistance (B) response for 22.5 vol% kaolinite in 10 mMol NaCl electrolyte with changing pH. The experimental procedure was the same as that for Hombitan S141 outlined in Chapter 5.**

The QCM ΔF response for this suspension may be a result of complex particle-sensor and particle-particle interactions within the near vicinity of the resonator surface and is therefore poorly understood. The good correlation between the QCM ΔR response and the bulk suspension yield stress is for this reason also poorly understood. Future work investigating the mechanism why this QCM response is observed for complex systems such as kaolinite is recommended. The near-surface structure of the kaolinite

clay particles could be probed using atomic force microscopy or cryogenic scanning electron microscopy and compared to literature describing the contact mechanics of kaolinite when each surface site experiences a different zeta potential [5]. This would however be a step after the aforementioned topics where a greater understanding between the differences in the QCM frequency and dissipation signal response when exposed to concentrated suspensions at varying pH is better understood.

## 8.4. Improvements to suspension viscoelasticity measurements

Chapter 6 has shown us that it is possible to measure changes in bulk viscoelasticity of concentrated particulate suspensions. The operational frequency of the QCM (MHz range) makes direct numerical comparisons to rheometer data (Hz range) difficult. The high frequencies of the QCM resonator may also result in a significant reduction in its penetration depth, meaning that less of the bulk suspension properties are measured. The low penetration depth implies that a larger portion of the signal will be surface sensitive, resulting in a greater amount of the signal to be lost due to particle-sensor link deformation (refer to amplitude tests in Chapter 6).

To overcome these potential downsides, QCM viscoelastic measurements should be performed using torsional resonators instead. Torsional resonators operate in the kHz frequency range, which would be more representative of rheometer data. The lower frequencies would also result in increased penetration depths, causing a greater portion of the QCM signal to represent the bulk particle-particle network viscoelastic behaviour. The amplitude of sensor oscillation should also be kept low (this can be done by changing the voltage input to the QCM device). A lower amplitude of oscillation would cause a reduction in partial slip and gross slip effects from taking place, resulting in an increased efficiency of energy transfer to the bulk sludge.

In addition to this, the QCM resonator vibrational energy dissipation pathways when the QCM surface is exposed to a particulate suspension could be modelled to better explain the effects responsible that result in the final QCM shifts.

## 8.5. References


1. Ichinose, I., H. Senzu, and T. Kunitake, *A Surface Sol-Gel Process of TiO2 and Other Metal Oxide Films with Molecular Precision*. Chemistry of Materials, 1997. **9**(6): p. 1296-&.
2. Graham, K. and J. Madeley, *Relation Between the Zeta Potential of Rutile and its Flotation with Sodium Dodecyl Sulphate*. Journal of Applied Chemistry, 1962. **12**(11): p. 485-489.
3. Eggins, B.R., *Chemical Sensors and Biosensors*. Vol. 28. 2008: John Wiley & Sons.
4. Johnson, S.B., et al., *Surface Chemistry-Rheology Relationships in Concentrated Mineral Suspensions*. International Journal of Mineral Processing, 2000. **58**(1-4): p. 267-304.
5. Chen, Q., et al., *QCM-D Study of Nanoparticle Interactions*. Advances in Colloid Interface Science, 2015.

# 9. Publications, Conferences, Awards and Scholarships

## 9.1. Publications directly associated with thesis

Botha, Johannes A, Timothy N Hunter, Weixuan Ding, Simon Biggs, Graham A Mackay, Robin Cowley, Simon E Woodbury, and David Harbottle. A Novel Technology for Complex Rheological Measurements. WM2016 Conference Proceedings: WM Symposia, 2016.

Botha, Johannes A, Weixuan Ding, Timothy N Hunter, Simon Biggs, Graham A Mackay, Robin Cowley, Simon E Woodbury, and David Harbottle. "Quartz Crystal Microbalance as a Device to Measure the Yield Stress of Colloidal Suspensions." Colloids and Surfaces A: Physicochemical and Engineering Aspects 546 (2018): 179-85.

## 9.2. Other publications

Ding, Weixuan, Johannes A Botha, Bruce C Hanson, and Ian T Burke. "Synthesis of Calcium Monouranate Particles Via an Aqueous Route." MRS Advances 1, no. 62 (2016): 4123-29.

Ding, Weixuan, Johannes A Botha, Bruce C Hanson, and Ian T Burke. "Aqueous Hydroxylation Mediated Synthesis of Crystalline Calcium Uranate Particles." Journal of Alloys and Compounds 688 (2016): 260-69.

## 9.3. Conferences

DISTINCTIVE 1st Annual Meeting, April 2015, Sheffield, UK. Poster presentation.

Waste Management Symposium, March 2016, Phoenix, Arizona, USA. Oral presentation.

DISTINCTIVE 2nd Annual Meeting, April 2016, Bristol, UK. Poster presentation.

DISTINCTIVE 3rd Annual Meeting, April 2017, York, UK. Oral presentation.

Research Frontiers in Decommissioning and Radioactive Waste management, December 2017, Leeds, UK. Poster presentation.

8th World Congress on particle Technology, April 2018, Orlando, Florida, USA. Oral presentation.

## 9.4. Awards and Scholarships

NNL Waste Management 2016 Bursary.

Award for Best Collaboration at the 2017 Research Frontiers in Decommissioning and Radioactive Waste Management.